

Spectroscopic Studies on the Biomolecular Recognition of Medicinally Important Ligands

THESIS

**SUBMITTED FOR THE DEGREE OF
DOCTOR OF PHILOSOPHY (SCIENCE)**

OF

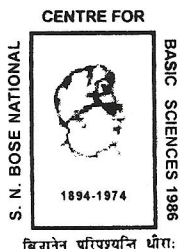
JADAVPUR UNIVERSITY

2014

BY

SOMA BANERJEE

**DEPARTMENT OF CHEMICAL, BIOLOGICAL AND
MACROMOLECULAR SCIENCES,
S. N. BOSE NATIONAL CENTRE FOR BASIC SCIENCES,
BLOCK JD, SECTOR III, SALT LAKE,
KOLKATA 700 098, INDIA**



सत्येन्द्र नाथ बसु राष्ट्रीय मौलिक विज्ञान केन्द्र
**SATYENDRA NATH BOSE NATIONAL
CENTRE FOR BASIC SCIENCES**

विज्ञानेन परिपश्यन्ति धीराः

CERTIFICATE FROM THE SUPERVISOR

This is to certify that the thesis entitled "Spectroscopic Studies on the Biomolecular Recognition of Medicinally Important Ligands" submitted by Smt. Soma Banerjee, who got her name registered on November 29, 2010 for the award of **Ph.D. (Science) degree** of **Jadavpur University**, is absolutely based upon her own work under the supervision of Prof. Samir Kumar Pal and that neither this thesis nor any part of it has been submitted for any degree/diploma or any other academic award anywhere before.


7th January 2014

(Signature of Supervisor/date with official seal)

Dr. SAMIR KUMAR PAL
Professor
S. N. Bose National Centre For Basic Sciences
Government of India
Block-JD, Sector-III, Salt Lake
Kolkata-700098

ब्लॉक जे० डी०, सेक्टर-३, साल्ट लेक, कोलकाता ७०००९८, BLOCK-JD, SECTOR III, SALT LAKE, KOKATA - 700 098

दूरभाष/ Phones : 0091-(0)33-2335 5705-8, 2335 3057/61, 2335 0312/1313

ई-मेल/ E-mail : root@bose.res.in

Webpage : <http://www.bose.res.in>

Fax : 0091-(0)33-2335 3477

FUNDED BY THE DEPARTMENT OF SCIENCE & TECHNOLOGY, GOVT. OF INDIA

निष्ठिवद्ध विज्ञान और प्रौद्योगिकी विभाग भारत सरकार द्वारा

To My Family

Acknowledgements

At this moment of accomplishment, I would like to express my heartfelt gratitude to Professor Samir Kumar Pal for giving me the opportunity to work under his supervision. This work would not have been possible without his valuable advice, constructive criticism and his extensive discussions around my work. His unflinching courage and conviction will always inspire me and I hope to continue to work with his noble thoughts.

I would also like to thank Dr. Rajib Kumar Mitra, S. N. Bose National Centre for Basic Sciences, Kolkata, India; Dr. Anirban Sidhanta & Dr. Debajit Bhowmik, Calcutta University, Kolkata (India), Prof. Gautam Basu, Bose Institute, India; Prof. Joydeep Dutta and Mr. Karthik Lakshman, Water Research Center, Sultan Qaboos University, Muscat, Oman and Prof. Masanori Tachiya, Advanced Industrial Science and Technology (AIST), Tsukuba (Japan) for fruitful collaborations. Great appreciation is extended to SNBNCBS staffs for their remarkable technical assistances in my research career. I owe a special thank to the University Grants Commission (UGC), India for my research fellowship, and Department of Science and Technology (DST), India for projects.

I would like to acknowledge my colleagues (Dr. Pramod Kumar Verma, Dr. Abhinandan Makhal, Ranajay, Tanumoy, Soumik, Subrata, Anupam, Surajit, Nirmal, Samim, Nabarun, Sushovan, Prosenjit, Dilip, Siddhi and Soumendra da) for providing a homely and cheerful environment, and also for assisting me in research. Specially, I have to thank Pramod da for introducing me to the experimental techniques and Siddhi for thesis proof-reading. I also want to thank all my friends for the good times I shared with them.

I would like to pay homage to my parents, for their blessings that have made me more courageous, dedicated and patient. I owe everything to them and they are the reasons for what I am today. I feel myself very fortunate to have Soumyadeep as my elder brother and Gargi as sister-in-law and Deepto and Dyuti as sweet nephew and niece, respectively. My acknowledgement looks incomplete without giving thanks to one of the most important persons of my life, Dr. Prashant Singh, my friend and fiancé. There are no words that can express my gratitude and appreciation for all that he have done and been for me.

Dated: 7th January, 2014
Department of Chemical, Biological
and Macromolecular Sciences,
S. N. Bose National Centre for Basic Sciences,
Block JD, Sec III, Salt Lake, Kolkata 700098, India.

Soma Banerjee
(Soma Banerjee)

Table of Contents

	Page
Chapter 1: Introduction	
1.1. Scope of the Spectroscopic Studies on the Biomolecular Recognition of Medicinally Important Ligands	1
1.2. Objective	4
1.3. Summary of the Work Done	7
I. Exploration of Molecular Details of a Model Medicinally Important Xanthine-Alkaloid Molecule, Caffeine in Aqueous Solution and Origin of its Interaction with Other Biologically Relevant Dyes/Drugs	7
A. Probing the Interior of Self-Assembled Caffeine Dimer at Various Temperatures	7
II. Interaction of Caffeine with a Model Fluorogenic Potent Mutagen Embedded in Various Biomimetic Self-Assemblies in Aqueous Medium	7
A. Caffeine Mediated Detachment of Mutagenic Ethidium from Various Nanoscopic Micelle: An Ultrafast Förster Resonance Energy Transfer Study	7
III. Spectroscopic Studies on the Interaction of Caffeine Molecules with a Potential Mutagen in DNA <i>in vitro</i> and <i>ex vivo</i> Conditions	8
A. Ultrafast Spectroscopic Study on Caffeine Mediated Dissociation of Mutagenic Ethidium from Synthetic DNA and Various Cell Nuclei	8

	Page
IV. Spectroscopic Studies on a Model Food Carcinogen in Various Restricted Environments: Exploration of the Molecular Basis for the Carcinogenic Activity	9
A. UVA Radiation Induced Ultrafast Electron Transfer from a Food Carcinogen Benzo[<i>a</i>]Pyrene to Organic Molecules, Biological Macromolecules and Inorganic Nano Structures	9
V. Ultrafast Spectroscopic Studies on the Nonradiative Energy Transfer from Various Vibronic Bands of the Food Carcinogen Benzo[<i>a</i>]pyrene in Various Biologically Relevant Environments in Aqueous Medium	9
A. A Potential Carcinogenic Pyrene Derivative under Förster Resonance Energy Transfer to Various Energy Acceptors in Nanoscopic Environments	9
1.4. Plan of Thesis	10
References	12

Chapter 2: An Overview of Steady-State, Dynamical, Theoretical Tools and Systems

2.1. Steady-State and Dynamical Tools	17
2.1.1. Solvation Dynamics	17
(i). Theory	17
(ii). Experimental Methods	22
2.1.2. Fluorescence Anisotropy	25
(i). Theory	26
(ii). Experimental Methods	28
2.1.3. Arrhenius Theory of Activation Energy	30
2.1.4. Förster Resonance Energy Transfer (FRET)	31

	Page
(i). Distance Distribution in Donor-Acceptor systems	34
2.1.5. 'Infelta-Tachiya' Model (Kinetic Model)	35
2.1.6. Adiabatic Compressibility	38
2.1.7. Twisted Intramolecular Charge Transfer	38
2.1.8. Photoinduced Electron Transfer	40
2.2. Systems	41
2.2.1. Organized Assemblies (Biomimetics)	41
A. Micelle	41
2.2.2. Proteins: Human Serum Albumin (HSA)	42
2.2.3. Deoxyribonucleic Acids (DNAs)	43
2.2.4. Molecular Probes	44
A. 4-[6'-(4-Methylpiperazino)-6,2'- bi[1H-benzimidazole]-2-yl]phenol, Hoechst 33258 (H258)	45
B. 4',6-Diamidino-2-phenylindole (DAPI)	45
C. Coumarin 500 (C500)	45
D. 2-p-toluidinonaphthalene-6-sulfonate (TNS)	45
E. Ethidium (Et)	45
F. 4-(dicyanomethylene)-2-methyl-6- (p-dimethylamino-styryl) 4H-pyran (DCM)	47
G. Acridine Orange (AO)	47
H. Crystal Violet (CV)	47
I. Benzo[<i>a</i>]pyrene (BP)	47
References	48

Chapter 3: Instrumentation and Sample Preparation

3.1. Instrumental Setups	54
3.1.1. Steady-State UV-Vis Absorption and Emission Measurement	54
3.1.2. Circular Dichroism (CD) Measurement	55
3.1.3. Time Correlated Single Photon Counting (TCSPC) Technique	57

	Page
3.1.4. Femtosecond-Resolved Fluorescence Upconversion Technique	58
3.1.5. Dynamic Light Scattering (DLS) Measurement	59
3.1.6. Fourier Transform Infrared (FTIR) Measurement	62
3.1.7. Density and Sound Velocity Measurement	63
3.1.8. Viscosity Measurement	64
3.1.9. Refractive Indices Measurement	65
3.2. Sample Preparation	66
3.2.1. Chemicals Used	66
3.2.2. Preparation of Micellar Solution	67
3.2.3. Preparation of Synthetic and Genomic DNA solutions	67
3.2.4. Preparation of Dye-DNA Complex	67
3.2.5. Preparation of BP-Protein Complex	67
3.2.6. Sample Preparation for Cellular Studies	68
3.2.7. Preparation of BP-ZnO Based Photodevice	68
3.2.8. Sample Preparation for NMR Experiments	69
3.2.9. Molecular Modeling Studies	69
3.2.10. Quantum Yield (QD) Calculation	70
References	71

**Chapter 4: Exploration of Molecular Details of a Model
Medicinally Important Xanthine-Alkaloid
Molecule, Caffeine in Aqueous Solution
and Origin of its Interaction with Other
Biologically Relevant Dyes/Drugs**

4.1. Introduction	73
4.2. Results and Discussion	76
4.2.1. Probing the Interior of Self-Assembled Caffeine Dimer at Various Temperatures	76
4.2.1.1. Characterization of caffeine dimer in aqueous solution	76

	Page
4.2.1.2. Complexation of caffeine dimer with 4-(dicyanomethylene)-2-methyl-6-(p-dimethyl- aminostyryl) 4H-pyran (DCM): Dynamics of solvation	81
4.2.1.3. Complexation of caffeine dimer with coumarin 500 (C500): General picture of the dynamics of solvation for caffeine dimer	88
4.2.1.4. TNS (2-(p-toluidino) naphthalene-6-sulfonate) in caffeine dimer: Excited state ultrafast charge transfer in the confinement	90
4.3. Conclusion	99
References	101

Chapter 5: Interaction of Caffeine with a Model Fluorogenic Potent Mutagen Embedded in Various Biomimetic Self-Assemblies in Aqueous Medium

5.1. Introduction	106
5.2. Results and Discussion	107
5.2.1. Caffeine Mediated Detachment of Mutagenic Ethidium from Various Nanoscopic Micelle: An Ultrafast Förster Resonance Energy Transfer Study	107
5.2.1.1. Caffeine mediated detachment of Et from various self-organized micelles	107
5.2.1.2. Application of kinetic models in the investigation of caffeine mediated dissociation of Et from SDS micelles	118
5.2.1.3. Interruption in FRET due to caffeine mediated expulsion of Et from epithelial cells: A fluorescence microscopic view	121
5.3. Conclusion	124
References	125

	Page
Chapter 6: Spectroscopic Studies on the Interaction of Caffeine Molecules with a Potential Mutagen in DNA <i>in vitro</i> and <i>ex vivo</i> Conditions	
6.1. Introduction	128
6.2. Results and Discussion	129
6.2.1. Ultrafast Spectroscopic Study on Caffeine Mediated Dissociation of Mutagenic Ethidium from Synthetic DNA and Various Cell Nuclei	129
6.2.1.1. Detachment of mutagenic Et from synthesized DNA: Temperature dependent study	129
6.2.1.2. Exploration of the molecular picture of caffeine-Et complex	134
6.2.1.3. Efficiency of caffeine in the expulsion of Et from various cell lines: Time gated fluorescence microscopic studies	138
6.3. Conclusion	143
References	144

**Chapter 7: Spectroscopic Studies on a Model Food Carcinogen
in Various Restricted Environments: Exploration
of the Molecular Basis for the Carcinogenic Activity**

7.1. Introduction	146
7.2. Results and Discussion	148
7.2.1. UVA Radiation Induced Ultrafast Electron Transfer from a Food Carcinogen Benzo[<i>a</i>]Pyrene to Organic Molecules, Biological Macromolecules and Inorganic Nano Structures	148
7.2.1.1. Electron transfer reaction from BP to BQ	149

	Page
7.2.1.2. Ultrafast charge transfer reactions between BP and biological macromolecules	154
7.2.1.3. Investigation on the ET reaction from BP to zinc oxide (ZnO) nanorods (NRs)	164
7.3. Conclusion	167
References	168

**Chapter 8: Ultrafast Spectroscopic Studies on the Nonradiative
Energy Transfer from Various Vibronic
Bands of the Food Carcinogen Benzo[*a*]pyrene
in Various Biologically Relevant Environments in
Aqueous Medium**

8.1. Introduction	172
8.2. Results and Discussion	174
8.2.1 A Potential Carcinogenic Pyrene Derivative under Förster Resonance Energy Transfer to Various Energy Acceptors in Nanoscopic Environments	174
8.2.1.1. Effect of different solvents on the excited state lifetime of BP	174
8.2.1.2. Photophysical characterization of the excited BP molecules	176
8.2.1.3. Differential behaviour of the vibronic bands of BP under FRET	180
8.2.1.4. Comparison of the differential behaviour of the vibronic bands of BP under FRET with that of different dyes in a 'dye blend' representing different electronic states	188

	Page
8.2.1.5. Verification of the introduced method of differential FRET calculation employing the standard theoretical framework and D-A distribution	188
8.3. Conclusion	195
References	196
List of Publications	199

Chapter 1

Introduction

1.1. Scope of the Spectroscopic Studies on the Biomolecular Recognition of Medicinally Important Ligands:

‘Biomolecular recognition’, a process by which biomolecules recognize and bind to their targets, plays a crucial role to all biological processes [1-2]. It is usually driven by many weak interactions like (i) the electrostatic interaction, (ii) the polarization of charge distributions by the interacting molecules leading to induction and dispersion forces, (iii) inter-atomic repulsion derived from Pauli-exclusion principle, (iv) “attractive force” arising largely from the entropy of the solvent and termed the hydrophobic effect. As the aqueous environment significantly reduces the impact of electrostatic and induction interactions, the hydrophobic effect is often the driving force behind the formation of specific biomolecule-target complexes [3]. In view of the fact that binding involves solvent release from the binding site, the exploration of the behavior of water molecules associated with a biomolecular target or any other molecule which can regulate the biomolecular recognition is of significant interest. Besides, such biomolecular recognition is often associated with conformational changes involving both binding and folding [4]. In this regard, spectroscopy has evolved as an efficient tool for the exploration of the dynamics of solvent molecules associated with biomolecules [5-6], ligands/biomolecular targets [7] along with the changes associated with the binding and release of such ligands from the biological macromolecules [8].

Recent developments in the exploration of biomolecular recognition and ligand association have gained significance in the pharmacological applications [9]. For example, binding of some plant alkaloids with biomolecules like DNA and RNA has shown to produce anticancer activity [10-12]. One of the most widely consumed xanthine alkaloid and a well known psychoactive stimulant is caffeine. Relatively higher consumption of the

molecule due to abundance of methylxanthines (mainly caffeine) in human diets, has directed extensive research on the activity of the molecule in the cellular environments in the recent past [13-14]. It is clearly demonstrated that caffeine has multiplicity of effects on cells [15]. Particularly, it has been shown in a number of earlier studies that caffeine has variety of roles on the molecular recognition of DNA by intercalating drugs [14, 16]. In this regard, investigation on the mode of association/complexation of caffeine molecules with the DNA intercalating drugs is significant for better understanding of the role of caffeine molecules on the biomolecular recognition of those drugs by DNA. The activity of such xanthine alkaloids as mood altering substance is within the central nervous system where it acts as stimulant, perhaps by competitive blockage of endogenous adenosine at A_1 and A_{2A} receptors [17]. From the brief survey of the earlier studies it is clear that caffeine can be used to host small ligands (drugs) and deliver/remove the same in a specific site of adenosine receptor or DNA. Earlier, spectroscopic and molecular modelling studies of caffeine complexes with other aromatic drugs reveal replacement of water molecules solvating the drugs by the more hydrophobic caffeine molecules [14]. Therefore, exploration of the dynamics of solvent relaxation around caffeine upon complexation with other aromatic molecules is essential for the understanding of the mechanisms lying behind such biomolecular recognition. As DNA-binding drugs reveal charge transfer (CT) reaction upon π -stacking with DNA base pairs [18-19], the possibility of CT reaction of any drug upon complexation with caffeine molecule would be an interest for the molecular understanding of the interaction of caffeine with the drug. Within the scope of the thesis, we investigated the therapeutic benefits of caffeine, which has recently gained attention as a promising agent in the fields of neurology [20], radiation biology [21] and cancer biology [22].

The key focus of this thesis is to explore the photophysical properties of the medicinally important ligands using steady-state and time resolved fluorescence spectroscopic techniques for the fundamental understanding of their biomolecular recognition. For example, we have explored the structural evolution of caffeine self-aggregation with temperature, since caffeine is consumed as low and high temperature beverages. Besides, we have investigated femtosecond-resolved dynamics of aqueous solvation within self-assembled dimeric structure of caffeine molecules employing

fluorescent hydrophobic ligands like 4-(dicyanomethylene)-2-methyl-6-(p-dimethylaminostyryl) 4H-pyran (DCM) and coumarin 500 (C500). In addition, we have also focused on the consequence of the retarded dynamics of solvation on the photo-induced electron transfer (ET) or charge transfer (CT) reaction of a model probe, 2-(p-toluidino) naphthalene-6-sulfonate (TNS) encapsulated in the caffeine dimer. By employing picosecond resolved Förster resonance energy transfer (FRET) studies between a DNA minor groove binder dye Hoeschst 33258 (H258, donor) and ethidium (Et, acceptor), a model DNA-intercalator as well as a potential mutagen, the efficacy of caffeine in dissociating Et molecule from nanometer sized biomimicking micelles of different charges (cationic hexadecyltrimethylammonium bromide (CTAB), neutral (polar) Triton X-100 (TX-100) and anionic sodium dodecyl sulfate (SDS)) have been explored. In addition, systematic investigation on caffeine induced dissociation of Et molecule from various synthetic DNA *in-vitro*, and various cell lines in *ex-vivo* conditions has also been reported in one of our works. In another study we have emphasized UVA radiation induced ET reaction as one of the key aspects of a potential carcinogen, benzo[*a*]pyrene (BP) in the presence of a wide variety of molecules covering organic para-benzoquinone (BQ), biological macromolecules like calf-thymus DNA (CT-DNA), human serum albumin (HSA) protein and inorganic zinc oxide (ZnO) nanorods (NRs). We have also revealed the importance of the consideration of differential spectral overlap of the vibronic bands of BP undergoing FRET as a consequence of dipole-dipole interaction with an organic molecule in a biologically relevant confined environment. The experimental tools used for exploring the biomolecular recognition involve femto- and picosecond-resolved solvent relaxation dynamics. The different experimental techniques employed for the structural and functional characterization of the biomolecules include steady state UV-vis absorption and fluorescence, picosecond resolved fluorescence spectroscopy, Fourier transform infrared spectroscopy (FTIR), NMR spectroscopy, circular dichroism, dynamic light scattering (DLS), fluorescence microscopy and scanning electron microscopy (SEM).

1.2. Objective:

Biomolecular recognition is vital to cellular processes intervened by the formation of complexes between biomolecular receptors and their ligands. Proper understanding of biomolecular recognition is one of the most essential issues in modern molecular biology and has direct application in drug discovery and design [23]. In this regard, exploration of the biomolecular recognition of some mutagens or carcinogens by DNA can highlight the pathways which can be targeted by some drugs to prevent the consequent mutation or carcinogenesis. On the other hand, the use of plants for medicinal purpose is probably as old as the history of mankind. Its use in the industrialized societies has led to the extraction and development of several alkaloids/drugs from plants [24]. Therefore, upon exploring the biomolecular recognition of some mutagens and carcinogens by DNA, the basic insights into the role of plant alkaloids on such biomolecular recognition would be imperative for the practical utilization of such alkaloids as drugs, which will be the key objective of this thesis.

Among various plant alkaloids, caffeine being one of the most popularly consumed drugs in the world has drawn attention in the field of modern research [25-26]. Investigations show that caffeine belongs to a class of chemicals that strongly enhance the cytotoxic effect of ionizing radiation and other DNA damaging agents, at concentrations that are not otherwise toxic for cells [13, 27]. It has also been established that caffeine disrupts DNA damage activated cell cycle checkpoints [28-29] as well as can modulate the binding of certain DNA damaging agents and reduces DNA directed toxicity [30-31]. The considerable water solubilisation of caffeine makes it a potential candidate for *in vivo* therapeutic applications and the consideration of the hydration dynamics of caffeine molecules becomes necessary for the crucial understanding of the drug-caffeine interaction in aqueous environment. In one of our studies [32], we have explored the hydration dynamics associated with caffeine dimer, which plays a key role in the biomolecular recognition of such xanthine alkaloids. It is well established that the solvent relaxation time scales influence the dynamics of charge transfer (CT) reactions by exerting a time dependent dielectric friction. In these cases the CT reaction rates are limited by the rate of solvent relaxation around the concerned molecule [33-35]. The twisted intramolecular

charge transfer (TICT) dynamics of a model drug, 2-(p-toluidino) naphthalene-6-sulfonate (TNS) in presence of caffeine has also been investigated to get an idea about the amount of energy required to release such model drugs from the caffeine bound state emphasizing the use of such xanthine alkaloids as a tool for targeted drug delivery.

The molecular recognition of DNA by certain drugs is known to get significantly perturbed in presence of caffeine [13-14, 16, 36-37]. Sometimes, explanation of specific role of caffeine in the molecular recognition of DNA in physiological milieu becomes cumbersome [38]. In this regard small biomimetic systems including nanoscopic micelles [39] could serve as an efficient mimic for the biological membranes, macromolecules and are also useful in organizing the reactants at a molecular level [39]. Although there have been many attempts to obtain a clear picture of the biomolecular recognition of DNA by various drugs in presence of caffeine, to the best of our knowledge no attempt has been made to use nanoscopic micelle for the better understanding of caffeine mediated molecular recognition of DNA by small ligands/drugs. One of our studies [40] aimed to look at the role of caffeine on the association of DNA binding drugs with the biomimetic systems employing FRET techniques.

Spectroscopic studies on the caffeine mediated de-intercalation of Et, a potential mutagen [41] from genomic DNA in solution at room temperature [42] highlights the therapeutic use of caffeine in animal model. However, a detail molecular picture of the de-intercalation mechanism and the universal application of such xanthine alkaloids in the extraction of Et from the nucleus of various cell lines are some of the issues that left unattended and have been addressed by us in one of our studies [43]. As caffeine is consumed through both hot and cold beverages, the effect of temperature on the efficacy of caffeine molecules to de-intercalate such mutagens from DNA is of significant interest and has also been investigated.

Reactions involving electron transfer (ET) and reactive oxygen species (ROS) play a pivotal role in carcinogenesis and cancer biochemistry [44]. ET reactions are well known for their importance in DNA damage [45] and recent findings suggest the role of ultrafast ET in inducing single strand and double strand breaks in DNA through reductive DNA damage [46]. One of the most potent carcinogens to which people are frequently exposed

[47-49] is benzo[*a*]pyrene (BP), a polycyclic aromatic hydrocarbon (PAH). In one of our studies [50], we emphasized UVA radiation induced ET reaction as one of the key aspects of BP in the presence of a wide variety of molecules covering organic para-benzoquinone (BQ), biological macromolecules like calf-thymus DNA (CT-DNA), human serum albumin (HSA) protein and inorganic zinc oxide (ZnO) nanorods (NRs). Physical consequences of BP association with CT-DNA have also been investigated. In addition, a BP-anchored ZnO NR-based photodevice has been designed to look into the electron donating property of BP by measuring wavelength dependent photocurrent.

BP being a pyrene derivative belongs to a class of PAHs and have several appealing photophysical properties which make it suitable for using as effective fluorescence probe [51-54]. The differential behavior of the individual vibronic bands, in the emission spectra of pyrene and its derivatives like BP, in response to change in temperature [55], polarity and refractive index [56] of the host solvent is well known while reports on such behavior of these bands while undergoing dipolar interactions with different molecules was lacking in the literature and has been investigated in one of our studies [57]. In our study we have emphasized the importance of the consideration of differential spectral overlap of the vibronic bands of BP undergoing FRET as a consequence of dipole-dipole interaction with an organic molecule in a confined environment. Our study may find importance in the FRET analysis of biologically relevant pyrene class of molecules.

1.3. Summary of the Work Done:

I. Exploration of Molecular Details of a Model Medicinally Important Xanthine-Alkaloid Molecule, Caffeine in Aqueous Solution and Origin of its Interaction with Other Biologically Relevant Dyes/Drugs:

A. Probing the Interior of Self-Assembled Caffeine Dimer at Various Temperatures [32]:

Caffeine (1,3,7-trimethylxanthine) is in a class of molecules with conjugated planar ring systems, which has shown variety of roles on the molecular recognition of DNA by intercalating drugs. In the present study we have exploited the dimeric nature of caffeine to host some hydrophobic molecules like DCM, C500 and TNS. Besides, exploration of the hydration dynamics associated with caffeine dimer, which plays a key role in the biomolecular recognition of such xanthine alkaloids suggests that weakly structured water molecules are associated with those dimers. The observed dynamical nature of water molecules associated with caffeine dimer makes it a suitable subject for biomolecular interaction where the bound water molecules can be displaced in presence of its receptor molecule facilitating the hydrophobic interaction. Furthermore our exploration of twisted intramolecular charge transfer (TICT) dynamics of TNS in presence of caffeine highlights the amount of energy required to release such model drugs from the caffeine bound state which may find significance in the use of such xanthine alkaloids as a tool for drug delivery.

II. Interaction of Caffeine with a Model Fluorogenic Potent Mutagen Embedded in Various Biomimetic Self-Assemblies in Aqueous Medium:

A. Caffeine Mediated Detachment of Mutagenic Ethidium from Various Nanoscopic Micelle: An Ultrafast Förster Resonance Energy Transfer Study [40]:

Small biomimetic systems including nanoscopic micelles serve as a functional mimic for the biological membranes and macromolecules. In the present study we have explored the efficacy of caffeine in dissociating ethidium (Et) molecule, a model DNA-intercalator as

well as a potential mutagen, from nanometer sized micelles of various charges. By using steady-state and picosecond resolved spectroscopic techniques, we have demonstrated the detachment of Et from various biomimicking micelles of different charges (cationic hexadecyltrimethylammonium bromide (CTAB), neutral (polar) Triton X-100 (TX-100) and anionic sodium dodecyl sulfate (SDS)) revealing the specificity of caffeine molecule for carrying out such dissociation. The picosecond resolved Förster resonance energy transfer (FRET) studies between a DNA minor groove binder dye Hoeschst 33258 (H258, donor) and Et (acceptor) have been employed to investigate the alteration in their association in presence of caffeine in the molecular level. We have applied a kinetic model developed by Infelta and Tachiya to understand the kinetics of energy transfer and the distribution of acceptor molecules in the micellar surface. Finally, our fluorescence micrographs of squamous epithelial cells validate the alteration of FRET efficiency between the donor and the acceptor due to the release of the latter in the presence of caffeine.

III. Spectroscopic Studies on the Interaction of Caffeine Molecules with a Potential Mutagen in DNA *in vitro* and *ex vivo* Conditions:

A. Ultrafast Spectroscopic Study on Caffeine Mediated Dissociation of Mutagenic Ethidium from Synthetic DNA and Various Cell Nuclei [43]:

In this study we have used steady-state and picosecond resolved fluorescence spectroscopy and time gated fluorescence microscopy in order to investigate the detachment of mutagenic Et from synthesized DNA of specific sequences *in vitro* and various types of cell lines including squamous epithelial cells collected from the inner lining of the human mouth, A549 (lung carcinoma), A375 (human skin), RAW (macrophage) and Vero (African green monkey kidney epithelium) cells in *ex vivo* conditions. Time-resolved fluorescence studies are consistent with a mechanism where caffeine-Et complex formation in bulk solution drives the dissociation of DNA-bound Et. In addition, temperature dependent picosecond resolved studies show the caffeine-Et complex to be stable over a wide range of temperature, within and beyond the normal physiological limit. A

combination of NMR spectroscopy and DLS experiments allowed us to propose a molecular model of caffeine-Et complex.

IV. Spectroscopic Studies on a Model Food Carcinogen in Various Restricted Environments: Exploration of the Molecular Basis for the Carcinogenic Activity:

A. UVA Radiation Induced Ultrafast Electron Transfer from a Food Carcinogen Benzo[*a*]Pyrene to Organic Molecules, Biological Macromolecules and Inorganic Nano Structures [50]:

Electron transfer (ET) reactions are important for their implications in both oxidative and reductive DNA damages. In the present study, we have highlighted the UVA radiation induced ET reaction as one of the key aspects of a potential food carcinogen, benzo[*a*]pyrene (BP), in the presence of a wide variety of molecules, biological macromolecules and inorganic nanostructures. The temperature-dependent steady-state, picosecond-resolved fluorescence lifetime and anisotropy studies reveal the effect of temperature on the perturbation of such ET reaction from BP to biological macromolecules, highlighting the temperature-dependent association of the carcinogen with those macromolecules. Furthermore, the electron donating property of BP has been established by measuring substantial wavelength-dependent photocurrent in BP-anchored ZnO NR-based photodevice which offers new physical insights for the carcinogenic study of BP.

V. Ultrafast Spectroscopic Studies on the Nonradiative Energy Transfer from Various Vibronic Bands of the Food Carcinogen Benzo[*a*]pyrene in Various Biologically Relevant Environments in Aqueous Medium:

A. A Potential Carcinogenic Pyrene Derivative under Förster Resonance Energy Transfer to Various Energy Acceptors in Nanoscopic Environments [57]:

Förster resonance energy transfer (FRET), which is also known as “spectroscopic ruler”, is very often used to measure the distance between two sites on a macromolecule. In this

study, we demonstrated that picosecond resolved Förster resonance energy transfer (FRET) from various vibronic bands in BP to be strongly dependent on the spectral overlap of an energy acceptor in a confined environment. Our study on the dipolar interactions between BP and different acceptors ethidium (Et), acridine orange (AO) and crystal violet (CV) at the surface of a model anionic micelle reveals the Förster distance (R_0) and the rate of energy transfer to be dependent on the individual spectral overlap of the vibronic bands of BP with the absorption spectra of different energy acceptors. The differential behaviour of the vibronic bands has been found to be comparable with that of different dyes (quantum dots; QDs) in a ‘dye-blend’ (mixture) under FRET to an energy acceptor. We have also shown that consideration of differential FRET from vibronic bands of BP and from the QDs in the ‘dye-blend’ is equally acceptable in the theoretical frameworks including ‘Infelta-Tachiya’ model and donor-acceptor (D-A) distribution analysis in the nano-environments.

1.4. Plan of Thesis:

The plan of the thesis is as follows:

Chapter 1: This chapter gives a brief introduction to the scope and motivation behind the thesis work. A brief summary of the work done is also included in this chapter.

Chapter 2: This chapter provides an overview of the dynamical, steady-state and theoretical tools, the structural aspects of biologically important systems (DNAs, proteins) and probes used in the research.

Chapter 3: Details of instrumentation, data analysis and experimental procedures have been discussed in this chapter.

Chapter 4: In this chapter, dimeric nature of caffeine showing efficacy in hosting hydrophobic molecules has been reported. Besides, the hydration dynamics associated with caffeine dimer have been explored. In addition, twisted intramolecular charge transfer (TICT) dynamics of TNS in presence of caffeine have also been demonstrated.

Chapter 5: The efficacy of caffeine in dissociating ethidium (Et) molecule, from nanometer sized micelles of various charges has been reported in this chapter by employing FRET techniques and kinetic models developed by Infelta and Tachiya.

Chapter 6: In this chapter, the caffeine mediated detachment of mutagenic Et from synthesized DNA of specific sequences *in vitro* and various types of cell lines including squamous epithelial cells collected from the inner lining of the human mouth, A549 (lung carcinoma), A375 (human skin), RAW (macrophage) and Vero (African green monkey kidney epithelium) cells in *ex vivo* conditions have been reported.

Chapter 7: In this chapter, we report the strong affinity of the carcinogen BP, under UVA radiation, to donate electrons to different class of molecules like para-benzoquinone (BQ), biological macromolecules like calf-thymus DNA and human serum albumin (HSA) and inorganic nano structures like zinc oxide (ZnO) nanorods (NRs) suggesting ET reaction as one of its vital characteristics responsible for its carcinogenic activity.

Chapter 8: This chapter deals with the importance of the consideration of differential spectral overlap of the vibronic bands of BP undergoing FRET as a consequence of dipole-dipole interaction with an organic molecule in a confined environment.

References

- [1] D. D. Boehr, R. Nussinov, P. E. Wright, The Role of Dynamic Conformational Ensembles in Biomolecular Recognition, *Nat. Chem. Biol.* 5 (2009) 789.
- [2] J. B. Zung, T. T. Ndou, I. M. Warner, Investigation of the Complexation of Pyrene and Naphthalene with Hydroxypropyl- β -Cyclodextrin, *Appl. Spectrosc.* 44 (1990) 1491.
- [3] K. Kahn, K. Plaxco, *Principles of Biomolecular Recognition*, Springer New York, 2010.
- [4] X. Chu, L. Gan, E. Wang, J. Wang, Quantifying the Topography of the Intrinsic Energy Landscape of Flexible Biomolecular Recognition, *Proc. Natl. Acad. Sci.* 110 (2013) E2342.
- [5] P. K. Verma, R. Saha, R. K. Mitra, S. K. Pal, Slow Water Dynamics at the Surface of Macromolecular Assemblies of Different Morphologies, *Soft Matter* 6 (2010) 5971.
- [6] D. Banerjee, A. Makhal, S. K. Pal, Sequence Dependent Femtosecond-Resolved Hydration Dynamics in the Minor Groove of DNA and Histone-DNA Complexes, *J. Fluoresc.* 19 (2009) 1111.
- [7] R. Saha, S. Rakshit, R. K. Mitra, S. K. Pal, Microstructure, Morphology, and Ultrafast Dynamics of a Novel Edible Microemulsion, *Langmuir* 28 (2012) 8309.
- [8] T. Mondol, S. Batabyal, A. Majumder, S. Roy, S. K. Pal, Recognition of Different DNA Sequences by a DNA-Binding Protein Alters Protein Dynamics Differentially, *FEBS Lett.* 586 (2012) 258.
- [9] R. Baron, J. A. McCammon, Molecular Recognition and Ligand Association, *Annu. Rev. Phys. Chem.* 64 (2013) 151.
- [10] M. Maiti, K. G. Suresh, Biophysical Aspects and Biological Implication on the Interaction of Benzophenanthridine Alkaloids with DNA, *Biophys. Rev.* 1 (2009) 119.
- [11] K. Bhadra, K. G. Suresh, Interaction of Berberine, Palmatine, Coralyne, and Sanguinarine to Quadruplex DNA: A Comparative Spectroscopic and Calorimetric Study, *Biochim. Biophys. Acta.* 1810 (2011) 485.
- [12] M. Hossain, A. Y. Khan, K. G. Suresh, Interaction of the Anticancer Plant Alkaloid Sanguinarine with Bovine Serum Albumin, *PloS one* 6 (2011) e18333.
- [13] C. P. Selby, A. Sancar, Molecular Mechanisms of DNA Repair Inhibition by Caffeine, *Proc. Natl. Acad. Sci.* 87 (1990) 3522.
- [14] R. W. Larsen, R. Jasuja, R. K. Hetzler, P. T. Muraoka, V. G. Andrada, D. M. Jameson, Spectroscopic and Molecular Modelling Studies of Caffeine Complexes with DNA Intercalators, *Biophys. J.* 70 (1996) 443.

- [15] J. R. Mercer, K. Gray, N. Figg, S. Kumar, M. R. Bennett, The Methyl Xanthine Caffeine Inhibits DNA Damage Signaling and Reactive Species and Reduces Atherosclerosis in ApoE^{-/-} Mice, *Arterioscler. Thromb. Vasc. Biol.* 32 (2012) 2461.
- [16] D. B. Davies, D. A. Veselkov, L. N. Djimant, A. N. Veselkov, Heteroassociation of Caffeine and Aromatic Drugs and their Competitive Binding with a DNA Oligomer, *Eur. Biophys. J.* 30 (2001) 354.
- [17] B. Johansson, L. Halldner, T. V. Dunwiddie, S. A. Masino, W. Poelchen, L. G. Llort, R. M. Escorihuela, A. F. Teruel, Z. W. Hallin, X. J. Xu, A. Hårdemark, C. Betsholtz, E. Herlenius, B. B. Fredholm, Hyperalgesia, Anxiety, and Decreased Hypoxic Neuroprotection in Mice Lacking the Adenosine A1 Receptor, *Proc. Natl. Acad. Sci.* 98 (2001) 9407.
- [18] E. L. S. Wong, J. J. Gooding, The Electrochemical Monitoring of the Perturbation of Charge Transfer through DNA by Cisplatin, *J. Am. Chem. Soc.* 129 (2007) 8950.
- [19] D. Řeha, M. Kabelá, F. Ryjáček, J. Šponer, J. E. Šponer, M. Elstner, S. Suhai, P. Hobza, Intercalators. 1. Nature of Stacking Interactions between Intercalators (Ethidium, Daunomycin, Ellipticine, and 4',6-Diaminide-2-phenylindole) and DNA Base Pairs. Ab Initio Quantum Chemical, Density Functional Theory, and Empirical Potential Study, *J. Am. Chem. Soc.* 124 (2002) 3366.
- [20] M. Alexander, A. L. Smith, T. S. Rosenkrantz, R. H. Fitch, Therapeutic Effect of Caffeine Treatment Immediately Following Neonatal Hypoxic-Ischemic Injury on Spatial Memory in Male Rats, *Brain Sci.* 3 (2013) 177.
- [21] M. Pujol, R. Puig, M. R. Caballín, L. Barrios, J. F. Barquinero, The Use of Caffeine to Assess High Dose Exposures to Ionising Radiation by Dicentric Analysis, *Radiat. Prot. Dosimetry* 149 (2012) 392.
- [22] S. Y. Suh, Y. S. Choi, S. C. Oh, Y. S. Kim, K. Cho, W. K. Bae, J. H. Lee, A. Seo, H. Y. Ahn, Caffeine as an Adjuvant Therapy to Opioids in Cancer Pain: A Randomized, Double-Blind, Placebo-Controlled Trial, *J. Pain Symptom Manage.* 46 (2013) 474.
- [23] Z. Yan, J. Wang, Specificity Quantification of Biomolecular Recognition and its Implication for Drug Discovery, *Sci. Rep.* 2 (2012) 1.
- [24] S. Akroum, D. Satta, K. Lalaoui, Antimicrobial, Antioxidant, Cytotoxic Activities and Phytochemical Screening of Some Algerian Medicinal Plants, *Eur. J. Sci. Res.* 2 (2009) 289.
- [25] H. A. Young, D. Benton, Caffeine Can Decrease Subjective Energy Depending on the Vehicle with Which It Is Consumed and When It Is Measured, *Psychopharmacology* 228 (2013) 243.

- [26] A. Birerdinc, M. Stepanova, L. Pawloski, Z. M. Younossi, Caffeine is Protective in Patients with Non-alcoholic Fatty Liver Disease, *Alimentary Pharmacology & Therapeutics* 35 (2012) 76.
- [27] R. Daniel, E. Marusich, E. Argyris, R. Y. Zhao, A. M. Skalka, R. J. Pomerantz, Caffeine Inhibits Human Immunodeficiency Virus Type 1 Transduction of Nondividing Cells, *J. Virol.* 79 (2005) 2058.
- [28] J. P. Murnane, J. E. Byfield, J. F. Ward, P. Calabro-Jones, Effects of Methylated Xanthines on Mammalian Cells Treated with Bifunctional Alkylating Agents, *Nature* 285 (1980) 326.
- [29] R. B. Painter, Effect of Caffeine on DNA Synthesis in Irradiated and Unirradiated Mammalian Cells, *J. Mol. Biol.* 143 (1980) 289.
- [30] M. Johnson, S. G. Bhuvan Kumar, R. Malathi, De-intercalation of Ethidium Bromide and Acridine Orange by Xanthine Derivatives and Their Modulatory Effect on Anticancer Agents: A study of DNA-directed Toxicity Enlightened by Time Correlated Single Photon Counting, *J. Biomol. Struct. & Dyn.* 20 (2003) 677.
- [31] M. Johnson, S. G. Bhuvan Kumar, R. Malathi, RNA Binding Efficacy of Theophylline, Theobromine and Caffeine, *J. Biomol. Struct. & Dyn.* 20 (2003) 687.
- [32] S. Banerjee, P. K. Verma, R. K. Mitra, G. Basu, S. K. Pal, Probing the Interior of Self-Assembled Caffeine Dimer at Various Temperatures, *J. Fluoresc.* 22 (2012) 753.
- [33] M. Maroncelli, J. MacInnis, G. R. Fleming, Polar Solvent Dynamics and Electron-Transfer Reactions, *Science* 243 (1989) 1674.
- [34] I. Rips, J. Jortner, Dynamic Solvent Effects on Outer-sphere Electron Transfer, *J. Chem. Phys.* 87 (1987) 2090.
- [35] J. T. Hynes, Outer-Sphere Electron-Transfer Reactions and Frequency-Dependent Friction, *J. Phys. Chem.* 90 (1986) 3701.
- [36] F. Traganos, J. Kapuscinski, Z. Darzynkiewicz, Caffeine Modulates the Effects of DNA-Intercalating Drugs in vitro: A Flow Cytometric and Spectrophotometric Analysis of Caffeine Interaction with Novantrone, Doxorubicin, Ellipticine, and the Doxorubicin Analogue AD198, *Cancer Res.* 51 (1991) 3682.
- [37] J. Kapuscinski, M. Kimmel, Thermodynamic Model of Mixed Aggregation of Intercalators with Caffeine in Aqueous Solution, *Biophys. Chem.* 46 (1993) 153.
- [38] F. Traganos, B. Kaminska-Eddy, Z. Darzynkiewicz, Caffeine Reverses the Cytotoxic and Cell Kinetic Effects of Novantrone (Mitoxantrone), *Cell Prolif.* 24 (1991) 305.
- [39] N. J. Turro, M. Grätzel, A. M. Braun, Photophysical and Photochemical Processes in Micellar Systems, *Angew. Chem. Intern. Ed.* 19 (1980) 675.

- [40] S. Banerjee, M. Tachiya, S. K. Pal, Caffeine-Mediated Detachment of Mutagenic Ethidium from Various Nanoscopic Micelles: An Ultrafast Förster Resonance Energy Transfer Study, *J. Phys. Chem. B* 116 (2012) 7841.
- [41] H. R. Mahler, P. S. Perlman, Effects of Mutagenic Treatment by Ethidium Bromide on Cellular and Mitochondrial Phenotype, *Arch. Biochem. Biophys.* 148 (1972) 115.
- [42] I. M. Johnson, S. G. B. Kumar, R. Malathi, De-intercalation of Ethidium Bromide and Acridine Orange by Xanthine Derivatives and their Modulatory Effect on Anticancer Agents: A Study of DNA-Directed Toxicity Enlightened by Time Correlated Single Photon Counting, *J. Biomol. Struct. Dyn.* 20 (2003) 677.
- [43] S. Banerjee, D. Bhowmik, P. K. Verma, R. K. Mitra, A. Sidhhanta, G. Basu, S. K. Pal, Ultrafast Spectroscopic Study on Caffeine Mediated Dissociation of Mutagenic Ethidium from Synthetic DNA and Various Cell Nuclei, *J. Phys. Chem. B* 115 (2011) 14776.
- [44] T. Toyooka, Y. Ibuki, M. Koike, N. Ohashi, S. Takahashi, R. Goto, Coexposure to Benzo[a]pyrene Plus UVA Induced DNA Double Strand Breaks: Visualization of Ku Assembly in the Nucleus Having DNA Lesions, *Biochem. Biophys. Res. Commun.* 322 (2004) 631.
- [45] C. Wan, T. Fiebig, S. O. Kelley, C. R. Treadway, J. K. Barton, A. H. Zewail, Femtosecond Dynamics of DNA-Mediated Electron Transfer, *Proc. Natl. Acad. Sci.* 96 (1999) 6014.
- [46] J. Nguyen, Y. Ma, T. Luo, R. G. Bristow, D. A. Jaffray, Q. B. Lu, Direct Observation of Ultrafast-Electron-Transfer Reactions Unravels High Effectiveness of Reductive DNA Damage, *Proc. Natl. Acad. Sci.* 108 (2011) 11778.
- [47] D. H. Phillips, Fifty Years of Benzo(a)pyrene, *Nature* 303 (1983) 468.
- [48] D. H. Phillips, Polycyclic Aromatic Hydrocarbons in the Diet, *Mutat. Res.* 443 (1999) 139.
- [49] H. Ling, J. M. Sayer, B. S. Plosky, H. Yagi, F. Boudsocq, R. Woodgate, D. M. Jerina, W. Yang, Crystal Structure of a Benzo[a]pyrene Diol Epoxide Adduct in a Ternary Complex with a DNA Polymerase, *Proc. Natl. Acad. Sci.* 101 (2004) 2265.
- [50] S. Banerjee, S. Sarkar, K. Lakshman, J. Dutta, S. K. Pal, UVA Radiation Induced Ultrafast Electron Transfer from a Food Carcinogen Benzo[a]pyrene to Organic Molecules, Biological Macromolecules and Inorganic Nano Structures, *J. Phys. Chem. B* 117 (2013) 3726.
- [51] M. Gratzel, J. K. Thomas, On the Dynamics of Pyrene Fluorescence Quenching in Aqueous Ionic Micellar Systems. Factors Affecting the Permeability of Micelles, *J. Am. Chem. Soc.* 95 (1973) 6885.

- [52] K. Kalyanasundaram, J. K. Thomas, Environmental Effects on Vibronic Band Intensities in Pyrene Monomer Fluorescence and Their Application in Studies of Micellar Systems, *J. Am. Chem. Soc.* 99 (1977) 2039.
- [53] J. D. Morrisett, H. J. Pownall, R. T. Plumlee, L. C. Smith, Z. E. Zehner, Multiple Thermotropic Phase Transitions in Escherichia coli Membranes and Membrane Lipids. A comparison of Results Obtained by Nitroxyl Stearate Paramagnetic Resonance, Pyrene Excimer Fluorescence, and Enzyme Activity Measurements, *J. Biol. Chem.* 250 (1975) 6969.
- [54] J. A. Sigalat, J. S. SanMartin, C. E. A. Morales, E. Zaballos, R. E. Galian, J. P. Prieto, Further Insight into the Photostability of the Pyrene Fluorophore in Halogenated Solvents, *ChemPhysChem* 13 (2012) 835.
- [55] M. R. Vigil, J. Bravo, T. D. Z. Atvars, J. Baselga, Photochemical Sensing of Semicrystalline Morphology in Polymers: Pyrene in Polyethylene, *Macromolecules* 30 (1997) 4871.
- [56] S. C. Beck, D. T. Cramb, Condensed Phase Dispersive Interactions of Benzo[a]pyrene with Various Solvents and with DNA: A Twist on Solvatochromism, *J. Phys. Chem. B* 104 (2000) 2767.
- [57] S. Banerjee, N. Goswami, S. K. Pal, A Potential Carcinogenic Pyrene Derivative under Forster Resonance Energy Transfer to Various Energy Acceptors in Nanoscopic Environments, *ChemPhysChem* 14 (2013) 3581.

Chapter 2

An Overview of Steady-State, Dynamical, Theoretical Tools and Systems

In order to investigate the various processes involved in the course of study on biomolecular recognition of medicinally important ligands, different steady-state, dynamical and theoretical tools have been employed. These include solvation dynamics, fluorescence anisotropy, determination of activation energy using Arrhenius theory, Förster resonance energy transfer (FRET), P(r) distribution from FRET, kinetic model developed by Infelta and Tachiya, densimetric and acoustic measurements, twisted intramolecular charge transfer (TICT) and photoinduced electron transfer (PET). In this chapter, we have included a brief discussion about the above mentioned dynamical tools. Overviews of the various systems and the probes used in the studies have also been provided.

2.1. Steady-State and Dynamical Tools:

2.1.1. Solvation Dynamics: Almost all biological macromolecules, proteins (enzymes) and DNAs are inactive in the absence of water. Hydration of a protein/enzyme/DNA is particularly important for their structural stability and function, especially their recognition by ligand molecules. This role of hydration in enzymatic activity and molecular recognition of biomolecules [1-4] have recently been reviewed in a number of publications.

(i) Theory: Solvation dynamics refer to the process of reorganization of solvent dipoles around a dipole created instantaneously or an electron/proton injected suddenly in a polar liquid. In order to understand the meaning and scope of solvation dynamics, let us first visualize the physical essence of the dynamical process involved for a solute molecule in a polar solvent [5-7]. A change in the probe (solute) is made at time $t=0$, by an excitation

pulse, which leads to the creation of a dipole. This dipole gives rise to an instantaneous electric field on the solvent molecules. The interaction of permanent dipoles of the solvent with the instantaneously created electric field, shifts the free energy minimum of the solvent to a non-zero value of the polarization. The solvent motion is crucial (Figure 2.1). Since the probe is excited instantaneously (a Franck-Condon transition as far as the nuclear degrees of freedom are concerned), the solvent molecules at $t=0$ find themselves in a relatively high-energy configuration. Subsequently, the solvent molecules begin to move and rearrange themselves to reach their new equilibrium positions (Figure 2.2). The nuclear motion involved can be broadly classified into rotational and translational motions. When the solvent is bulk water, rotational motion would also include hindered rotation, libration, while translation would include the intermolecular vibration due to the extensive

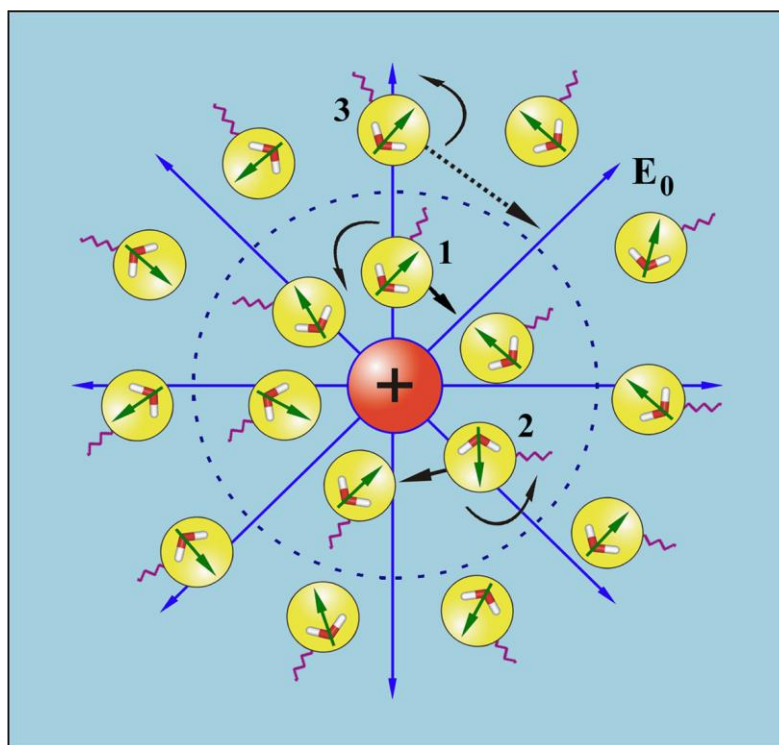


Figure 2.1. Schematic illustration of solvation of an ion (or dipole) by water. The neighboring molecules (numbered 1 and 2) can either rotate or translate to attain the minimum energy configuration. On the other hand, distant water molecule 3 can only rotate to attain minimum energy configuration. The field is shown as E_0 . The springs connected to the molecules are meant to denote hydrogen bonding.

hydrogen bonding. The two specific motions, libration and intermolecular vibration, are relatively high in frequency and are expected to play a dominant role in the initial part of solvation [8]. The molecular motions involved are shown schematically in Figure 2.1, and in Figure 2.3 we show a typical solvation time correlation function. For clarity, we approximate the motions responsible for the decay in different regions.

A simple way to address the dynamics of polar solvation is to start with the following expression for the solvation energy, $E_{\text{solv}}(t)$ [9],

$$E_{\text{solv}}(t) = -\frac{1}{2} \int d\mathbf{r} \mathbf{E}_0(\mathbf{r}) \cdot \mathbf{P}(\mathbf{r}, t) \quad (2-1)$$

where $\mathbf{E}_0(\mathbf{r})$ is the instantaneously created, position-dependent electric field from the ion or the dipole of the solute and $\mathbf{P}(\mathbf{r}, t)$ is the position and time-dependent polarization.

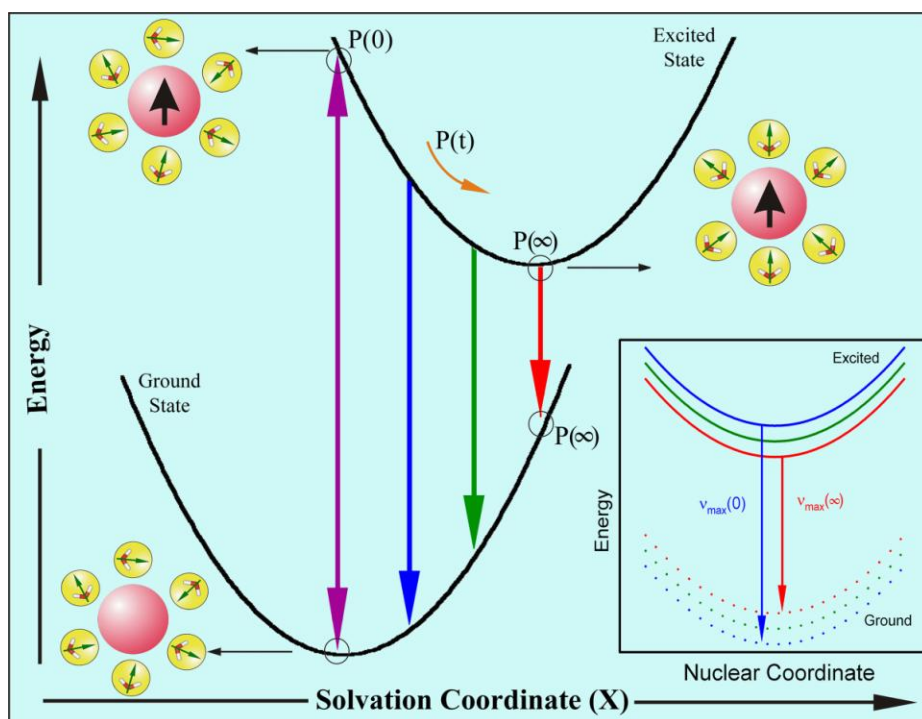


Figure 2.2. Schematic representation of the potential energy surfaces involved in solvation dynamics showing the water orientational motions along the solvation coordinate together with instantaneous polarization P . In the inset we show the change in the potential energy along the intramolecular nuclear coordinate. As solvation proceeds the energy of the solute comes down giving rise to a red shift in the fluorescence spectrum. Note the instantaneous P , e.g., $P(\infty)$, on the two connected potentials.

The latter is defined by the following expression,

$$\mathbf{P}(\mathbf{r},t) = \int d\Omega \mu(\Omega) \rho(\mathbf{r},\Omega,t) \quad (2-2)$$

where $\mu(\Omega)$ is the dipole moment vector of a molecule at position \mathbf{r} , and $\rho(\mathbf{r},\Omega,t)$ is the position, orientation and time-dependent density. Therefore, the time dependence of the solvation energy is determined by the time dependence of polarization that is in turn

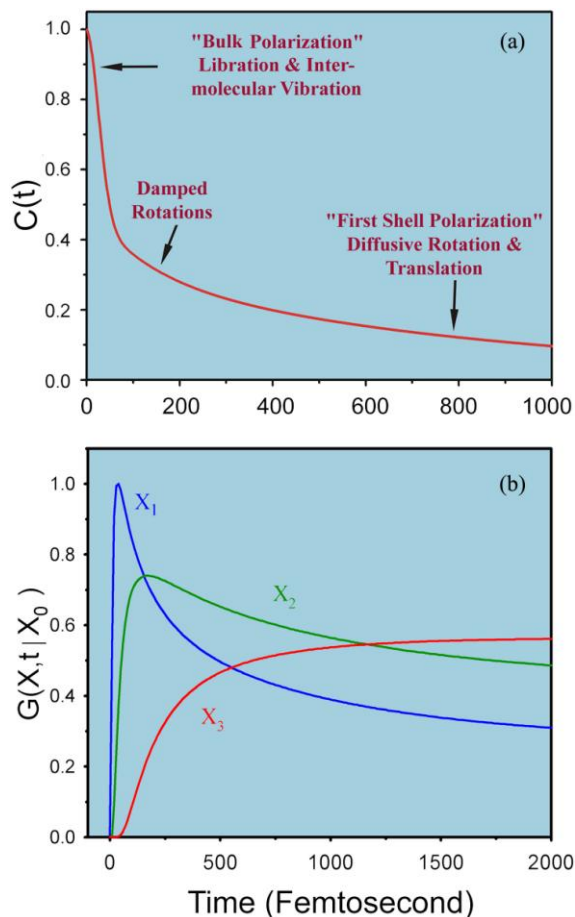


Figure 2.3. (a) A typical solvation time correlation function for water is shown here. The time correlation function exhibits three distinct regions: The initial ultrafast decay, an intermediate decay of about 200 fs and the last slow decay with time constant of 1 ps. The physical origin of each region is indicated on the plot itself; see text. (b) Green's function $G(X,t|X_0)$ for population relaxation along the solvation coordinate (X) is plotted against time in femtosecond. In G , X_0 is the initial position at $t=0$. This figure shows the position and time dependence of the population fluorescence intensity. At early times (when the population is at X_1) there is ultrafast rise followed by an ultrafast decay. At intermediate times (when the population is at X_2) there is a rise followed by a slow decay as shown by the green line. At long times when the population is nearly relaxed (position X_3 , red line) we see only a rise.

determined by the time dependence of the density. If the perturbation due to the probe on dynamics of bulk water is negligible, then the time dependence of polarization is dictated by the natural dynamics of the liquid.

The theoretical analysis of the time-dependent density is usually carried out using a molecular hydrodynamic approach that is based on the basic conservation (density, momentum and energy) laws and includes the effects of intermolecular (both spatial and orientational) correlations. The latter provides the free energy surface on which solvation proceeds. The equation of motion of the density involves both orientational and translational motions of the solvent molecules. The details of the theoretical development are reported in literature [5]; here we shall present a simple physical picture of the observed biphasic solvation dynamics.

Within linear response theory, the solvation correlation function is directly related to the solvation energy as,

$$C(t) = \frac{\langle \delta E(0) \cdot \delta E(t) \rangle}{\langle \delta E^2 \rangle} = \frac{\langle E(t) \rangle - \langle E(\infty) \rangle}{\langle E(0) \rangle - \langle E(\infty) \rangle} \quad (2-3)$$

where δE is the fluctuation of solvation energy from the average, equilibrium value. Note that the equality in equation (2-3) indicates the direct relation for the average of the fluctuations over the equilibrium distribution (left) and the non-equilibrium function (right) which relates to observables; without $\langle E(\infty) \rangle$ the correspondence is clear, and $\langle E(\infty) \rangle$ is rigorously the result of the equilibrium term in the numerator and for normalization in the denominator.

The ultrafast component in the solvation time correlation function (see Figure 2.3 (a)), originates from the initial relaxation in the steep collective solvation potential. The collective potential is steep because it involves the total polarization of the system [5-6]. This initial relaxation couples mainly to the hindered rotation (i.e., libration) and the hindered translation (i.e., the intermolecular vibration), which are the available high frequency modes of the solvent; neither long amplitude rotation nor molecular translation are relevant here. The last part in the decay of the solvation correlation function involves larger amplitude rotational and translational motions of the nearest neighbor molecules in the first solvation shell. In the intermediate time, one gets contributions from the

moderately damped rotational motions of water molecules. In a sense, with the above description one recovers the famous Onsager’s “inverse snow-ball” picture of solvation [10]. The slowest time constant is ~ 1 ps, which is determined by the individual rotational and translational motions of the molecules in the “first solvation shell” nearly close to the probe. The femtosecond component is dominated by the high frequency hindered rotational and translational (vibration) [8, 11-12] polarization.

Figure 2.2 shows a schematic of the solvation potential and the orientational motions for the water molecules involved. From the shape of the potential, it can be seen that the transient behavior for the population during solvation should be a decay function on the blue edge of the spectrum and a rise function on the red edge. These wavelength-dependent features can be explained nicely within a generalized model of relaxation in which a Gaussian wave packet relaxes on a harmonic surface. The relaxation is non-exponential and a Green’s function can describe the approach of the wave packet along the solvation coordinate, X , to its equilibrium value. For the general non-Markovian case it is given by [13],

$$G(X,t|X_0) = \frac{1}{\sqrt{2\pi\langle X^2 \rangle [1 - C^2(t)]}} \exp \left[-\frac{[X - X_0 C(t)]^2}{2\langle X^2 \rangle [1 - C^2(t)]} \right] \quad (2-4)$$

where $\langle X^2 \rangle$ is the equilibrium mean square fluctuation of the polarization coordinate in the excited state surface, $C(t)$ is the solvation correlation function described in equation (2-3) and X_0 is the initial value of the packet on the solvation coordinate. Equation (2-4) describes the motion of the wave packet (polarization density) beginning at $t=0$ (X_0) as a delta function and according to the solvation time correlation function. As $t \rightarrow \infty$, $C(t) \rightarrow 0$ and we recover the standard Gaussian distribution. Initially, ($t \rightarrow 0$), the exponential is large, so the decay is ultrafast, but at long times, the relaxation slows down, ultimately to appear as a rise. In Figure 2.3 (b), we present calculations of $G(X,t|X_0)$ at different positions along the solvation coordinate giving decays at X_1 and X_2 , but with different time constants, and a rise at X_3 , as demonstrated experimentally.

(ii) Experimental Methods: In order to study solvation stabilization of a probe in an environment, a number of fluorescence transients are taken at different wavelengths across the emission spectrum of the probe. As described earlier, blue and red ends of the emission

spectrum are expected to show decay and rise, respectively in the transients. The observed fluorescence transients are fitted by using a nonlinear least square fitting procedure to a function

$$\left(X(t) = \int_0^t E(t')R(t-t')dt' \right) \quad (2-5)$$

comprising of convolution of the IRF ($E(t)$) with a sum of exponentials

$$\left(R(t) = A + \sum_{i=1}^N B_i \exp(-t/\tau_i) \right) \quad (2-6)$$

with pre-exponential factors (B_i), characteristic lifetimes (τ_i) and a background (A). Relative concentration in a multi-exponential decay is finally expressed as;

$$\alpha_n = \frac{B_n}{\sum_{i=1}^N B_i}. \quad (2-7)$$

The relative contribution of a particular decay component (f_n) in the total fluorescence is defined as,

$$f_n = \frac{\tau_n B_n}{\sum_{i=1}^N B_i \tau_i} \times 100. \quad (2-8)$$

The quality of the curve fitting is evaluated by reduced chi-square (0.9-1.1) and residual data. The purpose of the fitting is to obtain the decays in an analytical form suitable for further data analysis.

To construct time resolved emission spectra (TRES) we follow the technique described in references [14-15]. As described above, the emission intensity decays are analyzed in terms of the multi-exponential model,

$$I(\lambda, t) = \sum_{i=1}^N \alpha_i(\lambda) \exp(-t/\tau_i(\lambda)) \quad (2-9)$$

where $\alpha_i(\lambda)$ are the pre-exponential factors, with $\sum \alpha_i(\lambda) = 1.0$. In this analysis we compute a new set of intensity decays, which are normalized so that the time-integrated intensity at each wavelength is equal to the steady-state intensity at that wavelength. Considering $F(\lambda)$ to be the steady-state emission spectrum, we calculate a set of $H(\lambda)$ values using,

$$H(\lambda) = \frac{F(\lambda)}{\int_0^{\infty} I(\lambda, t) dt} \quad (2-10)$$

which for multiexponential analysis becomes,

$$H(\lambda) = \frac{F(\lambda)}{\sum_i \alpha_i(\lambda) \tau_i(\lambda)} \quad (2-11)$$

Then, the appropriately normalized intensity decay functions are given by,

$$I'(\lambda, t) = H(\lambda) I(\lambda, t) = \sum_{i=1}^N \alpha'_i(\lambda) \exp\left(-t/\tau_i(\lambda)\right) \quad (2-12)$$

where $\alpha'_i(\lambda) = H(\lambda) \alpha_i(\lambda)$. The values of $I'(\lambda, t)$ are used to calculate the intensity at any wavelength and time, and thus the TRES. The values of the emission maxima and spectral width are determined by nonlinear least-square fitting of the spectral shape of the TRES. The spectral shape is assumed to follow a lognormal line shape [14],

$$I(\bar{\nu}) = I_0 \exp\left\{-\left[\ln 2 \left(\frac{\ln(\alpha + 1)}{b}\right)^2\right]\right\} \quad (2-13)$$

with $\alpha = \frac{2b(\bar{\nu} - \bar{\nu}_{\max})}{\Delta} - 1$ where I_0 is amplitude, $\bar{\nu}_{\max}$ is the wavenumber of the emission

maximum and spectral width is given by, $\Gamma = \Delta \left[\frac{\sinh(b)}{b} \right]$. The terms b and Δ are asymmetry and width parameters, respectively and equation (2-9) reduces to a Gaussian function for $b=0$.

The time-dependent fluorescence Stokes shifts, as estimated from TRES are used to construct the normalized spectral shift correlation function or the solvent correlation function $C(t)$ and is defined as,

$$C(t) = \frac{\bar{\nu}(t) - \bar{\nu}(\infty)}{\bar{\nu}(0) - \bar{\nu}(\infty)} \quad (2-14)$$

where, $\bar{\nu}(0)$, $\bar{\nu}(t)$ and $\bar{\nu}(\infty)$ are the emission maxima (in cm^{-1}) of the TRES at time zero, t and infinity, respectively. The $\bar{\nu}(\infty)$ value is considered to be the emission frequency beyond which insignificant or no spectral shift is observed. The $C(t)$ function represents

the temporal response of the solvent relaxation process, as occurs around the probe following its photoexcitation and the associated change in the dipole moment.

2.1.2. Fluorescence Anisotropy: Anisotropy is defined as the extent of polarization of the emission from a fluorophore. Anisotropy measurements are commonly used in biochemical applications of fluorescence. It provides information about the size and shape of proteins or the rigidity of various molecular environments. Anisotropy measurements have also been used to measure protein-protein associations, fluidity of membranes and for immunoassays of numerous substances. These measurements are based on the principle of photoselective excitation of those fluorophore molecules whose absorption transition dipoles are parallel to the electric vector of polarized excitation light. In an isotropic solution, fluorophores are oriented randomly. However, upon selective excitation, partially oriented population of fluorophores with polarized fluorescence emission results. The relative angle between the absorption and emission transition dipole moments determines the maximum measured anisotropy (r_0). The fluorescence anisotropy (r) and polarization (P) are defined by,

$$r = \frac{I_{\parallel} - I_{\perp}}{I_{\parallel} + 2I_{\perp}} \quad (2-15)$$

$$P = \frac{I_{\parallel} - I_{\perp}}{I_{\parallel} + I_{\perp}} \quad (2-16)$$

where I_{\parallel} and I_{\perp} are the fluorescence intensities of vertically and horizontally polarized emission when the fluorophore is excited with vertically polarized light. Polarization and anisotropy are interrelated as,

$$r = \frac{2P}{3 - P} \quad (2-17)$$

$$\text{and} \quad P = \frac{3r}{2 + r} \quad (2-18)$$

Although polarization and anisotropy provides the same information, anisotropy is preferred since the latter is normalized by total fluorescence intensity ($I_T = I_{\parallel} + 2I_{\perp}$) and in case of multiple emissive species anisotropy is additive while polarization is not. Several phenomena, including rotational diffusion and energy transfer, can decrease the

measured anisotropy to values lower than maximum theoretical values. Following a pulsed excitation the fluorescence anisotropy, $r(t)$ of a sphere is given by,

$$r(t) = r_0 \exp(-t/\phi) \quad (2-19)$$

where r_0 is the anisotropy at time $t=0$ and ϕ is the rotational correlation time of the sphere.

(i) Theory: For a radiating dipole, the intensity of light emitted is proportional to the square of the projection of the electric field of the radiating dipole onto the transmission axis of the polarizer. The intensity of parallel and perpendicular projections are given by,

$$I_{\parallel}(\theta, \psi) = \cos^2 \theta \quad (2-20)$$

$$I_{\perp}(\theta, \psi) = \sin^2 \theta \sin^2 \psi \quad (2-21)$$

where θ and ψ are the orientational angles of a single fluorophore relative to the z and y -axes, respectively (Figure 2.4 (a)). In solution, fluorophores remain in random distribution and the anisotropy is calculated by excitation photoselection. Upon photoexcitation by polarized light, the molecules having absorption transition moments aligned parallel to the electric vector of the polarized light have the highest probability of absorption. For the excitation polarization along z -axis, all molecules having an angle ψ with respect to the y -axis will be excited. The population will be symmetrically distributed about the z -axis. For experimentally accessible molecules, the value of ψ will be in the range from 0 to 2π with equal probability. Thus, the ψ dependency can be eliminated.

$$\langle \sin^2 \psi \rangle = \frac{\int_0^{2\pi} \sin^2 \psi d\psi}{\int_0^{2\pi} d\psi} = \frac{1}{2} \quad (2-22)$$

$$\text{and } I_{\parallel}(\theta) = \cos^2 \theta \quad (2-23)$$

$$I_{\perp}(\theta) = \frac{1}{2} \sin^2 \theta \quad (2-24)$$

Consider a collection of molecules oriented relative to the z -axis with probability $f(\theta)$. Then, measured fluorescence intensities for this collection after photoexcitation are,

$$I_{\parallel} = \int_0^{\pi/2} f(\theta) \cos^2 \theta d\theta = k \langle \cos^2 \theta \rangle \quad (2-25)$$

$$I_{\perp} = \int_0^{\pi/2} f(\theta) \sin^2 \theta d\theta = \frac{k}{2} \langle \sin^2 \theta \rangle \quad (2-26)$$

where $f(\theta)d\theta$ is the probability that a fluorophore is oriented between θ and $\theta+d\theta$ and is given by,

$$f(\theta)d\theta = \cos^2 \theta \sin \theta d\theta \quad (2-27)$$

k is the instrumental constant. Thus, the anisotropy (r) is defined as,

$$r = \frac{3\langle \cos^2 \theta \rangle - 1}{2} \quad (2-28)$$

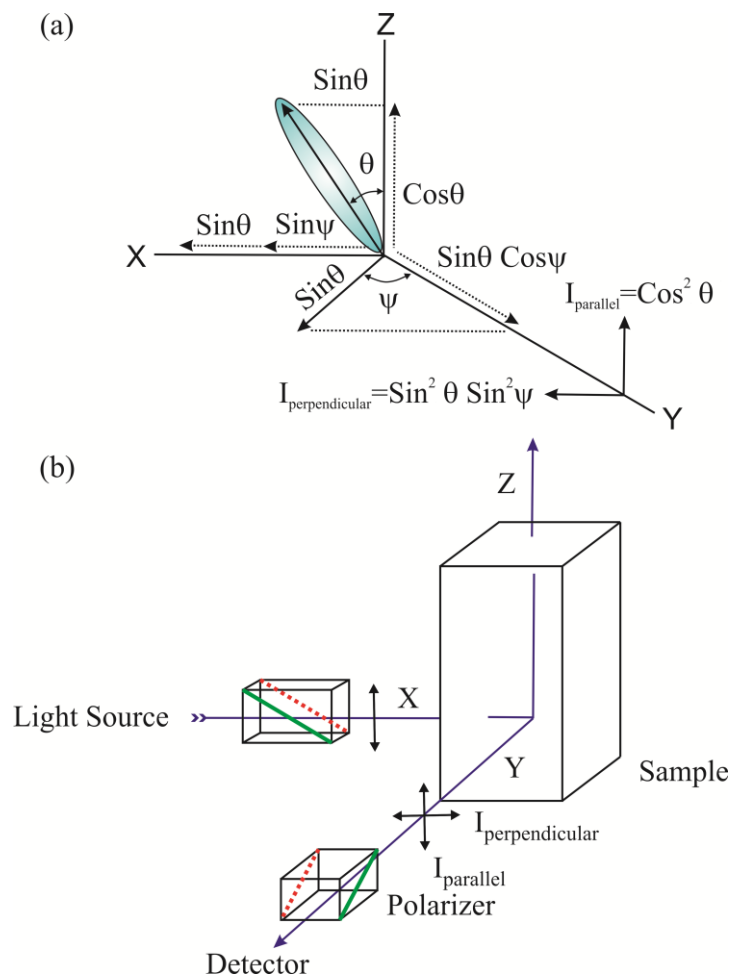


Figure 2.4. (a) Emission intensity of a single fluorophore (blue ellipsoid) in a coordinate system. (b) Schematic representation of the measurement of fluorescence anisotropy.

when $\theta=54.7^\circ$ i.e. when $\cos^2\theta=1/3$, the complete loss of anisotropy occurs. Thus, the fluorescence taken at $\theta=54.7^\circ$ with respect to the excitation polarization is expected to be free from the effect of anisotropy and is known as magic angle emission. For collinear absorption and emission dipoles, the value of $\langle\cos^2\theta\rangle$ is given by the following equation,

$$\langle\cos^2\theta\rangle = \frac{\int_0^{\pi/2} \cos^2\theta f(\theta)d\theta}{\int_0^{\pi/2} f(\theta)d\theta} \quad (2-29)$$

Substituting equation (2-27) in equation (2-29) one can get the value of $\langle\cos^2\theta\rangle=3/5$ and anisotropy value to be 0.4 (from equation (2-28)). This is the maximum value of anisotropy obtained when the absorption and emission dipoles are collinear and when no other depolarization process takes place. However, for most fluorophores, the value of anisotropy is less than 0.4 and it is dependent on the excitation wavelength. It is demonstrated that as the displacement of the absorption and emission dipole occurs by an angle γ relative to each other, it causes further loss of anisotropy (reduction by a factor 2/5) [15] from the value obtained from equation (2-28). Thus, the value of fundamental anisotropy, r_0 is given by,

$$r_0 = \frac{2}{5} \left(\frac{3\cos^2\gamma - 1}{2} \right) \quad (2-30)$$

For any fluorophore randomly distributed in solution, with one-photon excitation, the value of r_0 varies from -0.2 to 0.4 for γ values varying from 90° to 0° .

(ii) Experimental Methods: For time resolved anisotropy ($r(t)$) measurements (Figure 2.4 (b)), emission polarization is adjusted to be parallel and perpendicular to that of the excitation polarization. Spencer and Weber [16] have derived the relevant equations for the time dependence of $I_{\parallel}(t)$ (equation (2-31)) and $I_{\perp}(t)$ (equation (2-32)) for single rotational and fluorescence relaxation times, ϕ and τ_f , respectively,

$$I_{\parallel}(t) = \exp(-t/\tau_f) (1 + 2r_0 \exp(-t/\phi)) \quad (2-31)$$

$$I_{\perp}(t) = \exp(-t/\tau_f) (1 - r_0 \exp(-t/\phi)) \quad (2-32)$$

The total fluorescence is given by,

$$F(t) = I_{\parallel}(t) + 2I_{\perp}(t) = 3\exp(-t/\tau_f) = F_0 \exp(-t/\tau_f) \quad (2-33)$$

The time dependent anisotropy, $r(t)$ is given by,

$$r(t) = \frac{I_{\parallel}(t) - I_{\perp}(t)}{I_{\parallel}(t) + 2I_{\perp}(t)} = r_0 \exp(-t/\phi) \quad (2-34)$$

$F(t)$ depends upon τ_f and $r(t)$ only upon ϕ so that these two lifetimes can be separated. This separation is not possible in steady-state measurements. It should be noted that the degree of polarization (P) is not independent of τ_f and is therefore not as useful as r . For reliable measurement of $r(t)$, three limiting cases can be considered,

- (a) If $\tau_f < \phi$, the fluorescence decays before the anisotropy decays, and hence only r_0 can be measured.
- (b) If $\phi < \tau_f$, in contrast to steady-state measurements, ϕ can be measured in principle. The equations (2-31) and (2-32) show that the decay of the parallel and perpendicular components depends only upon ϕ . The experimental disadvantage of this case is that those photons emitted after the lapse of a few rotational correlation times, ϕ can not contribute to the determination of ϕ , but can be avoided with a good signal-to-noise ratio.
- (c) If $\phi \approx \tau_f$, then it becomes the ideal situation since almost all photons are counted within the time (equal to several rotational relaxation times) in which $r(t)$ shows measurable changes.

For systems with multiple rotational correlation times, $r(t)$ is given by,

$$r(t) = r_0 \sum_i \beta_i e^{-t/\phi_i} \quad (2-35)$$

where $\sum_i \beta_i = 1$. It should be noted that the instrument monitoring the fluorescence, particularly the spectral dispersion element, responds differently to different polarizations of light, thus emerging the need for a correction factor. For example, the use of diffraction gratings can yield intensities of emission, which depend strongly upon orientation with respect to the plane of the grating. It is necessary when using such instruments to correct for the anisotropy in response. This instrumental anisotropy is usually termed as G-factor (grating factor) and is defined as the ratio of the transmission efficiency for vertically

polarized light to that for horizontally polarized light ($G = I_{\parallel} / I_{\perp}$). Hence, values of fluorescence anisotropy, $r(t)$ corrected for instrumental response, would be given by [17],

$$r(t) = \frac{I_{\parallel}(t) - GI_{\perp}(t)}{I_{\parallel}(t) + 2GI_{\perp}(t)} \quad (2-36)$$

The G-factor at a given wavelength can be determined by exciting the sample with horizontally polarized excitation beam and collecting the two polarized fluorescence decays, one parallel and other perpendicular to the horizontally polarized excitation beam. G-factor can also be determined following longtime tail matching technique [17]. If $\phi < \tau_f$, it can be seen that the curves for $I_{\parallel}(t)$ and $I_{\perp}(t)$ should become identical. If in any experiment they are not, it can usually be assumed that this is due to a non-unitary G-factor. Hence normalizing the two decay curves on the tail of the decay eliminates the G-factor in the anisotropy measurement.

2.1.3. Arrhenius Theory of Activation Energy: The dynamics of solvation at a biomolecular interface can be exploited to give information about the energetics of the participating water molecules [9]. Water present at the surface of biomolecules or biomimicking systems can broadly be distinguished as bound type (water hydrogen bonded to the interface) and bulk type water (Figure 2.5). In the water layer around the protein surface, the interaction with water involves hydrogen bonding to the polar and charged groups of the surface. The strength of this bonding varies from group to group. When strongly bonded to the protein, the water molecules cannot contribute to solvation dynamics because they can neither rotate nor translate. But the hydrogen bonding is transient, and there is a dynamic equilibrium between the free and the bound water molecules. The potential of interaction can be represented by a double-well structure to symbolize the processes of bond breaking and bond forming. In general, the bonded water molecules become free by translational and rotational motions. The experimental observations of a biphasic behavior of hydration indicated the presence of bound and free water in the surface layer.

bound \leftrightarrow free (rotating and translating)

The slow component of the solvation, is related to the rate constant for bound to free water interconversion k_{bf} as,

$$\frac{1}{\tau_{solv}} \approx k_{bf} = \frac{k_B T}{h} e^{-\frac{\Delta G_{bf}^{\circ}}{RT}} \quad (2-37)$$

where, ΔG_{bf}° is the binding energy for bound to free water interconversion, k_B is the Boltzmann constant, T , the absolute temperature and h is the Planck constant. This dynamic equilibrium is found to be dependent on external parameters like temperature, pressure etc. The temperature dependence of the solvation follows the Arrhenius equation and yields the activation energy needed for the conversion of bound and free forms [18].

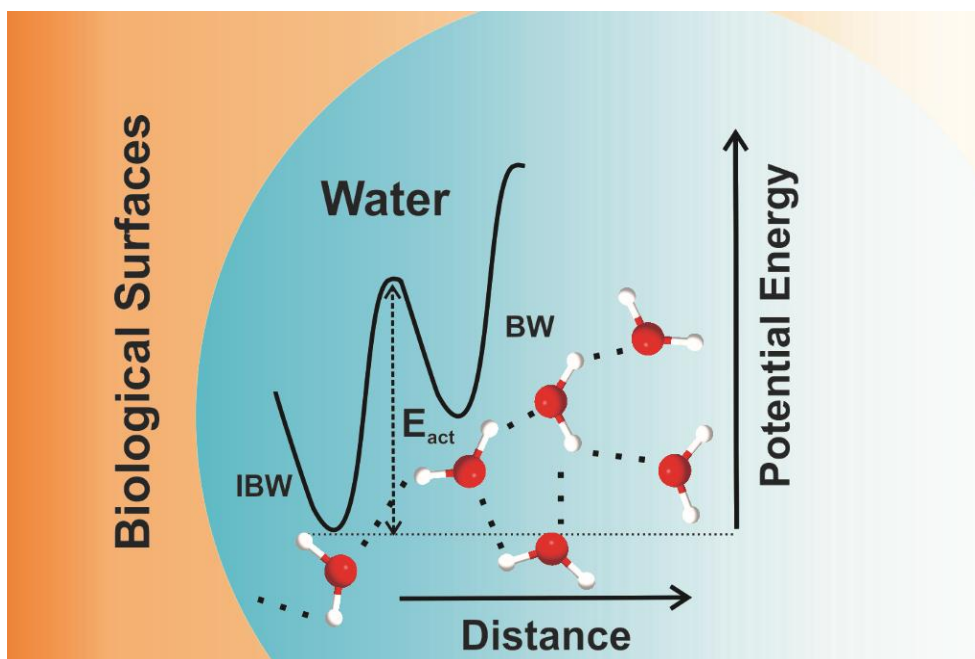


Figure 2.5. Schematic representation of different types of water molecules present at various bimolecular interfaces and the corresponding activation energy barrier.

2.1.4. Förster Resonance Energy Transfer: Förster resonance energy transfer (FRET) is an electrodynamic phenomenon involving the non-radiative transfer of the excited state energy from the donor dipole (D) to an acceptor dipole (A) in the ground state (Figure 2.6 (a)). FRET has got wide applications in all fluorescence applications including medical diagnostics, DNA analysis and optical imaging. Since FRET can measure the size of a protein molecule or the thickness of a membrane, it is also known as “spectroscopic ruler” [19]. FRET is very often used to measure the distance between two sites on a

macromolecule. Basically, FRET is of two types: (a) Homo-molecular FRET and (b) Hetero-molecular FRET. In the former case the same fluorophore acts both as energy donor and acceptor, while in the latter case two different molecules act as donor and acceptor.

Each donor-acceptor (D-A) pair participating in FRET is characterized by a distance known as Förster distance (R_0) i.e., the D-A separation at which energy transfer is 50% efficient. The R_0 value ranges from 20 to 60 Å. The rate of resonance energy transfer (k_T) from donor to an acceptor is given by [15],

$$k_T = \frac{1}{\tau_D} \left(\frac{R_0}{r} \right)^6 \quad (2-38)$$

where τ_D is the lifetime of the donor in the absence of acceptor and r is the donor to acceptor (D-A) distance. The rate of transfer of donor energy depends upon the extent of overlap of the emission spectrum of the donor with the absorption spectrum of the acceptor ($J(\lambda)$), the quantum yield of the donor (Q_D), the relative orientation of the donor and acceptor transition dipoles (κ^2) and the distance between the donor and acceptor molecules (r) (Figure 2.6 (b)). In order to estimate FRET efficiency of the donor and hence to determine distances between donor-acceptor pairs, the methodology described below is followed [15]. R_0 is given by,

$$R_0 = 0.211 [\kappa^2 n^{-4} Q_D J(\lambda)]^{1/6} \quad (\text{in } \text{Å}) \quad (2-39)$$

where n is the refractive index of the medium, Q_D is the quantum yield of the donor and $J(\lambda)$ is the overlap integral. κ^2 is defined as,

$$\kappa^2 = (\cos \theta_T - 3 \cos \theta_D \cos \theta_A)^2 = (\sin \theta_D \sin \theta_A \cos \varphi - 2 \cos \theta_D \cos \theta_A)^2 \quad (2-40)$$

where θ_T is the angle between the emission transition dipole of the donor and the absorption transition dipole of the acceptor, θ_D and θ_A are the angles between these dipoles and the vector joining the donor and acceptor and φ is angle between the planes of the

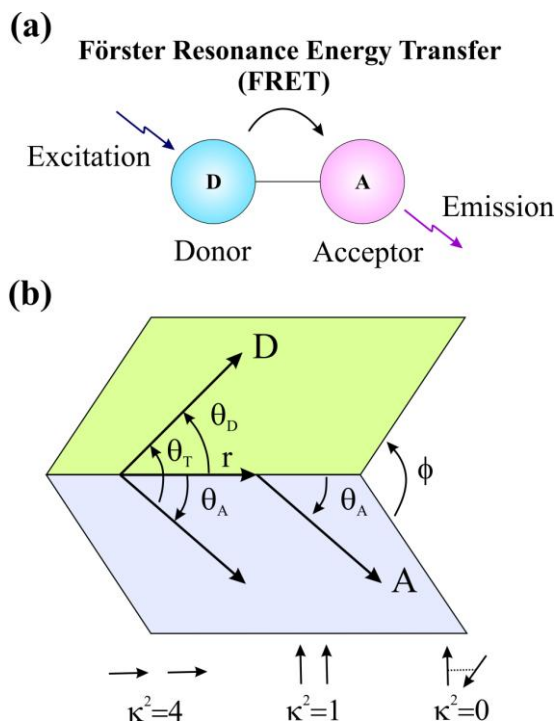


Figure 2.6. (a) Schematic illustration of the Förster resonance energy transfer (FRET) process. (b) Dependence of the orientation factor κ^2 on the directions of the emission and absorption dipoles of the donor and acceptor, respectively.

donor and acceptor (Figure 2.6 (b)). κ^2 value can vary from 0 to 4. For collinear and parallel transition dipoles, $\kappa^2=4$; for parallel dipoles, $\kappa^2=1$; and for perpendicularly oriented dipoles, $\kappa^2=0$. For donor and acceptors that randomize by rotational diffusion prior to energy transfer, the magnitude of κ^2 is assumed to be $2/3$. However, in systems where there is a definite site of attachment of the donor and acceptor molecules, to get physically relevant results, the value of κ^2 has to be estimated from the angle between the donor emission and acceptor absorption dipoles [20]. $J(\lambda)$, the overlap integral, which expresses the degree of spectral overlap between the donor emission and the acceptor absorption, is given by,

$$J(\lambda) = \frac{\int_0^{\infty} F_D(\lambda) \varepsilon_A(\lambda) \lambda^4 d\lambda}{\int_0^{\infty} F_D(\lambda) d\lambda} \quad (2-41)$$

where $F_D(\lambda)$ is the fluorescence intensity of the donor in the wavelength range of λ to $\lambda+d\lambda$ and is dimensionless. $\epsilon_A(\lambda)$ is the extinction coefficient (in $M^{-1}cm^{-1}$) of the acceptor at λ . If λ is in nm, then $J(\lambda)$ is in units of $M^{-1}cm^{-1}nm^4$.

Once the value of R_0 is known, the efficiency of energy transfer can be calculated. The efficiency of energy transfer (E) is the fraction of photons absorbed by the donor which are transferred to the acceptor and is defined as,

$$E = \frac{k_T(r)}{\tau_D^{-1} + k_T(r)} \quad (2-42)$$

or

$$E = \frac{R_0^6}{r^6 + R_0^6} \quad (2-43)$$

The transfer efficiency is measured using the relative fluorescence intensity of the donor, in absence (F_D) and presence (F_{DA}) of the acceptor as,

$$E = 1 - \frac{F_{DA}}{F_D} \quad (2-44a)$$

For D-A systems decaying with multiexponential lifetimes, E is calculated from the amplitude weighted lifetimes $\langle\tau\rangle = \sum_i \alpha_i \tau_i$ of the donor in absence (τ_D) and presence (τ_{DA}) of the acceptor as,

$$E = 1 - \frac{\tau_{DA}}{\tau_D} \quad (2-44b)$$

The D-A distances can be measured using equations (2-43), (2-44a) and (2-44b). The distances measured using equations (2-44a) and (2-44b) are revealed as R^S (steady-state measurement) and R^{TR} (time-resolved measurement), respectively. In one of the studies from our group [21], we have shown that the energy transfer efficiency E , calculated from steady-state experiment (equation 2-44a) might be due to re-absorption of donor emission, but not due to dipole-dipole interaction (FRET).

(i) Distance Distribution in Donor-Acceptor Systems: Distance distribution between donor and acceptor can be estimated according to the procedure described in the literature [15, 22]. The observed fluorescence transients of the donor in absence of acceptor in a micelle can be fitted using a nonlinear least-squares fitting procedure (software SCIENTIST) to the following function,

$$I_D(t) = \int_0^t E(t')P(t-t)dt' \quad (2-45)$$

which comprises the convolution of the instrument response function (IRF) ($E(t)$) with exponential ($P(t) = \sum_i \alpha_{Di} \exp(-t/\tau_{Di})$). The convolution of the distance distribution function $P(r)$ in the fluorescence transients of donor in presence of acceptor in the system under studies (micelle) is estimated using the same software (SCIENTIST) in the following way.

The intensity decay of donor-acceptor pair, spaced at a distance 'r', is given by

$$I_{DA}(r,t) = \sum_i \alpha_{Di} \exp \left[-\frac{t}{\tau_{Di}} - \frac{t}{\tau_{Di}} \left(\frac{R_0}{r} \right)^6 \right] \quad (2-46)$$

and the intensity decay of the sample considering $P(r)$ is given by,

$$I_{DA}(t) = \int_{r=0}^{\infty} P(r)I_{DA}(r,t)dr \quad (2-47)$$

Where $P(r)$ consist of the following terms:

$$P(r) = \frac{1}{\sigma\sqrt{2\pi}} \exp \left[-\frac{1}{2} \left(\frac{\bar{r}-r}{\sigma} \right)^2 \right] \quad (2-48)$$

In this equation \bar{r} is the mean of the Gaussian with a standard deviation of σ . Usually distance distributions are described by the full width at half maxima. This half width is given by $hw = 2.354\sigma$.

2.1.5. 'Infelta-Tachiya' Model (Kinetic Model): In some of our studies [23-24] we have employed a kinetic model developed by Infelta and Tachiya for better understanding of the distribution of energy acceptors (quenchers) around the micelles. The decay of excited probes in a micelle may be described by the following kinetic model [23]:



where P_n^* and P_n stand for a micelle containing n quencher molecules with and without an excited probe, respectively. k_0 is the total decay constant of the excited state in absence of a quencher. k_q is the rate constant for quenching of an excited probe in a micelle containing one quencher molecule. In this kinetic model, it is assumed that the distribution of the number of quenchers attached to one micelle follows a Poisson distribution, [25] namely,

$$p(n) = (m^n / n!) \exp(-m) \quad (2-51)$$

where m is the mean number of quenchers in a micelle.

$$m = k_+[A]/k_- \quad (2-52)$$

where k_+ is the rate constant for entry of a quencher molecule into a micelle, while k_- is the rate constant for exit of a quencher molecule from a micelle containing one quencher molecule. “A” stands for a quencher molecule in the aqueous phase. Based upon the above model, the equation for the total concentration $P^*(t)$ of excited probes at time t is given by [23]:

$$P^*(t) = P^*(0) \exp\left[-\left(k_0 + \frac{k_0 k_+[A]}{k_- + k_q}\right)t - \frac{k_q^2 k_+[A]}{k_-(k_- + k_q)^2} \{1 - \exp[-(k_- + k_q)t]\}\right] \quad (2-53)$$

If k_- is much smaller than k_q , equation (2-53) reduces to,

$$P^*(t) = P^*(0) \exp\{-k_0 t - m[1 - \exp(-k_q t)]\} \quad (2-54)$$

The observed fluorescence transients can be fitted using a nonlinear least squares fitting procedure (software SCIENTISTTM) to a function ($X(t) = \int_0^t E(t')P(t-t')dt'$) comprising of the convolution of the instrument response function (IRF) ($E(t)$) with exponential ($P^*(t) = P^*(0) \exp\{-k_0 t - m[1 - \exp(-k_q t)]\}$). The purpose of this fitting is to obtain the decays in an analytic form suitable for further data analysis.

In case of quantum dots (QDs), along with the quencher/acceptor (in case of energy transfer process), there exist some unidentified traps that further cause quenching of the lifetime of excited QD probe, which are also taken into account. If the distribution of the number of unidentified traps around the donor QDs follows a Poisson distribution with the average number (m_t), the decay curves of the excited state of QDs in solvent in absence and presence of acceptor are described by: [26]

$$P^*(t,0) = P^*(0) \exp \{-k_0 t - m_t [1 - \exp(-k_{qt} t)]\} \quad (2-55)$$

$$P^*(t,m) = P^*(0) \exp \{-k_0 t - m_t [1 - \exp(-k_{qt} t)] - m [1 - \exp(-k_q t)]\} \quad (2-56)$$

where the quenching rate constant (k_{qt}) by unidentified traps may be different from that (k_q) by acceptor.

In one of our studies [23], we have also employed extended Infelta-Tachiya kinetic model as described by the following equation [27],

$$P^*(t) = P^*(0) \exp \left[-\gamma t + \mu (\exp^{-\beta t} - 1) \right] \quad (2-57)$$

Where γ , μ , and β are functions of the rate constants of probe migration (k), quenching (k_q), and quencher exchange either by micelle collision (k_e) or via the aqueous phase (k_-) and are explicitly defined as,

$$\gamma = k_0 + k + m a_2 k_q / \beta \quad (2-58)$$

$$\mu = m k_q^2 / \beta^2 \quad (2-59)$$

$$\beta = k_q + a_2 \quad (2-60)$$

$$a_2 = k_e [M] + k_- \quad (2-61)$$

In the expressions (2-58)-(2-61), k_0 , m and $[M]$ stand for the deactivation rate constant of the excited probe in absence of quencher, the average number of quenchers per micelle, and the micelle concentration, respectively.

2.1.6. Adiabatic Compressibility: Adiabatic compressibility, (β_s) of a solution ($w_0=5$) can be determined by measuring the solution density (ρ_s) and the sound velocity (u_s) and applying the Laplace's equation,

$$\beta_s = \frac{1}{\rho_s u_s^2} \quad (2-62)$$

The apparent specific volume of solubilized water φ_v is given by,

$$\varphi_v = \frac{1}{\rho_{\text{solv}}} + \frac{\rho_{\text{solv}} - \rho_s}{c_w \rho_{\text{solv}}} \quad (2-63)$$

where c_w is the concentration of the water molecules in the micellar solution, ρ_{solv} and ρ_s are the densities of the solvent and the solution respectively. The partial apparent adiabatic compressibility (φ_k) of the solubilized is obtained from the following relation,

$$\varphi_k = \beta_s \left(2\varphi_v - 2[u] - \frac{1}{\rho_{\text{solv}}} \right) \quad (2-64)$$

$[u]$ is the relative specific sound velocity increment given by,

$$[u] = \frac{u_s - u_{\text{solv}}}{u_{\text{solv}} c_w} \quad (2-65)$$

u_{solv} and u_w are the sound velocities in solvent and solubilized water respectively.

2.1.7. Twisted Intramolecular Charge Transfer: While interpretation of solvent-dependent emission spectra appears simple, this is a very complex topic. The complexity is due to the variety of interactions that can result in spectral shifts. The theory for general solvent effects is often inadequate for explaining the detailed behavior of fluorophores in a variety of environments. The Jablonski diagram for solvent effects should also reflect the possibility of specific solvent-fluorophore interactions that can lower the energy of the excited state. In addition to specific solvent-fluorophore interactions, many fluorophores can form an internal charge transfer (ICT) state, or a twisted intramolecular charge transfer

(TICT) state (Figure 2.7). For instance, suppose the fluorophore contains both an electron-donating and an electron-accepting group. Such groups could be amino and carbonyl groups, respectively, but numerous other groups are also known. Following excitation there can be an increase in charge separation within the fluorophore. If the solvent is polar, then a species with charge separation (the ICT state) may become the lowest energy state. In a nonpolar solvent the species without charge separation, the so called locally excited (LE) state, may have the lowest energy. Hence, the role of solvent polarity is not only to lower the energy of the excited state due to general solvent effects, but also to govern which state has the lowest energy. In some cases, formation of the ICT state requires rotation of groups on the fluorophore to form the TICT state. Formation of ICT states is not contained within the theory of general solvent effects. Some probes display charge transfer in the excited state. In a highly viscous environment, the molecule cannot distort as needed for charge transfer, and the decay is radiative. In a less viscous environment, the molecule displays internal rotation and charge transfer, which results in radiation-less decay.

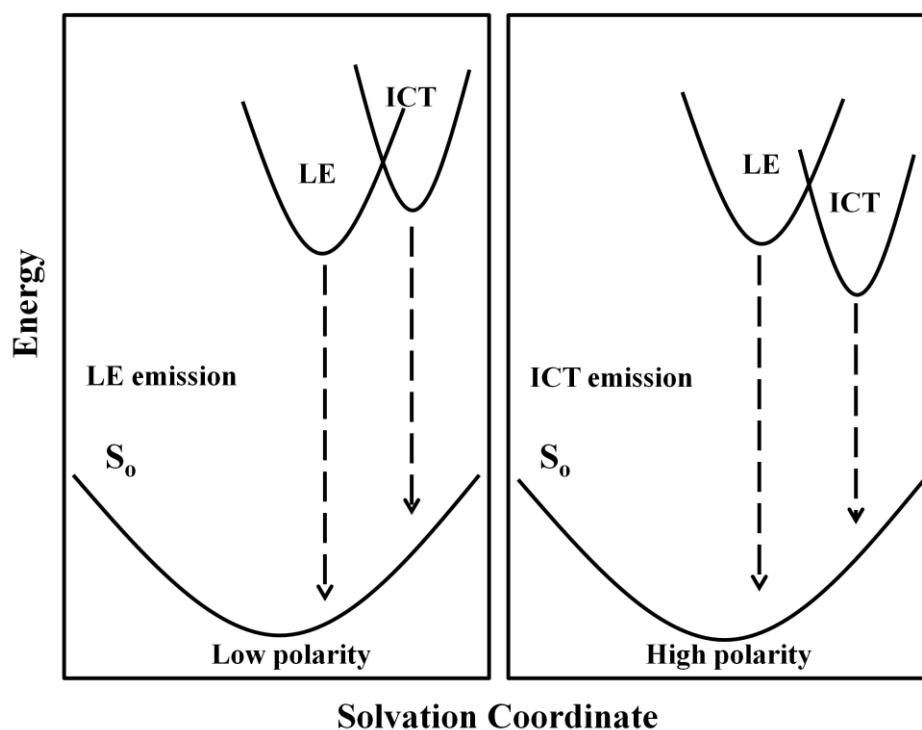


Figure 2.7. Effect of solvent polarity on the energies of LE and ICT states [28].

2.1.8. Photoinduced Electron Transfer: There are several mechanisms for quenching of a fluorophore such as intersystem crossing or the heavy atom effect, electron exchange or Dexter interactions, photoinduced electron transfer (PET), and FRET. In PET, a complex is formed between the electron donor (D_p) and the electron acceptor (A_p). The subscript P is used to identify the quenching as due to a PET mechanism. This charge transfer complex can return to the ground state without emission of a photon, but in some cases, exciplex emission is observed. Finally, the extra electron on the acceptor is returned to the electron donor. The direction of electron transfer in the excited state is determined by the oxidation and reduction potential of the ground and excited states. Upon excitation the electron donor transfers an electron to the acceptor with a rate k_p , forming the charge transfer complex $[D_p^+ A_p^-]^*$ (Figure. 2.8). This complex may emit as an exciplex ($h\nu_E$) or be quenched and return to the ground state. The important part of this process is the decrease in total energy of the charge transfer complex. The energy decreases because the ability to donate or accept electrons changes when a fluorophore is in the excited state. Excitation provides the energy to drive charge separation. D_p and A_p do not form a complex when both are in the ground state because this is energetically unfavorable. The energy released by electron transfer can also change if the ions become solvated and/or separated in a solvent with a high dielectric constant.

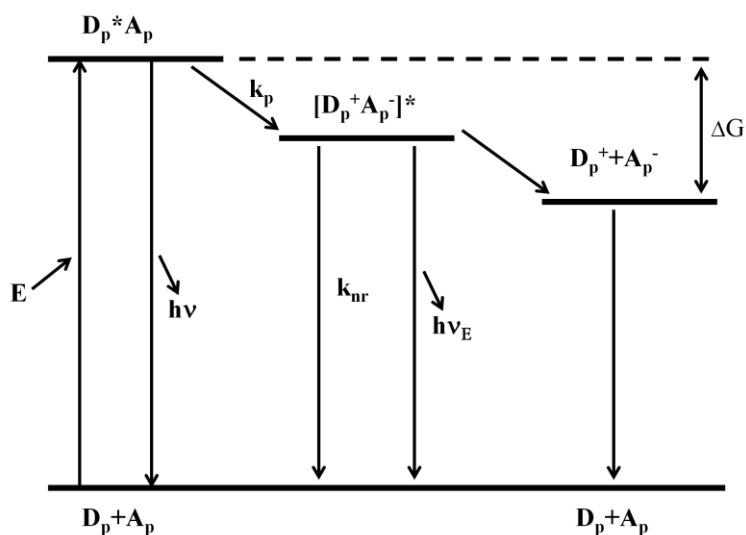


Figure 2.8. Energy diagram for photoinduced electron transfer (PET). The excited molecule is assumed to be the electron donor. ν and ν_E are emission from the fluorophore and exciplex, respectively.

2.2. Systems:

2.2.1. Organized Assemblies (Biomimetics): Amphiphilic molecules like surfactant, aggregates to form macromolecular assemblies like micelles and reverse micelles, which very often resemble the structural properties of biomolecules. In the following section, we will discuss about these entities.

A. Micelles: Micelles are spherical or nearly spherical aggregates of amphiphilic surfactant molecules formed in aqueous solution above a concentration known as critical micellar concentration (CMC). Micelles are formed above a critical temperature called “Kraft point” which is different for different surfactants. Micellar aggregates have diameter varying within 10 nm and the aggregation number, i.e., the number of surfactant molecules per micelle, ranges from 20 to 200. Israelachvili et al. [29] have proposed that surfactant molecular packing considerations are determinant in the formation of large surfactant aggregates. In particular, it is considered that the surfactant packing parameter θ ($\theta=v/\sigma l$, where v is the surfactant molecular volume, σ is the area per polar head, and l is the length of hydrophobic part) gives a good idea of the shape of aggregates which will form spontaneously [29]. It is considered that normal or direct rod-like micelles are formed when $2<\theta<3$ [30]. Micelles can be both neutral (triton X-100) and ionic (sodium dodecyl sulfate, SDS (anionic) and hexadecyltrimethylammonium bromide, CTAB (cationic)). The structure of a typical micelle is schematically shown in Figure 2.9. The core of a micelle is essentially “dry” and consists of the hydrocarbon chains with the polar and charged head groups projecting outward toward the bulk water. The stern layer, surrounding the core, comprises of the ionic or polar head groups, bound counter ions and water molecules. Between the stern layer and the bulk water there is a diffused Guoy-Chapman (GC) layer, which contains the free counter ions and water molecules. In non-ionic polyoxyethylated surfactants e.g. triton X-100 (TX-100), the hydrocarbon core is surrounded by a palisade layer, which consists of the polyoxyethylene groups hydrogen-bonded to water molecules [31]. Small angle X-ray and neutron scattering have provided detailed information on the structure of the CTAB micelles [32-33]. According to these studies, CMC and aggregation number of CTAB micelle are 0.8 mM and 52 respectively and the thickness of the stern layer is 6-9 Å [32-35]. The overall radius of CTAB micelle is about 50 Å. For TX-100 micelle, the CMC, thickness of the palisade layer and overall radius of the hydrophobic

core are reported to be 0.1 mM, 51 Å and 25-27 Å, respectively and that of SDS micelles are 8.6 mM [36], 33 Å [37] and 5 Å, respectively [38].

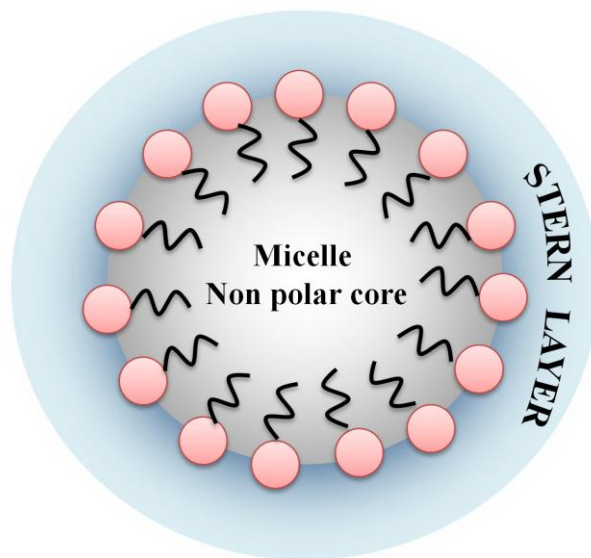


Figure 2.9. Schematic representation of the structure of a micelle.

2.2.2. Proteins: Human Serum Albumin: Human serum albumin (HSA) is a multi-domain protein (Figure 2.10) forming the major soluble protein constituent (60 % of the blood serum) of the blood circulatory system [39]. HSA (molecular weight 66,479 Da) is a heart-shaped tridomain protein with each domain comprising of two identical subdomains- A and B with each domain depicting specific structural and functional characteristics [40]. HSA having 585 amino acid residues assumes solid equilateral triangular shape with sides ~ 80 Å and depth ~ 30 Å [41]. Its amino acid sequence comprises of 17 disulfide bridges distributed over all domains, one free thiol (Cys34) in domain-I and a tryptophan residue (Trp214) in domain-IIA. About 67 % of HSA is α -helical while the rest of the structure being turns and extended polypeptides [41]. Each domain contains 10 principle helices (h1-h10). Subdomains-A and B share a common motif that includes h1, h2, h3 and h4 for subdomain-A, and h7, h8, h9, h10 for subdomain-B. The non-existence of disulfide linkage connecting h1 and h3 in subdomain-IA is an exception. HSA is engaged with various physiological functions involving maintenance of osmotic blood pressure, transportation of

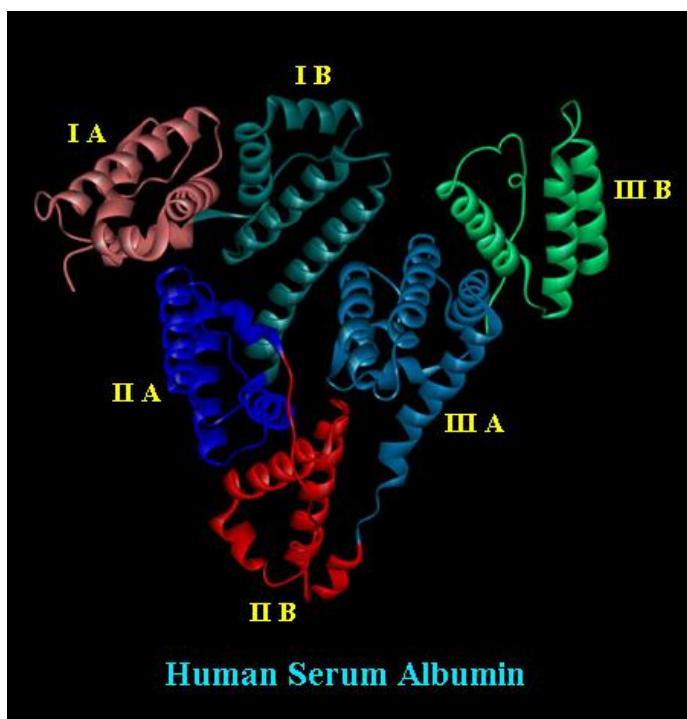


Figure 2.10. X-ray crystallographic structure (PDB code: 1N5U) of HSA depicting the different domains.

a wide variety of ligands in and out of the physiological system. The protein binds various kinds of ligands [42] including photosensitizing drugs [43] and the principal binding regions are located in subdomains–IIA and IIIA of which IIIA binding cavity is the most active one [41] and binds digitoxin and ibuprofen. Extremely hydrophobic probes are reported to reside in the subdomain IIIA of the protein even at its thermally unfolded states [44].

2.2.3. Deoxyribonucleic Acids (DNAs): Nucleic acids form the central molecules in transmission, expression and conservation of genetic information. DNA serves as carrier of genetic information [45]. The classic example of how biological function follows from biomolecular structure comes from the elucidation of double helical structure of DNA by Watson and Crick [46]. DNAs are polynucleotides with each nucleotide comprising of deoxyribose sugar, purine and pyrimidine bases and phosphate groups. The main bases whose intermolecular hydrogen bonding holds the DNA strands together are adenine, guanine, thymine and cytosine. There are generally three forms of DNA: the A, B and Z-

form. Native DNA, however, exists in B-form. Native DNA is about a metre long and comprises of hundreds of base pairs. The distance between two base pairs in B-DNA is 3.4 Å [47]. In about 4 M NaCl, B-form is converted into Z-form. DNA structures consist of major and minor grooves and intercalation spaces through which DNA interacts with ligands. There are two modes of interaction of DNA with ligands: (i) intercalation, where the planar polycyclic heteroaromatic ligands occupy the space in between the base pairs of DNA and interact through π - π interaction (Figure 2.11) [48], and (ii) groove binding where the ligands bind in the major and minor grooves of DNA [49]. The water molecules at the surface of DNA are critical to the structure and to the recognition by other molecules, proteins and drugs [1].

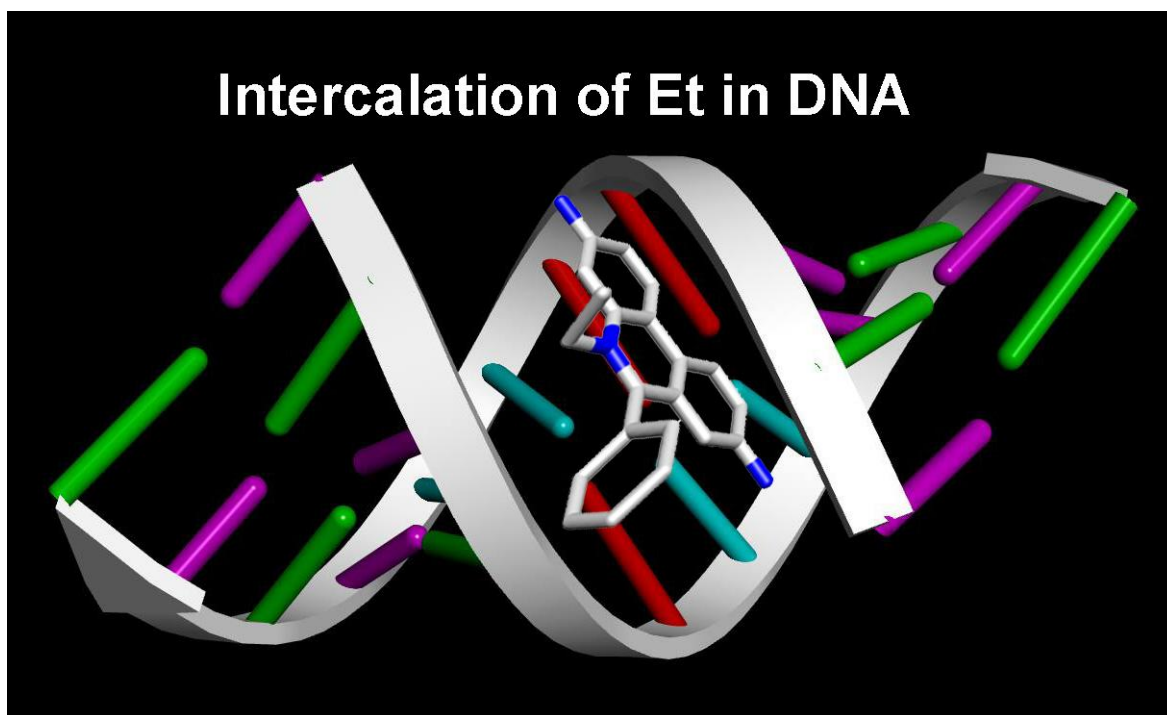


Figure 2.11. Schematic representation of ethidium (Et) intercalated in DNA. The DNA structure having sequence CGCGAATTCGCG was made by employing the WEBLAB VIEWERLITE program and the structure of Et was drawn using commercially available ChemBio3D (from CambridgeSoftTM) ultra software.

2.2.4. Molecular Probes: In this section we will discuss about the different probe molecules that have been used in the course of study.

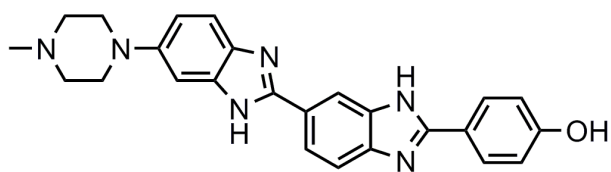
A. 4-[6'-(4-Methylpiperazino)-6,2'-bi[1H-benzimidazole]-2-yl]phenol, Hoechst 33258 (H258): The commercially available probe H258 is widely used as fluorescent cytological stain of DNA. Since it has affinity for the double stranded DNA, H258 can affect transcription/translation, and block topomerase/helicase activities. The dye is also used as a potential antihelminthic drug. X-ray crystallographic and NMR studies of the dye bound to a dodecamer DNA shows that the dye is bound to A-T rich sequence of the DNA minor groove. The binding constant of the dye to double stranded DNA at low [dye]:[DNA] ratio is found to be $5 \times 10^5 \text{ M}^{-1}$. In addition to DNA, the probe H258 can also bind to the surface of SDS micelles [23, 50].

B. 4',6-Diamidino-2-phenylindole (DAPI): The dye DAPI is another commercially available fluorescent cytological stain for DNA. Studies on the DAPI-DNA complexes show that the probe exhibits a wide variety of interactions of different strength and specificity with DNA [51].

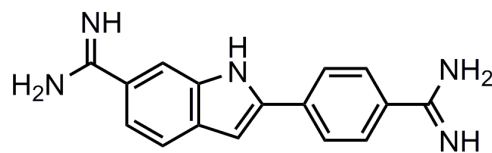
C. Coumarin 500 (C500): The solvation probe C500 is sparingly soluble in water and shows reasonably good solubility in isooctane. In bulk water the absorption peak (400 nm) is significantly red shifted compared to that in isooctane (360 nm). The emission peak of C500 in bulk water (500 nm) also shows a 90 nm red shift compared to that in isooctane (excitation at 350 nm). The significantly large solvochromic effect (solvation) in the absorption and emission spectra of C500 makes the dye an attractive solvation probe for microenvironments. The photophysics of the probe have also been studied in detail [52].

D. 2-p-toluidinonaphthalene-6-sulfonate (TNS): TNS is a well known probe for many biological systems [53] (see Figure 2.12). In aqueous solution, the emission quantum yield of TNS is very small (0.001) with emission peak at $\sim 490 \text{ nm}$ and the lifetime is also very short (60 ps) [54]. TNS has multiple absorption peaks at 270, 320 and 360 nm. Its molar extinction coefficient at 350 nm is $6640 \text{ M}^{-1} \text{ cm}^{-1}$. On binding to the less polar interior of the organized media, the emission intensity increases markedly by about 200 fold with huge blue shift [53]. The fluorescence enhancement of TNS in organized media is attributed to suppression of the main nonradiative pathway, namely, twisted intramolecular charge transfer (TICT) in the relatively nonpolar interior of the organized assemblies [55].

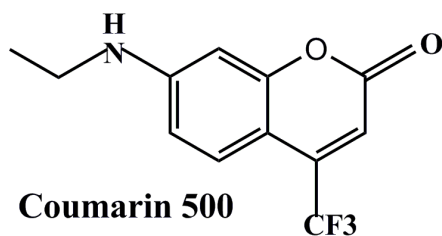
E. Ethidium (Et): Ethidium (Et) is a well known fluorescent probe (Figure 2.12) for DNA, which readily intercalates into the DNA double helix [56]. Compared to the case of



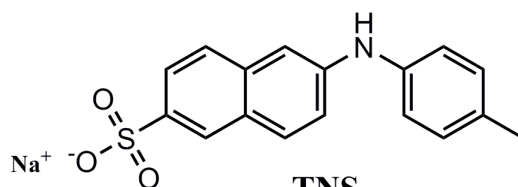
H258



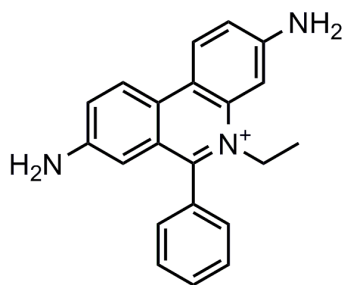
DAPI



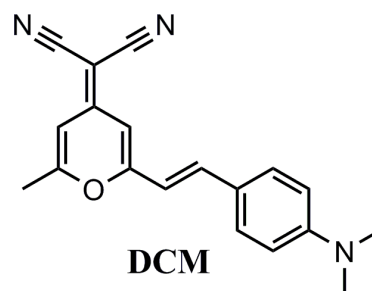
Coumarin 500



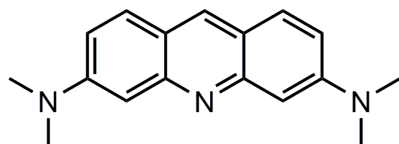
TNS



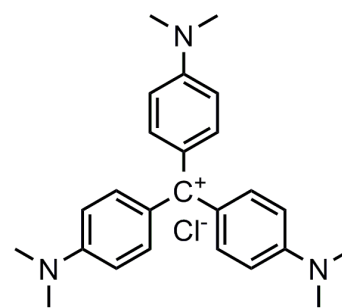
Ethidium (Et)



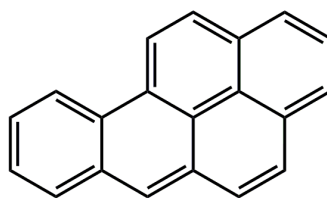
DCM



Acridine orange



Crystal violet



Benzo[a]pyrene

Figure 2.12. Schematic representation of the probes used in the course of study.

bulk water, the emission intensity and lifetime of Et increase nearly 11 times when Et intercalates into the double helix of DNA. This remarkable fluorescence enhancement of Et is utilized to study the motion of DNA segments, significantly enhanced quenching of DNA bound Et by various agents, and the interaction of DNA with surfactants and drug [57]. Apart from DNA, Et can also bind to biomimetic systems like micelles [20, 23].

F. 4-(dicyanomethylene)-2-methyl-6-(p-dimethylamino-styryl) 4H-pyran (DCM): The laser dye DCM, is completely insoluble in water, and has selective binding affinity to the micellar surface [58]. The dye is completely hydrophobic (nonpolar) in the ground state. However, UV excitation increases dipole moment of the probe making it polar and hence increases its hydrophilicity in the excited state. Thus the excited DCM diffuses from the micellar surface (relatively nonpolar) towards polar bulk water phase revealing a fluorescence emission signature (temporal line width) of the excursion through multiple environments in the excited state [59].

G. Acridine Orange (AO): The fluorescent cationic dye AO can bind to both DNA and RNA through intercalation and electrostatic interaction respectively [60]. Besides, AO is also known to interact with SDS micelle through both hydrophobic and electrostatic interactions as the hydrophobic aromatic rings of the AO molecule remain within the hydrophobic core of the SDS micelle, and the charged intracyclic imino group and the two terminal polar amino groups remain outward directed toward the stern layer [61-63].

H. Crystal Violet (CV): CV has a positively charged ammonium ion and three aromatic rings (Figure 2.12), used as a staining material. It can bind to the negatively charged phosphate backbone of DNA and negatively charged amino acids of proteins. It is highly soluble in water and other polar solvents. Its concentration is determined using extinction coefficient, $112,000 \text{ M}^{-1}\text{cm}^{-1}$ at 509 nm [64]. The interaction of CV probe molecules on SDS micelle has been investigated previously and concluded to reside at the surface of the micelle [65].

I. Benzo[a]pyrene (BP): It is a potent environmental carcinogen which can bind to DNA, extremely hydrophobic and belongs to the class of polycyclic aromatic hydrocarbons (PAHs) [66]. Being a pyrene derivative it is characterized by a high quantum yield near unity in micellar solutions [24] along with multiple vibronic bands in its emission spectrum [66].

References

- [1] S. K. Pal, A. H. Zewail, Dynamics of Water in Biological Recognition, *Chem. Rev.* 104 (2004) 2099.
- [2] J. A. Rupley, G. Careri, Protein Hydration and Function, *Adv. Prot. Chem.* 41 (1991) 37.
- [3] Y. Pocker, Water in Enzyme Reaction: Biophysical Aspects of Hydration-Dehydration Processes, *Cell. Mol. Life Sci.* 57 (2000) 1008.
- [4] J. A. Kornblatt, M. J. Kornblatt, Water as it Applies to the Function of Enzymes, *Int. Rev. Cytol.* 215 (2002) 49.
- [5] B. Bagchi, R. Biswas, Polar and Nonpolar Solvation Dynamics, Ion Diffusion and Vibrational Relaxation: Role of Biphasic Solvent Response in Chemical Dynamics, *Adv. Chem. Phys.* 109 (1999) 207.
- [6] B. Bagchi, Dynamics of Solvation and Charge Transfer in Dipolar Liquids, *Ann. Rev. Phys. Chem.* 40 (1989) 115.
- [7] G. R. Fleming, M. Cho, Chromophore-Solvent Dynamics, *Ann. Rev. Phys. Chem.* 47 (1996) 109.
- [8] R. Jimenez, G. R. Fleming, P. V. Kumar, M. Maroncelli, Femtosecond Solvation Dynamics of Water, *Nature* 369 (1994) 471
- [9] S. K. Pal, J. Peon, B. Bagchi, A. H. Zewail, Biological Water: Femtosecond Dynamics of Macromolecular Hydration, *J. Phys. Chem. B* 106 (2002) 12376.
- [10] L. Onsager, Comments on "Effects of Phase Density on Ionization Process and Electron Localization in Fluids" by J. Jortner and A. Gathon, *Can. J. Chem.* 55 (1977) 1819.
- [11] R. M. Stratt, M. Maroncelli, The Emerging Molecular View of Solvation Dynamics and Vibrational Relaxation, *J. Phys. Chem.* 100 (1996) 12981.
- [12] C. P. Hsu, X. Song, R. A. Marcus, Time-Dependent Stokes Shift and its Calculation from Solvent Dielectric Dispersion Data, *J. Phys. Chem. B* 101 (1997) 2546.
- [13] J. T. Hynes, Outer-Sphere Electron-Transfer Reactions and Frequency-Dependent Friction, *J. Phys. Chem.* 90 (1986) 3701.

- [14] M. L. Horng, J. A. Gardecki, A. Papazyan, M. Maroncelli, Subpicosecond Measurements of Polar Solvation Dynamics: Coumarin 153 Revisited, *J. Phys. Chem.* 99 (1995) 17311.
- [15] J. R. Lakowicz, *Principles of Fluorescence Spectroscopy*, Kluwer Academic/Plenum, New York, 1999.
- [16] R. D. Spencer, G. Weber, Measurement of Subnanosecond Fluorescence Lifetimes with a Cross-Correlation Phase Fluorometer, *Ann. N. Y. Acad. Sci.* 158 (1969) 361.
- [17] D. V. O'Connor, D. Philips, *Time Correlated Single Photon Counting*, Academic Press, London, 1984.
- [18] R. K. Mitra, S. S. Sinha, S. K. Pal, Temperature-Dependent Hydration at Micellar Surface: Activation Energy Barrier Crossing Model Revisited, *J. Phys. Chem. B* 111 (2007) 7577.
- [19] L. Stryer, Fluorescence Energy Transfer as a Spectroscopic Ruler, *Ann. Rev. Biochem.* 47 (1978) 819.
- [20] D. Banerjee, S. K. Pal, Simultaneous Binding of Minor Groove Binder and Intercalator to Dodecamer DNA: Importance of Relative Orientation of Donor and Acceptor in FRET, *J. Phys. Chem. B* 111 (2007) 5047.
- [21] P. Majumder, R. Sarkar, A. K. Shaw, A. Chakraborty, S. K. Pal, Ultrafast Dynamics in a Nanocage of Enzymes: Solvation and Fluorescence Resonance Energy Transfer in Reverse Micelles, *J. Colloid Interface Sci.* 290 (2005) 462.
- [22] S. Batabyal, T. Mondol, S. K. Pal, Picosecond-Resolved Solvent Reorganization and Energy Transfer in Biological and Model Cavities, *Biochimie* 95 (2013) 1127.
- [23] S. Banerjee, M. Tachiya, S. K. Pal, Caffeine-Mediated Detachment of Mutagenic Ethidium from Various Nanoscopic Micelles: An Ultrafast Förster Resonance Energy Transfer Study, *J. Phys. Chem. B* 116 (2012) 7841.
- [24] S. Banerjee, N. Goswami, S. K. Pal, A Potential Carcinogenic Pyrene Derivative under Forster Resonance Energy Transfer to Various Energy Acceptors in Nanoscopic Environments, *ChemPhysChem* 14 (2013) 3581.
- [25] M. Tachiya, Application of a Generating Function to Reaction Kinetics in Micelles. Kinetics of Quenching of Luminescent Probes in Micelles, *Chem. Phys. Lett.* 33 (1975) 289.

- [26] S. Sadhu, M. Tachiya, A. Patra, A Stochastic Model for Energy Transfer from CdS Quantum Dots/Rods (Donors) to Nile Red Dye (Acceptors), *J. Phys. Chem. C* 113 (2009) 19488.
- [27] M. H. Gehlen, M. V. Auweraer, F. C. D. Schryver, Fluorescence Quenching in Micellar Microdomains. Analysis of an Approximate Solution to the Fluorescence Decay Including Exchange of Probe and Quencher, *Langmuir* 8 (1992) 64.
- [28] C. O. Pabo, R. T. Sauer, J. M. Sturtevant, M. Ptashne, The λ -Repressor Contains Two Domains, *Proc. Natl. Acad. Sci.* 76 (1979) 1608.
- [29] J. N. Israelachvili, D. J. Mitchell, B. W. Ninham, Theory of Self-Assembly of Hydrocarbon Amphiphiles into Micelles and Bilayers, *J. Chem. Soc. Faraday Trans.* 272 (1976) 1525.
- [30] D. J. Mitchell, B. W. Ninham, Micelles, Vesicles and Microemulsions, *J. Chem. Soc. Faraday Trans.* 77 (1981) 601.
- [31] H. H. Paradies, Shape and Size of a Nonionic Surfactant Micelle. Triton X-100 in Aqueous Solution, *J. Phys. Chem.* 84 (1980) 599.
- [32] S. S. Berr, Solvent Isotope Effects on Alkyltrimethylammonium Bromide Micelles as a Function of Alkyl chain Length, *J. Phys. Chem.* 91 (1987) 4760.
- [33] S. S. Berr, E. Caponetti, J. S. Johnson, J. R. R. M. Jones, L. J. Magid, Small-Angle Neutron Scattering from Hexadecyltrimethylammonium Bromide Micelles in Aqueous Solutions, *J. Phys. Chem.* 90 (1986) 5766.
- [34] X. G. Lei, G. H. Zhao, Y. C. Liu, N. J. Turro, Influence of Binding Strength of Added Electrolytes on the Properties of Micelles and of Micellized Radical Pairs, *Langmuir* 8 (1992) 475.
- [35] H. L. Tavernier, F. Laine, M. D. Fayer, Photoinduced Intermolecular Electron Transfer in Micelles: Dielectric and Structural Properties of Micelle Headgroup Regions, *J. Phys. Chem. A* 105 (2001) 8944.
- [36] N. J. Turro, X. G. Lei, K. P. Ananthapadmanabhan, M. Aronson, Spectroscopic Probe Analysis of Protein-Surfactant Interactions: The BSA/SDS System, *Langmuir* 11 (1995) 2525.
- [37] P. A. Hassan, S. R. Raghavan, E. W. Kaler, Microstructural Changes in SDS Micelles Induced by Hydrotropic Salt, *Langmuir* 18 (2002) 2543.

- [38] A. K. Shaw, S. K. Pal, Activity of Subtilisin Carlsberg in Macromolecular Crowding, *J. Photochem. Photobiol. B* 86 (2007) 199.
- [39] J. F. Foster, *Some Aspects of the Structure and Conformational Properties of Serum Albumin*, Pergamon, Oxford, 1977.
- [40] M. Dockal, D. C. Carter, F. Rümer, The Three Recombinant Domains of Human Serum Albumin: Structural Characterization and Ligand Binding Properties, *J. Biol. Chem.* 274 (1999) 29303.
- [41] X. M. He, D. C. Carter, Atomic Structure and Chemistry of Human Serum Albumin, *Nature* 358 (1992) 209.
- [42] J. Ghuman, P. A. Zunszain, I. Petitpas, A. A. Bhattacharya, M. Otagiri, S. Curry, Structural Basis of the Drug-Binding Specificity of Human Serum Albumin, *J. Mol. Biol.* 353 (2005) 38.
- [43] M. Wardell, Z. Wang, J. X. Ho, J. Robert, F. Ruker, J. Ruble, D. C. Carter, The Atomic Structure of Human Methemalbumin at 1.9 Å, *Biochem. Biophys. Res. Commun.* 291 (2002) 813.
- [44] S. S. Sinha, R. K. Mitra, S. K. Pal, Temperature-Dependent Simultaneous Ligand Binding in Human Serum Albumin, *J. Phys. Chem. B* 112 (2008) 4884.
- [45] O. Avery, C. Macleod, M. McCarty, Studies on the Chemical Nature of the Substances Inducing Transformation of the Substances Inducing Transformation of Pneumococcal Types, *J. Expt. Med.* 7 (1944) 137.
- [46] J. D. Watson, F. H. C. Crick, Molecular Structure of Nucleic Acids, *Nature* 171 (1953) 737.
- [47] D. L. Nelson, M. M. Cox, *Lehninger Principles of Biochemistry*, Worth, New York, 2000.
- [48] L. S. Lerman, The Structure of DNA-Acridine Complex, *Proc. Natl. Acad. Sci. USA* 49 (1963) 94.
- [49] P. B. Dervan, Molecular Recognition of DNA by Small Molecules, *Bioorg. Med. Chem.* 9 (2001) 2215.
- [50] D. Banerjee, S. K. Pal, Ultrafast Charge Transfer and Solvation of DNA Minor Groove Binder: Hoechst 33258 in Restricted Environments, *Chem. Phys. Lett.* 432 (2006) 257.

- [51] W. D. Wilson, F. A. Tanious, H. K. Barton, R. L. Jones, K. Fox, R. L. Wydra, L. Strekowski, DNA Sequence Dependent Binding Modes of 4',6-Diamidino-2-phenylindole (DAPI), *Biochemistry* 29 (1990) 8452.
- [52] S. Nad, H. Pal, Photophysical Properties of Coumarin 500 (C500): Unusual Behaviour in Nonpolar Solvents, *J. Phys. Chem. A* 107 (2003) 501.
- [53] W. O. McClure, G. M. Edelman, Fluorescent Probes for Conformational States of Proteins. I. Mechanism of Fluorescence of 2-p-toluidinylnaphthalene-6-sulphonate, a Hydrophobic Probe, *Biochemistry* 5 (1966) 1908.
- [54] S. Mukherjee, P. Sen, A. Halder, S. Sen, P. Dutta, K. Bhattacharyya, Solvation Dynamics in a Protein-Surfactant Aggregate. TNS in HSA-SDS, *Chem. Phys. Lett.* 379 (2003) 471.
- [55] K. Bhattacharyya, M. Chowdhury, Environmental and Magnetic Field Effects on Exciplex and Twisted Charge Transfer Emission, *Chem. Rev.* 93 (1993) 507.
- [56] D. P. Millar, R. J. Robbins, A. H. Zewail, Torsion and Bending of Nucleic Acids Studied by Subnanosecond Time Resolved Fluorescence Depolarized of Intercalated Dyes, *J. Chem. Phys.* 76 (1982) 2080.
- [57] S. K. Pal, D. Mandal, K. Bhattacharyya, Photophysical Processes of Ethidium Bromide in Micelles and Reverse Micelles, *J. Phys. Chem. B* 102 (1998) 11017.
- [58] S. K. Pal, D. Sukul, D. Mandal, S. Sen, K. Bhattacharyya, Solvation Dynamics of DCM in Micelles, *Chem. Phys. Lett.* 327 (2000) 91.
- [59] R. Sarkar, A. K. Shaw, M. Ghosh, S. K. Pal, Ultrafast Photoinduced Deligation and Ligation Dynamics: DCM in Micelle and Micelle-Enzyme Complex, *J. Photochem. Photobiol. B* 83 (2006) 213.
- [60] J. Kapuscinski, Z. Darzynkiewicz, Increased Accessibility of Bases in DNA upon Binding of Acridine Orange, *Nucleic Acids Res.* 11 (1983) 7555.
- [61] A. K. Shaw, S. K. Pal, Fluorescence Relaxation Dynamics of Acridine Orange in Nanosized Micellar Systems and DNA, *J. Phys. Chem. B* 111 (2007) 4189.
- [62] J. W. Park, H. Chung, Aggregation and Dissolution of Cationic Dyes with an Anionic Surfactant, *Bull. Korean. Chem. Soc.* 7 (1986) 113.
- [63] A. M. Wiosetek-Reske, S. Wysocki, Spectral Studies of N-nonyl Acridine Orange in Anionic, Cationic and Neutral Surfactants, *Spectrochim. Acta A* 64 (2006) 1118.

- [64] H. Langhals, Color Chemistry: Synthesis, Properties and Applications of Organic Dyes and Pigments, *Angew. Chem. Int. Ed.* 43 (2004) 5291.
- [65] G. Revillod, I. R. Antoine, E. Benichou, C. Jonin, P. F. Brevet, Investigating the Interaction of Crystal Violet Probe Molecules on Sodium Dodecyl Sulfate Micelles with Hyper-Rayleigh Scattering, *J. Phys. Chem. B* 109 (2005) 5383.
- [66] S. C. Beck, D. T. Cramb, Condensed Phase Dispersive Interactions of Benzo[a]pyrene with Various Solvents and with DNA: A Twist on Solvatochromism, *J. Phys. Chem. B* 104 (2000) 2767.

Chapter 3

Instrumentation and Sample Preparation

In this chapter the details of instrumental setup and sample preparation techniques used in our studies have been described.

3.1. Instrumental Setups:

3.1.1. Steady-State UV-Vis Absorption and Emission Measurement: Steady-state UV-Vis absorption and emission spectra of the probe molecules were measured with Shimadzu UV-2450 spectrophotometer and Jobin Yvon Fluoromax-3 fluorimeter, respectively. Schematic ray diagrams of these two instruments are shown in Figures 3.1 and 3.2.

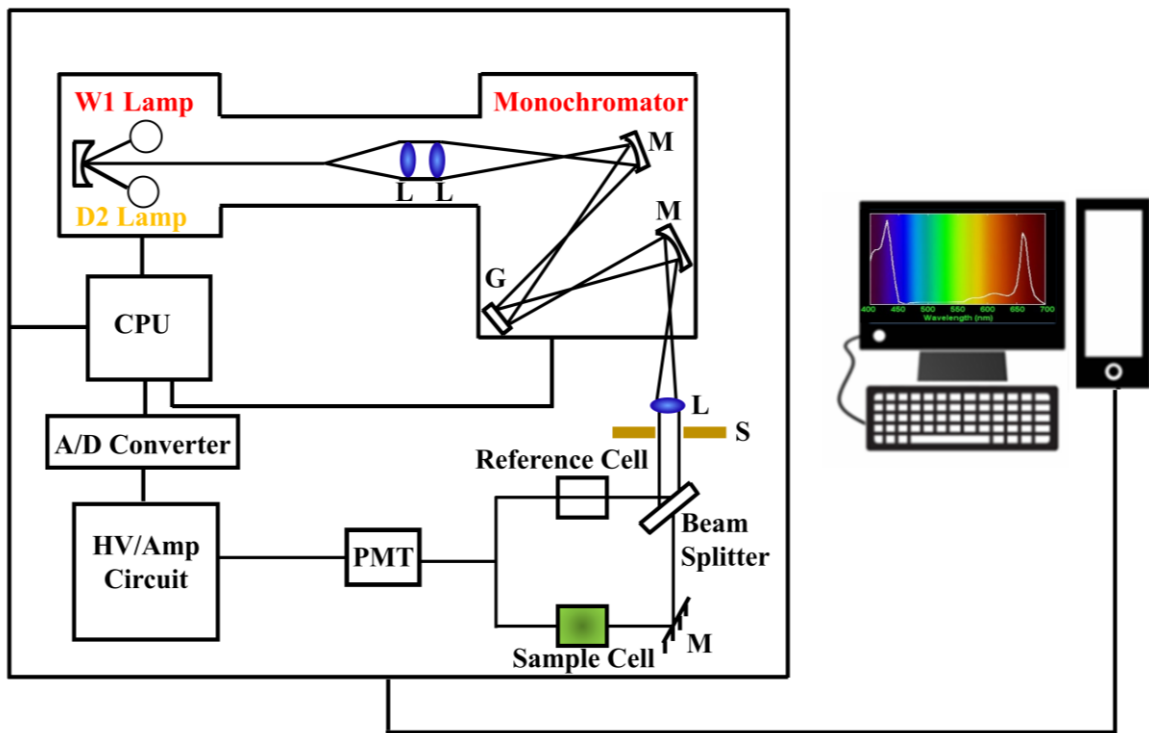


Figure 3.1. Schematic ray diagram of an absorption spectrophotometer. Tungsten halogen (W1) and Deuterium lamps (D2) are used as light sources in the visible and UV regions, respectively. M, G, L, S, PMT designate mirror, grating, lens, shutter and photomultiplier tube, respectively. CPU, A/D converter and HV/Amp indicate central processing unit, analog to digital converter and High-voltage/Amplifier circuit, respectively.

The working principle of CD measurement is as follows: when a plane polarized light passes through an optically active substance, not only do the left (L) and right (R) circularly polarized light rays travel at different speeds, $c_L \neq c_R$, but these two rays are absorbed to different extents, i.e., $A_L \neq A_R$. The difference in the absorbance of the left and right circularly polarized light, i.e., $\Delta A = A_L - A_R$, is defined as circular dichroism [1]. CD spectroscopy follows Beer-Lambert law. If I_0 is the intensity of light incident on the cell, and I , that of emergent light, then absorbance is given by,

$$A = \log_{10} \left(\frac{I_0}{I} \right) = \epsilon cl \quad (3-1)$$

where, A is proportional to concentration (c) of optically active substance and optical path length (l). If ' c ' is in moles L^{-1} and ' l ' is in cm , then ϵ is called the molar absorptivity or molar extinction coefficient. In an optically active medium, two absorbances, A_L and A_R are considered, where $A_L = \log_{10}(I_0/I_L)$ and $A_R = \log_{10}(I_0/I_R)$. At the time of incidence on the sample, intensity of left and right circularly polarized light are same, i.e. $I_0 = I_L = I_R$. Any micrograph passes periodically changing light through the medium, oscillating between left and right circular polarization, and the difference in absorbances are recorded directly [2].

$$\Delta A = A_L - A_R = \log_{10} \left(\frac{I_0}{I_L} \right) - \log_{10} \left(\frac{I_0}{I_R} \right) = \log_{10} \left(\frac{I_R}{I_L} \right) \quad (3-2)$$

or
$$\Delta A = (\Delta \epsilon) cl \quad (3-3)$$

As seen from equation 3.2, I_0 does not appear in this final equation, so there is no need for a reference beam. The instruments are, therefore, of single beam type. Most of the CD spectropolarimeters, although they measure differential absorption, produce a CD spectrum in units of ellipticity (θ) expressed in millidegrees versus λ , rather than ΔA versus λ . The relation between ellipticity and CD is given by,

$$\theta = \frac{2.303 \times 180 \times (A_L - A_R)}{4\pi} \text{ degrees} \quad (3-4)$$

To compare the results from different samples, optical activity is computed on a molar or residue basis. Molar ellipticity, $[\theta]$ is defined as,

$$[\theta] = \frac{\theta}{cl} \quad (3-5)$$

where, ' θ ' is in degrees, ' c ' is in molesL^{-1} and ' l ' is in cm. The unit of molar ellipticity is $\text{deg M}^{-1} \text{cm}^{-1}$.

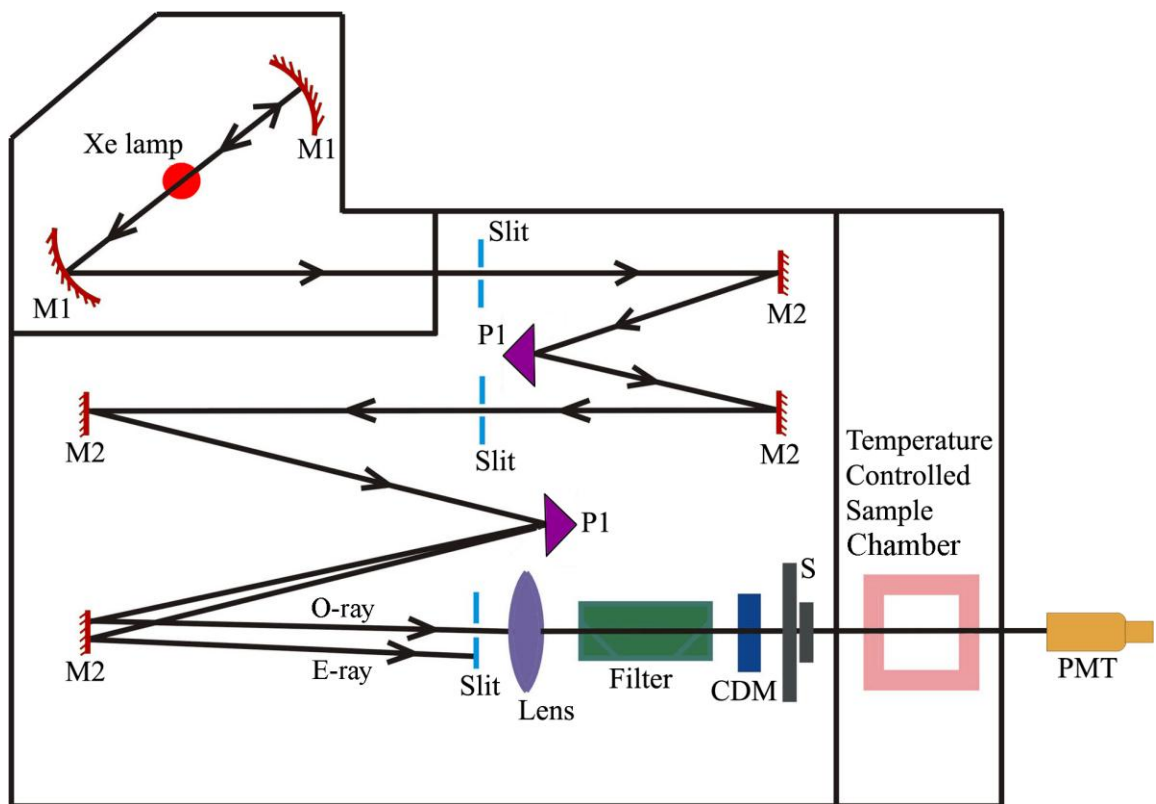


Figure 3.3. Schematic ray diagram of a Circular Dichroism (CD) spectropolarimeter. M1, M2, P1, S, PMT, CDM, O-ray and E-ray represent concave mirror, plain mirror, reflecting prism, shutter, photomultiplier tube, CD-modulator, ordinary ray and extraordinary ray, respectively.

3.1.3. Time-Related Single Photon Counting (TCSPC) Technique: All the picosecond-resolved fluorescence transients were recorded using TCSPC technique. The schematic block diagram of a TCSPC system is shown in Figure 3.4. TCSPC setup from Edinburgh instruments, U.K., was used during fluorescence decay acquisitions. The instrument response functions (IRFs) of the laser sources at different excitation wavelengths varied between 60 ps to 80 ps. The fluorescence from the sample was detected by a photomultiplier after dispersion through a grating monochromator [3]. For all transients, the polarizer in the emission side was adjusted to be at 54.7° (magic angle) with respect to the polarization axis of excitation beam. For 290-300 nm laser excitation, we have used a femtosecond-coupled TCSPC setup in which the sample was excited by the

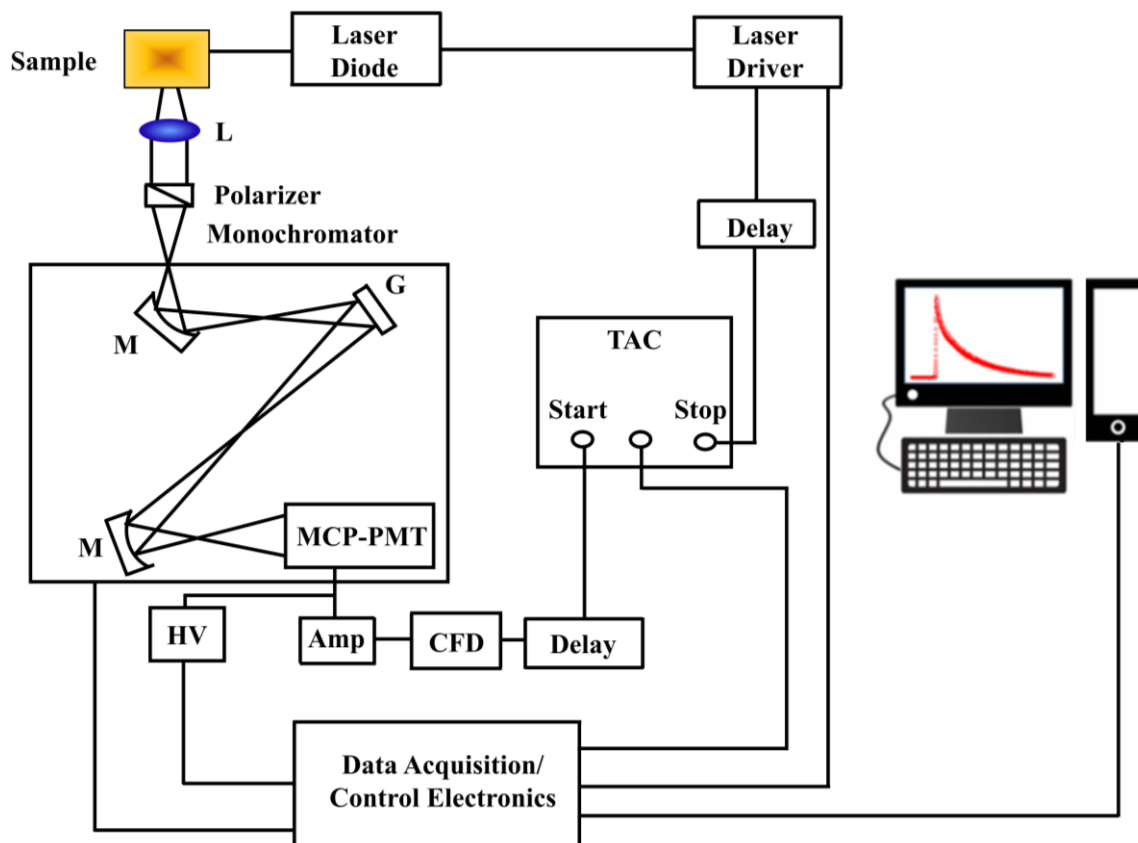


Figure 3.4. Schematic ray diagram of a time correlated single photon counting (TCSPC) spectrophotometer. A signal from microchannel plate photomultiplier tube (MCP-PMT) is amplified (Amp) and connected to start channel of time to amplitude converter (TAC) via constant fraction discriminator (CFD) and delay. The stop channel of the TAC is connected to the laser driver via a delay line. L, M, G and HV represent lens, mirror, grating and high voltage source, respectively.

third harmonic laser beam (290-300 nm) of the 870-900 nm (0.5 nJ per pulse) using a modelocked Ti-sapphire laser with an 80 MHz repetition rate (Tsunami, Spectra-Physics), pumped by a 10 W Millennia (Spectra-Physics) followed by a pulse-peaker (rate 8 MHz) and a third harmonic generator (model 3980, Spectra-Physics). The third harmonic beam was used for excitation of the sample inside the TCSPC instrument (IRF = 70 ps) and the second harmonic beam was collected for the start pulse.

3.1.4. Femtosecond-Resolved Fluorescence Upconversion Technique: The femtosecond-resolved fluorescence spectroscopy was carried out using a femtosecond upconversion setup (FOG 100, CDP, Figure 3.5) in which the sample was excited at 385 nm, using the second harmonic of a mode-locked Ti-sapphire laser with 80 MHz repetition rate (Tsunami, Spectra Physics), pumped by 10 W Millennia (Spectra Physics). The

fundamental beam was passed through a periscopic arrangement (P) (Figure 3.5) before getting frequency doubled in a nonlinear crystal, NC1 (1 mm BBO, $\theta = 25^\circ$, $\phi = 90^\circ$). This beam was then sent into a rotating circular cell of 1 mm thickness containing the sample via a dichroic mirror (DM), a polarizer and a mirror (M6). The resulting fluorescence emission was collected, refocused with a pair of lenses (L4 and L5) and mixed with the fundamental beam (770 nm) coming through a delay line to yield an upconverted photon signal in a nonlinear crystal, NC2 (0.5 mm BBO (β -barium borate), $\theta = 10^\circ$, $\phi = 90^\circ$). The upconverted light was dispersed in a double monochromator and detected using photon counting electronics. A cross-correlation function obtained using the Raman scattering from water displayed a full width at half maximum (FWHM) of 165 fs. The femtosecond fluorescence decays were fitted using a Gaussian shape for the exciting pulse.

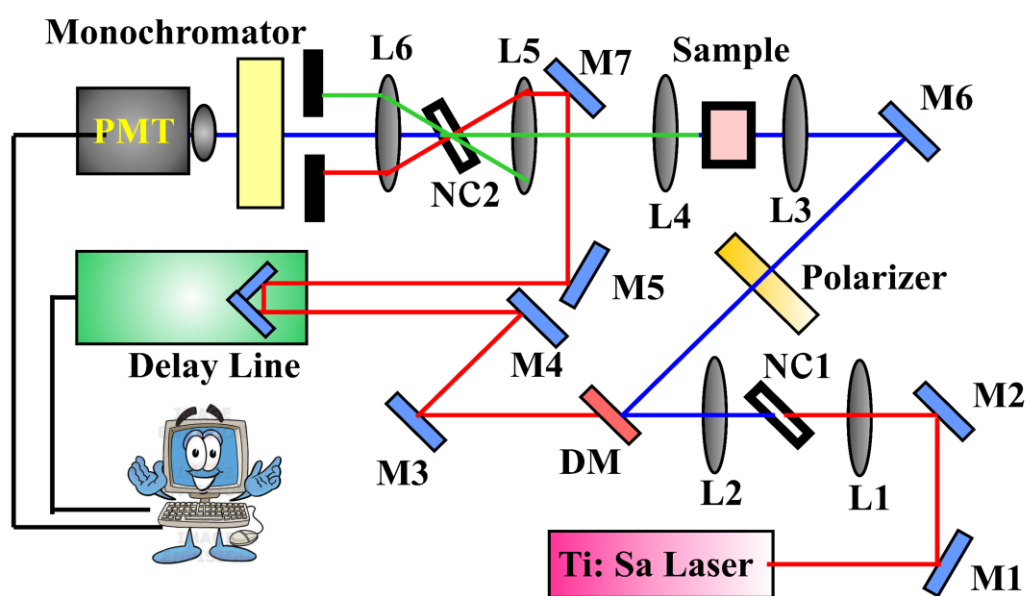


Figure 3.5. Schematic diagram of a femtosecond fluorescence upconversion experimental setup. A BBO crystal (NC1) is used for second harmonic generation, which provides a pump beam in the UV region. Another BBO crystal (NC2) generates the upconversion signal of pump and probe beams. L and M indicate lenses and mirrors, respectively. M1, M2, M3, M4, M5, and M7 are IR mirrors whereas M6 is a UV mirror. DM is dichroic mirror, and P is periscope.

3.1.5. Dynamic Light Scattering (DLS) Measurement: DLS, also known as photon correlation spectroscopy (PCS) or quasi-elastic light scattering (QELS) is one of the most popular techniques used to determine the hydrodynamic size of the particle. DLS

measurements were performed on a Nano S Malvern instrument, (U.K.) employing a 4 mW He-Ne laser ($\lambda = 632.8 \text{ nm}$) and equipped with a thermostatted sample chamber. The instrument allows DLS measurements in which all the scattered photons are collected at 173° scattering angle (Figure 3.6). The instrument measures the time dependent fluctuation in intensity of light scattered from the particles in solution at a fixed scattering angle [4]. The ray diagram of the DLS setup is shown in Figure 3.6.

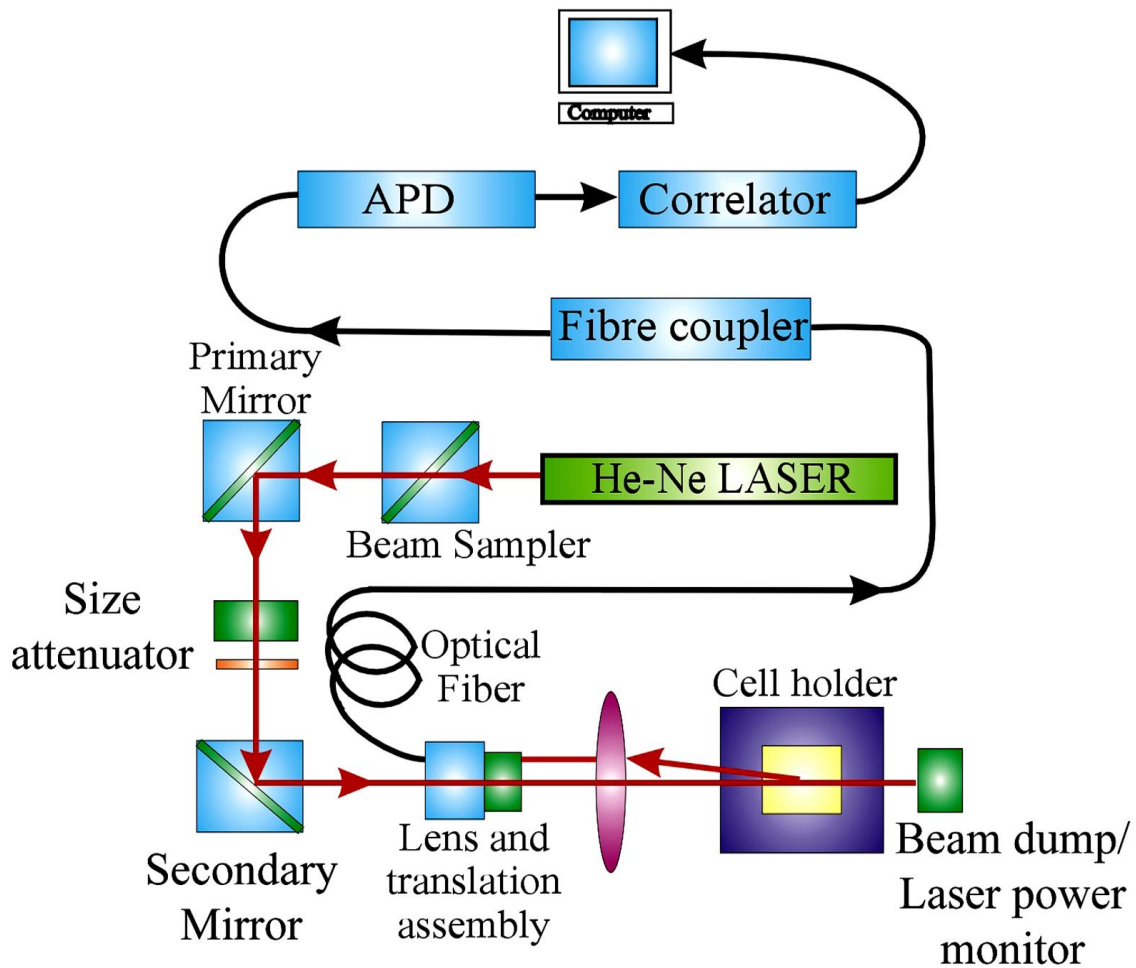


Figure 3.6. Schematic ray diagram of dynamic light scattering (DLS) instrument. The avalanche photo diode (APD) is connected to preamplifier/amplifier assembly and finally to correlator. It has to be noted that lens and translational assembly, laser power monitor, size attenuator, laser are controlled by the computer.

It has been seen that particles in dispersion are in a constant, random Brownian motion and this causes the intensity of scattered light to fluctuate as a function of time. The correlator used in a DLS instrument constructs the intensity autocorrelation function $G(\tau)$ of the scattered intensity,

$$G(\tau) = \langle I(t)I(t + \tau) \rangle \quad (3-6)$$

where τ is the time difference (the sample time) of the correlator. For a large number of monodisperse particles in Brownian motion, the correlation function (given the symbol G) is an exponential decaying function of the correlator time delay τ ,

$$G(\tau) = A[1 + B \exp(-2\Gamma\tau)] \quad (3-7)$$

where A is the baseline of the correlation function, B is the intercept of the correlation function. Γ is the first cumulant and is related to the translational diffusion coefficient as, $\Gamma = Dq^2$, where q is the scattering vector and its magnitude is defined as,

$$q = \left(\frac{4\pi n}{\lambda_0} \right) \sin\left(\frac{\theta}{2}\right) \quad (3-8)$$

where n is the refractive index of dispersant, λ_0 is the wavelength of the laser and θ , the scattering angle. For polydisperse samples, the equation can be written as,

$$G(\tau) = A \left[1 + B |g^{(1)}(\tau)|^2 \right] \quad (3-9)$$

where the correlation function $g^{(1)}(\tau)$ is no longer a single-exponential decay and can be written as the Laplace transform of a continuous distribution $G(\Gamma)$ of decay times,

$$g^{(1)}(\tau) = \int_0^{\infty} G(\Gamma) \exp(-\Gamma\tau) d\Gamma \quad (3-10)$$

The scattering intensity data in DLS were processed using the instrumental software to obtain the hydrodynamic diameter (d_H) and the size distribution of the scatterer in each sample. In a typical size distribution graph from the DLS measurement, X-axis shows a distribution of size classes in nm, while the Y-axis shows the relative intensity of the scattered light. The diffusion coefficient (D) can be calculated using d_H of the particle by using the Stoke-Einstein relation,

$$D = \frac{k_B T}{3\pi\eta d_H} \quad (3-11)$$

where k_B , T , d_H , η are Boltzmann constant, temperature in Kelvin, hydrodynamic diameter and viscosity, respectively.

3.1.6. Fourier Transform Infrared (FTIR) Measurement: FTIR spectroscopy is a technique that can provide very useful information about functional groups in a sample. An infrared spectrum represents the fingerprint of a sample with absorption peaks which correspond to the frequencies of vibrations between the bonds of the atoms making up the material. Because each different material is a unique combination of atoms, no two compounds produce the exact same infrared spectrum. Therefore, infrared spectroscopy can result in a positive identification (qualitative analysis) of all different kinds of material. In addition, the size of the peaks in the spectrum is a direct indication of the amount of material present. The two-beam Michelson interferometer is the heart of FTIR

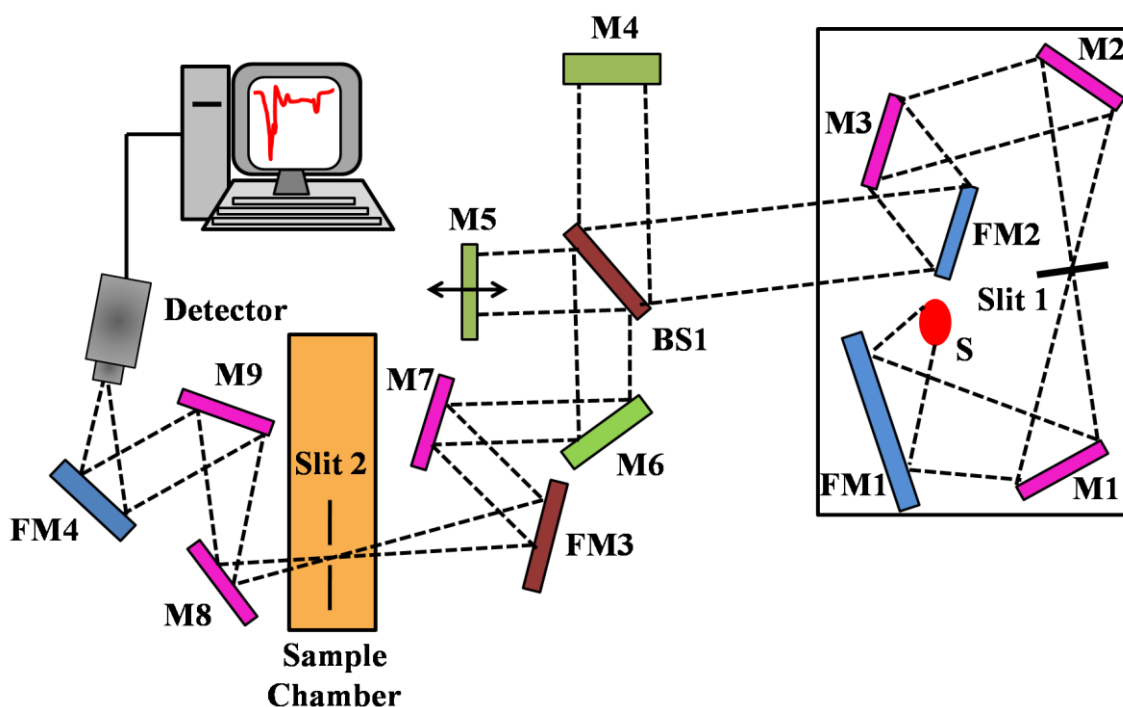


Figure 3.7. Schematic of Fourier Transform Infrared (FTIR) spectrometer. It is basically a Michelson interferometer in which one of the two fully-reflecting mirrors is movable, allowing a variable delay (in the travel-time of the light) to be included in one of the beams. *M*, *FM* and *BS1* represent the mirror, focussing mirror and beam splitter, respectively. *M5* is a moving mirror.

spectrometer. It consists of a fixed mirror (M4), a moving mirror (M5) and a beam-splitter (BS1), as illustrated in Figure 3.7. The beam-splitter is a laminate material that reflects and

transmits light equally. The collimated IR beam from the source is partially transmitted to the moving mirror and partially reflected to the fixed mirror by the beam-splitter. The two IR beams are then reflected back to the beam-splitter by the mirrors. The detector then sees the transmitted beam from the fixed mirror and reflected beam from the moving mirror, simultaneously. The two combined beams interfere constructively or destructively depending on the wavelength of the light (or frequency in wavenumbers) and the optical path difference introduced by the moving mirror. The resulting signal is called an interferogram which has the unique property that every data point (a function of the moving mirror position) which makes up the signal has information about every infrared frequency which comes from the source. Because the analyst requires a frequency spectrum (a plot of the intensity at each individual frequency) in order to make identification, the measured interferogram signal cannot be interpreted directly. A means of “decoding” the individual frequencies is required. This can be accomplished *via* a well-known mathematical technique called the Fourier transformation. This transformation is performed by the computer which then presents the user with the desired spectral information for analysis. FTIR measurements were performed on a JASCO FTIR-6300 spectrometer (transmission mode). Each spectrum consists of 100 scans (1500–4000 cm^{-1}) acquired at 0.5 cm^{-1} resolution.

3.1.7. Density and Sound Velocity Measurement: The density and sound velocity measurements were done in DSA 5000 from Anton Paar. The instrument measures density and sound velocity with accuracies of $10^{-6} \text{ g cm}^{-3}$ and 10 cm s^{-1} respectively. The density and velocity are measured according to the following measuring principle. A U-shaped glass tube of known volume and mass is filled with the liquid sample and excited electronically by a Piezo element (Figure 3.8). The U-tube is kept oscillating continuously at the characteristic frequency f . Optical pick-ups record the oscillation period P as $P = 1/f$. This frequency is inversely proportional to the density, ρ of the filled-in sample. The reference oscillator speeds up the measurements when aiming at various measuring temperatures. The density is calculated as,

$$\rho = A \times P^2 - B \quad (3-12)$$

where A and B are parameters. Once the instrument has been adjusted with air and water, the density of the sample can be determined. Hence related parameters can be calculated from the density.

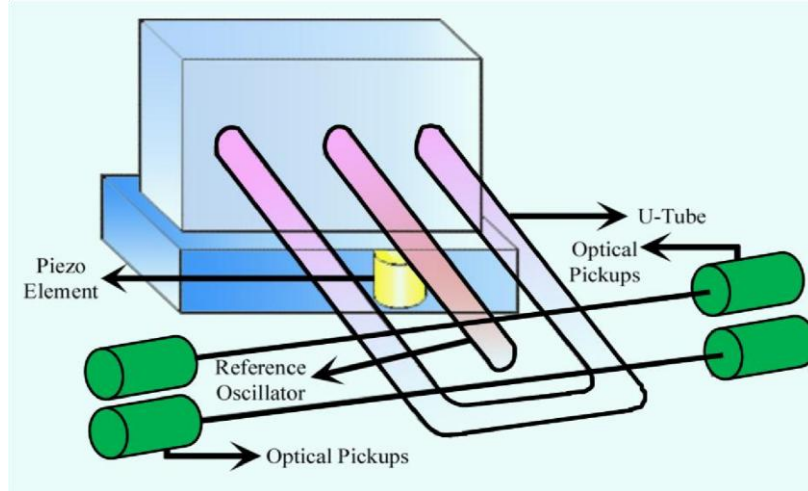


Figure 3.8. Schematic representation of the density and sound velocity measurement setup.

3.1.8. Viscosity Measurement: The viscosities of the mixtures were measured by an automated micro viscometer (AVMn) from Anton Paar (Austria). The viscosities of the sample are measured by Höppler falling ball principle. The basic concept is to measure the elapsed time required for the ball to fall under gravity through a sample-filled tube inclined at an angle. The tube is mounted on a pivot bearing which quickly allows rotation of the tube by 180 degrees, thereby allowing a repeat test to run immediately. Several measurements are taken and the average time is converted into a final viscosity value in centipoise (cP).

The dynamic viscosity in Höppler falling ball method is calculated by the following equation:

$$\eta = t(\rho_1 - \rho_2)K * F \quad (3-13)$$

where: η is the dynamic viscosity [mPa.s]; t travelling time of the ball [s]; ρ_1 density of the ball [g cm^{-3}]; ρ_2 density of the sample [g cm^{-3}]; K ball constant [$\text{mPa}\cdot\text{cm}^3 \text{g}^{-1}$]; F working angle constant.

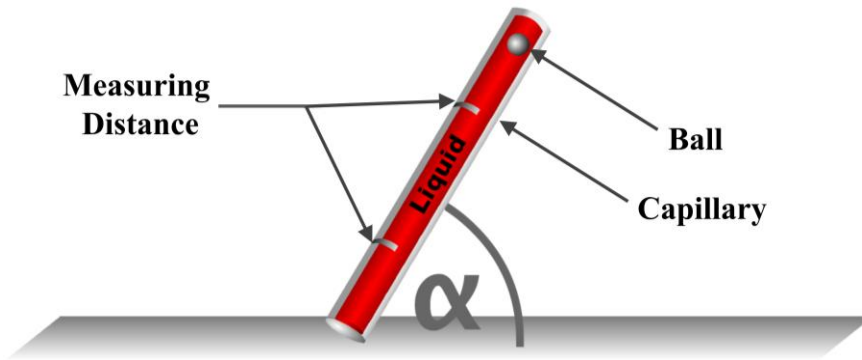


Figure 3.9. Schematic representation of the automated micro viscometer.

3.1.9. Refractive Indices Measurement: Refractive indices of the solutions were measured by using a Rudolph J357 automatic refractometer. The instrument measures the refractive indices using sodium D-line of wavelength 589.3 nm with accuracies ± 0.00004 .

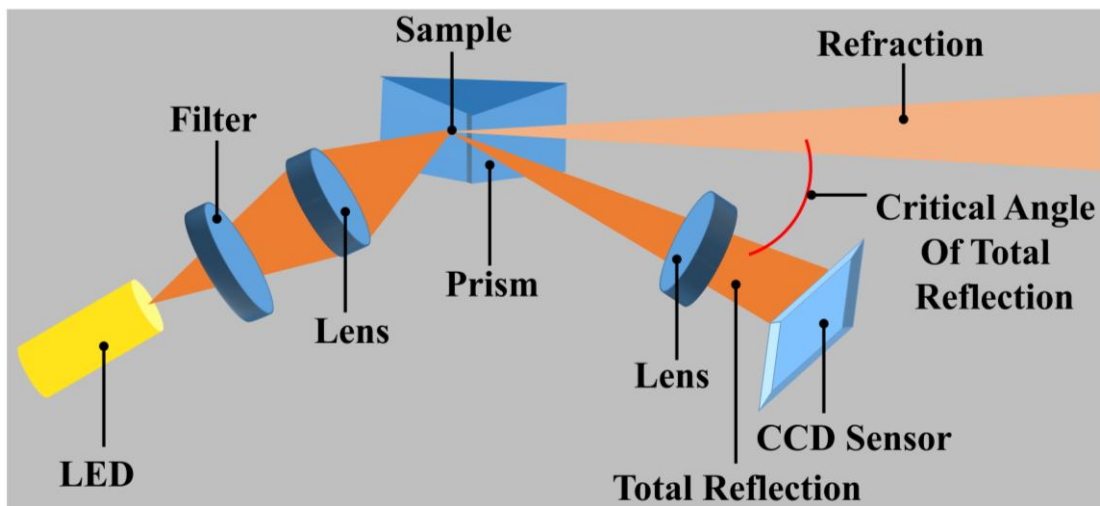


Figure 3.10. Schematic representation of the refractometer.

The measurement of the refractive index of the sample is based on the determination of the critical angle of total reflection. A light source, usually a long-life LED, is focused onto a prism surface via a lens system. Due to the focusing of light to a spot at the prism surface, a wide range of different angles is covered. As the measured sample is in direct contact with the measuring prism. Depending on its refractive index, the incoming light below the

critical angle of total reflection is partly transmitted into the sample, whereas for higher angles of incidence the light is totally reflected. This dependence of the reflected light intensity from the incident angle is measured with a high-resolution sensor array. From the video signal taken with the CCD sensor the refractive index of the sample can be calculated.

3.2. Sample Preparation: In this section the different sample preparation methods have been discussed.

3.2.1. Chemicals Used: The chemicals, spectroscopic probes, and biomolecules (DNAs and proteins) were procured from the following sources. All the aqueous solutions were prepared using double distilled water. The chemicals phosphate buffer (disodium hydrogen phosphate, monosodium hydrogen phosphate), benzo[*a*]pyrene (BP), hoechst 33258 (H258), crystal violet (CV), 2-(*p*-toluidino) naphthalene-6-sulfonate (TNS), acridine orange (AO), zinc nitrate hexahydrate, $Zn(NO_3)_2 \cdot 6H_2O$ and hexamethylenetetramine, $C_6H_{12}N_4$ were obtained from Sigma/Aldrich. Caffeine (99.99%), Merocyanine 540, hexadecyltrimethylammonium bromide (CTAB), para-benzoquinone (BQ) and platinum chloride, $H_2PtCl_6 \cdot H_2O$ were obtained from Fluka. The fluorescent probes 4-(dicyanomethylene)-2-methyl-6-(*p*-dimethylamino-styryl)-4H-pyran (DCM), coumarin 500 (C500) were purchased from Exciton. 4',6-diamidino-2-phenylindole (DAPI) was obtained from Molecular Probes. Sodium dodecyl sulphate (SDS) and Triton X-100 (TX-100) were acquired from Fisher Scientific and Romil respectively. Three quantum dots (QDs), namely Lake Placid Blue (LPB; crystal diameter 1.9 nm; QD480), Birch yellow (Bir-yellow; crystal diameter 3.2 nm; QD570), and Maple red-orange (Map-red; crystal diameter 5.2 nm; QD625) having emission maxima at 480, 570 and 625 nm respectively in toluene were purchased from Evident Technology, USA. Dioxane, dimethyl sulfoxide (DMSO), diethyl ether, heptane, dimethyl formamide (DMF) and acetonitrile were obtained from Spectrochem while ethanol, methanol, ethylene glycol, acetone, benzene and zinc acetate dihydrate, $Zn(CH_3COO)_2 \cdot 2H_2O$ were obtained from Merck. The biomolecules Calf thymus-DNA (CT-DNA) and Human serum albumin (HSA) were obtained from Sigma/Aldrich. The purified (reverse phase cartridge) synthetic DNA oligonucleotides of 12 bases (dodecamer) with sequence CGCGAATTCGCG were

obtained from TriLink. All the chemicals and the biomolecules were of highest purity available and used without further purification.

3.2.2. Preparation of Micellar Solutions: The micellar solutions were prepared by dissolving surfactant salts in double distilled water. Micellar solutions of the probe were prepared by adding known concentrated aqueous probe solution to micellar solution of desired concentration with simultaneous stirring of the mixture for an hour. In all the FRET experiments, the concentrations of micelles were much higher than that of the acceptors to ensure that no more than one acceptor is held by one micelle. In order to prevent homomolecular energy transfer between donor molecules and to ensure efficient energy transfer between the donor and acceptor in the micellar solution, the concentration of the donor molecules was kept low. Furthermore, in the micellar solution [donor]/[micelle] ratio was maintained in a way that avoids the existence of multiple donors in the same micelle [5].

3.2.3. Preparation of Synthetic and Genomic DNA solutions: To reassociate the single strand DNA into self-complimentary ds-DNA [(CGCGAATTCGCG)₂] thermal annealing was performed as per the methodology prescribed by the vendor. All the DNA samples were prepared in 0.05 M phosphate buffer to maintain its double helix structure [6]. In the spectroscopic studies, DNA concentration is expressed in terms of base pair concentration. The nucleotide concentrations were determined by absorption spectroscopy using the average extinction coefficient per nucleotide of the DNA ($6600 \text{ M}^{-1}\text{cm}^{-1}$ at 260 nm) [7].

3.2.4. Preparation of Dye-DNA Complex: In order to prepare dye-DNA complexes, aqueous solution of the dyes Et were added to the synthetic oligonucleotides and stirred for 1 hour to ensure complete complexation of the dye. BP-DNA complexes were prepared as per the methodology reported previously [8] by Geacintov et al. In the fluorescence experiments of BP and CT-DNA, concentration of BP was 1 μM while that of CT-DNA was 1 mM. For steady state and time resolved studies the [dye]:[DNA] ratio was kept low to ensure complete complexation of the probe [9].

3.2.5. Preparation of BP-Protein Complex: Human serum albumin (HSA) solutions were all prepared in 0.01 M phosphate buffer. The concentration of protein in the solutions were determined by absorption spectroscopy using the average extinction coefficient of $36,500 \text{ M}^{-1} \text{ cm}^{-1}$ at 280 nm [10]. The concentrations of BP and HSA used in the fluorescence

experiments were 1 μM and 200 μM respectively [11] and the solution of the BP-HSA complex was allowed to stir for 6 hours before performing experiments.

3.2.6. Sample Preparation for Cellular Studies: Squamous epithelial cells were collected from human mouth, spreaded on glass slides and stained with Et solution followed by thorough destaining under phosphate buffer saline (PBS). A549 (lung carcinoma), A375 (human skin), RAW (macrophage) and Vero (African green monkey kidney epithelium) cells were grown in Ham's F-10 medium, 10% bovine fetal serum, 2 mM glutamine, 25 U/ml penicillin, and 25 U/ml streptomycin at 37°C with 5% CO₂, as described previously [12].

3.2.7. Preparation of BP-ZnO Based Photodevice: Detailed processes for the hydrothermal growth of the single crystalline ZnO NRs are described in our previous reports [13-14]. Briefly, a 1 mM Zinc acetate dihydrate, Zn(CH₃COO)₂·2H₂O, solution in isopropanol was used to prepare the ZnO seed layer on a fluorinated tin oxide (FTO) substrate followed by annealing in air at 350°C for 5 h. A 20 mM aqueous solution of zinc nitrate hexahydrate, Zn(NO₃)₂·6H₂O, and hexamethylenetetramine, C₆H₁₂N₄ (Aldrich), was used as a precursor solution for ZnO NR growth and the seeded FTO substrates were dipped into it at 90°C for 40 h. As-grown ZnO NRs on the FTO substrates were then taken out from the precursor solution and rinsed with deionized (DI) water several times to remove unreacted residues from the substrate. Finally, the substrates with ZnO NRs were annealed at 350°C for 1 h in air and dipped into 3.9 mM DMSO solution of BP and kept in the dark. After 24 h the photoelectrodes were removed from the BP solution and rinsed several times with DMSO in order to remove weakly adsorbed dye molecules. Since BP does not have any functional group through which it can bind to inorganic NRs, the only possible way of binding is physisorption. Platinized FTO glass was used as a counter electrode where a thin platinum layer was deposited on FTO-coated glass substrates by thermal decomposition of platinum chloride, H₂PtCl₆·H₂O, at 385°C for 15 min. The counter electrode was then placed on top of the photoelectrode and a single layer of 50 μm thick surlyn 1702 (Dupont) was used as a spacer between the two electrodes. The photodevices were then sealed and filled with the liquid electrolyte, consisting of 0.5 M lithium iodide (LiI), 0.05 M iodine (I₂) and 0.5 M 4-tert-butylpyridine (TBP) in acetonitrile (ACN), through two small holes (ϕ = 1 mm) drilled on the counter electrode. Finally, the

two holes were sealed by surlyn to prevent electrolyte leakage. A control ZnO NR photoelectrode without BP was also prepared for comparison.

3.2.8. Sample Preparation for NMR Experiments: The samples were prepared in HPLC water and ^1H -NMR experiments were performed using a Bruker DRX 500 MHz spectrometer. ^1H -signals were assigned either by comparing with literature [15] or by performing TOCSY and NOESY / ROESY experiments using standard protocols.

3.2.9. Molecular Modeling Studies: For the molecular modeling studies, we have followed the procedure as reported earlier for the calculation of caffeine hetero-dimer with a number of DNA-intercalating dyes [16]. We have used commercially available ChemBio3D (from CambridgeSoftTM) ultra software. The force field employed for these calculations is MM2 with default parameters provided with the software. Conjugate gradient methods were used to search for geometry-optimized structures with a convergence criterion of 0.0001 kcal/Å. The minimized energy values of the various complexes as investigated in our studies (caffeine-caffeine, caffeine-DCM, caffeine-C500, and caffeine-TNS) are obtained by first geometry optimizing each component of the complex in vacuum. These geometry-optimized components were then brought together in a face to face orientation and to within van der Waals radii and re-optimized. Relative binding energies were determined by subtracting the sum of the geometry-optimized energies of the isolated components from the total energy obtained for the geometry-optimized complex. In general the lowest energy conformation is that in which the caffeine is oriented directly over the conjugated rings of the various dyes with an average face to face distance of 3.5 Å. It must be pointed out that the orientation of the caffeine relative to the dyes in the geometry-optimized complexes is not unique. For example, small displacement (~ 1 Å) and rotation of the caffeine by 180 degree relative to a dye ring system does not significantly alter the relative binding energy. The relative binding energies derived from molecular mechanics methods can be further deconvoluted into individual components that makeup the total energy. However, we have recognized that the dominant force in the formation of such complexes appears to be van der Waals interactions resulting in maximal ring overlap between the two molecules of the complexes.

3.2.10. Quantum Yield (Q_D) Calculation: Q_D , the quantum yield of BP in the micellar solution, was calculated according to the equation [17],

$$Q = Q_R \left(\frac{I}{I_R} \right) \left(\frac{OD_R}{OD} \right) \left(\frac{n^2}{n_R^2} \right) \quad (3-14)$$

where Q and Q_R are the quantum yield of BP in SDS micelle and reference (Hoechst 33258 in SDS), I and I_R are the integrated fluorescence intensities of BP and reference, OD and OD_R are the optical densities of BP and reference at the excitation wavelength, and n and n_R are the refractive indices of BP and reference solutions. The absolute quantum yield of Hoechst 33258 [18] in SDS was taken to be 0.54. Refractive indices of the solutions were measured by using Rudolph J357 automatic refractometer. The quantum yield of BP in SDS micelle has been found to be near unity and relative Q_D of BP in SDS micelle at different emission peaks has been calculated upon deconvoluting the BP emission at its emission peaks around 410, 430 and 455 nm and has been calculated to be 0.45, 0.43 and 0.10 respectively.

References

- [1] A. Rodger, B. Nordén, *Circular dichroism and linear dichroism*, Oxford University Press, 1997.
- [2] N. Berova, K. Nakanishi, *Circular dichroism: Principles and applications*, Wiley-VCH, 2000.
- [3] D. V. O'Connor, D. Philips, *Time Correlated Single Photon Counting*, Academic Press, London, 1984.
- [4] R. Pecora, *Dynamic light scattering: Applications of photon correlation spectroscopy*, Springer, 1985.
- [5] S. Banerjee, N. Goswami, S. K. Pal, A Potential Carcinogenic Pyrene Derivative under Forster Resonance Energy Transfer to Various Energy Acceptors in Nanoscopic Environments, *ChemPhysChem* 14 (2013) 3581.
- [6] T. Douki, Effect of Denaturation on the Photochemistry of Pyrimidine Bases in Isolated DNA, *J. Photochem. Photobiol. B* 82 (2006) 45.
- [7] S. K. Pal, L. Zhao, A. H. Zewail, Water at DNA Surfaces: Ultrafast Dynamics in Minor Groove Recognition, *Proc. Natl. Acad. Sci.* 100 (2003) 8113.
- [8] N. E. Geacintov, T. Prusik, J. M. Khosrofian, Properties of Benzopyrene-DNA Complexes Investigated by Fluorescence and Triplet Flash Photolysis Techniques, *J. Am. Chem. Soc.* 98 (1976) 6444.
- [9] S. Banerjee, D. Bhowmik, P. K. Verma, R. K. Mitra, A. Sidhanta, G. Basu, S. K. Pal, Ultrafast Spectroscopic Study on Caffeine Mediated Dissociation of Mutagenic Ethidium from Synthetic DNA and Various Cell Nuclei, *J. Phys. Chem. B* 115 (2011) 14776.
- [10] S. N. Khan, B. Islam, A. U. Khan, Probing Midazoan Interaction with Human Serum Albumin and its Effect on Structural State of Protein, *Int. J. Integ. Biol.* 1 (2007) 102.
- [11] S. Banerjee, S. Sarkar, K. Lakshman, J. Dutta, S. K. Pal, UVA Radiation Induced Ultrafast Electron Transfer from a Food Carcinogen Benzo[a]pyrene to Organic Molecules, Biological Macromolecules and Inorganic Nano Structures, *J. Phys. Chem. B* 117 (2013) 3726.
- [12] A. Sidhanta, J. M. Backer, D. Shields, Inhibition of Phosphatidic Acid Synthesis Alters the Structure of the Golgi Apparatus and Inhibits Secretion in Endocrine Cells, *J. Biol. Chem.* 275 (2000) 12023.

- [13] S. Sarkar, A. Makhal, T. Bora, K. Lakshman, A. Singha, J. Dutta, S. K. Pal, Hematoporphyrin–ZnO Nanohybrids: Twin Applications in Efficient Visible-Light Photocatalysis and Dye-Sensitized Solar Cells, *ACS Appl. Mater. Interfaces* 4 (2012) 7027.
- [14] S. Sarkar, A. Makhal, K. Lakshman, T. Bora, J. Dutta, S. K. Pal, Dual-Sensitization via Electron and Energy Harvesting in CdTe Quantum Dots Decorated ZnO Nanorod-Based Dye-Sensitized Solar Cells, *J. Phys. Chem. C* 116 (2012) 14248.
- [15] J. Sitkowski, L. Stefaniak, L. Nicol, M. L. Martin, G. J. Martin, G. A. Webb, Complete Assignments of the ¹H, ¹³C and ¹⁵N NMR Spectra of Caffeine, *Spectrochim. Acta Part A Mol. Biomol. Spectrosc.* 51 (1995) 839.
- [16] R. W. Larsen, R. Jasuja, R. K. Hetzler, P. T. Muraoka, V. G. Andrada, D. M. Jameson, Spectroscopic and Molecular Modelling Studies of Caffeine Complexes with DNA Intercalators, *Biophys. J.* 70 (1996) 443.
- [17] N. Goswami, A. Makhal, S. K. Pal, Toward an Alternative Intrinsic Probe for Spectroscopic Characterization of a Protein, *J. Phys. Chem. B* 114 (2010) 15236.
- [18] D. Banerjee, S. K. Pal, Simultaneous Binding of Minor Groove Binder and Intercalator to Dodecamer DNA: Importance of Relative Orientation of Donor and Acceptor in FRET, *J. Phys. Chem. B* 111 (2007) 5047.

Chapter 4

Exploration of Molecular Details of a Model Medicinally Important Xanthine-Alkaloid Molecule, Caffeine in Aqueous Solution and Origin of its Interaction with Other Biologically Relevant Dyes/Drugs:

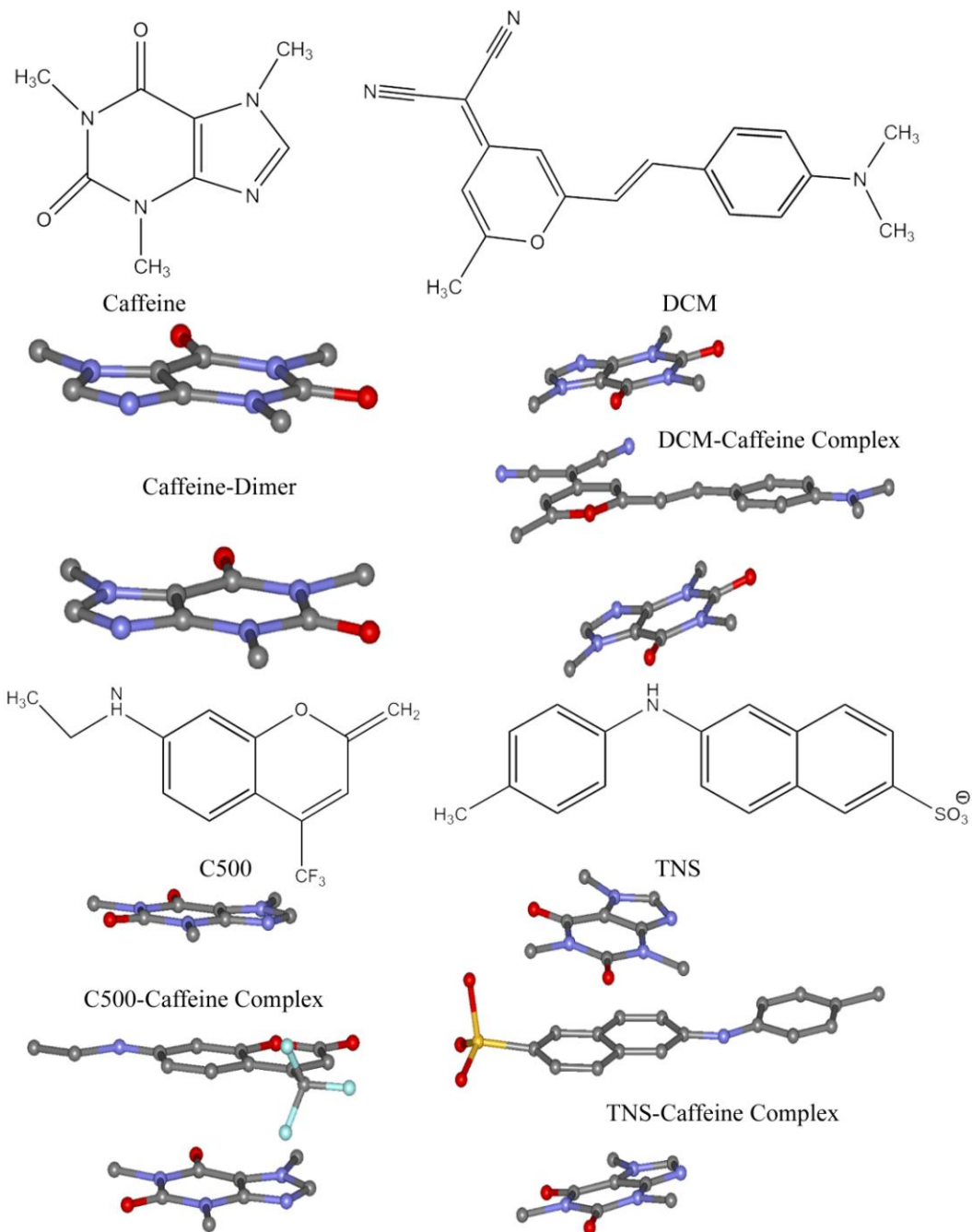
4.1. Introduction:

Caffeine (1,3,7-trimethylxanthine) is in a class of molecules with conjugated planar ring systems that constitute the most widely distributed naturally occurring methylxanthines and regularly consumed by human beings from various dietary sources (e.g. coffee, tea, cola beverages, chocolates). Relatively higher consumption of the molecule due to abundance of methylxanthines (mainly caffeine) in human diets, has directed extensive research on the activity of the molecule in the cellular environments in the recent past [1-2]. It is clearly demonstrated that caffeine has multiplicity of effects on cells. Particularly, it has been shown in a number of earlier studies that caffeine has variety of roles on the molecular recognition of DNA by intercalating drugs [2-3]. For example, when combined with a wide range of DNA-damaging agents (e.g. mitomycin C, cytophosphamide, cisplatin, hydroxyl urea), caffeine enhances cell killing [4-6]. On the other hand another set of studies have indicated that caffeine can diminish the cytotoxic/cytostatic effects of doxorubicin, ethidium bromide [7-10] and reverses cytotoxic effect of the antitumor agent mitoxantrone, ellipticine and doxorubicin analogues [11]. The rational answer of the obvious question from the earlier studies that why does caffeine potentiate toxic effects in one group of drugs while having opposite effect on others, would be the specific molecular interaction of caffeine with individual drug molecule underlying in the “interceptor” action of caffeine [2-3]. For the physiological activity of the drugs in presence of caffeine another mechanism of action called “protector”, has been proposed, in which there is competition between caffeine and another aromatic drug for the binding sites on DNA [3, 11]. The activity of the molecule as mood altering substance is within the central nervous system

where it acts as stimulant, perhaps by competitive blockage of endogenous adenosine at A₁ and A_{2A} receptors [12].

From the brief survey of the earlier studies it is clear that caffeine can be used to host small ligands (drugs) and deliver/remove the same in a specific site of adenosine receptor or DNA. In other words the molecular basis of use of the well known molecules as drug delivery/recovery system needs some attention. It is well known that specific interaction of a molecule/macromolecule with each other in aqueous solutions heavily depends on hydration of the molecule/macromolecules [13]. In this regard caffeine should be considered as an interesting system because of the simultaneous presence of –CH₃ and –OH groups on its structure (Scheme 4.A). The structure of the molecule limits the solubility in water because of the self association of the molecule by hydrophobic interaction and it is also responsible for complexation with other drug molecules in aqueous solutions. A detail NMR followed by molecular modelling studies confer that most stable self aggregation of caffeine is its dimeric form [14-15]. Earlier, spectroscopic and molecular modelling studies of caffeine complexes with other aromatic drugs reveal replacement of water molecules solvating the drugs by the more hydrophobic caffeine molecules [2]. The studies have also concluded that caffeine could make complex with drugs via π - π type of interaction. In a recent Monte Carlo simulation study similar binding mechanism of caffeine with DNA-base pairs has been proposed [16].

It has to be noted that the most of the DNA-binding drugs reveal charge transfer (CT) reaction upon π -stacking with DNA base pairs [17-18]. Thus the possibility of CT reaction of any drug upon complexation with caffeine molecule would be an interest for the molecular understanding of the interaction of caffeine with the drug. It is well established that the solvent relaxation time scales influence the dynamics of charge transfer reactions by exerting a time dependent dielectric friction. In these cases the CT reaction rates are limited by the rate of solvent relaxation around the concerned molecule [19-21]. However, till date no attempt has been made to explore the dynamics of solvent relaxation around caffeine upon complexation with other aromatic molecules. The dynamics of CT of small molecules upon complexation with caffeine also remain unexplored and are the motives of the present study.



Scheme 4.A. The molecular structure of caffeine and the fluorescent probes DCM, C500, and TNS along with their complexes with caffeine dimer.

In the present study, we have explored the structure of caffeine aggregation by DLS and FTIR techniques. Temperature dependent DLS studies followed by densimetric and sonometric measurements of the caffeine molecules in aqueous solutions explore the structural evolution of caffeine self-aggregation with temperature. These studies are of

particular interest as caffeine is consumed as low and high temperature beverages. Here we have also explored the details of the complexation (solubilisation) of caffeine with a hydrophobic (completely insoluble in water) model probe 4-(dicyanomethylene)-2-methyl-6-(p-dimethylaminostyryl) 4H-pyran (DCM), a well known fluorescent reporter for the relaxation of solvent molecules, in water. Our molecular modeling on the complexation of DCM with caffeine molecules reveals that two caffeine molecules make stack geometry in order to encapsulate DCM inside the dimeric structure (Scheme 4.A). We have measured solvation response of water molecules around the probe DCM at 80°C in the host caffeine dimer with limited number of water molecules and compared the time scales of the solvation with bulk water at elevated temperature. In order to establish the general nature of the solvation dynamics (independent of probe), we have used another well known solvation probe coumarin 500 (C500), where similar complexation geometry with the caffeine molecules has been modelled. Polarization gated fluorescence upconversion and time correlated single photon counting (TCSPC) have been employed to confirm the geometrical restriction of the probes under investigation. In order to investigate the consequence of the slower solvation of water molecules and restricted geometry on the photo-induced charge transfer reaction, we have studied twisted intramolecular charge transfer (TICT) of the probe 2-(p-toluidino) naphthalene-6-sulfonate (TNS) in the dimer at various temperatures. Our detail experimental evidences clearly establish caffeine dimer as an excellent host of small molecules, which could be useful to the further research on the application of the well consumed beverage as a potential carrier of drug for targeted delivery system.

4.2. Results and Discussion:

4.2.1. Probing the Interior of Self-Assembled Caffeine Dimer at Various Temperatures [22]:

4.2.1.1. Characterization of caffeine dimer in aqueous solution. As shown in Table 4.1 and Scheme 4.A, our molecular modeling studies reveal a stable stacked dimer of caffeine molecules with stabilization energy of ~ 10 kcal/mole. Our estimated value of the stabilization energy is close proximity of the reported value of 39.9 kJ/mole (~ 9.5

kcal/mole) from the molecular modeling (using Gaussian package) and X-ray crystallographic studies [23]. As a direct evidence of the formation of caffeine aggregates, we perform temperature and concentration dependent DLS measurements of aqueous caffeine solution (Figure 4.1). High concentration of caffeine in aqueous solution (0.9 M) is reached at a high temperature of 80°C. We observe a hydrodynamic diameter of ~ 1 nm with no signature of any larger sized aggregates, and this feature does not show any significant change with the variation of temperature from 5° to 80°C (Figure 4.1). A similar size distribution is observed when the concentration of the solution is increased from 45 mM to 900 mM. Since the radius of caffeine molecule is 3.76 Å [24] the observed hydrodynamic diameter of ~ 1 nm in caffeine solution does not support the probability of formation of large caffeine aggregate over the studied temperature and concentration range.

To reconfirm the self-association of caffeine, we also carry out FTIR and densimetric measurements, and the results are shown in Figure 4.2. Figure 4.2 (a) shows the FTIR transmittance spectra for caffeine at different concentrations. The spectrum is in good agreement with previously reported studies [14, 25]. The major information of caffeine stretching is confined in the 1700-1640 cm⁻¹ region in which two major peaks are obtained, one in the 1692-1700 cm⁻¹ region (band 1) due to the stretching of the isolated carbonyl, and the other one in the 1641-1647 cm⁻¹ region (band 2), due to the stretching of the conjugated carbonyl. Less intense bands are produced in the 1570 cm⁻¹ region due to C=N and C=C stretching vibrations of the purine ring. As can be observed from Figure 4.2 (a), negligible change in the peak position of band 1 and band 2 occurs with increase in the caffeine concentration indicating the presence of no higher order aggregates [25]. It can also be noted here that in case of stacked dimers of caffeine, full hydration of the carbonyl group is hindered due to steric hindrance, which may in turn cause a wavenumber shift of C=O stretching mode by ~20 cm⁻¹. Thus the present result concludes the presence of the dimers with relatively lower hydration of caffeine which corroborates the compressibility studies (see later). Our observation complies with earlier studies [14] involving theoretical Monte Carlo simulation, FTIR and NMR spectroscopies revealing that caffeine molecules associate to form stacked dimers in water that are energetically more favourable than monomers.

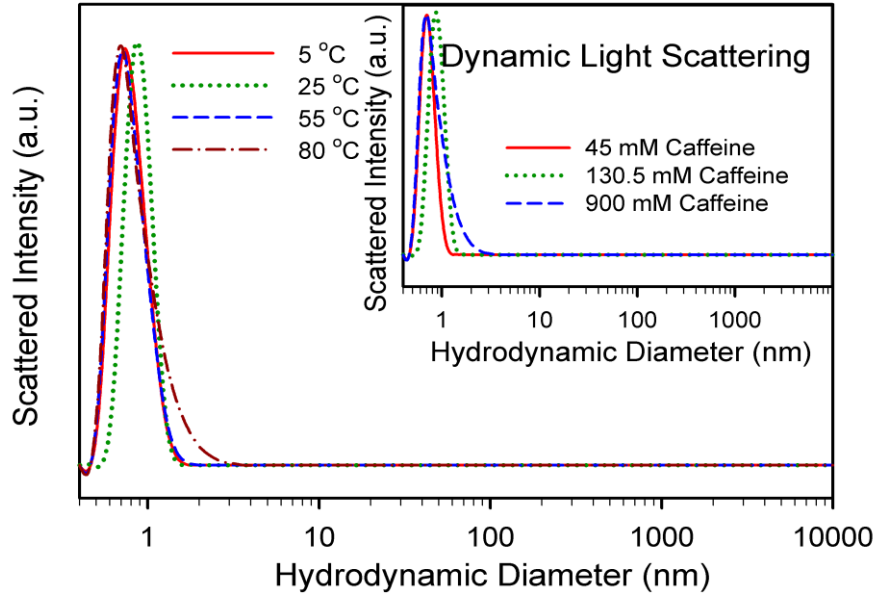


Figure 4.1. Hydrodynamic diameter (as obtained from DLS measurements) of 130.5 mM aqueous caffeine solution at three different temperatures. DLS measurements of caffeine solution with three different concentrations at 25°C are shown in the inset.

In order to understand the nature of hydration in caffeine aggregates, we perform density and sound velocity measurements and the results are depicted in Figure 4.2 (b) and Table 4.2. As observed from Figure 4.2 (b) and Table 4.2, the apparent molar volume (ϕ_v) decreases with increasing concentration of caffeine. However, the concentration vs. ϕ_v plot does not produce a good linear fit generally observed for many small ionic compounds. We attempt to fit the curves in a polynomial of concentration (c),

$$\phi_v = \phi_v^0 + \sum_{i=1}^n S_{v_i} c^i \quad (4-1)$$

and found the ϕ_v^0 values as 8.192×10^{-4} , 8.326×10^{-4} , 8.478×10^{-4} and $8.602 \times 10^{-4} \text{ m}^3 \text{ kg}^{-1}$ at 10, 20, 30 and 40°C, respectively, which are relatively large compared to the small solute molecules but are considerably close to the values reported for large organic molecules [26]. The departure from linear behavior of caffeine molecules strongly suggests its association behavior in aqueous solution as has been found from the FTIR and DLS measurements.

The ultrasonic velocity and adiabatic compressibility (β) decreases with increasing caffeine concentration (Figure 4.2 (c) and Table 4.2), a trend similar to that observed for electrolyte solutes [27-28] in which increasing electrolyte concentration makes more water molecules to electrorestrict resulting in a decrease in the fraction of bulk water in the solution. This is unusual for a neutral molecule like caffeine to show a negative $d\beta/dc$ slope. However, the slope $d\beta/dc$ is very small for caffeine indicating a low hydration number associated with caffeine, similar to that reported earlier [24]. It is known that $d\beta/dc$ is negative for structured water while it is positive for the non-structured one. A small negative value of $d\beta/dc$ thus indicates that the hydration water molecules are rather weakly attached to the caffeine dimers.

Table 4.1: Summary of molecular modeling of caffeine-dye complexes. Error $\pm 7\%$

Complex	Total Energy* (E) (kcal/mole)	Complex Energy# (kcal/mole)	ΔE^\ddagger (kcal/mole)
CAF-CAF	55.56	45.53	-10.03
CAF-DCM	51.91	40.7	-11.21
CAF-DCM-CAF	79.69	57.48	-22.21
CAF-C500	46.89	36.18	-10.71
CAF-C500-CAF	74.67	52.91	-21.68
CAF-TNS (Phenyl side)	28.58	20.85	-7.73
CAF-TNS (Naphthalene side)	28.58	18.41	-17.32
CAF-TNS-CAF (Both CAF are in Phenyl side)	56.36	39.04	-17.32
CAF-TNS-CAF (One CAF is in Phenyl side another is in Naphthalene side)	56.36	29.29	-27.07
CAF-TNS-CAF (Both CAF are in Naphthalene side)	56.36	28.07	-28.29

CAF=Caffeine

*Mathematical sum of energy (E) for each molecule in the complex.

#Total energy calculated for various configurations of the molecular complexes.

‡Difference between mathematical sum of energies of individual molecules and calculated energies of each complex.

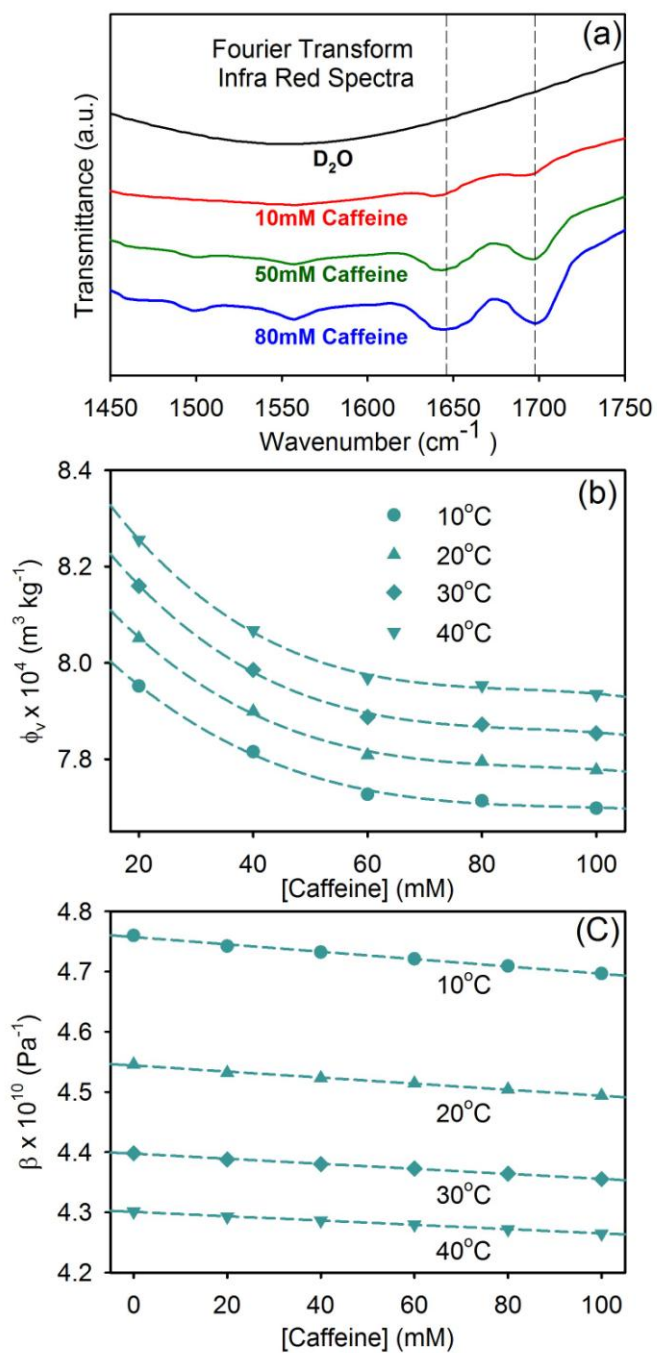


Figure 4.2. (a) FTIR spectra of caffeine solutions at different concentrations (10 mM, 50 mM and 80 mM). The broken line indicate C=O stretch frequencies. (b) Partial molar volume of caffeine as a function of caffeine concentration in solution at different temperatures. The broken lines are polynomial fits. (c) Adiabatic compressibility of aqueous caffeine solution as a function of caffeine concentration at different temperatures. The broken lines are linear fits.

Table 4.2: Apparent molar volume (ϕ_v) and adiabatic compressibility (β) of caffeine solutions at different temperatures. Error $\pm 7\%$

[Caffeine] mM	Density (g cm ⁻³)	Sound velocity (m s ⁻¹)	$\phi_v \times 10^4$ (m ³ kg ⁻¹)	$\beta \times 10^{10}$ (Pa ⁻¹)
Temp. = 10°C				
0	1.000841	1448.87	-	4.7596
20	1.001634	1450.99	7.9516	4.7420
40	1.002533	1451.87	7.8152	4.7320
60	1.003482	1452.88	7.7269	4.7209
80	1.004383	1454.08	7.7136	4.7089
100	1.005299	1455.36	7.6979	4.6963
Temp. = 20°C				
0	0.999320	1483.72	-	4.5456
20	1.000079	1485.43	8.0513	4.5317
40	1.000956	1486.20	7.8992	4.5230
60	1.00188	1486.98	7.8082	4.5141
80	1.002754	1487.98	7.7949	4.5041
100	1.003647	1489.04	7.7771	4.4937
Temp. = 30°C				
0	0.996749	1510.31	-	4.3878
20	0.997474	1511.56	8.1598	4.3802
40	0.998334	1512.21	7.9855	4.3726
60	0.999240	1512.84	7.8878	4.3642
80	1.000094	1513.64	7.8725	4.3553
100	1.000966	1514.54	7.8540	4.3878
Temp. = 40°C				
0	0.993308	1529.91	-	4.3011
20	0.994007	1530.85	8.2555	4.2928
40	0.994851	1531.36	8.0676	4.2863
60	0.995737	1531.87	7.9687	4.2796
80	0.996571	1532.61	7.9529	4.2719
100	0.997422	1533.23	7.9346	4.2648

4.2.1.2. Complexation of caffeine dimer with 4-(dicyanomethylene)-2-methyl-6-(p-dimethylaminostyryl) 4H-pyran (DCM): Dynamics of solvation. The molecular modeling studies on the caffeine-DCM complexation (Table 4.1, Scheme 4.A) confirm that ternary complex of two molecules of caffeine and one DCM molecule (22.21 kcal/mole) is much stable compared to the hetero dimer of caffeine and DCM (11.21 kcal/mole), which has almost similar stabilization energy of caffeine dimer. DCM, being completely insoluble in water, can be solubilized only within some self organized assemblies in aqueous solution [29]. We monitor the solubility of DCM in caffeine solution as a function of caffeine concentration by measuring the optical density of DCM at the absorption maximum (Figure 4.3 (a)). From the plot it is evident that the solubility of DCM increases

linearly beyond 40 mM, and at 140 mM caffeine concentration 1 μ M DCM can be solubilized in the solution. Therefore it can be concluded that 1.4×10^5 molecules of caffeine are involved to solubilize 1 molecule of DCM. Two different conditions can give rise to such result. Firstly, if caffeine forms a large aggregate with critical concentration of 40 mM and secondly, if there is a hetero-association of caffeine with DCM at high caffeine concentration. The probability of caffeine forming large aggregate with critical concentration of 40 mM can be ruled out from the DLS experimental result where we found no signature of aggregate formation in the solution of 140 mM caffeine with dissolved DCM (data not shown). The relatively high solubility of DCM in caffeine solution compared to its water-insolubility strongly suggests the self-association of caffeine providing a hydrophobic environment wherein DCM can be solubilized. Since DCM has been found to be completely insoluble in aqueous solution of sucrose, urea and guanidine hydrochloride even at a high concentration of 6 M each, the result clearly signifies the entrapment of the probe within caffeine dimers rather aqueous solution with perturbed hydrogen bonding networks.

Figure 4.3 (b) shows the relative emission intensity of DCM in aqueous caffeine solution as a function of caffeine concentration and the inset shows the corresponding emission spectra. The Figure shows significant increase in the emission intensity beyond 40 mM caffeine concentration which corroborates the absorption results (Figure 4.3 (a)). In aqueous solution of caffeine, the only probable location of hydrophobic DCM is some hydrophobic pocket. Thus the increase in emission intensity is exclusively due to the relocation of DCM molecule in the hydrophobic environment of low order caffeine aggregates. Earlier studies show that the emission maximum of DCM is produced at 636 nm in micelles [30]. In microemulsion system the DCM emission peak is blue shifted compared to that in micelles and suffers a progressive red shift from 570 nm to 625 nm with increasing water content of the microemulsion [31]. The present observation of the peak at \sim 635 nm reveals a hydrophobic environment around DCM molecule which is more or less comparable to that in micelles and large microemulsions, which in turn is close to that obtained in highly polar solvents (like methanol, ethyl acetate, acetonitrile) [32-33].

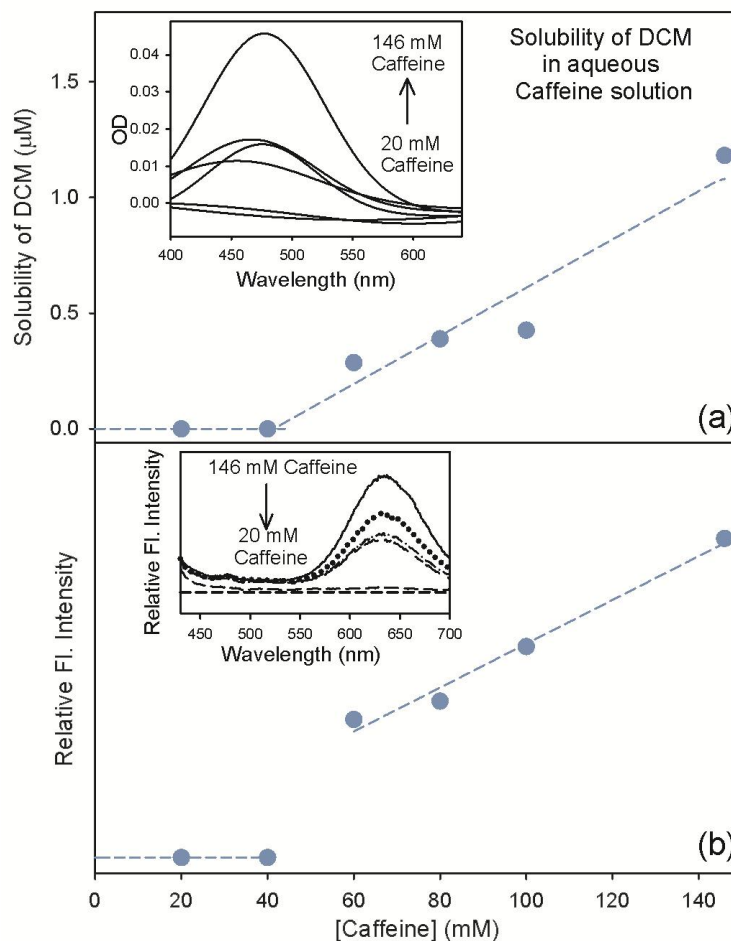


Figure 4.3. (a) Solubility of DCM at different caffeine concentrations as obtained from absorption measurements. The corresponding absorption spectra are shown in the inset. (b) Relative fluorescence intensity of DCM at its emission maxima in various caffeine concentrations. The inset shows the corresponding fluorescence spectra.

We now focus on the dynamics of water molecules (solvation) associated with the caffeine dimers. Figure 4.4 (a) depicts the picosecond resolved fluorescence transients of DCM in 146 mM caffeine aqueous solution at 25°C. As observed from the Figure, the fluorescence transients at the blue end (580 nm), peak (630 nm) and at the red end (690 nm) do not differ considerably and there is no rise component in the red end, a situation markedly different from the other self-aggregated systems like micelles [30]. The transients can be fitted biexponentially with time components of ~350 ps and ~800 ps, resulting in an average lifetime of ~750 ps. It has to be noted that the convolution cis-trans isomerization dynamics of the probe DCM, [34] which is evident in the nonpolar solvents

could be of potential concern in the solvation time scales. However, later works on the exploration of solvation dynamics using the probe DCM have accounted a consequent strong coupling between the locally excited (LE) and charge transfer (CT) states [35] (~300 fs) in bulk polar solvents rather the isomerization dynamics [36]. The absence of considerable difference in the wavelength dependent fluorescence transients rules out the existence of any slow solvation dynamics, which is typical for aggregates like micelles. This result identifies the hydrated water molecules to be loosely bound to the caffeine dimers as has previously been inferred from compressibility measurements. Identical result is obtained at 80°C using a high caffeine concentration of 900 mM (data not shown), concluding that the nature of aggregation and hydration dynamics does not change with temperature as has been observed from the DLS measurements (Figure 4.1). In order to study the geometrical restriction on the encapsulated DCM, in other word to investigate the change in the overall hydrodynamic diameter of the caffeine-DCM complex in aqueous solution, we measure the time resolved fluorescence anisotropy of DCM at 25°C in 146 mM caffeine solution (Figure 4.4 (a), inset). The transient can be fitted single exponentially with a time constant of 0.31 ns which is almost similar to that in ethanol (0.27 ns) but faster than that in micelles [30], thus corroborates with the other experimental results ruling out the possibility of formation of higher order aggregates of caffeine in solution. The rotational relaxation time, τ_r of the probe is related to the local microviscosity η_m experienced by the probe molecule through the Stokes–Einstein–Debye equation (SED) [37-38],

$$\tau_r = \eta_m V_h / k_B T \quad (4-2)$$

where k_B is the Boltzmann constant, T is the temperature and V_h is the hydrodynamic volume of the probe. Using the τ_r value in Eq. (4-2), the hydrodynamic volume of the probe is found to be $1.11 \times 10^{-27} \text{ m}^3$ in ethanol and $1.39 \times 10^{-27} \text{ m}^3$ in caffeine solution. The slightly higher hydrodynamic volume of the probe in the latter system assures the interaction of the probe with the caffeine molecules and simultaneously confirms the absence of higher order aggregates of caffeine in aqueous solution. To have a detailed understanding of the microenvironment around DCM at higher temperatures, we measure temperature dependence of the rotational relaxation dynamics. It is observed that τ_r decreases gradually with increasing temperature indicating that the probe experiences less

rotational hindrance at higher temperature (Table 4.3). The ease of rotation with increasing temperature can be related to an activation energy barrier crossing model and the microviscosity changes with temperature following the relation [39]

$$\eta_m = \eta_m^0 \exp\left(\frac{-E^*}{RT}\right) \quad (4-3)$$

Where E^* is the activation energy for the viscous flow. The plot of $\ln(\eta_m)$ against $1/T$ (Figure 4.4 (b)) can be linearly fitted within an experimental error of $\pm 1.5\%$. Aqueous micellar solutions show a relatively large deviation from linear behavior ($\pm 10\%$) of temperature dependent microviscosity, which can be explained by the presence of higher

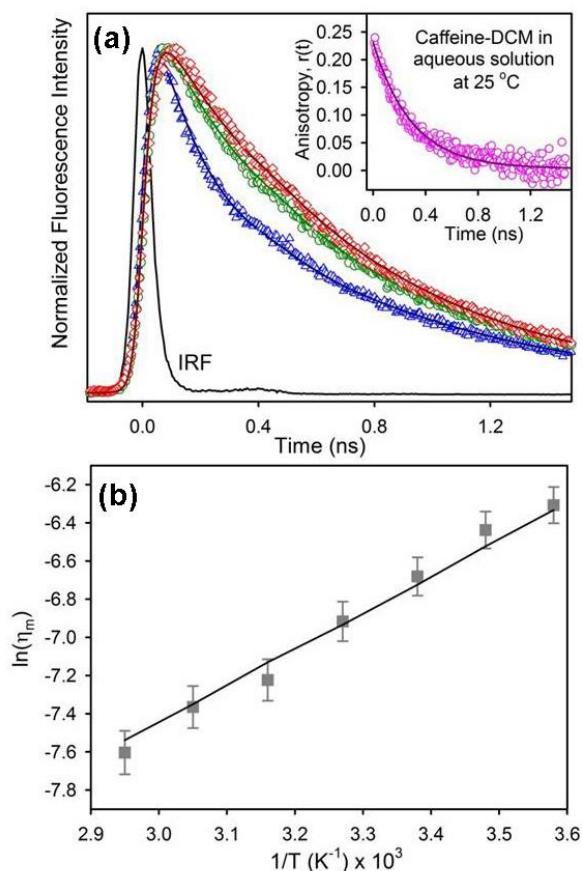


Figure 4.4. (a) Picosecond resolved fluorescence transients of DCM in 146 mM caffeine solution at 25°C shown at three characteristic wavelengths of 580 nm (blue triangles), 630 nm (green circles) and 690 nm (red diamonds). The Instrument response function (IRF) is shown for comparison (Excitation at 409 nm). The solid lines are exponential fittings. The insets shows time resolved anisotropy, $r(t)$ of DCM in the corresponding solution. The solid line is exponential fit. (b) Plot of $\ln(\eta_m)$ against $1/T$ for caffeine solution. The solid line is a linear fit.

Table 4.3: Temperature-dependent rotational relaxation time constants (τ_r) of DCM in 146 mM aqueous caffeine solution (r_0 defines anisotropy at time $t = 0$). Error $\pm 7\%$

Temperature ($^{\circ}\text{C}$)	r_0	τ_r (ps)
06	0.25	484
14	0.24	413
23	0.25	314
33	0.23	240
43	0.23	171
55	0.20	143
66	0.20	109

order aggregates in the solution in the close proximity of Kraft temperature [39]. The relatively strong linear behavior in the caffeine system confirms the low order self-associated stacked caffeine dimers. The obtained E^* value of $3.7 \text{ kcal mol}^{-1}$ is comparable to that of the bulk water ($3.9 \text{ kcal mol}^{-1}$), but considerably smaller than micellar systems [39].

To ascertain the dynamical states of water molecules associated with the caffeine dimer, we measure the femtosecond resolved fluorescence spectra of DCM in caffeine solution. In order to ensure high signal to noise ratio, we measure the transients at 80°C where the caffeine solubility is high enough (900 mM) to provide high signal from the fluorophore. We have also checked the stability of the probe at such elevated temperature in our system and found it to be highly stable. Figure 4.5 (a) depicts the femtosecond resolved transients in the blue end (560 nm), peak (620 nm) and in the red end (700 nm). As can be observed from the Figure, the transient in the blue end can be fitted triexponentially with three decay components of 0.46 ps (86%), 22.7 ps (11%) and 519 ps (3%). On the other hand, the red end transient exhibits a distinct rise component of 0.94 ps with a decay component of 510 ps. This is a clear indication of the solvation of the dye and we construct the TRES (see Figure 4.5 (b), inset) as per the procedure described in the methodology. From the time dependent Stokes shift we measure the solvent correlation function, $C(t)$ and plot it against time (Figure 4.5 (b)). The curve is well fitted biexponentially with time constants of 0.6 ps (82%) and 5.85 ps (18%) (Table 4.4) with a considerable Stokes shift of 800 cm^{-1} . It should be noted here that we miss a considerable fraction of Stokes shift due to our limited instrumental resolution, and we determined the loss in the dynamic Stokes shift using the procedure developed by Fee and Maroncelli [40], where $v(0)$ can be calculated by the following equation:

$$\nu_{em}^p(0) = \nu_{abs}^p - [\nu_{abs}^{np} - \nu_{em}^{np}] \quad (4-4)$$

where ν_{abs}^p , ν_{abs}^{np} , and ν_{em}^{np} are the absorption peak in polar solvent, absorption peak in nonpolar solvent, and emission peak in nonpolar solvent, respectively. In the present study, we use dioxane as the nonpolar solvent with absorption and emission maxima of DCM at 455 and 554 nm, respectively. Aqueous solution of caffeine is used as the polar solvent in which DCM produces an absorption peak at 480 nm. We calculate a 34% loss in the

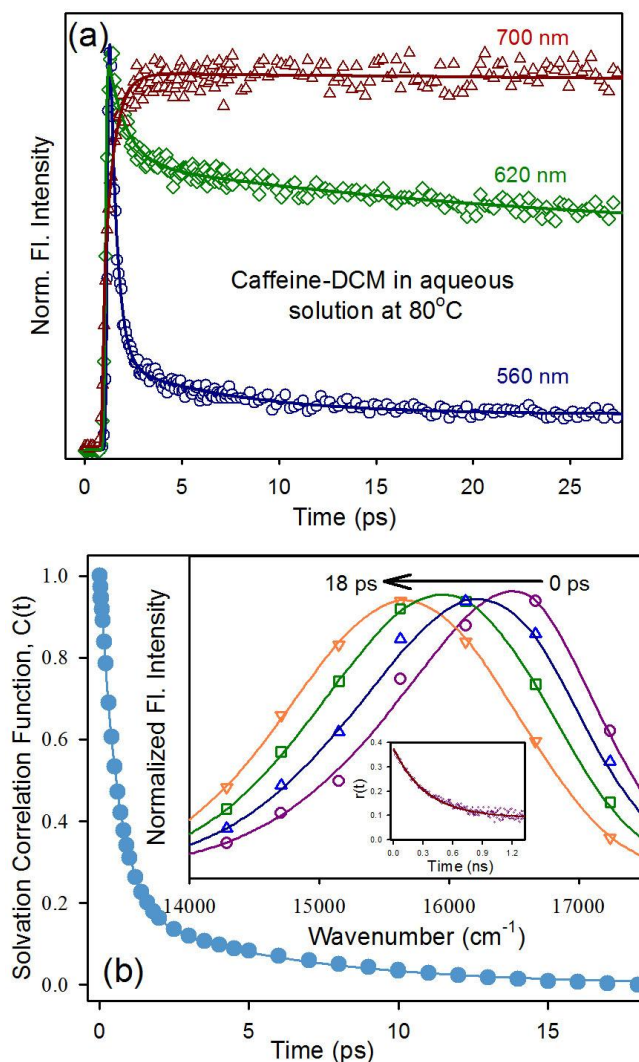


Figure 4.5. (a) Femtosecond resolved fluorescence transients of DCM in 900 mM caffeine at 80°C at three characteristic wavelengths. (b) Solvation correlation function, $C(t)$ of the corresponding sample. The solid line is exponential fit. The bigger inset shows the time-resolved emission spectra (TRES) along with the anisotropy (smaller inset) of the same sample.

dynamical Stokes shift within the experimental time resolution. The observed $C(t)$ decay is much slower than that of the pure water [41] (126 fs (20%) and 880 fs (35%)) wherein about half of the solvation process occurs in a time scale of experimental time resolution of 30 fs. A previous femtosecond-resolved study from our group shows that the solvation time scale of C500 in water is 0.3 and 0.7 ps at room temperature and it reduces to 0.3 ps at 55°C. In presence of a large ion like guanidium hydrochloride the process becomes slower with time constants of 0.5 and 2.1 ps at room temperature and 0.8 ps at 55°C. All these time scales are however, faster than those observed for caffeine solutions even at elevated temperature confirming the structured nature of the hydrated water molecules in caffeine solution with respect to an ionic solution. On the other hand these time scales are rather comparable [42] or faster [43] in reverse micelles or micelles [30] confirming our finding that caffeine is aggregated as dimers in aqueous solution and with a rather weakly structured water network around it. The smaller inset inside Figure 4.5 (b) inset shows fluorescence anisotropy of DCM at 80°C in 900 mM caffeine solution. The transient can be fitted single exponentially with a time constant of 0.33 ns (Table 4.4) which is close to the one obtained for the probe in 146 mM caffeine at 25°C. Since DCM is extremely insoluble in water and its solubility in aqueous caffeine solution is only possible due to its confinement inside caffeine dimer, the rotational time constant obtained for the probe actually signifies the time required for rotation of the caffeine in dimeric form. In view of the fact that the anisotropic time scale is much longer compared to the obtained solvation time scales of the same sample it can be concluded that the solvation time scales obtained reflects the dynamics of the bound water around the caffeine dimer and not due to the dynamics of caffeine dimer close to one another at such a high concentration (900 mM).

4.2.1.3. Complexation of caffeine dimer with coumarin 500 (C500): General picture of the dynamics of solvation for caffeine dimer. To confirm the solvation time scales around caffeine dimer at room temperature we repeated the femto second resolved experiment using another solvation probe C500 which unlike DCM is sparingly soluble in water. Since solubility of C500 in 100 mM caffeine solution is high enough to provide good signal from the fluorophore we did not use high caffeine concentration. Molecular modeling studies (Table 4.1 and Scheme 4.A) on the association of C500 with caffeine

also reveal stacked ternary complex of two caffeine molecules and one C500 molecule. We have also checked the stability of the probe at such elevated temperature in our system and found it to be highly stable just like DCM as mentioned before. Since C500 was dissolved in 100 mM caffeine we were able to check the results both at room temperature and at 80°C. Figure 4.6 (a) depicts the femtosecond resolved transients at room temperature in the blue end (450 nm), peak (500 nm) and in the red end (600 nm). As can be observed from the Figure, the transient in the blue end can be fitted triexponentially with three decay components of 0.65 ps (82%), 4.35 ps (15%) and 5 ns (3%). On the other hand, the red end transient exhibits a distinct rise component of 0.67 ps with decay components of 57 ps and 5 ns. This is a clear indication of the solvation of the dye and we construct the TRES (see Figure 4.6 (b), inset) as per the procedure described in chapter 2 (section 2.2.1). From the time dependent Stokes shift we measure the solvent correlation function, $C(t)$ and plot it against time (Figure 4.6 (b)). The curve is well fitted biexponentially with time constants of 0.8 ps (59%) and 5.42 ps (41%) (Table 4.4). The recovery of similar solvation time scales even after changing the solvation probe reconfirms the dynamical nature of water molecules associated with caffeine dimer. The smaller inset inside Figure 4.6 (b) inset shows fluorescence anisotropy of C500 at 20°C in 100 mM caffeine solution. The transient can be fitted single exponentially with a time constant of 55 ps (Table 4.4). The solvation time scales obtained at 80°C using C500 are found to be 0.44 ps (94%) and 25 ps (6%) (data not shown). The lack of significant weight of the slower component in the dynamics indicates the release of the probe C500 from the caffeine dimer to the solvent (water). Since the concerned probe C500 is sparingly soluble in water and with temperature its

Table 4.4: Femtosecond-resolved solvation correlation functions $C(t)$ for DCM and C500 in aqueous caffeine solution at different temperatures(T) along with the corresponding rotational relaxation time constants (τ_r). Error $\pm 7\%$

Aqueous caffeine solution containing probe	T(°C)	C(t) in ps		τ_r (ps)
		τ_1	τ_2	
DCM	80	0.6 (82%)	5.85 (18%)	330
C500	20	0.8 (59%)	5.42 (41%)	55
	80	0.44 (94%)	25 (6%)	41

solubility increases, the solvation time scales thus obtained reflects the nature of dynamics of water molecules associated with the probe C500 and not with the caffeine dimer.

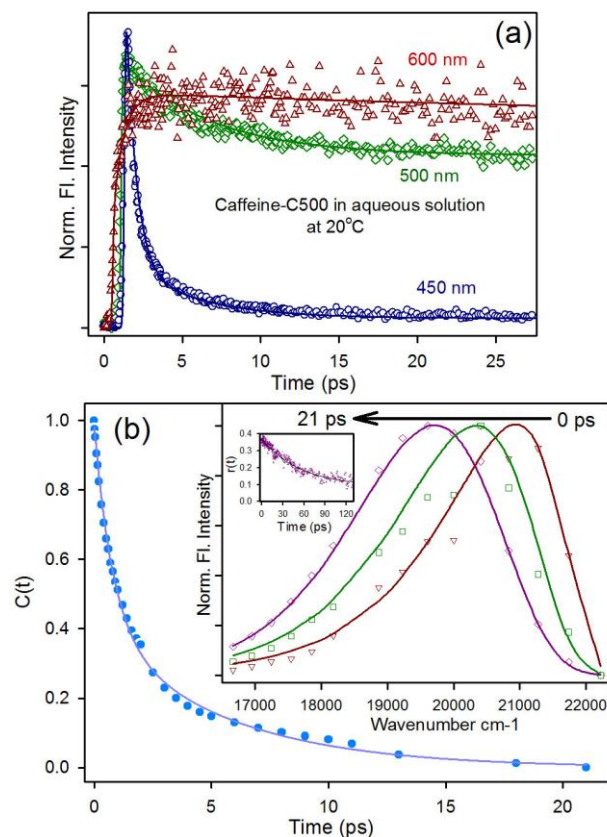


Figure 4.6. (a) Femtosecond resolved fluorescence transients of C500 in 100 mM caffeine at 20°C at three characteristic wavelengths. (b) Solvation correlation function, $C(t)$ of the corresponding sample. The solid line is exponential fit. The bigger inset shows the time-resolved emission spectra (TRES) along with the anisotropy (smaller inset) of the same sample.

4.2.1.4. TNS (2-(p-toluidino) naphthalene-6-sulfonate) in caffeine dimer: Excited state ultrafast charge transfer in the confinement.

In order to investigate the consequence of the geometrical restriction of guest molecules in the caffeine dimer and the relatively slower dynamics of solvation in the interior of the dimer, we have studied excited state charge transfer reaction of a model probe TNS in the microenvironment. Upon UV excitation TNS undergoes a twisted intramolecular charge transfer (TICT) reaction, which significantly depends on the local solvation and geometrical restriction on the probe [44].

By observing the picosecond to nanosecond dynamics of population and polarization-analyzed anisotropy for the TNS-caffeine complex, we can also elucidate the nature of local solvation and polarity in the interior of the caffeine dimer. As shown in Table 4.1 and Scheme 4.A, our molecular modeling reveals most stable complex of TNS with caffeine molecules to be ternary aggregate of two molecules of caffeine and one molecule of TNS in stacked geometry. It is evident that the stacking of the caffeine molecules in the close proximity of naphthalene ring offers more stabilization compared to other complex geometry.

Interaction of caffeine with TNS was studied by NMR spectroscopy. The aromatic resonances of TNS are shown in the bottommost panel of Figure 4.7 (a). A complete assignment of all resonances was possible using standard 2D correlation experiments. Each resonance is annotated with atom numbers consistent with Figure 4.7 (b). All protons showed upfield shifts upon addition of caffeine as shown in Figure 4.7 (a) and 4.7 (c). The titration data were fitted with the following equation [45]

$$\delta_{obs} = \delta_0 + \frac{\Delta\delta^{sat}}{2K_M[T]_T} \left[1 + K_M([C]_T + [T]_T) - \sqrt{\{1 + K_M([C]_T + [T]_T)\}^2 - 4K_M^2[C]_T[T]_T} \right] \quad (4-5)$$

where δ_{obs} , δ_0 and $\Delta\delta^{sat}$ stand respectively for TNS chemical shifts at a given caffeine concentration, in absence of caffeine and change in chemical shift in presence of large excess of caffeine; K_M , $[C]_T$ and $[T]_T$ stand for caffeine-TNS association constant, total caffeine and TNS concentrations, respectively. The naphthyl ring protons (except for position 3) showed an average K_M value of $57.4 \pm 5.7 \text{ M}^{-1}$ while the phenyl protons and H3 of the naphthyl ring showed a slightly lower K_M . These two groups of protons are also clearly different from each other when one considers the observed change in the chemical shift at 50 mM caffeine as depicted in Figure 4.7 (b), the naphthyl protons showed almost double the amount of upfield shift compared to that of the phenyl group (and H3). The observed upfield shifts indicate stacking interaction between TNS and caffeine. The greater effect felt by the naphthyl ring also indicates that caffeine mainly stacks on the naphthyl ring, which corroborates with our molecular modeling studies mentioned before. The odd behavior of the H3 proton (low net upfield shift), when compared to the behavior of all other naphthyl protons, can be explained if one considers a concomitant change in the twist of the TNS molecule upon caffeine binding. The H3 proton, closest to the phenyl ring,

experiences paramagnetic shielding / de-shielding effect of the phenyl ring, the exact nature of which will depend on the relative orientation of the naphthyl/phenyl rings. Upon caffeine binding, while all naphthyl protons feel uniform upfield shift, the H3 proton will feel an additional effect from the phenyl ring that will depend upon how the relative orientation of the naphthyl/phenyl ring (twist) changes upon complexation with caffeine. In summary, NMR experiments show the following: i) TNS binds caffeine with a $K_M \sim 57 M^{-1}$, ii) the mechanism of binding is stacking between caffeine and the TNS naphthyl ring, iii) stacking is accompanied by a change of the twist angle in the TNS molecule.

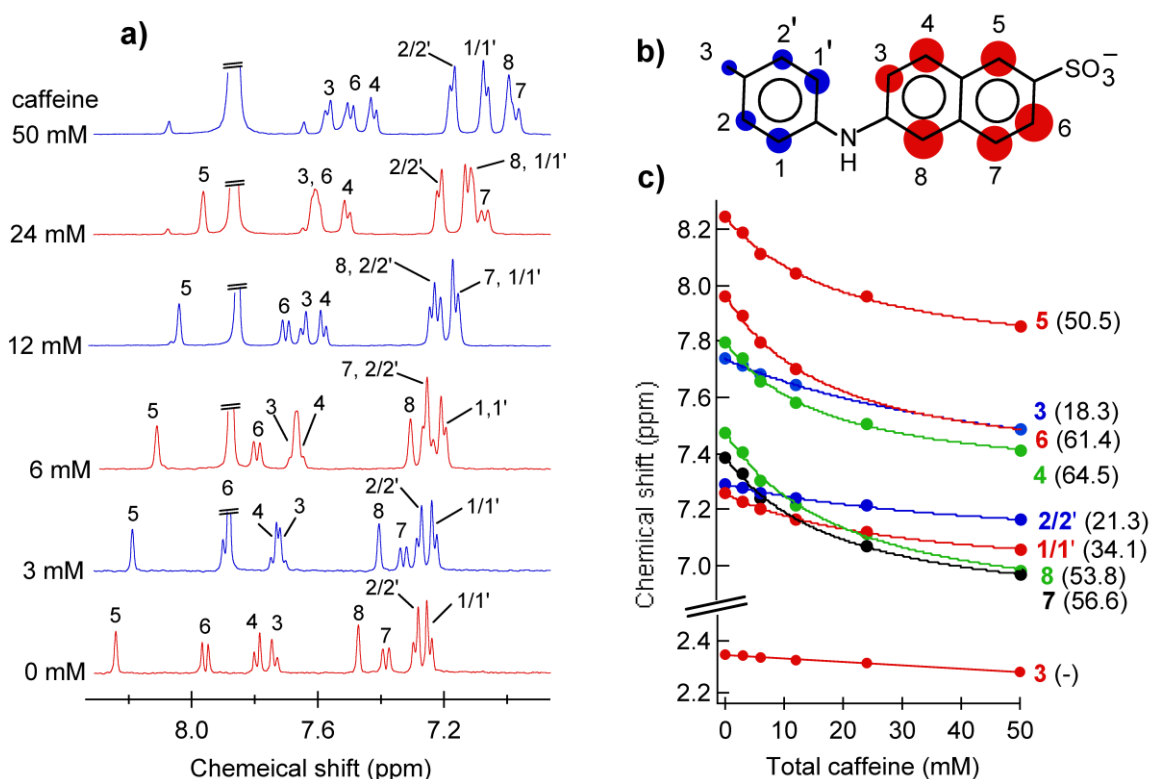


Figure 4.7. (a) NMR spectra (aromatic region) of 2 mM TNS in absence and presence of caffeine (caffeine signals are capped by a double bar) at 27 C and pH 7.2. The resonances are annotated (see atom numbering shown in panel b). (b) A cartoon of TNS molecule. The relative sizes of the blue (phenyl ring) and the red (naphthyl ring) circles correspond to the relative change in chemical shift of TNS protons upon addition of 50 mM caffeine (see panel c). (c) Change in chemical shift of TNS protons upon caffeine titration. Association constants (K_M) obtained by fitting the titration data with Eq. (4-5) are indicated within parenthesis (in units of M^{-1}).

Figure 4.8 (a) shows the steady state emission spectra of TNS ($\lambda_{ex} = 375$ nm) in water in absence and presence of caffeine. TNS is almost non-fluorescent in water

(quantum yield, $\phi_f = 0.001$) with a very short fluorescence life time ($\tau_f = 60$ ps) [46]. The extremely low quantum yield (0.001) in water [41, 46], indicates that the CT state dynamics are dominated by non-radiative processes, for instance, the fast intersystem crossing as proposed in the literature [47]. As evident from the Figure 4.8 (a) the fluorescence intensity of the probe shows a linear enhancement with increase in caffeine concentration. The remarkable sensitivity of TNS is due to the non-radiative twisted intramolecular charge transfer (TICT) process whose rate increases very rapidly with the polarity of the medium [47-48]. The dramatic enhancement of the fluorescence intensity of TNS in presence of caffeine is due to the relocation of TNS molecules in the hydrophobic interior of caffeine dimers, which in turn makes the TNS molecules more rigid, retarding the TICT process in a manner comparable to cyclodextrin (CD) cavity or the micellar aggregates [49-51]. The binding constant (K_M) of TNS with caffeine has been calculated from its steady state emission spectroscopy using the relation suggested by Almgren *et al.*, [52]

$$\frac{I_\infty - I_0}{I_t - I_0} = 1 + \frac{1}{K_M [M]} \quad (4-6)$$

where I_∞ , I_t and I_0 , denote, respectively, the emission intensities at infinite caffeine concentration, at an intermediate caffeine concentration and in the absence of caffeine, $[M]$, the caffeine concentration. We plot $(I_\infty - I_0)/(I_t - I_0)$ against $1/[M]$ which produces good linear fit (Figure 4.8 (b)) and K_M calculated to be 57 M^{-1} which exactly coincides with the one calculated from our NMR experiments. The binding constant of TNS with Triton X-100 (TX) micelles [46] has been reported earlier as $3.5 \times 10^5 \text{ M}^{-1}$ while that with β -cyclodextrins (CD) [53-54] is $2 \times 10^3 \text{ M}^{-1}$. The observed binding constant of TNS with caffeine is orders of magnitude less compared to those with micelles and cyclodextrins, and consequently model drugs could faster be released from the caffeine dimer compared to the other hosts. The free energy change (ΔG^0) associated with the complex formation between TNS and caffeine using the equation can be obtained as,

$$\Delta G^0 = -RT \ln K_M \quad (4-7)$$

and the ΔG^0 value obtained for the present system is $-2.4 \text{ kcal mol}^{-1}$ which is comparable to the activation energy of viscous flow (see later).

Picosecond resolved fluorescence of TNS in presence of caffeine is presented in Figure 4.9. The time resolved emission studies lend further support to the contention that TICT process of TNS gets retarded in presence of caffeine due to the confinement of the probe within the caffeine dimer because of which the lifetime of the fluorophore increases. Figure 4.9 indicates that while in aqueous solution lifetime of TNS is extremely short (60 ps) [46], in presence of caffeine the fluorescence decay of TNS becomes much slower. The average lifetime of the fluorophore (Table 4.5) increases from 60 ps in water to 168 ps and 270 ps in presence of 8 and 66 mM caffeine, respectively. The linear enhancement in the

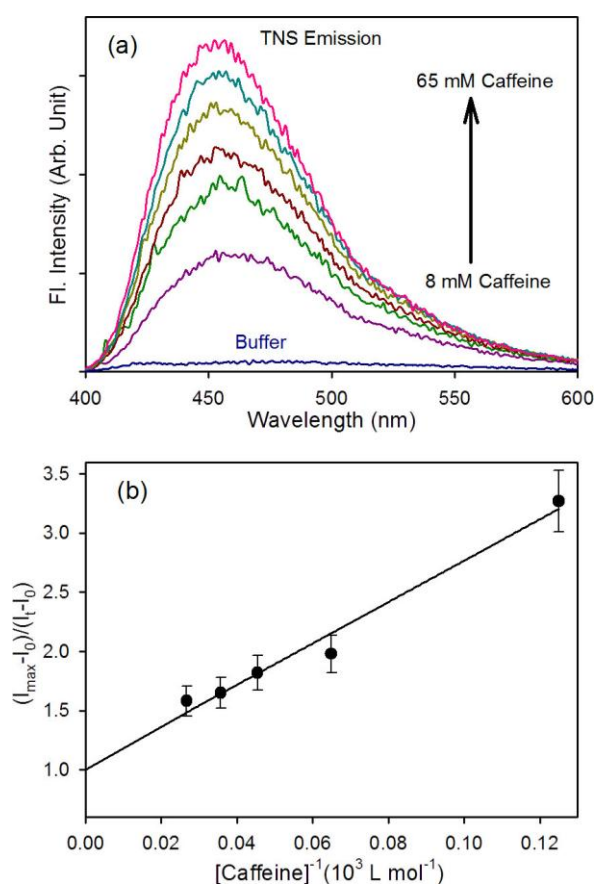


Figure 4.8. (a) Emission spectra of 50 μM TNS in absence and presence different caffeine concentration ($\lambda_{ex}=375\text{nm}$). (b) Almgren plot (see text) of TNS (50μM) for various caffeine concentrations.

lifetime of the fluorophore with increase in the caffeine concentration finds analogy with previous studies [49-51, 54] Thermodynamic Study on the Effects of P-Cyclodextrin Inclusion with Anilidonaphthalenesulfonates where it has been reported that the lifetime of

TNS increases ~40 fold in presence of 15 mM β -CD compared to water. As seen in case of CD cavity and micellar aggregates,[49, 51] the twisting motion of the probe gets restricted in presence of caffeine which results in the blockage of the nonradiative TICT process, leading to the enhancement of fluorescence lifetime. To get more insight on the restriction of the probe in caffeine dimer, we measure the time resolved fluorescence anisotropy of TNS in water and in presence of 100 mM caffeine (Figure 4.9, inset). In water the transient can be fitted single exponentially with the time constant of 89 ps while it is 318 ps in presence of 100 mM caffeine. Applying SED (Eq. (4-2)) as mentioned before, the hydrodynamic volume of the probe found to be $0.4 \times 10^{-27} \text{ m}^3$ in water and $1.45 \times 10^{-27} \text{ m}^3$ in presence of 100 mM caffeine. The increase in the hydrodynamic volume of the probe provides evidence of the heteroassociation of the fluorophore with caffeine dimer [14] which corroborates with the molecular modeling studies represented in Scheme 4.A and Table 4.1 and the NMR results as has been mentioned before.

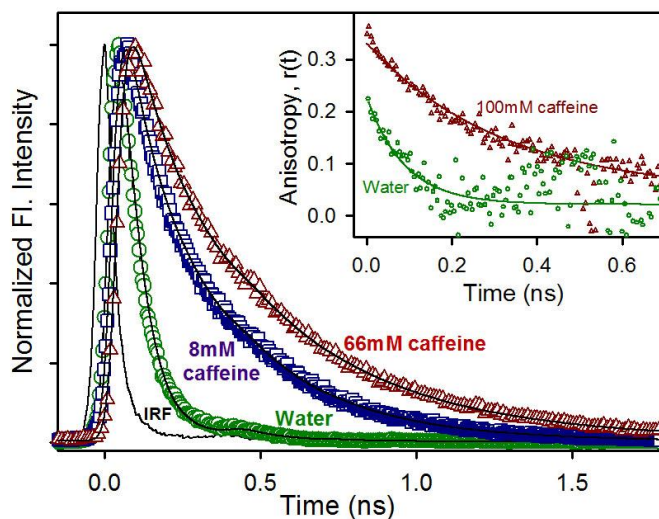


Figure 4.9. Picosecond resolved fluorescence transients of TNS in water (\circ) and in presence of 8 mM (\square) and 66 mM (Δ) caffeine. The inset shows the fluorescence anisotropy of TNS in water (\circ) and in presence of 100 mM (Δ) caffeine.

The temperature dependent fluorescence transient of TNS in presence of 100 mM caffeine is depicted in Figure 4.10 (a) and Table 4.6. The average lifetime ($\langle \tau \rangle = \sum a_i \tau_i$ where τ_i represents the lifetime and a_i represents the relative contribution of the i^{th} component) of the fluorophore when associated with caffeine decreases from 355 ps to 192

ps as temperature rises from 6°C to 75°C. Rise in temperature leading to the dissociation of TNS-caffeine complex releases TNS into the water facilitating the non-radiative TICT process which results faster fluorescence decay of the probe as observed. The result is in good agreement with the temperature dependent time resolved fluorescence anisotropy of TNS in 100 mM caffeine (Figure 4.10 (a) inset). The rotational time constant of TNS decreases from 363 ps at 9°C to 80 ps at 81°C (Table 4.7). The ease of rotation of TNS with rise in temperature reconfirms release of TNS into water from caffeine bound state due to thermal dissociation of TNS-caffeine complex. The temperature dependence of the average lifetime of the fluorophore can be exploited to obtain the activation energy of

Table 4.5: Change in fluorescence lifetime of TNS with increase in caffeine concentration.

[Caffeine] mM	τ_1 (ps)	τ_2 (ps)	τ_3 (ps)	Average lifetime $\langle t \rangle$ (ps)
0	60 (100%)			60
8	39 (46%)	242 (48%)	567 (6%)	168
15	39 (40%)	236 (46%)	519 (14%)	197
28	39 (37%)	251 (47%)	567 (16%)	223
37	39 (35%)	237 (43%)	549 (22%)	236
46	42 (36%)	258 (45%)	594 (19%)	244
58	46 (35%)	262 (43%)	608 (22%)	263
66	50 (37%)	287 (43%)	640 (20%)	270

τ represents the time constant and the numbers in the parenthesis represent relative contribution of the component. Error $\pm 7\%$

the TICT process of the fluorophore through the Arrhenius equation [55]. Figure 4.10 (b) shows the Arrhenius plot for TNS in 100 mM caffeine and activation energy (E_{act}) has been estimated as $1.8 \pm 0.3\%$ kcal mol⁻¹, the activation energy thus obtained reflects the energy barrier for the transition of the locally excited (LE) state to the CT state of the probe TNS. In contrast to the nearly barrierless twisting motion of the probe in pure water, the energy barrier of such motion of the probe increases upon binding to caffeine as has been observed upon binding to protein [44] due to the lower micropolarity on binding sites. In order to estimate microviscosities we have used the simple SED (Eq. (4-2)).

Microviscosity is the friction experienced by a probe molecule at the microscopic scale; it is an important parameter for characterizing the local environment because modest changes in local viscosity lead to variation in physical as well as chemical properties. The microviscosity changes with temperature following the relation mentioned before in Eq. (4-3). The plot of $\ln \eta_m$ against $1/T$ (Figure 4.10 (c)) can be linearly fitted within the experimental error of $\pm 1\%$. The E^* value is estimated to be $3.7 \text{ kcal mol}^{-1}$ which exactly corroborates with the E^* value obtained using DCM (mentioned before) in place of TNS and thus confirms that both DCM and TNS shares similar microenvironment around them in aqueous caffeine solution i.e both of them are confined within the caffeine dimer (Scheme 4.A, Table 4.1). It has to be noted here that the activation energy estimated for the transition of LE state to the CT state of the probe TNS is lower compared to that of the viscous flow which indicates that the CT state of the probe is stabilized by labile water molecules at higher temperature even before the probe dissociates from the caffeine dimer. The activation energy of the viscous flow along with the change in free energy associated with the complexation of TNS with caffeine gives us an idea about the amount of energy that is required to release the probe from the caffeine bound state, which is noteworthy for choosing caffeine as a tool for targeted drug delivery.

Table 4.6: Change in fluorescence lifetime of TNS in presence of 100 mM caffeine with rise in temperature (T).

T (°C)	τ_1 (ps)	τ_2 (ps)	τ_3 (ps)	Average lifetime $\langle \tau \rangle$ (ps)
6	1069 (13.7%)	432 (42.2%)	60 (44.1%)	355
16	1069 (8.7%)	432 (48.6%)	60 (42.7%)	329
24	1069 (5.8%)	432 (50.5%)	60 (43.7%)	306
34	1099 (4.8%)	388 (57.1%)	54 (38.1%)	295
46	761 (7.5%)	330 (56%)	43 (36.5%)	257
65	1294 (1.6%)	299 (57.6%)	23 (40.8%)	202
75	1141 (1.7%)	259 (63.9%)	22 (34.4%)	192

τ represents the time constant and the numbers in the parenthesis represent relative contribution of the component. Error $\pm 7\%$

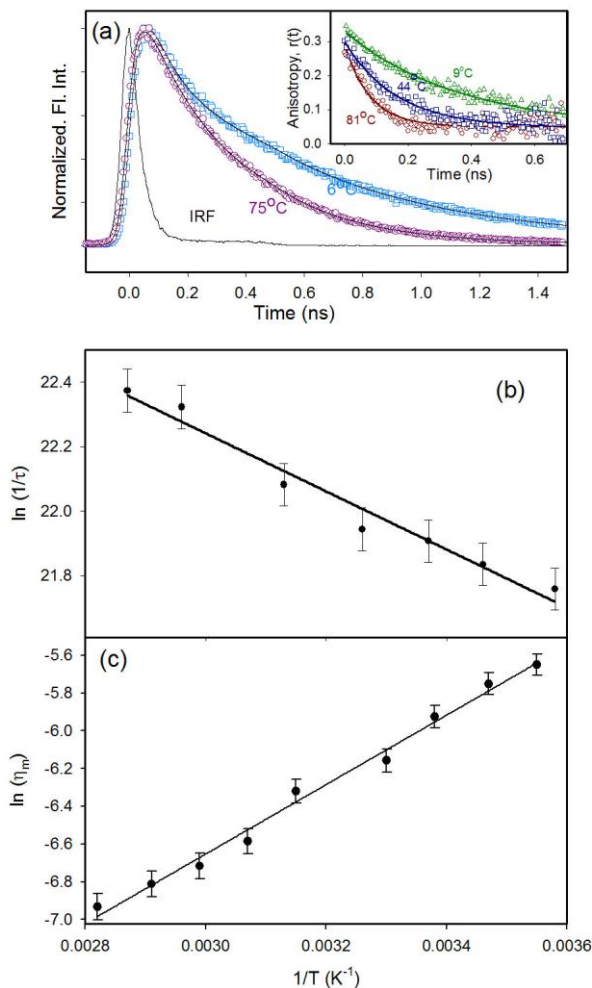


Figure 4.10. (a) Temperature dependent fluorescence transients of TNS-caffeine complex at 6°C (\square) and 75°C (\circ). The inset shows the anisotropy of TNS in presence of caffeine at 9°C (Δ), 44°C (\square) and 81°C (\circ). (b) The plot of $\ln(1/\tau)$ against $1/T$ for TNS-caffeine solution. The solid line is the corresponding numerical fit of the Arrhenius equation (see text). (c) The plot of $\ln \eta_m$ against $1/T$ for TNS-caffeine solution. The solid line is the corresponding numerical fit of Arrhenius type plot (see text).

Table 4.7: Temperature-dependent rotational relaxation time constants (τ_r) of TNS in 100 mM aqueous caffeine solution (r_0 defines anisotropy at time $t = 0$). Error $\pm 7\%$

Temperature (°C)	r_0	τ_r (ps)
9	0.35	363
15	0.35	321
23	0.30	262
30	0.35	203
44	0.30	165
53	0.30	123
62	0.26	105
71	0.29	93
81	0.27	80

4.3. Conclusion:

In the present study we have exploited the dimeric nature of caffeine to host some hydrophobic molecules like DCM, C500 and TNS. The results of the molecular modeling calculations provide a mechanistic model of confinement of such molecules within the caffeine dimer that is consistent with the in vitro studies involving NMR experiments. We have explored the hydration dynamics associated with caffeine dimer, which plays a key role in the biomolecular recognition of such xanthine alkaloids. The DLS studies associated with FTIR, sonometric, densimetric and steady state optical experiments clearly reveal the dimeric nature of the caffeine molecules in aqueous solution which is consistent with the previously reported studies. While the sonometric/densimetric studies explore the static picture of hydration around the caffeine dimers, picosecond/femtosecond resolved experiments demonstrate the key time scales associated with the dynamics of hydration. The femtosecond resolved fluorescence study at 80°C reveals solvation of the probe with time scales of 0.6 ps and 5.85 ps, which are slower than that in bulk water but faster than micelles or reverse micelles confirming the weakly structured nature of the hydrated water molecules. The dynamics of water molecules as revealed by C500 show solvation time scale of 0.3 and 0.7 ps at room temperature and it reduces to 0.3 ps at 55°C. In presence of a large ion like guanidium hydrochloride the process becomes slower with time constants of 0.5 and 2.1 ps at room temperature and 0.8 ps at 55°C. All these time scales are however, faster than those observed for caffeine solutions even at elevated temperature confirming the structured nature of the hydrated water molecules in caffeine solution with respect to an ionic solution. Our polarization gated picosecond resolved experiment on the confined DCM and TNS in the caffeine dimer at various temperature explores the activation energy (E^*) for the viscous flow and has been found to be comparable to that of bulk water, which further suggests that very weakly structured water molecules are associated with the caffeine dimers. Very slow water dynamics being a characteristic of strongly bonded water molecules, would have prevented the interaction of such xanthine alkaloids with biomolecules whereas very fast dynamical nature of bound water would not have allowed the formation of caffeine dimer itself. The observed dynamical nature of water molecules associated with caffeine dimer makes it a suitable subject for biomolecular interaction where the bound water molecules can be displaced in presence of

its receptor molecule facilitating the hydrophobic interaction. Our observations may find the relevance in the exploration of such biomolecular recognition of the most widely consumed caffeine molecules in physiologically relevant environments. Furthermore our exploration of TICT dynamics of TNS in presence of caffeine gives us an idea about the amount of energy required to release such model drugs from the caffeine bound state and this may find significance in further investigation of the use of such xanthine alkaloids as a tool for targeted drug delivery.

References

- [1] C. P. Selby, A. Sancar, Molecular Mechanisms of DNA Repair Inhibition by Caffeine, *Proc. Natl. Acad. Sci.* 87 (1990) 3522.
- [2] R. W. Larsen, R. Jasuja, R. K. Hetzler, P. T. Muraoka, V. G. Andrada, D. M. Jameson, Spectroscopic and Molecular Modelling Studies of Caffeine Complexes with DNA Intercalators, *Biophys. J.* 70 (1996) 443.
- [3] D. B. Davies, D. A. Veselkov, L. N. Djimant, A. N. Veselkov, Heteroassociation of Caffeine and Aromatic Drugs and their Competitive Binding with a DNA Oligomer, *Eur. Biophys. J.* 30 (2001) 354.
- [4] V. J. McKelvey, P. G. McKenna, Enhanced Synergism Between Caffeine and Mitomycin C in the Induction of Cytogenetic Aberrations in Thymidine Kinase-Deficient Friend Murine Erythroleukaemia Cells, *Mutagenesis* 1 (1986) 173.
- [5] D. Mourelatos, J. Dozi-Vassiliades, A. Kotsis, C. Gourtsas, Enhancement of Cytogenetic Damage and of Antineoplastic Effect by Caffeine in Ehrlich Ascites Tumor Cells Treated with Cyclophosphamide in vivo, *Cancer Res.* 48 (1988) 1129.
- [6] H. C. Andersson, B. A. Kihlman, Effects of G2 Treatments with Inhibitors of DNA Synthesis and Repair on Chromosome Damage Induced by X-rays and Chemical Clastogens in Root Tips of *Vicia Faba* Comparison with Corresponding Effects in Cultured Human Lymphocytes, *Mutat. Res.* 181 (1987) 173.
- [7] W. E. Ross, L. A. Zwelling, K. W. Kohn, Relationship between Cytotoxicity and DNA Strand Breakage Produced by Adriamycin and Other Intercalating Agents, *Int. J. Radiat. Oncol. Biol. Phys.* 5 (1979) 1221.
- [8] G. Iliakis, M. Nusse, R. Ganapathi, I. Egner, A. Yen, Differential Reduction by Caffeine of Adriamycin Induced Cell Killing and Cell Cycle Delays in Chinese Hamster v79 Cells, *Int. J. Radiat. Oncol. Biol. Phys.* 12 (1986) 1987.
- [9] R. Ganapathi, D. Grabowski, H. Schmidt, A. Yen, G. Iliakis, Modulation of Adriamycin and N-Trifluoroacetyladiamycin-14-valerate Induced Effects on Cell Cycle Traverse and Cytotoxicity in P388 Mouse Leukemia Cells by Caffeine and the Calmodulin Inhibitor Trifluoperazine, *Cancer Res.* 46 (1986) 5553.

- [10] H. Kimura, T. Aoyama, Decrease in Sensitivity to Ethidium Bromide by Caffeine, Dimethylsulfoxide or 3-Aminobenzamide Due to Reduced Permeability, *J. Pharmacobio-Dyn.* 12 (1989) 589.
- [11] F. Traganos, B. Kaminska-Eddy, Z. Darzynkiewicz, Caffeine Reverses the Cytotoxic and Cell Kinetic Effects of Novantrone (Mitoxantrone), *Cell Prolif.* 24 (1991) 305.
- [12] B. Johansson, L. Halldner, T. V. Dunwiddie, S. A. Masino, W. Poelchen, L. G. Llort, R. M. Escorihuela, A. F. Teruel, Z. W. Hallin, X. J. Xu, A. Hårdemark, C. Betsholtz, E. Herlenius, B. B. Fredholm, Hyperalgesia, Anxiety, and Decreased Hypoxic Neuroprotection in Mice Lacking the Adenosine A1 Receptor, *Proc. Natl. Acad. Sci.* 98 (2001) 9407.
- [13] S. Vajda, R. Jimenez, S. J. Rosenthal, V. Fidlert, G. R. Fleming, E. W. Castner Jr, Femtosecond to Nanosecond Solvation Dynamics in Pure Water and Inside the γ -Cyclodextrin Cavity, *J. Chem. Soc. Faraday Trans.* 91 (1995) 867.
- [14] V. I. Danilov, A. V. Shestopalova, Hydrophobic Effect in Biological Associates: A Monte Carlo Simulation of Caffeine Molecules Stacking, *Int. J. Quantum Chem.* 35 (1989) 103.
- [15] M. Falk, W. Chew, J. A. Walter, W. Kwiatkowski, K. D. Barclay, G. A. Klassen, Molecular Modelling and NMR Studies of the Caffeine Dimer, *Can. J. Chem.* 76 (1998) 48.
- [16] M. D. Kalugin, A. V. Teplukhin, Study of Caffeine–DNA Interaction in Aqueous Solution by Parallel Monte Carlo Simulation *J. Struct. Chem.* 50 (2009) 841.
- [17] E. L. S. Wong, J. J. Gooding, The Electrochemical Monitoring of the Perturbation of Charge Transfer through DNA by Cisplatin, *J. Am. Chem. Soc.* 129 (2007) 8950.
- [18] D. Řeha, M. Kabelá, F. Ryjáek, J. Šponer, J. E. Šponer, M. Elstner, S. Suhai, P. Hobza, Intercalators. 1. Nature of Stacking Interactions between Intercalators (Ethidium, Daunomycin, Ellipticine, and 4',6-Diaminide-2-phenylindole) and DNA Base Pairs. Ab Initio Quantum Chemical, Density Functional Theory, and Empirical Potential Study, *J. Am. Chem. Soc.* 124 (2002) 3366.
- [19] M. Maroncelli, J. MacInnis, G. R. Fleming, Polar Solvent Dynamics and Electron-Transfer Reactions, *Science* 243 (1989) 1674.

- [20] I. Rips, J. Jortner, Dynamic Solvent Effects on Outer-sphere Electron Transfer, *J. Chem. Phys.* 87 (1987) 2090.
- [21] J. T. Hynes, Outer-Sphere Electron-Transfer Reactions and Frequency-Dependent Friction, *J. Phys. Chem.* 90 (1986) 3701.
- [22] S. Banerjee, P. K. Verma, R. K. Mitra, G. Basu, S. K. Pal, Probing the Interior of Self-Assembled Caffeine Dimer at Various Temperatures, *J. Fluoresc.* 22 (2012) 753.
- [23] L. Carlucci, A. Gavezzotti, Molecular Recognition and Crystal Energy Landscapes: An X-ray and Computational Study of Caffeine and Other Methylxanthines, *Chem. Eur. J.* 11 (2005) 271
- [24] D. V. Jahagirdar, B. R. Arbad, A. A. Walvekar, A. G. Shankarwar, M. K. Lande, Studies in Partial Molar Volumes, Partial Molar Compressibilities and Viscosity B-Coefficients of Caffeine in Water at Four Temperatures, *J. Mol. Liq.* 85 (2000) 361.
- [25] A. A. Maevsky, B. I. Sukhorukov, IR Study of Base Stacking Interactions, *Nucl. Acids Res.* 8 (1980) 3029.
- [26] F. J. Millero, A. L. Surdo, C. Shin, The Apparent Molal Volumes and Adiabatic Compressibilities of Aqueous Amino Acids at 25 Degree C, *J. Phys. Chem.* 82 (1978) 784.
- [27] R. Benz, Some Thermodynamic Properties Of The System PuCl₃—KCl From Electromotive Force Data, *J. Phys. Chem.* 65 (1961) 81.
- [28] J. O. M. Bockris, P. P. S. Saluja, Ionic Solvation Numbers from Compressibilities and Ionic Vibration Potentials Measurements, *J. Phys. Chem.* 76 (1972) 2140.
- [29] S. K. Pal, D. Sukul, D. Mandal, S. Sen, K. Bhattacharyya, Solvation Dynamics of DCM in Micelles, *Chem. Phys. Lett.* 327 (2000) 91.
- [30] R. Sarkar, A. K. Shaw, M. Ghosh, S. K. Pal, Ultrafast Photoinduced Deligation and Ligation Dynamics: DCM in Micelle and Micelle-Enzyme Complex, *J. Photochem. Photobiol. B* 83 (2006) 213.
- [31] S. K. Pal, D. Mandal, D. Sukul, K. Bhattacharyya, Solvation Dynamics of 4-(dicyanomethylene)-2-methyl-6-(p-dimethylaminostyryl)-4H-pyran (DCM) in a Microemulsion, *Chem. Phys. Lett.* 312 (1999) 178.
- [32] M. Wu, W. Gu, W. Li, X. Zhu, F. Wang, S. Zhao, Preparation and Characterization of Ultrafine Zinc Sulfide Particles of Quantum Confinement, *Chem. Phys. Lett.* 224 (1994) 557.

- [33] P. V. D. Meulen, H. Zhang, A. M. Jonkman, M. Glasbeek, Subpicosecond Solvation Relaxation of 4-(Dicyanomethylene)-2-methyl-6-(p-(dimethylamino)styryl)-4H-pyran in Polar Liquids, *J. Phys. Chem.* 100 (1996) 5367.
- [34] J. M. Drake, M. L. Lesiecki, D. M. Camaioni, Photophysics and Cis-Trans Isomerization of DCM, *Chem. Phys. Lett.* 113 (1985) 530.
- [35] H. Zhang, A. M. Jonkman, P. V. D. Meulen, M. Glasbeek, Femtosecond Studies of Charge Separation in Photo-excited DCM in Liquid Solution, *Chem. Phys. Lett.* 224 (1994) 551.
- [36] D. C. Easter, A. P. Baronavski, Ultrafast Relaxation in the Fluorescent State of the Laser Dye DCM, *Chem. Phys. Lett.* 201 (1993) 153.
- [37] L. A. Philips, S. P. Webb, J. H. Clark, High-Pressure Studies of Rotational Reorientation Dynamics: The Role of Dielectric Friction, *J. Chem. Phys.* 83 (1985) 5810.
- [38] B. Kalman, N. Clarke, L. B. A. Johansson, Dynamics of a New Fluorescent Probe, 2,5,8,11-tetra-tert-butylperylene in Solution, Cubic Lyotropic Liquid Crystals, and Model Membranes, *J. Phys. Chem.* 93 (1989) 4608.
- [39] R. Zana, Microviscosity of Aqueous Surfactant Micelles: Effect of Various Parameters, *J. Phys. Chem. B* 103 (1999) 9117.
- [40] R. S. Fee, M. Maroncelli, Estimating the Time-Zero Spectrum in Time-Resolved Emission Measurements of Solvation Dynamics, *Chem. Phys.* 183 (1994) 235.
- [41] R. Jimenez, G. R. Fleming, P. V. Kumar, M. Maroncelli, Femtosecond Solvation Dynamics of Water, *Nature* 369 (1994) 471
- [42] R. E. Riter, D. W. Willard, N. E. Levinger, Water Immobilization at Surfactant Interfaces in Reverse Micelles, *J. Phys. Chem. B* 102 (1998) 2705.
- [43] E. M. Corbeil, N. E. Levinger, Dynamics of Polar Solvation in Quaternary Microemulsions, *Langmuir* 19 (2003) 7264.
- [44] D. Zhong, S. K. Pal, A. H. Zewail, Femtosecond Studies of Protein -DNA Binding and Dynamics: Histone I, *ChemPhysChem* 2 (2001) 219
- [45] K. Hirose, A Practical Guide for the Determination of Binding Constants, *J. Incl. Phenom. Macrocycl. Chem.* 39 (2001) 193.
- [46] A. Datta, D. Mandal, S. K. Pal, S. Das, K. Bhattacharyya, Interaction of Triton X-100 with Cyclodextrins. A Fluorescence Study, *J. Chem. Soc., Faraday Trans.* 94 (1998) 3471.

- [47] T. L. Chang, H. C. Cheung, A Model for Molecules with Twisted Intramolecular Charge Transfer Characteristics: Solvent Polarity Effect on the Nonradiative Rates of Dyes in a Series of Water-Ethanol Mixed Solvents, *Chem. Phys. Lett.* 173 (1990) 343.
- [48] K. Bhattacharyya, M. Chowdhury, Environmental and Magnetic Field Effects on Exciplex and Twisted Charge Transfer Emission, *Chem. Rev.* 93 (1993) 507.
- [49] N. Sarkar, K. Das, D. Nath, K. Bhattacharyya, Interaction of Urea with Fluorophores Bound to Cyclodextrins. Fluorescence of p-Toluidino Naphthalene Sulphonate, *Chem. Phys. Lett.* 196 (1992) 491.
- [50] A. Nakamura, K. Saitoh, F. Toda, Fluctuation in Structure of Inclusion Complexes of Cyclodextrins with Fluorescent Probes, *Chem. Phys. Lett.* 187 (1991) 110.
- [51] N. Sarkar, K. Das, D. Nath, K. Bhattacharyya, Salt Effect on the Hydrophobic Binding of p-Toluidino Naphthalene Sulphonate with Cyclodextrins, *Chem. Phys. Lett.* 218 (1994) 492.
- [52] M. Almgren, F. Grieser, J. K. Thomas, Dynamic and Static Aspects of Solubilization of Neutral Arenes in Ionic Micellar Solutions, *J. Am. Chem. Soc.* 101 (1979) 279.
- [53] D. J. Jobe, R. E. Verrall, R. Palepu, V. C. Reinsborough, Fluorescence and Conductometric Studies of Potassium 2-(p-Toluidinyl)naphthalene-6-sulfonate/Cyclodextrin/Surfactant Systems, *J. Phys. Chem.* 92 (1988) 3582.
- [54] G. C. Catena, F. V. Bright, Thermodynamic Study on the Effects of beta-Cyclodextrin Inclusion with Anilinonaphthalenesulfonates, *Anal. Chem.* 61 (1989) 905.
- [55] P. Sen, S. Mukherjee, A. Halder, K. Bhattacharyya, Temperature Dependence of Solvation Dynamics in a Micelle. 4-Aminophthalimide in Triton X-100, *Chem. Phys. Lett.* 385 (2004) 357.

Chapter 5

Interaction of Caffeine with a Model Fluorogenic Potent Mutagen Embedded in Various Biomimetic Self-Assemblies in Aqueous Medium:

5.1. Introduction:

The molecular recognition of DNA by small ligands/drugs in presence of caffeine, a xanthine alkaloid, in aqueous solution is well known [1-3]. Earlier it is shown that the intercalation of novantrone, ellipticine, doxorubicin and ethidium bromide to DNA is significantly perturbed in presence of caffeine [2, 4-5]. Other studies also reveal similar observations [6-8]. A detail spectroscopic investigation from our laboratory [9] demonstrates the efficacy of caffeine in the removal of Et from synthetic self-complimentary oligonucleotides and from different cell lines. The significant alteration of molecular recognition of DNA in caffeine solution has been concluded to depend on the 'protector' and 'interceptor' properties of caffeine [4-5, 10]. In the 'protector' mode of activity, there is a strong competition between caffeine and aromatic drug for the binding sites on DNA whereas in the 'interceptor' mode of its activity, caffeine forms hetero-complexes with a number of aromatic DNA intercalators, which account for the observed changes of biological activity of these drugs in the presence of caffeine. Sometimes, explanation of specific role of caffeine in the molecular recognition of DNA in physiological milieu becomes cumbersome [10]. In this regard small biomimetic systems including nanoscopic micelles [11] could serve as an efficient mimic for the biological membranes, macromolecules and are also useful in organizing the reactants at a molecular level [11]. For example, cationic hexadecyltrimethylammonium bromide (CTAB) micelle may act as a good mimic of histone protein [12], neutral (polar) Triton X-100 (TX-100) micelle may mimic a protein cavity [13] and anionic sodium dodecyl sulfate (SDS) micelle can serve as a good alternative of the DNA surface [14-15]. Till date, however, no attempt has been made to use nanoscopic micelle for the better understanding of caffeine mediated

molecular recognition of DNA by small ligands/ drugs and is the motive of our present study.

In the present study we have used ethidium (Et) bromide salt as model ligand probe, which is a well known DNA intercalator [16-17] and a potential mutagen [18]. The micelles used in our study are cationic CTAB, neutral (polar) TX-100 and anionic SDS with distinct hydrodynamic diameter as measured by dynamic light scattering (DLS) experiment. The probe Et shows distinct spectroscopic signature, particularly excited state lifetime in various biologically relevant environments. We have used steady state and picosecond resolved fluorescence spectroscopy in order to investigate the detachment of Et from various self-organized micelles. In the case of DNA mimicking SDS micelles we have used another probe Hoechst 33258 (H258) as energy donor to Et acceptor at the surface and employ FRET (Förster resonance energy transfer) for the analysis of fluorescence quenching of the donor H258. Standard FRET analysis on the donor-acceptor (D-A) pair at the SDS micelle shows significant perturbation on the energy transfer efficiency upon addition of caffeine in the solution. Further analysis of the experimental results employing both the general and extended version of well known 'Infrared-Tachiya model' distinctly reveals change in acceptor distribution at the micellar surface in the presence of caffeine in the aqueous solution. We have used DLS in order to confirm the structural integrity of the micelles in the caffeine solution. Furthermore, we have employed fluorescence microscopy to monitor the said perturbation in FRET efficiency on squamous epithelial cell nuclei in presence of caffeine.

5.2. Results and Discussion:

5.2.1. Caffeine Mediated Detachment of Mutagenic Ethidium from Various Nanoscopic Micelle: An Ultrafast Förster Resonance Energy Transfer Study [19]:

5.2.1.1. Caffeine mediated detachment of Et from various self-organized micelles.

Figure 5.1 (a) shows the fluorescence transients of the mutagenic ethidium (Et) in various micellar systems of different charge nature in absence and presence of caffeine. Both Et and CTAB being cationic, ionic interaction between the two will not be favoured but the

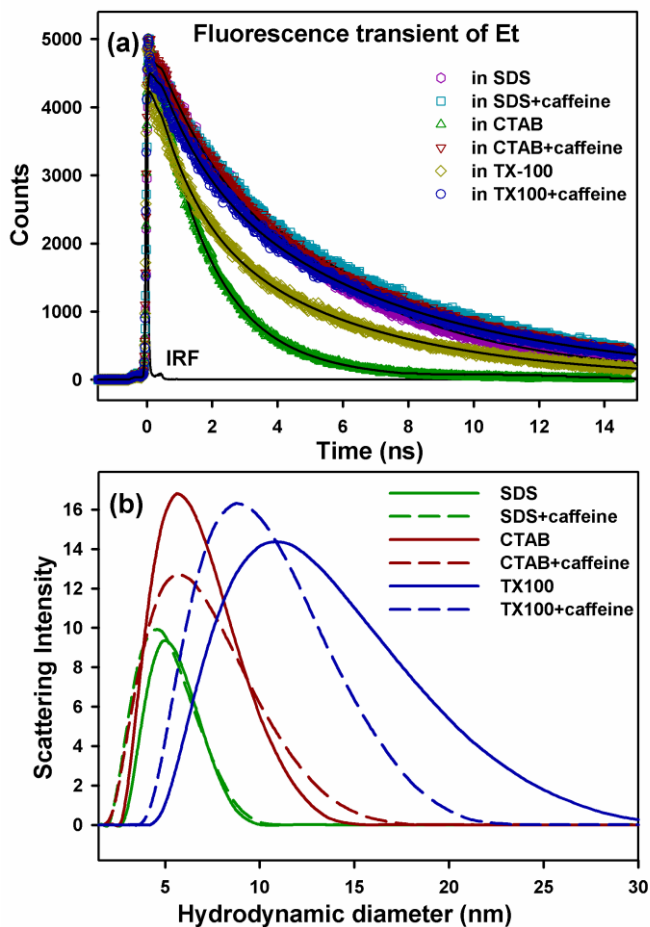


Figure 5.1. (a) Fluorescence transients of Et in SDS, CTAB and TX-100 micellar systems and (b) diameter size of those micelles, in presence and absence of caffeine.

possibility of hydrophobic interaction between them cannot be ruled out. This was the reason behind our selection of cationic CTAB and neutral (polar) TX-100 micelles. As evidenced from our lifetime results (Table 5.1), beyond the critical micelle concentration (CMC) of CTAB, Et interacts with the micelles to some extent which is only possible through its interior binding. Et in the cationic CTAB micelles reveals fluorescence lifetimes of 1.4 ns (51%) and 2.5 ns (49%). However, on addition of caffeine in the solution, the lifetime values become 1.9 ns (14%) and 7.2 ns (86%) revealing a major slower component (7.2 ns), characteristic of Et-caffeine complexation (Table 5.2). The faster component is close to the lifetime of Et in water which is ~ 1.5 ns [16]. In the case of anionic SDS micelles significant detachment of Et in the caffeine solution is also evident

Table 5.1: The fluorescence lifetime components τ_1 and τ_2 represent fluorescence lifetimes of the sample while τ_r represents rotational relaxation time constants of the same and r_0 defines anisotropy at time $t=0$. Figures in parentheses show relative contribution. Error $\pm 5\%$

Ethidium in	Fluorescence lifetime		Fluorescence anisotropy	
	τ_1 (ns)	τ_2 (ns)	τ_r (ns)	r_0
Water	1.6 (100%)		0.110	0.24
100 mM caffeine	2.3 (15%)	7.0 (85%)	0.210	0.23
0.2 mM CTAB	1.6 (100%)		0.100	0.30
0.2 mM CTAB + 100 mM caffeine	1.7 (13%)	6.9 (87%)	0.170	0.34
0.4 mM CTAB	1.6 (100%)		0.110	0.35
0.4 mM CTAB + 100 mM caffeine	1.7 (14%)	7.0 (86%)	0.180	0.34
0.6 mM CTAB	1.6 (100%)		0.110	0.32
0.6 mM CTAB + 100 mM caffeine	1.8 (15%)	6.9 (85%)	0.160	0.37
2 mM CTAB	1.1 (34%)	1.9 (66%)	0.100	0.32
2 mM CTAB + 100 mM caffeine	1.8 (14%)	6.9 (86%)	0.170	0.38
20 mM CTAB	1.2 (45%)	2.1 (55%)	0.110	0.32
20 mM CTAB + 100 mM caffeine	1.8 (14%)	6.9 (86%)	0.180	0.35
40 mM CTAB	1.2 (40%)	2.0 (60%)	0.120	0.29
40 mM CTAB + 100 mM caffeine	1.7 (14%)	6.9 (86%)	0.190	0.33
80 mM CTAB	1.4 (68%)	2.7 (32%)	0.120	0.33
80 mM CTAB + 100 mM caffeine	1.7 (14%)	6.9 (86%)	0.190	0.32

(Figure 5.1 (a) and Table 5.2). Our SDS concentration dependent absorption studies along with the time resolved fluorescence and anisotropy measurements on Et both in absence and presence of caffeine (Figure 5.2 and Table 5.3) is in good agreement with the model

Table 5.2: The lifetime components of ethidium (Et) in aqueous solvent and in micellar compartments with and without caffeine: τ represents the time constant in ns and the figures in the parenthesis represent relative contribution of the component. Surfactant as well as caffeine concentrations maintained at 100 mM. Error $\pm 5\%$

Sample	τ_1 (ns)	τ_2 (ns)
Et in water	1.6 (100%)	
Et in aqueous caffeine solution	7.0 (84.5%)	2.3 (15.5%)
Et in CTAB	1.4 (51%)	2.46 (49%)
Et in CTAB + caffeine	1.9 (14%)	7.2 (86%)
Et in SDS	1.46 (5%)	5.15 (95%)
Et in SDS + caffeine	2.06 (12%)	7.25 (88%)
Et in TX-100	1.21 (16%)	5.37 (84%)
Et in TX-100 + caffeine	1.45 (10%)	6.77 (90%)

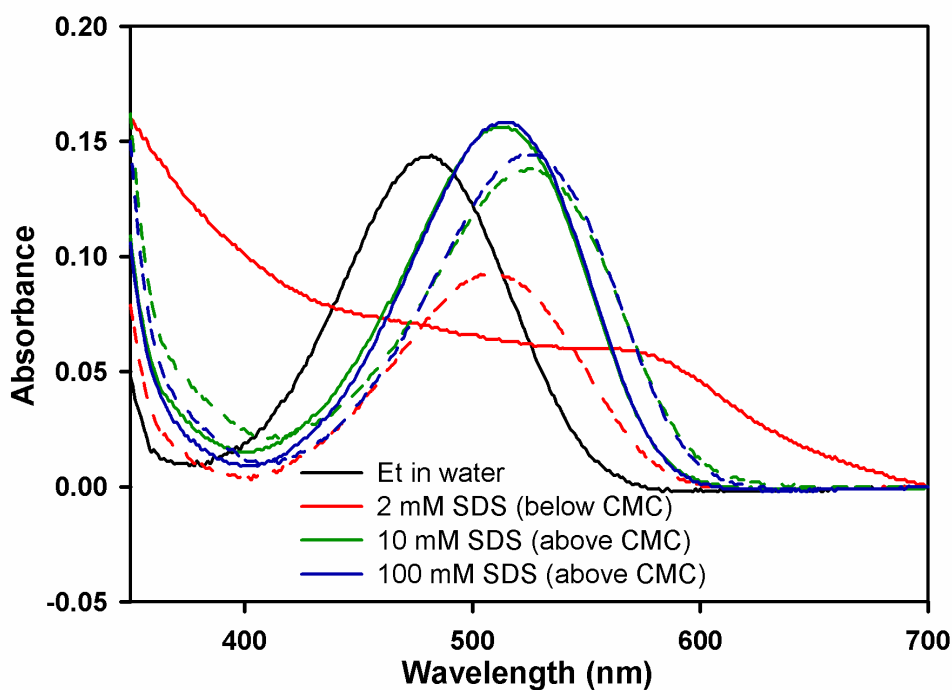


Figure 5.2. Absorption of ethidium (Et) at different concentrations of SDS with (broken line) and without (bold line) caffeine.

where Et attaches to SDS micelles with its positively charged moiety towards the negatively charged head group of the SDS micelles and hydrophobic part inside the micelles. From the difference in optical density (O.D) value of Et in SDS micelles in absence and presence of caffeine we calculated the amount of Et released from the micelles by caffeine taking the molar extinction coefficient of Et in SDS micelles as $4120 \text{ M}^{-1} \text{ cm}^{-1}$ at 476 nm. It has been found that from 25 μM micelle-bound EtBr, 18.5 μM of Et gets

released from the micelles by caffeine while 6.5 μM Et still remains attached to the micelles. As evidenced from the UV-vis absorption spectra along with the fluorescence lifetime and anisotropy measurements of Et at different concentrations of neutral (polar) surfactant TX-100 (Figure 5.3 and Table 5.4), Et neither binds to TX-100 monomers nor to TX-100 micelles at lower concentrations (8.2×10^{-3} mM micellar concentration). However, at high micellar concentration (1mM), we observe bathochromic shift in the absorption peak of Et compared to that in water which reflects association of Et with TX-100 micelles positioning the quarternary Nitrogen of Et towards the hydrophilic head group of the micelles i.e towards the ethylene oxide part and hydrophobic part being buried inside. The proposed model corroborates with the fluorescence anisotropy results (Table 5.4) where we find longer rotational time constant of Et at 100 mM TX-100 concentration. However, detail analysis of the absorption and time resolved spectroscopy results show that caffeine

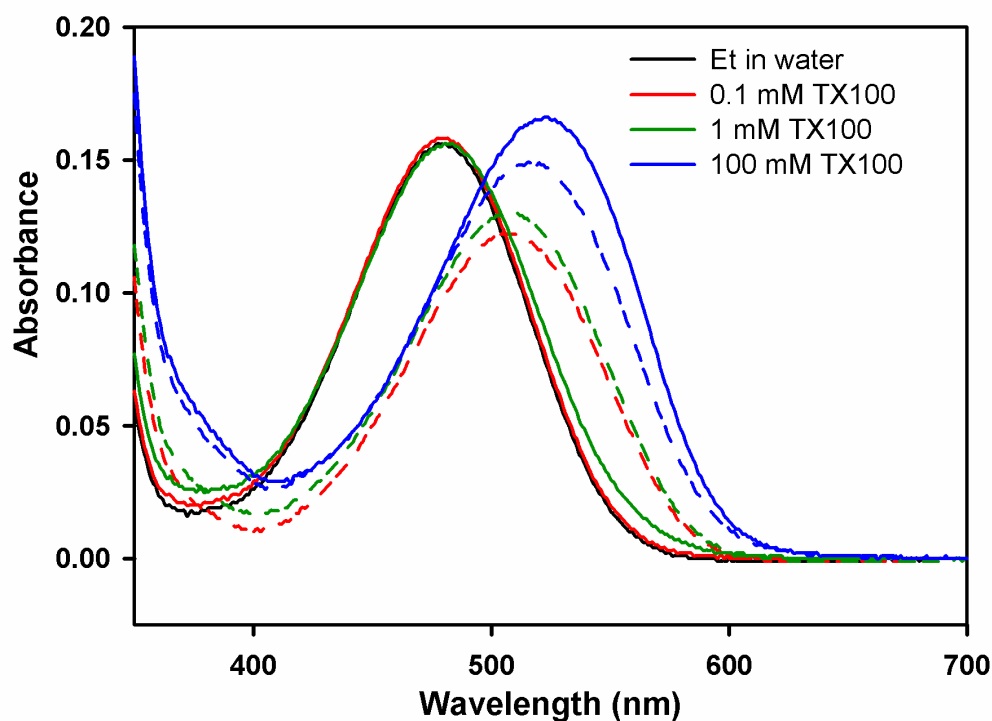


Figure 5.3. Absorption of ethidium (Et) at different concentrations of TX-100 with (broken line) and without (bold line) caffeine.

Table 5.3: The fluorescence lifetime components τ_1 and τ_2 represent fluorescence lifetimes of the sample while τ_{r1} and τ_{r2} represent rotational relaxation time constants of the same and r_0 defines anisotropy at time $t=0$. Figures in parentheses show relative contribution. Error $\pm 5\%$

Ethidium in	Fluorescence lifetime		Fluorescence anisotropy		
	τ_1 (ns)	τ_2 (ns)	τ_{r1} (ns)	τ_{r2}	r_0
Water	1.6 (100%)		0.110		0.24
100 mM caffeine	2.3 (15%)	7.0 (85%)	0.210		0.23
2 mM SDS	1.6 (89%)	0.08(11%)	0.070 (100%)		0.38
2 mM SDS + 100 mM caffeine	1.7 (11%)	6.6 (89%)	0.180 (100%)		0.31
4 mM SDS	1.8 (83%)	0.13 (17%)	0.09 (100%)		0.37
4 mM SDS + 100 mM caffeine	1.8 (13%)	6.8 (87%)	0.18 (100%)		0.29
6 mM SDS	2.4 (87%)	0.64 (13%)	0.28 (100%)		0.23
6 mM SDS + 100 mM caffeine	1.2 (6%)	6.1 (94%)	0.18 (100%)		0.29
10 mM SDS	1.1 (5%)	4.7 (95%)	1.0 (57%)	0.09 (43%)	0.27
10 mM SDS + 100 mM caffeine	1.3 (6%)	6.4 (94%)	1.6 (47%)	0.19 (53%)	0.25
20 mM SDS	1.4 (9%)	4.7 (91%)	3.4 (34%)	0.39 (66%)	0.24
20 mM SDS + 100 mM caffeine	1.5 (8%)	6.4 (92%)	1.3 (46%)	0.08 (54%)	0.32
40 mM SDS	1.4 (10%)	4.8 (90%)	2.3 (40%)	0.36 (60%)	0.19
40 mM SDS + 100 mM caffeine	1.7 (10%)	6.5 (90%)	2.1 (46%)	0.22(54%)	0.29
80 mM SDS	1.4 (9%)	4.8 (91%)	2.2 (42%)	0.38 (58%)	0.27
80 mM SDS + 100 mM caffeine	1.6 (10%)	6.3 (90%)	2.9 (37%)	0.39 (63%)	0.33
100 mM SDS	1.4 (9%)	4.8 (91%)	1.9 (44%)	0.23 (56%)	0.22
100 mM SDS + 100 mM caffeine	1.5 (9%)	6.2 (91%)	2.9 (43%)	0.35 (57%)	0.32

fails to detach Et from TX 100 micelles unlike SDS and CTAB micelles. Our DLS studies on differently charged micellar systems (Figure 5.1 (b)) show the structural integrity of the micelles both in absence and presence of caffeine. Since the hydrodynamic radii of the micelles remain similar even after the addition of caffeine, it can be concluded that caffeine molecules are not associated with the micelles. In order to show the detachment of Et at the molecular level from the anionic SDS micelles, which is considered to be mimic of the DNA surface [14], we have employed Förster resonance energy transfer (FRET) from another ligand H258 on the surface of the micelles to the bound Et. The FRET which is known to be molecular ruler [20] is an effective technique to find out the distance between two ligands, donor and acceptor, having overlap of the emission and absorption spectrum of the donor and acceptor respectively. Figure 5.4 shows that there is sufficient spectral overlap between the emission spectrum of the H258 and the absorption spectrum

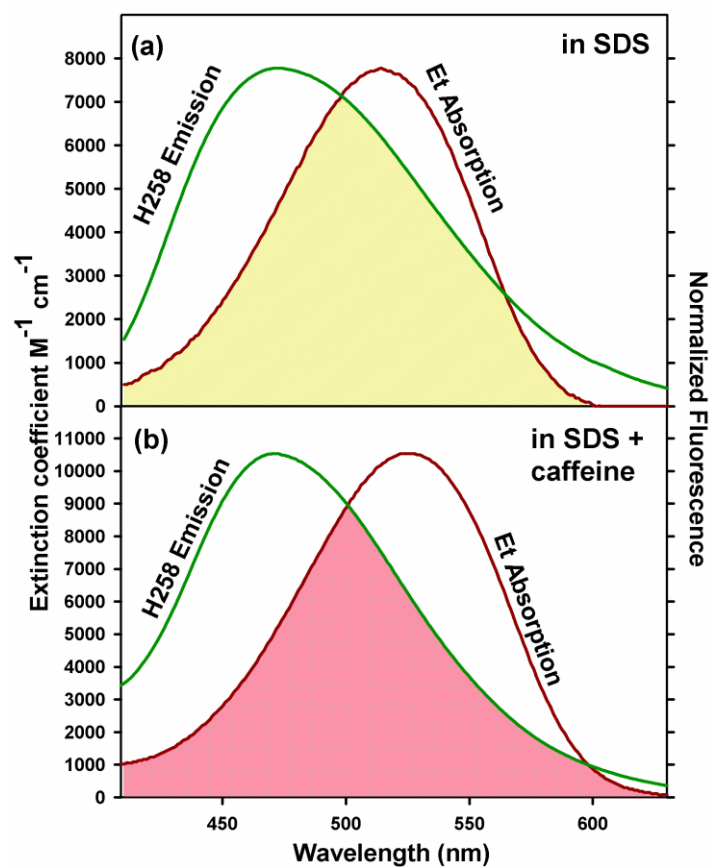


Figure 5.4. The spectral overlap of H258 emission and Et absorption in (a) 20 mM SDS in absence and (b) presence of 100 mM caffeine.

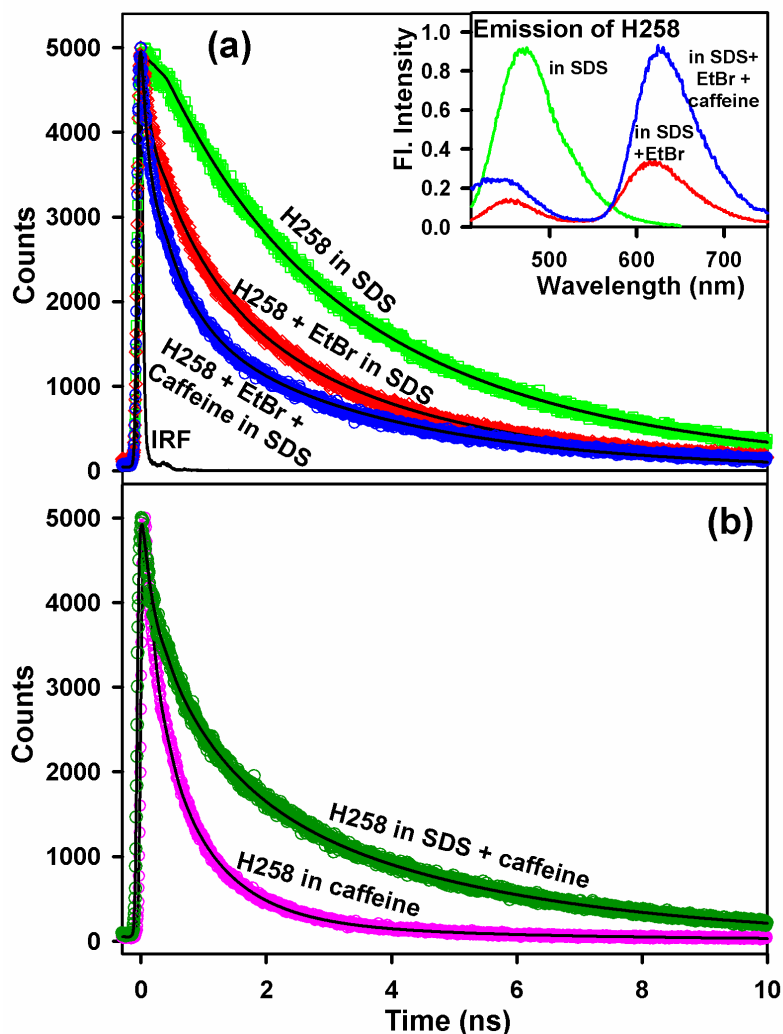


Figure 5.5. The temporal decay of H258 (0.2 μM), H258-Et ($[\text{Et}] = 155 \mu\text{M}$) and H258-Et-caffeine ($[\text{caffeine}] = 100 \text{ mM}$) in (a) 20 mM SDS and that of H258-caffeine in (b) SDS and water. The emission spectra of H258, H258-Et and H258-Et-caffeine in (inset (a)) SDS. All the samples are excited at $\lambda_{\text{ex}} = 375 \text{ nm}$ and fluorescence transients monitored at $\lambda_{\text{em}} = 470 \text{ nm}$.

of the Et in SDS micelles both in absence and presence of caffeine. As shown in the Figure, $J(\lambda)$, the overlap integral, which expresses the degree of spectral overlap between the donor emission and the acceptor absorption changes in presence of caffeine.

The minor groove binder H258 shows single exponential fluorescence decay of 3.38 ns in SDS micelles (Figure 5.5 (a), Table 5.5). Previous work from our group [15] finds the location of H258 on the surface of SDS micelles and not in the interior of it based on steady state emission and time resolved anisotropy studies of the probe in the micellar

environment. Presence of Et (acceptor) in the solution makes the decay faster (867 ps (17%) and 98 ps (2%)) (Table 5.5), revealing simultaneous binding of H258 and Et in the micellar surface with average distance of 2.16 nm, consistent with earlier studies [17]. The

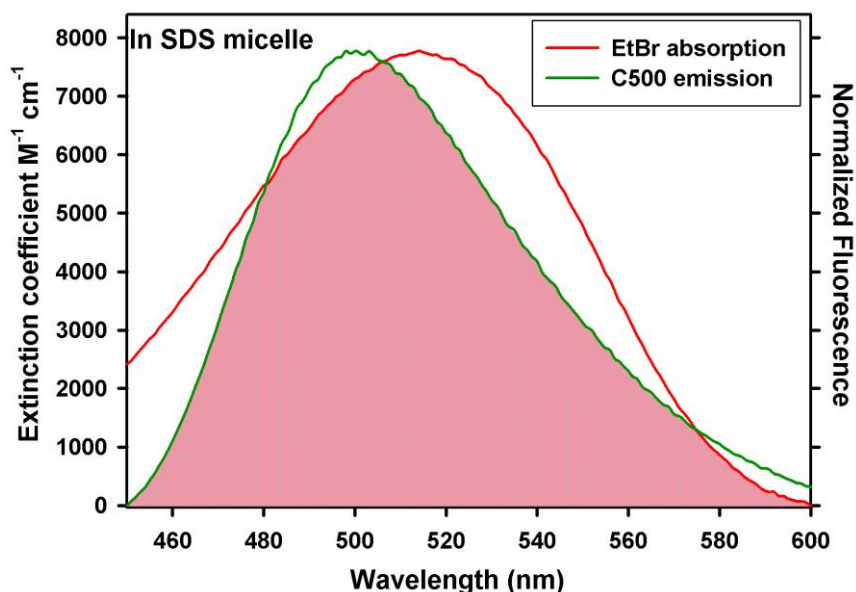


Figure 5.6. The spectral overlap of C500 emission and Et absorption in (a) 20 mM SDS (at 70°C).

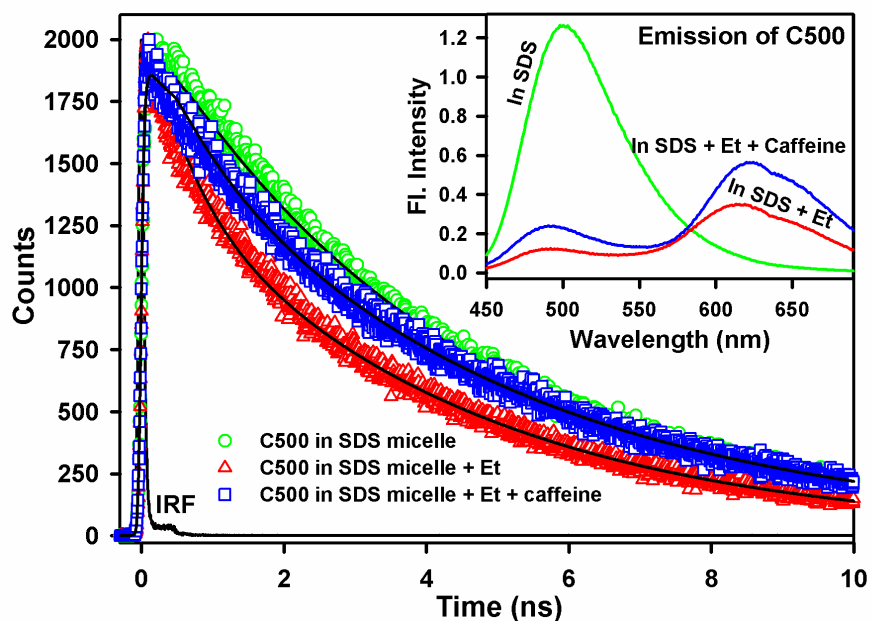


Figure 5.7. The temporal decay of C500 in SDS micelles at 70°C in presence and absence of acceptor Et ($[Et] = 155 \mu\text{M}$) and caffeine ($[\text{caffeine}] = 100 \text{ mM}$) in 20 mM SDS. The corresponding emission spectra are given in inset.

fast time component τ_3 listed in Table 5.5 is around IRF however, within the resolution of our TCSPC setup. The binding of Et on the surface of SDS micelles is also reasonable from the time resolved studies reported earlier [21] where the fluorescence lifetime and relative quantum yield of Et, bound to SDS, are shown to be intermediate between those in water and in alcohol reflecting that Et binds to the surface of anionic SDS micelles due to its inherent positive charge. Upon addition of caffeine in solution the fluorescence decay becomes faster apparently revealing closer association of H258 and Et (1.94 nm). Relative enhancement of the Et emission (steady state) in H258 coated SDS micelles in presence of caffeine (inset Figure 5.5 (a)) is also in the favour of the above conclusion. However, upon the addition of caffeine, FRET between H258 and Et is interrupted as Et is released from

Table 5.4: The fluorescence lifetime components τ_1 and τ_2 represent fluorescence lifetimes of the sample while τ_{r1} and τ_{r2} represent rotational relaxation time constants of the same and r_0 defines anisotropy at time $t=0$. Numbers in parentheses show relative contribution. Error $\pm 5\%$

Ethidium in	Fluorescence lifetime		Fluorescence anisotropy		
	τ_1 (ns)	τ_2 (ns)	τ_{r1} (ns)	τ_{r2} (ns)	r_0
Water	1.6 (100%)		0.110		0.24
100 mM caffeine	2.3 (15%)	7.0 (85%)	0.210		0.23
0.1 mM TX-100	1.6 (100%)		0.108		0.35
0.1 mM TX-100 + 100 mM caffeine	2.0 (16%)	7.0 (84%)	0.175		0.36
1 mM TX-100	1.6 (100%)		0.103		0.33
1 mM TX-100 + 100 mM caffeine	1.9 (15%)	6.9 (85%)	0.196		0.30
100 mM TX-100	1.1 (16%)	4.5 (84%)	0.053 (81%)	1.51 (19%)	0.38
100 mM TX-100 + 100 mM caffeine	1.6 (15%)	6.5 (85%)	0.08 (80%)	1.17 (20%)	0.37

the micelles in presence of caffeine and such interruption results in the increase in the fluorescence intensity of H258 band. As shown in Figure 5.5 (b) and Table 5.5, fluorescence decay of H258 in the micelles becomes faster upon addition of caffeine as a consequence of partial detachment of H258 from the micellar surface. Thus, the fate of the H258-Et complex upon addition of caffeine is found to be inconclusive from the standard

FRET analysis. We have repeated our experiment with another donor coumarin 500 (C500) which does not interact with caffeine at high temperature ($\sim 70^\circ\text{C}$) as has been reported by our earlier studies [22], however, both caffeine dimer as well as caffeine-Et complex has been reported by us to be stable even at high temperatures at around 70°C [9]. Hence, we repeated the experiments with the donor coumarin 500 (C500) at 70°C (Figure 5.6 and 5.7, Table 5.6) and found that in absence of caffeine 33% donor molecules participate in FRET with 87% energy transfer efficiency (E) whereas in presence of caffeine only 19% donor molecules participate in FRET with E as 80% which is due to the caffeine mediated release of acceptor Et molecules from the SDS micelles. The donor-acceptor distance (r) also increases from 2.89 nm to 3.16 nm in presence of caffeine.

Table 5.5: The lifetime components of H258 in various environments: τ represents the time constant in ns and the numbers in the parenthesis represent relative contribution of the component. [H258] = 0.2 μM , [SDS] = 20 mM, [Et] = 155 μM and [caffeine] = 100 mM. Error $\pm 5\%$

Sample	τ_1 (ns)	τ_2 (ns)	τ_3 (ns)
H258 in SDS	3.38 (100%)		
H258 in SDS + Et	3.38 (81%)	0.87 (17%)	0.1 (2%)
H258 in SDS + Et + caffeine	3.38 (80%)	0.55 (17%)	0.08 (3%)
H258 in SDS + caffeine	3.38 (91%)	0.36 (9%)	
H258 in water	3.82 (95%)	0.14 (5%)	
H258 in water + Et	3.82 (69%)	0.49 (21%)	0.09 (10%)
H258 in water + Et + caffeine	3.82 (34%)	0.14 (13%)	0.78 (53%)
H258 in water + caffeine	3.82 (31%)	0.81 (55%)	0.16 (14%)

Table 5.6: The lifetime components of C500 at 70°C in various environments: τ represent the time constants in ns and the numbers in the parenthesis represent relative contribution of the components. Error $\pm 5\%$

Sample	τ_1 (ns)	τ_2 (ns)
C500 in SDS	4.33 (100%)	
C500 in SDS + Et	4.33 (67%)	0.56 (33%)
C500 in SDS + Et + caffeine	4.33 (81%)	0.84 (19%)
C500 in SDS + caffeine	4.33 (100%)	
C500 in water	3.34 (100%)	

5.2.1.2. Application of kinetic models in the investigation of caffeine mediated dissociation of Et from SDS micelles. For better understanding of the fate of the association between H258 and Et in presence of caffeine, it is essential to know the distribution of Et molecules around the micelles before and after the addition of caffeine, because this is a governing factor for efficient energy transfer. In this regard, we applied the kinetic model developed by Infelta and Tachiya as mentioned in chapter 2 section 2.1.5. In one of our systems, along with the Et quencher molecules, there exist some caffeine molecules that also causes quenching of the lifetime of the excited probe (H258) due to its partial release from the micelle and these are also taken into account. If the distribution of the number of caffeine mediated detached donor molecules from the micellar surface follows Poisson distribution with the average number (m_c), the decay curve of the excited state of H258 in micelle in presence of caffeine without and with the Et molecules are described by [23],

$$P^*(t) = P^*(0) \exp \{-k_0 t - m_c [1 - \exp(-k_{qc} t)]\} \quad (5-1)$$

$$P^*(t) = P^*(0) \exp \{-k_0 t - m_c [1 - \exp(-k_{qc} t)] - m [1 - \exp(-k_q t)]\} \quad (5-2)$$

where the quenching rate constant (k_{qc}) by caffeine molecules may be different from that (k_q) by Et molecules. We have determined the values of the parameters m_c , k_{qc} , k_0 , m , and k_q by fitting the equations (2-54), (5-1) and (5-2) to the decay curves in the absence and presence Et and caffeine molecules (Figure 5.8 and Table 5.7). We have also employed extended Infelta-Tachiya kinetic model as described in chapter 2 under section 2.1.5. The quenching parameters k_0 , m , and k_q derived from the extended Infelta-Tachiya model (Figure 5.8 inset and Table 5.8) found to be comparable with those derived from the generalized version of Infelta-Tachiya model.

Figure 5.8 shows the time resolved fluorescence transients of H258 in absence and presence of caffeine and Et molecules, fitted with equations (2-54), (5-1) and (5-2) whereas Figure 5.8 inset shows the same fitted with equation (2-57). As evident from the figure, the models describe the decay curves reasonably well. The quenching parameters are summarized in Table 5.7 and Table 5.8. Upon fitting the decay curves of H258 with the kinetic models mentioned before, it is clear that the distribution of Et molecules on the micellar surface changes significantly after the addition of caffeine. As summarized in Table 5.7 and Table 5.8, the mean number of Et molecules associated with the micelle (m)

reduces after the addition of caffeine. Thus caffeine shows efficiency in the detachment of Et from the micellar surface. The quenching rate constant (k_q) due to the acceptor (Et) molecules increases in presence of caffeine revealing closer association between the remaining Et and H258 molecules on the micellar surface which is consistent with the results obtained from FRET study and steady state emission spectroscopy as mentioned before. However, standard FRET analysis failed to monitor the detachment of the bound Et molecules from the micellar surface in presence of caffeine quantitatively. We have also employed Infelta-Tachiya model on our FRET study using C500 as the donor which does not interact with caffeine molecules at the experimental conditions [22](Figure 5.9 and Table 5.9). The results clearly show decrease in the mean number of Et molecules associated with the micelle upon addition of caffeine due to the caffeine mediated release of Et from the SDS micelle. Furthermore, we determine the equilibrium constant for solubilization of Et in SDS micelles before and after the addition of caffeine. The total concentrations $[M]$ and $[Q]$ of micelles and Et introduced in solution are related through the following equation,

$$m[M] + [A] = [Q] \quad (5-3)$$

$$m = k_+[A]/k_- \quad (5-4)$$

where $[A]$ is the concentration of Et in the aqueous phase. Elimination of $[A]$ from equation (5-3) and (5-4) yields,

$$K = k_+/k_- = m/([Q] - m[M]) \quad (5-5)$$

where K is the equilibrium constant (k_+/k_-) for the solubilization of Et in micelles and calculated to be 2.3×10^4 and $3.3 \times 10^3 \text{ M}^{-1}$ in absence and presence of caffeine respectively. K has been calculated for different concentrations of Et in absence of caffeine and has been found to be similar. The significant decrease in the value of equilibrium constant (K) for solubilization of Et in micelles upon addition of caffeine confirms the efficacy of caffeine molecules in the detachment of Et from the biomimetic systems like micelles.

Table 5.7: Values of the quenching parameters using the simplified version of the kinetic model developed by Infelta-Tachiya

System	k_0 (ns ⁻¹)	m	k_q (ns ⁻¹)	m_c	k_{qc} (ns ⁻¹)
Micelle bound H258	0.31	-	-	-	-
Micelle bound H258 + Et	0.31	0.66	1.08	-	-
Micelle bound H258 + Et + caffeine	0.31	0.31	5.34	0.89	1.11

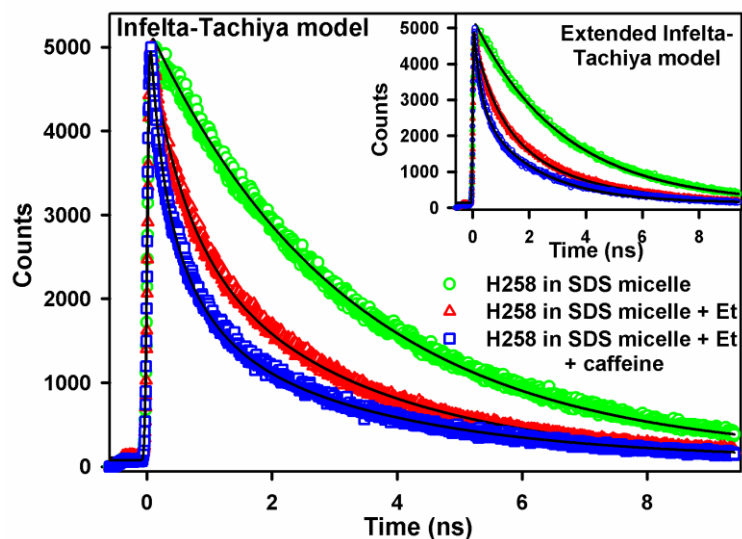


Figure 5.8. Time resolved fluorescence decay curves of H258 in SDS micelles in absence and presence of caffeine and Et. The bold lines represent the fitting of the curves by the generalized version as well as the extended version (inset) of the kinetic models developed by Infelta and Tachiya (see text).

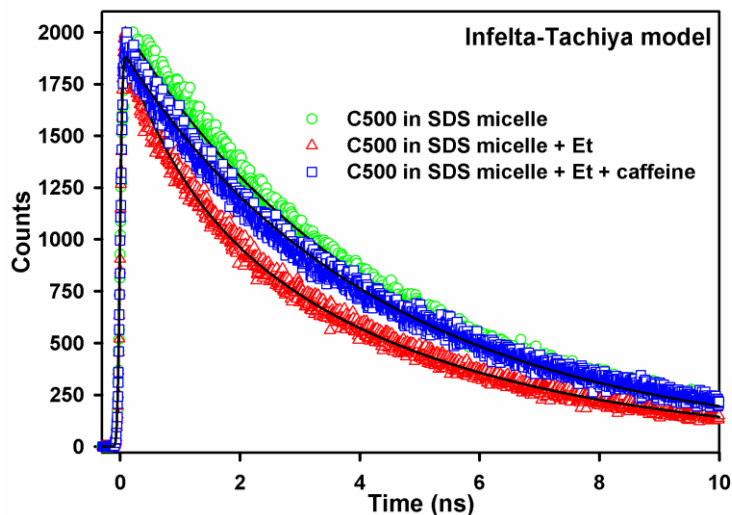


Figure 5.9. Time resolved fluorescence decay curves of C500 in SDS micelles in absence and presence of caffeine and Et. The bold lines represent the fitting of the curves by the generalised version of the kinetic models developed by Infelta and Tachiya.

Table 5.8: Values of the quenching parameters using the extended version of the kinetic model developed by Infelta-Tachiya

System	k_0 (ns ⁻¹)	k (ns ⁻¹)	m	k_q (ns ⁻¹)
Micelle bound H258	0.31	-	-	-
Micelle bound H258 + Et	0.31	-	0.82	0.57
Micelle bound H258 + Et + caffeine	0.31	0.17	0.69	2.92

Table 5.9: Values of the quenching parameters using the simplified version of the kinetic model developed by Infelta-Tachiya: Error $\pm 5\%$

System	k_0	m	k_q
Micelle bound C500	0.23		
Micelle bound C500 + Et	0.23	0.35	0.70
Micelle bound C500 + Et + caffeine	0.23	0.02	0.70

5.2.1.3. Interruption in FRET due to caffeine mediated expulsion of Et from epithelial cells: A fluorescence microscopic view.

Significant perturbation of FRET efficiency from the donor H258 to the acceptor Et has been revealed even from our cellular studies. Figure 5.10 shows the fluorescence micrographs of the squamous epithelial cells stained with both the donor (H258) and the acceptor (Et) fluorophores. The donor emits in the blue region of the visible spectrum (Figure 5.4) whereas the acceptor emits in the red region of the same. H258 and Et, being well known DNA minor groove binder [24] and DNA intercalator [16-17] respectively, and both being cell permeable [9, 25], stain the nuclei of the cells. Upon specifically exciting the donor dye molecules under UV light at 360 nm we observe only the red (acceptor) emission from the nuclei of the cells, which emphasizes the FRET from the donor to the acceptor. However, as shown in Figure 5.10, upon the addition of caffeine (+ caffeine), we find the red emission from the acceptor changes to the blue emission of the donor with time, showing significant perturbation in the FRET efficiency between the two. Photobleaching of the donor (H258) and acceptor (Et) molecules both in absence and presence of caffeine have been monitored by us in our control studies (data not shown) where we find no signature of acceptor photobleaching both in absence and presence of caffeine within the experimental time frame. Donor H258 molecules also do not undergo photobleaching in presence of caffeine but significant photobleaching of the donor molecules in absence of caffeine has been observed. It has to be noted that the emission intensity of the donor even after 800 seconds of caffeine treatment is less than that in

absence of the acceptor (image not shown) most probably due to the fraction of acceptor molecules that still remained associated with the DNA in the nuclei even after the addition of caffeine. Possibility of removal of some of the donor molecules from the nucleus cannot be ruled out. Whereas, in the control experiment, in which the cells were treated only with the phosphate buffer saline (PBS) without caffeine (- caffeine), we find no significant change in the red emission from the nuclei with time. To highlight the observed perturbation in FRET efficiency from H258 to Et in presence of caffeine in a more quantitative manner, the average intensity of the red (acceptor) and blue (donor) emission from the nuclei in each micrograph has been plotted against time for both test (+ caffeine) and control (- caffeine) experiments as shown in Figure 5.11 (a) and (b), respectively. In Figure 5.11 (a), the drop in emission intensity of the acceptor with time has been fitted biexponentially (within $\pm 10\%$ error) with the characteristic time constants of 122 and 550 seconds, which exactly coincides with that of the biexponential fit of the rise of the donor emission intensity with time within the error limit. As shown in Figure 5.11 (b), in control experiment (- caffeine) there is a slight decrease in the red emission intensity of the acceptor due to the partial detachment of Et from the cell nuclei by the PBS buffer which leads to the slight increase in the blue emission intensity of the donor. As we observe slight increase in the blue fluorescence intensity of the donor it can be concluded that the donor H258 molecules undergo photobleaching at a much slower rate compared to the buffer mediated release of non-specifically bound EtBr. The respective decay and rise of the acceptor and donor can be fitted single exponentially within the same error limit with a characteristic time component of 550 seconds, which coincides with the slower time component obtained in presence of caffeine. Thus this slower time component of 550 seconds can be assigned to the caffeine independent release of Et from the cell nuclei by the buffer itself and the faster time component (122 second) is achieved solely due to the presence of caffeine. Therefore, the caffeine-mediated release of the bound Et from cell nuclei is almost 5 times faster compared to the solvent alone. It has to be noted that the time constant for the release of Et from the nuclei of squamous epithelial cells reported here, is much slower than that proposed in our earlier work [9], which accounts for the lower caffeine concentration purposely used in our present work to vividly show the alteration of FRET.

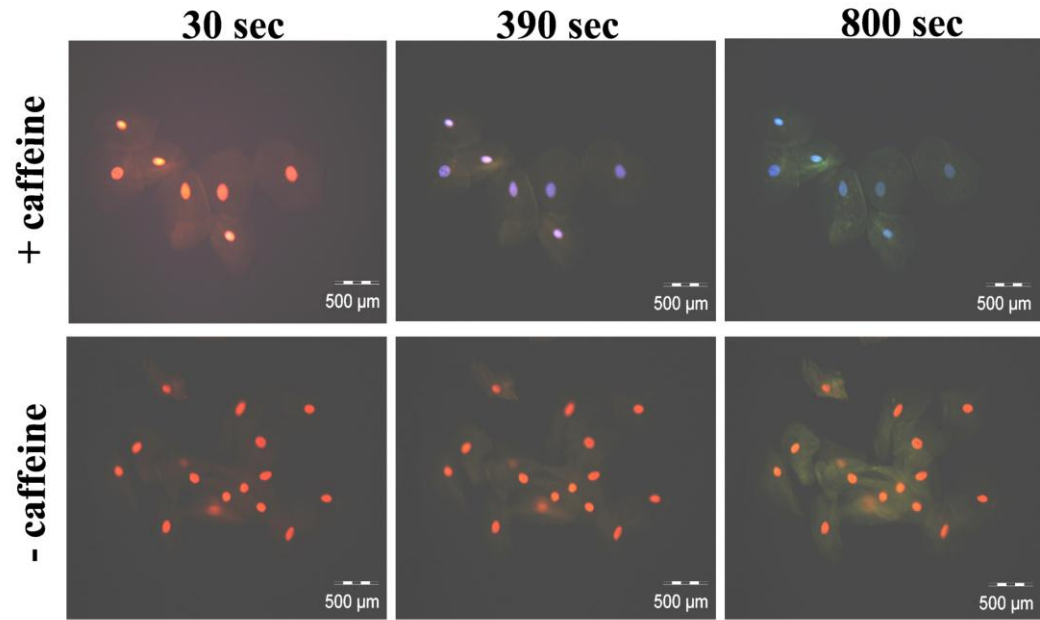


Figure 5.10. Fluorescence micrographs of squamous epithelial cells doubly stained with H258 and Et after 30, 390 and 800 seconds upon treatment with caffeine (+ caffeine) along with the control sets (- caffeine) treated with PBS without caffeine.

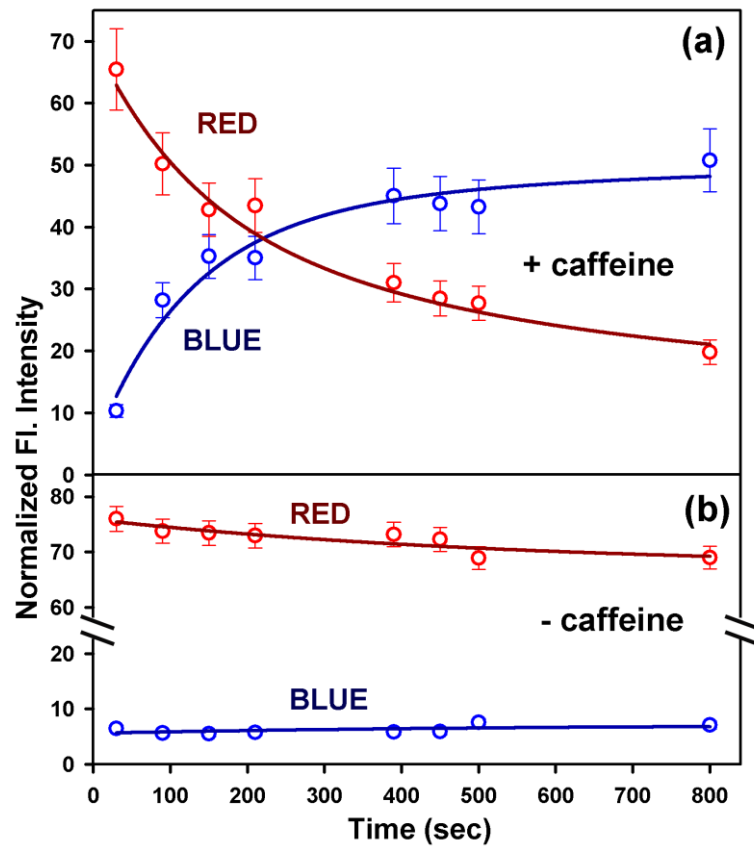


Figure 5.11. Rate of change in the intensity of red and blue emission from the doubly stained squamous epithelial cells (a) upon treatment with caffeine (+ caffeine) and (b) upon treatment with PBS without caffeine (- caffeine) taken as control.

5.3. Conclusion:

Our study finds caffeine as an efficient drug for the removal of a model DNA-intercalator Et from both negatively charged SDS and positively charged CTAB micelles without or with negligible perturbation of their structural integrity. However, caffeine fails to show such activity in case of neutral (polar) TX-100 micelles. The FRET study focuses on the efficacy of caffeine molecules in altering the association between two DNA binding ligands H258 and Et residing on a micellar surface. However, in our system, standard FRET fails to provide an explicit picture of such alteration in the association between the two DNA-binding ligands on the biomimetic system in presence of caffeine. Our analysis of the experimental results employing the well established kinetic model developed by Infelta and Tachiya, helps to recognize the efficacy of caffeine molecules in the detachment of Et from the biomimetic system. The result of our cellular studies further emphasizes on the perturbation of FRET efficiency from H258 to Et in presence of caffeine. Our study may help to carry out further experiments in the fields of medicine where caffeine can be taken as an active ingredient to protect cells from various cell damaging agents like DNA-intercalators.

References

- [1] C. P. Selby, A. Sancar, Molecular Mechanisms of DNA Repair Inhibition by Caffeine, *Proc. Natl. Acad. Sci.* 87 (1990) 3522.
- [2] F. Traganos, J. Kapuscinski, Z. Darzynkiewicz, Caffeine Modulates the Effects of DNA-Intercalating Drugs in vitro: A Flow Cytometric and Spectrophotometric Analysis of Caffeine Interaction with Novantrone, Doxorubicin, Ellipticine, and the Doxorubicin Analogue AD198, *Cancer Res.* 51 (1991) 3682.
- [3] J. Kapuscinski, M. Kimmel, Thermodynamic Model of Mixed Aggregation of Intercalators with Caffeine in Aqueous Solution, *Biophys. Chem.* 46 (1993) 153.
- [4] D. B. Davies, D. A. Veselkov, L. N. Djimant, A. N. Veselkov, Heteroassociation of Caffeine and Aromatic Drugs and their Competitive Binding with a DNA Oligomer, *Eur. Biophys. J.* 30 (2001) 354.
- [5] R. W. Larsen, R. Jasuja, R. K. Hetzler, P. T. Muraoka, V. G. Andrada, D. M. Jameson, Spectroscopic and Molecular Modelling Studies of Caffeine Complexes with DNA Intercalators, *Biophys. J.* 70 (1996) 443.
- [6] J. Piosik, M. Zdunek, J. Kapuscinski, The Modulation by Xanthines of the DNA-damaging Effect of Polycyclic Aromatic Agents: Part II. The Stacking Complexes of Caffeine with Doxorubicin and Mitoxantrone, *Biochemical Pharmacology* 63 (2002) 635.
- [7] E. Bedner, L. Du, F. Traganos, Z. Darzynkiewicz, Caffeine Dissociates Complexes Between DNA and Intercalating Dyes: Application for Bleaching Fluorochrome-Stained Cells for their Subsequent Restaining and Analysis by Laser Scanning Cytometry, *Cytometry* 43 (2001) 38.
- [8] I. M. Johnson, S. G. B. Kumar, R. Malathi, De-intercalation of Ethidium Bromide and Acridine Orange by Xanthine Derivatives and their Modulatory Effect on Anticancer Agents: A Study of DNA-Directed Toxicity Enlightened by Time Correlated Single Photon Counting, *J. Biomol. Struct. Dyn.* 20 (2003) 677.
- [9] S. Banerjee, D. Bhowmik, P. K. Verma, R. K. Mitra, A. Sidhanta, G. Basu, S. K. Pal, Ultrafast Spectroscopic Study on Caffeine Mediated Dissociation of Mutagenic Ethidium from Synthetic DNA and Various Cell Nuclei, *J. Phys. Chem. B* 115 (2011) 14776.
- [10] F. Traganos, B. Kaminska-Eddy, Z. Darzynkiewicz, Caffeine Reverses the Cytotoxic and Cell Kinetic Effects of Novantrone (Mitoxantrone), *Cell Prolif.* 24 (1991) 305.

- [11] N. J. Turro, M. Grätzel, A. M. Braun, Photophysical and Photochemical Processes in Micellar Systems, *Angew. Chem. Intern. Ed.* 19 (1980) 675.
- [12] D. Zhong, S. K. Pal, A. H. Zewail, Femtosecond Studies of Protein-DNA Binding and Dynamics: Histone I, *ChemPhysChem* 2 (2001) 219.
- [13] S. K. Pal, J. Peon, A. H. Zewail, Biological Water at the Protein Surface: Dynamical Solvation Probed Directly with Femtosecond Resolution, *Proc. Natl. Acad. Sci.* 99 (2002) 1763.
- [14] R. K. Mitra, S. S. Sinha, S. K. Pal, Interactions of Nile Blue with Micelles, Reverse Micelles and a Genomic DNA, *J. Fluoresc.* 18 (2008) 423.
- [15] D. Banerjee, S. K. Pal, Ultrafast Charge Transfer and Solvation of DNA Minor Groove Binder: Hoechst 33258 in Restricted Environments, *Chem. Phys. Lett.* 432 (2006) 257.
- [16] R. Sarkar, S. K. Pal, Ligand-DNA Interaction in a Nanocage of Reverse Micelle, *Biopolymers* 83 (2006) 675.
- [17] D. Banerjee, S. K. Pal, Simultaneous Binding of Minor Groove Binder and Intercalator to Dodecamer DNA: Importance of Relative Orientation of Donor and Acceptor in FRET, *J. Phys. Chem. B* 111 (2007) 5047.
- [18] H. R. Mahler, P. S. Perlman, Effects of Mutagenic Treatment by Ethidium Bromide on Cellular and Mitochondrial Phenotype, *Arch. Biochem. Biophys.* 148 (1972) 115.
- [19] S. Banerjee, M. Tachiya, S. K. Pal, Caffeine-Mediated Detachment of Mutagenic Ethidium from Various Nanoscopic Micelles: An Ultrafast Förster Resonance Energy Transfer Study, *J. Phys. Chem. B* 116 (2012) 7841.
- [20] A. K. Shaw, R. Sarkar, S. K. Pal, Direct Observation of DNA Condensation in a Nano-Cage by Using a Molecular Ruler, *Chem. Phys. Lett.* 408 (2005) 366.
- [21] S. K. Pal, D. Mandal, K. Bhattacharyya, Photophysical Processes of Ethidium Bromide in Micelles and Reverse Micelles, *J. Phys. Chem. B* 102 (1998) 11017.
- [22] S. Banerjee, P. K. Verma, R. K. Mitra, G. Basu, S. K. Pal, Probing the Interior of Self-Assembled Caffeine Dimer at Various Temperatures, *J. Fluoresc.* 22 (2012) 753.
- [23] S. Sadhu, K. K. Halder, A. Patra, Size Dependent Resonance Energy Transfer between Semiconductor Quantum Dots and Dye Using FRET and Kinetic Model, *J. Phys. Chem. C* 114 (2010) 3891.

- [24] R. Sarkar, S. K. Pal, Interaction of Hoechst 33258 and Ethidium with Histone1-DNA Condensates, *Biomacromolecules* 8 (2007) 3332.
- [25] T. R. Chen, In situ Detection of Mycoplasma Contamination in Cell Cultures by Fluorescent Hoechst 33258 Stain, *Experimental Cell Research* 104 (1977) 255.

Chapter 6

Spectroscopic Studies on the Interaction of Caffeine Molecules with a Potential Mutagen in DNA *in vitro* and *ex vivo* Conditions:

6.1. Introduction:

Molecular recognition of DNA in *in vitro* condition by small ligands/drugs in presence of caffeine, a widely consumed stimulant, is well studied [1-3]. Earlier, a set of studies have indicated that caffeine can diminish the cytotoxic/cytostatic effects of doxorubicin, ethidium (Et) bromide [4-5] and reverses cytotoxic effect of the antitumor agent mitoxantrone, eilipticine and doxorubicin analogues [6]. Spectroscopic studies on the de-intercalation of Et, a potential mutagen [7] from genomic DNA in solution at room temperature is also reported in the literature [8]. Such studies essentially intended to conclude the therapeutic use of caffeine, a xanthine alkaloid, in animal model. However, a detail molecular picture of the de-intercalation mechanism and the universal application of such xanthine alkaloids in the extraction of Et from the nucleus of various cell lines are missing from the reported studies and is one of the motives of our present report. The mechanism of de-intercalation both within and beyond the temperatures of physiological interest is also sparse in the reported literature and is one of the motives of the present study.

In this study, we have used steady state and picosecond resolved fluorescence spectroscopy and time gated fluorescence microscopy in order to investigate the detachment of mutagenic Et from synthesized DNA of specific sequences *in vitro* and various types of cell lines including squamous epithelial cells collected from the inner lining of the human mouth, A549 (lung carcinoma), A375 (human skin), RAW (macrophage) and Vero (African green monkey kidney epithelium) cells in *ex vivo* conditions. For the investigation of the efficacy of the caffeine induced detachment of the intercalative mutagen from the DNA within and beyond the physiological temperature, we

have performed temperature dependent spectroscopic measurement on the Et-DNA systems in presence and absence of caffeine molecule. A detail structural analysis employing NMR experiments followed by dynamic light scattering (DLS) studies on the caffeine-Et complex explores the molecular picture of such complexes. Our time gated fluorescence microscopic studies on various live and fixed cell lines indicate that the efficiency of Et extraction by the xanthine alkaloid is inconsistent and not very much intuitive from the above mentioned *in-vitro* studies.

6.2. Results and Discussion:

6.2.1. Ultrafast Spectroscopic Study on Caffeine Mediated Dissociation of Mutagenic Ethidium from Synthetic DNA and Various Cell Nuclei [9]:

6.2.1.1. Detachment of mutagenic Et from synthesized DNA: Temperature dependent study. In Figure 6.1 steady state and time resolved studies on the Et intercalated to the synthetic DNA are presented. As shown in the Figure 6.1 (a) Et in water produces an emission peak at 623 nm (excited at 409 nm) [10]. In presence of 100 mM caffeine, the peak exhibits a blue shift to 615 nm with a subsequent increase in the intensity. The blue shift of the emission peak signifies a hydrophobic environment experienced by Et which might be due to the caffeine-Et hetero-association as evidenced by some previous works [10-11]. When completely intercalated in the DNA oligomer at [DNA]:[Et] = 8:1 [10], the emission of Et exhibits substantial blue shift to produce the fluorescence maximum at 600 nm with an order of magnitude increase in the intensity with respect to that in water. The observed blue shift and enhanced intensity is due to strong intercalation of Et into the hydrophobic interior of the DNA [10]. As 100 mM caffeine solution is added into the DNA-Et complex, the emission intensity decreases with a little red shift to 605 nm. The red shift can be explained in terms of the de-intercalative property of caffeine that releases certain amount of Et from the DNA bound state either to the caffeine bound state or to the free form in the buffer. Our steady state fluorescence emission results strongly corroborate with earlier studies [8]. However, conclusive spectroscopic evidences of the de-intercalated Et in the hetero-association with caffeine was absent in the earlier studies [8].

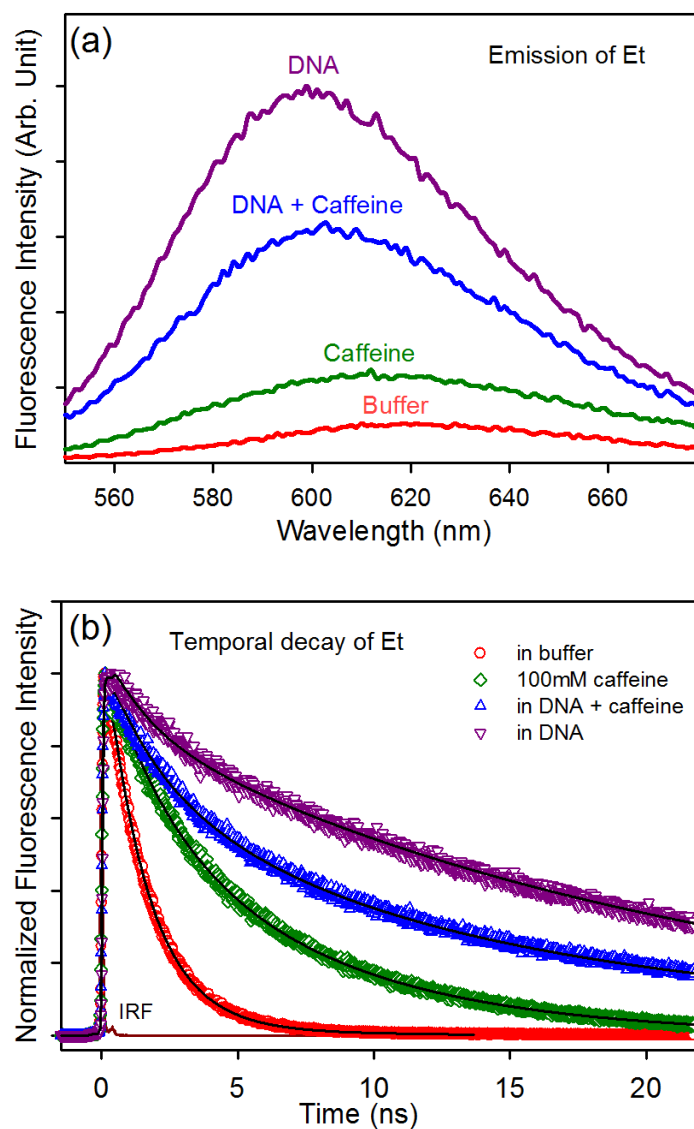


Figure 6.1. (a) Steady state emission of ethidium in various environments. (b) Time resolved fluorescence transients of ethidium (from bottom) in buffer, caffeine ($[caffeine] = 100 \text{ mM}$), DNA ($[DNA]:[Et] = 8:1$) in presence and absence of caffeine.

Deconvolution of the emission spectra of Et in DNA in presence and absence of caffeine suggests $\sim 40\%$ of the bound Et releases from DNA upon addition of caffeine but whether the released Et gets bound to caffeine or remains free in the solution cannot be concluded from the steady state results within such a narrow shift of emission maxima. A similar picture evolves from the time resolved study (Figure 6.1 (b), Table 6.1). Et in buffer shows single exponential fluorescence decay with a time constant of 1.6 ns which is close to the

Table 6.1: The lifetime components (τ_1 , τ_2 , τ_3) with corresponding amplitudes (A_1 , A_2 , A_3) of Et in various environments. Error $\pm 5\%$

Sample	τ_1 (ns)	$A_1\%$	τ_2 (ns)	$A_2\%$	τ_3 (ns)	$A_3\%$
Et in buffer	1.6	100				
Et in 100 mM caffeine	7	84.5	2.3	15.5		
[Et]:[DNA] = 1:8	1.5	2	21	98		
[Et]:[DNA] = 1:8 in presence of 100 mM caffeine	7	22	23	74	1.8	4

earlier reported values [8, 10]. In caffeine solution the decay pattern becomes biexponential with time constants of 2.3 ns (15.5%) and 7 ns (84.5%). When intercalated in DNA, the decay pattern of Et emission gets considerably slower with time constants of 1.5 ns (2%) and 21 ns (98%). Note that the insignificant contribution of the fast component in the transient confirms the presence of a very low fraction of Et free in buffer. On the other hand the longer time component 21 ns is assigned to the lifetime of Et molecules intercalated to DNA [10]. When 100 mM caffeine is added to Et-DNA complex the decay process becomes faster and can only be fitted triexponentially with time constants of 1.8 ns (4%), 7 ns (22%) and 23 ns (74%). These time constants can easily be identified with those of Et in buffer, hetero-association with caffeine and intercalation with DNA, respectively and fits to the heterogeneous model of Et in the aqueous solution of DNA in presence of caffeine. The triexponential nature of the decay pattern signifies the presence of at least three different environment of residence of Et in the solution. If the contribution from each environment is assumed to add up linearly in the total decay process, then it can be inferred that addition of caffeine reduces the fraction of Et molecules bound to DNA from 98% to 74% and the released Et mostly gets bound to caffeine as indicated by the 7 ns component (22%) and a small fraction (2%) goes into the buffer. The uncertainty range in the lifetime measurements is $\pm 7\%$. Our experimental result strongly upholds the de-intercalative activity of caffeine reported by Johnson et al. [8]. However, our work finds inimitability in characterising the 7ns component (characteristic lifetime of Et complexed with caffeine) which further clarifies the process. By measuring the relative weightage of the 21 ns

component, which is a signature of the total population of Et bound to DNA, and knowing the total concentration of Et and DNA molecules in the solution, we calculate the binding constant (K) of the ligand Et with DNA using the following equation [10].

$$K = \frac{[Et - DNA]}{([Et] - [Et - DNA]) \times ([DNA] - [Et - DNA])} \quad (6-1)$$

Where [Et-DNA], ([Et]-[Et-DNA]), ([DNA]-[Et-DNA]) represents concentration of Et-DNA complex, free Et and free DNA in the solution respectively. The binding constant of Et with DNA is calculated to be $15.4 \pm 1.1 \times 10^4 \text{ M}^{-1}$ which is comparable to the binding constant value of Et with genomic DNAs reported earlier [10, 12]. In presence of caffeine the binding constant value reduces to $7.6 \pm 0.5 \times 10^3 \text{ M}^{-1}$ as part of the free Et is sequestered by free caffeine leading in this way to a shift of the equilibrium between Et not bound to DNA and Et bound to DNA, whereas the value for caffeine solution is calculated to be $54.6 \pm 3.8 \text{ M}^{-1}$ which is also in close approximation of that reported earlier [12]. We calculate the free energy change associated with the complex formation using the equation (4-7) and it is found that the difference in the free energy between the intercalated Et ($-29.6 \pm 0.2 \text{ KJ mol}^{-1}$) and Et-DNA-caffeine complex ($-22.15 \pm 0.15 \text{ KJ mol}^{-1}$) is more than compensated by the binding of Et with caffeine ($-9.9 \pm 0.2 \text{ KJ mol}^{-1}$), which makes the de-intercalation process of caffeine energetically favourable.

To determine the thermal stability of the caffeine-Et complex we perform temperature dependent time resolved experiments (Figure 6.2). We first monitor the release of DNA intercalated Et into the buffer with rise in temperature as depicted in Figure 6.2 (a). As the temperature rises DNA melts with subsequent release of the intercalated Et into buffer as evidenced through the rise in amplitude of the faster lifetime component of ~2 ns from 3% to 45% as temperature rises from 18 to 71°C (Table 6.2). Upon addition of 100 mM caffeine in the DNA-Et system we monitor the temperature dependent change in the lifetime of the Et as shown in Figure 6.2 (b) and Table 6.3. While in the absence of caffeine, Et is released from the intercalated to the free state in buffer with the progress in DNA melting, in presence of caffeine most of the released Et, from the DNA intercalated state, heteroassociates with the available caffeine in the solution as has been observed from the rise in the amplitude of the lifetime component of Et characteristic

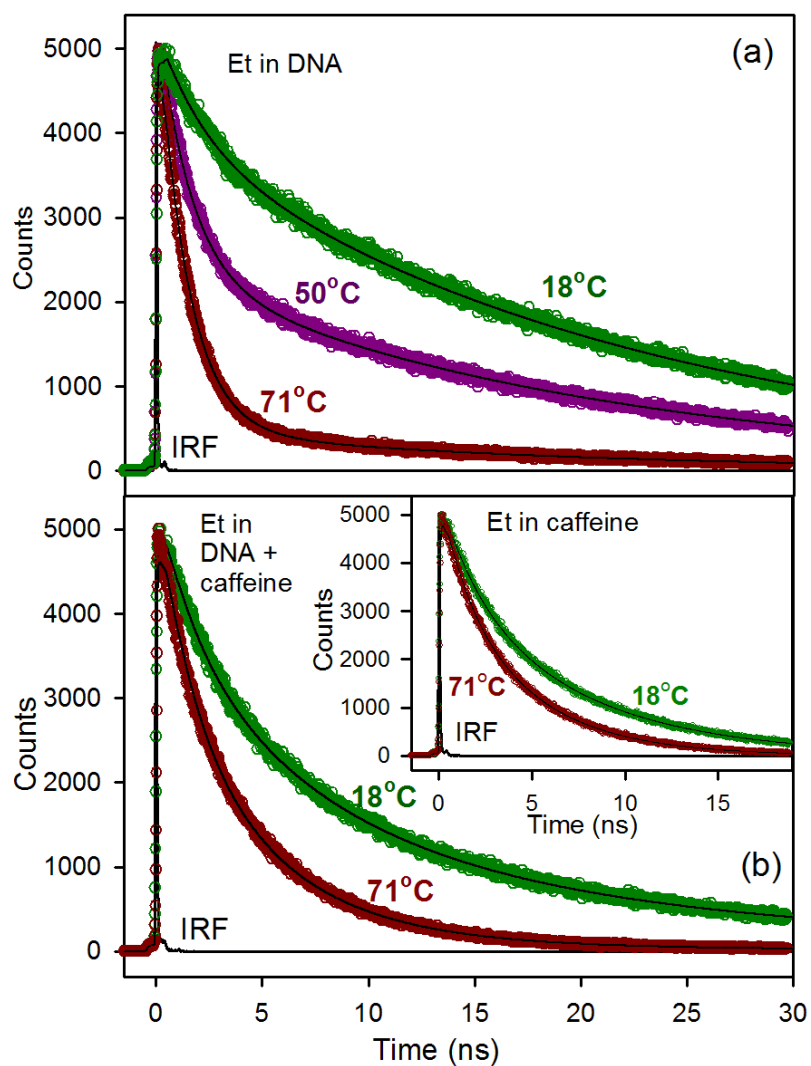


Figure 6.2. Temperature dependent time resolved fluorescence transients of (a) $[DNA]:[Et] = 8:1$ in absence and (b) in presence of caffeine ($[caffeine] = 100 \text{ mM}$) and $12.5 \mu\text{M}$ Et in presence of caffeine (inset (b)).

of its hetero-association with caffeine, with minor rise in the amplitude of the faster component of $\sim 2 \text{ ns}$ from 5% to 14% over the same range of temperature. Since most of the released Et from the DNA bound state remains in a strong hetero-association with the caffeine molecules in the solution even at high temperature at around 71°C it can be concluded that the complex that forms between caffeine and Et is thermally stable and caffeine can perform its de-intercalative activity even at high temperature. For further confirmation of the thermal stability of the caffeine-Et complex we monitor the temperature dependent fluorescence transient of Et in presence of high caffeine

concentration (Figure 6.2 (b) inset and Table 6.4). As depicted in Figure 6.2 (b) (inset) and Table 6.4 the amplitude of the faster component of ~ 2 ns, which represents the fraction of free Et present in buffer, does not change with rise in temperature which reconfirms the high stability of caffeine-Et complex both within and beyond the physiological temperatures.

Table 6.2: Variation of fluorescence transients of DNA bound Et ([DNA]:[Et] = 8:1) with temperature: τ represents the time constant and A represents relative contribution of the component. Error $\pm 5\%$

Temperature ($^{\circ}\text{C}$)	$\tau_1(\text{ns})$	$A_1\%$	$\tau_2(\text{ns})$	$A_2\%$
18	22	97	2.1	3
30	22	95	2.1	5
42	21	95	1.6	5
52	20	91	1.5	9
61	19	79	1.4	21
71	18	55	1.4	45

Table 6.3: Variation of fluorescence transients of DNA bound Et ([DNA]:[Et] = 8:1) with temperature in presence of 100 mM caffeine: τ represents the time constant and A represents relative contribution of the component. Error $\pm 5\%$

Temperature ($^{\circ}\text{C}$)	$\tau_1(\text{ns})$	$A_1\%$	$\tau_2(\text{ns})$	$A_2\%$	$\tau_3(\text{ns})$	$A_3\%$
18	22	60	7	35	1.7	5
30	22	57	6.4	38	1.5	5
42	22	46	6.05	48	1.35	6
52	22	35	5.67	58	1.36	7
61	22	21	5.5	65	1.69	14
71	22	10	4.68	76	1.5	14

Table 6.4: Variation of fluorescence transients of Et (12.5 μM) with temperature in presence of 100 mM caffeine: τ represents the time constant and A represents relative contribution of the component. Error $\pm 5\%$

Temperature ($^{\circ}\text{C}$)	$\tau_1(\text{ns})$	$A_1\%$	$\tau_2(\text{ns})$	$A_2\%$
18	7.15	88	2	12
30	6.6	89	1.8	11
41	6.06	89	1.7	11
50	5.56	88	1.7	12
61	5	88	1.6	12
71	4.4	88	1.5	12

6.2.1.2. Exploration of the molecular picture of caffeine-Et complex. The mode of interaction of caffeine with the DNA intercalator Et was studied using NMR spectroscopy. All observable protons in Et and caffeine were assigned and were followed in a NMR

experiment where 1.78 mM Et was titrated with caffeine. The changes in the chemical shift of Et protons ($\Delta\delta_{\text{obs}} = \delta_{\text{with caffeine}} - \delta_{\text{no caffeine}}$) are shown in Figure 6.3 (a). All proton signals (the Et CH₂ signal overlapped with H₂O signal and was not monitored) exhibited a hyperbolic change indicating Et-caffeine binding. Changes in $\Delta\delta_{\text{obs}}$ of individual ¹H-chemical resonances in Et, upon titration with caffeine, were fitted with Eq. (6-2) [13]

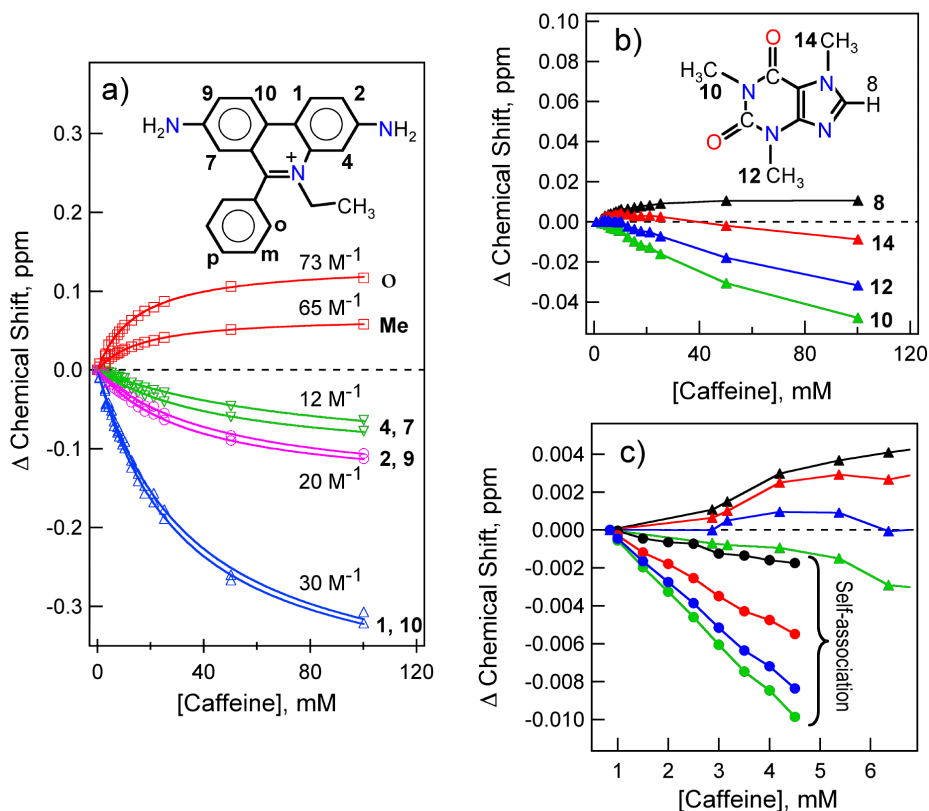


Figure 6.3. ¹H-chemical shift changes observed during titration of Et (1.78 mM) by caffeine (pH 7.0, 25°C): a) Et, b) caffeine. ¹H resonance signals are annotated with atom numbers, corresponding to the molecules shown in the panels. The continuous lines in panel (a) correspond to the best fits with Eq. (6-2) with the corresponding K_a values reported above each fit. Panel (c) shows changes in caffeine ¹H-chemical shifts for early data points (0-6 M) of panel (b) along with ¹H-chemical shift changes in caffeine due to self-association (concentration dependence) in the same concentration range. Atom numbering (colors) in panel (c) is identical to that in panel (b).

(which is a modified form of the Eq. (4-5)) for obtaining the association constant K_a ($[C]_T$ and $[E]_T$ are the total concentrations of caffeine and Et respectively and $\Delta\delta^{\text{max}}$ is the value of $\Delta\delta_{\text{obs}}$ for a large excess of $[C]_T$).

$$\Delta\delta_{\text{obs}} = \frac{\Delta\delta^{\text{max}}}{2K_a[E]_T} \left[1 + K_a([C]_T + [E]_T) - \sqrt{\{1 + K_a([C]_T + [E]_T)\}^2 - 4K_a^2[C]_T[E]_T} \right] \quad (6-2)$$

As can be observed from Figure 6.3 (a), K_a values were different depending on which protons one monitored; $K_a \sim 12 \text{ M}^{-1}$ (positions 4 and 7), $\sim 20 \text{ M}^{-1}$ (positions 2 and 9), $\sim 30 \text{ M}^{-1}$ (positions 1 and 2) and $\sim 65\text{-}73 \text{ M}^{-1}$ (for CH_3 and the ortho proton of Et benzene ring); the latter matching best with the estimate from time-resolved data (this work) and a

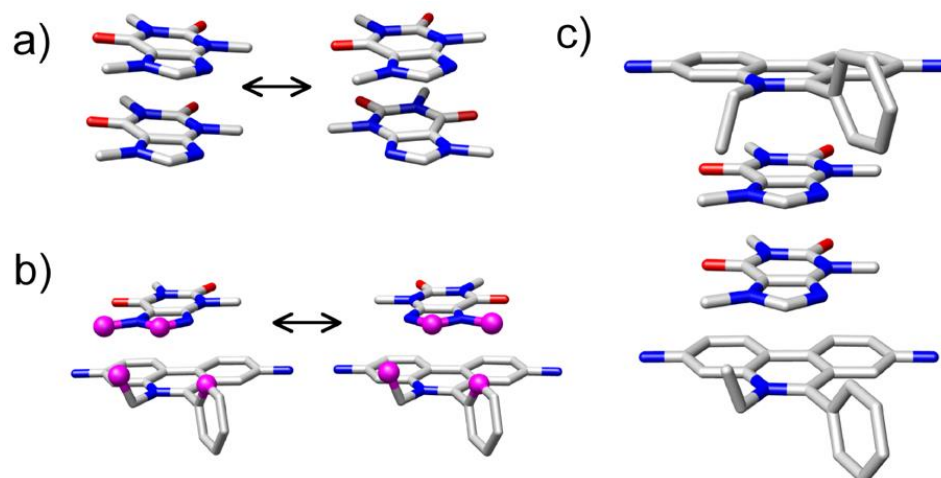


Figure 6.4. a) Inter-converting caffeine dimers (stacked on each other). b) A model for inter-converting 1:1 complex of caffeine and Et, compatible with NMR titration data. ^1H -resonances that exhibited upfield shift upon complex formation (positions 8 and 14 in caffeine, and *o* and *Me* in Et; Figure 6.3) are shown as ball and stick model (magenta). c) A model of 2:2 caffeine:Et complex compatible with caffeine:caffeine stacking (panel a) and caffeine:Et stacking (panel b). The structures were energy minimized to remove steric clashes.

previous report based on UV-Vis absorption spectroscopy. The range of K_a values obtained from NMR spectroscopy reflects structural heterogeneity of the Et:caffeine complex, undetected by optical spectroscopy. This is consistent with the broad distribution observed from DLS studies around a dominant conformation (discussed later; see Figure 6.5 (a)). The nature of the dominant conformation can be understood by a careful analysis of ring current shifts observed in Et as a function of added caffeine. During Et-caffeine interaction, the degree of change in $\Delta\delta_{\text{obs}}$ (and K_a) varied in a symmetric fashion (equivalence of 1-10, 2-9 and 4-7 positions) across Et molecule. In addition, while positions 1, 10, 2, 9, 4 and 7 exhibited a negative $\Delta\delta_{\text{obs}}$, the benzyl ortho position and the CH_3 protons of Et showed a positive $\Delta\delta_{\text{obs}}$. The major cause of chemical shift change in Et, due to interaction with caffeine, must originate from ring current shifts, producing positive and negative $\Delta\delta_{\text{obs}}$. Placement of an Et proton directly above the caffeine ring (stacking)

will produce a negative $\Delta\delta_{\text{obs}}$ while positioning of Et protons in the plane of the caffeine ring will produce a positive $\Delta\delta_{\text{obs}}$.

Based on the NMR data (symmetry of K_a and $|\Delta\delta_{\text{obs}}|$) and the assumption that the sign of $\Delta\delta_{\text{obs}}$ originates from the ring current effect, a model for a 1:1 complex of caffeine:Et was constructed as shown in Figure 6.4 (b). Caffeine and Et molecules are stacked in the 1:1 model where the CH_3 and the ortho-benzyl protons of Et (shown as magenta spheres in Figure 6.4 (b)) protrude towards the plane of the caffeine ring giving rise to the observed positive $\Delta\delta_{\text{obs}}$. The stacked caffeine can flip, effectively making its effect on the Et symmetric. The flipping is consistent with a model of caffeine dimer where two forms of caffeine dimers (flipped and un-flipped stacking, Figure 6.4 (a)) have been observed [14]. Our model suggests that two protons in caffeine, positions 8 and 14 (shown as magenta spheres in Figure 6.4 (b)), should also exhibit a positive $\Delta\delta_{\text{obs}}$ (ring current effect from Et). To validate this, caffeine chemical shifts were monitored in the Et titration experiment of Figure 6.3 (a) and are shown in Figure 6.3 (b). Indeed positions 8 and 14 of caffeine showed a positive $\Delta\delta_{\text{obs}}$ as expected from the model. This becomes more clear in Figure 6.3 (c) where the early data points are shown (up to 4:1 caffeine:Et ratio) along with caffeine self association data (all resonance in the self association show negative $\Delta\delta_{\text{obs}}$).

In order to determine the size of the complex formed between caffeine and Et, we performed DLS experiments and the results are shown in Figure 6.5 (a). The DLS data, with broad peaks for caffeine, in presence and in absence of Et, indicate a distribution of populations around a dominant structure and consistent with NMR data. The DLS-derived hydrodynamic diameter (corresponding to the peak of the distributions) of 100 mM caffeine is 8.4 Å. This increases to 14.2 Å upon addition of 25 μM Et. Fluorescence anisotropic studies on Et (Figure 6.5 (b)), in presence of caffeine, yielded a hydrodynamic diameter of 12.3 Å, slightly lower than the DLS-derived value. To compare with the experimental values, hydrodynamic diameters of caffeine dimer (Figure 6.4 (a)) and the 2:2 caffeine-Et complex (Figure 6.4 (c)) were estimated using the program Hydropro[15]. The calculated diameters, 8.9 Å for caffeine dimer, and, 13.0 Å for the 2:2 caffeine-Et complex, are compatible with the experimental data. The above analysis shows that the major component of pure caffeine is the dimeric form. In presence of Et, caffeine:Et complexes with a 2:2 (or higher) stoichiometry dominates. Incidentally, no peaks were

obtained at higher hydrodynamic radii indicating the absence of any higher order aggregation.

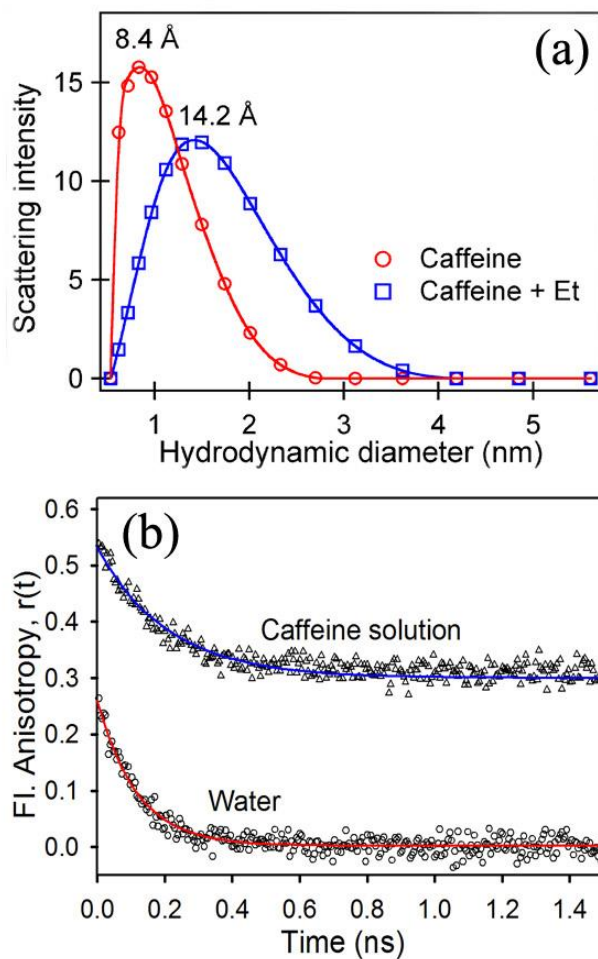


Figure 6.5. (a) Dynamic light scattering of 100 mM caffeine with (blue squares) and without (red circles) 25 μM ethidium. (b) Fluorescence anisotropy of Et in water (\circ) and in presence of 100 mM (Δ) caffeine. The base line for anisotropy of Et in caffeine solution has been shifted vertically by 0.3 for better clarity.

6.2.1.3. Efficiency of caffeine in the expulsion of Et from various cell lines: Time gated fluorescence microscopic studies. Our spectroscopic results reflecting the efficacy of caffeine in the extraction of Et upon forming a caffeine-Et complex with it provoke us to get a microscopic view of such activity of caffeine molecules. In order to study in biological milieu we have used some animal cell lines. Figure 6.6 (a) shows the fluorescence micrographs of both live and fixed A549 cells stained with Et and

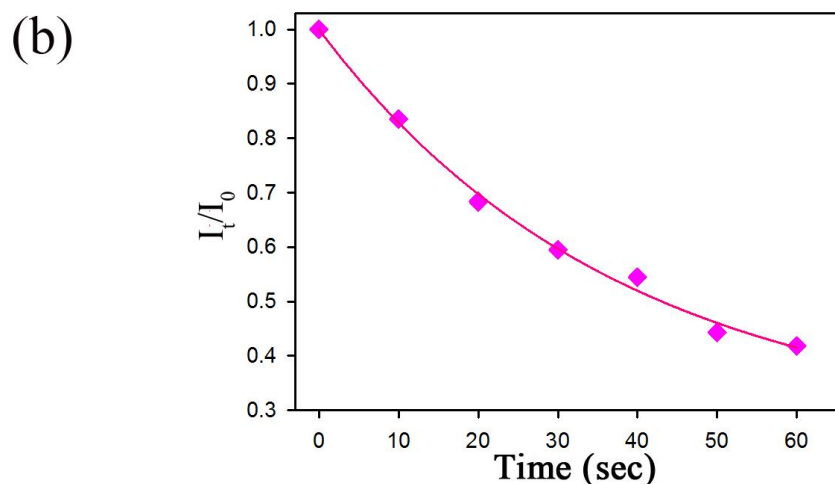
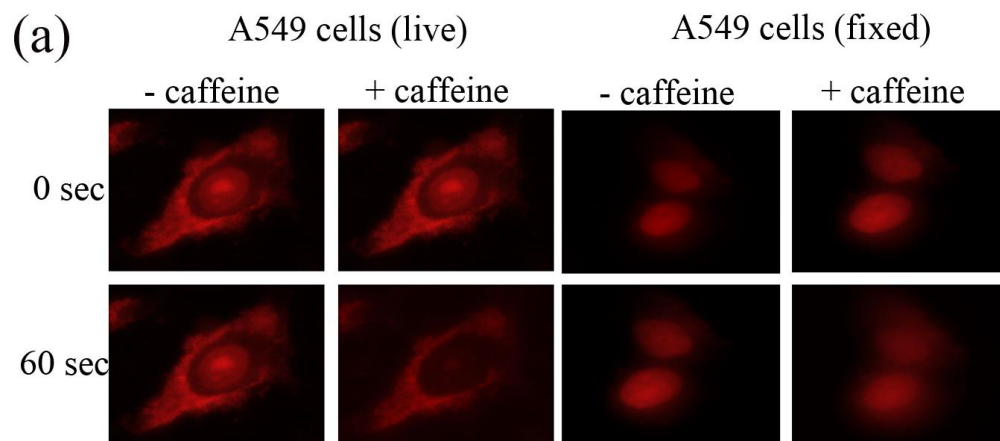


Figure 6.6. (a) Fluorescence micrographs of both live and fixed Et stained A549 cells initially and after 60 seconds upon treatment with caffeine (+ caffeine) along with the control sets (- caffeine) treated with PBS without caffeine. (b) Rate of leaching out of Et from nucleus of live A549 lung carcinoma cells when treated with caffeine. I_t and I_0 represents the emission intensity of Et at time t and initially, respectively.

subsequently treated with caffeine (+ caffeine) and for control experiment identical sets of stained cells were treated with PBS without caffeine (- caffeine). Comparing the fluorescence micrographs of both live and fixed '+ caffeine' and '- caffeine' cells after 60 seconds of treatment we observe there is a significant drop in the emission intensity of Et from the nucleus of the live A549 cells treated with caffeine. The drop in emission intensity of Et can be explained in terms of the efficiency of caffeine molecules in removal of Et from the nucleus of those live cells. As evident from the fluorescence micrographs of

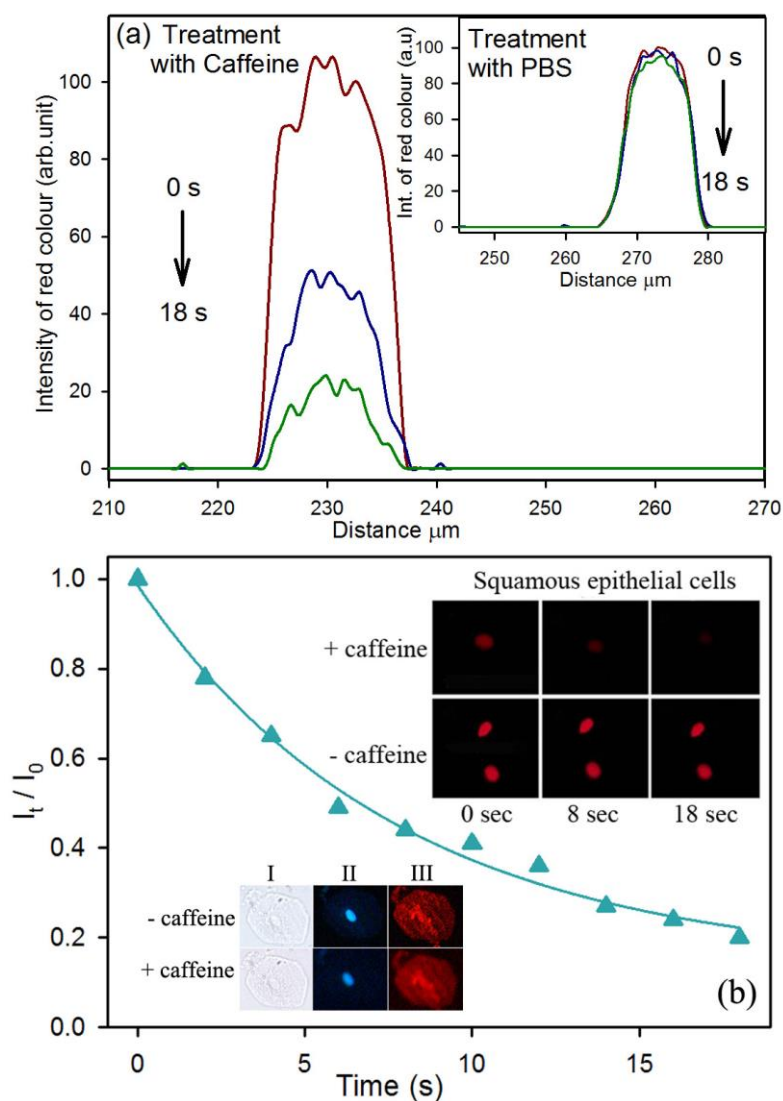


Figure 6.7. (a) Reduction in intensity of red colour with time when squamous epithelial cells treated with caffeine and PBS as control (inset). (b) Rate of leaching out of Et from nucleus of squamous epithelial cells when treated with caffeine. I_t and I_0 represents the emission intensity of Et at time t and initially, respectively. Upper right inset shows the fluorescence micrographs of Et stained same cells initially, after 8 seconds and after 18 seconds upon treatment with caffeine along with the control sets. Lower left inset shows the morphology of the same cell line before and after 5 minutes upon caffeine treatment under bright field (I) and fluorescence micrographs of the same stained with DAPI (II) and Merocyanine 540 (III).

Figure 6.6 (a), the efficacy of caffeine in the extraction of Et from the nucleus of fixed cells is less compared to the live ones. In order to get an insight on the kinetics of the extraction process we plot I_t/I_0 against time (Figure 6.6 (b)), where I_t represents emission intensity of Et in nucleus at time t and I_0 represents the same initially just after

the addition of caffeine to the live A549 stained cells. We fit the curve with single exponential decay and find the extraction of Et from the cell nucleus of live A549 cells by caffeine with a characteristic time constant of 38 seconds.

After monitoring the effect of caffeine on A549 cells we proceed with squamous epithelial cells taken from human mouth. Et being a potential intercalator of DNA[16], binds only in the nucleus of the cell and the red emission observed in the micrographs (Figure 6.7 (b) upper right inset) are due to the Et that emits in the red region (~ 600nm) [10]. As can be observed from the Figure, when the stained cells are treated with caffeine (+ caffeine), Et is released from the nucleus at a very fast rate. The intensity of red colour of the cells is blurred with time which indicates release of Et from the nucleus. In control experiment (- caffeine) cells retain almost the entire amount of Et in their nucleus. In order to highlight the de-intercalative property of caffeine in a more quantitative manner, the intensity of the red colour of Et from cell nucleus, which is proportional to the amount of Et present, has been plotted at regular time interval for both the systems ('- caffeine' and '+ caffeine') where the x-coordinate represents distance in the horizontal plane where the cell lies (Figure 6.7 (a)). As evident from the Figure the intensity of red colour is considerably high at the position that corresponds to the cell nucleus and it falls rapidly after 8 seconds (blue line) upon treatment with caffeine solution, whereas a negligible change is produced in control set (- caffeine) within the same time scale (Figure 6.7 (a), inset). After 18 seconds, '+ caffeine' cells show negligible amount of Et left in their nucleus (green line) while no significant change has been observed in '- caffeine' cells. As a control study to rule out the possibility of cell disruption upon treatment with caffeine, we have taken the cell images (Figure 6.7 (b), lower left inset) under bright field before and after treating them with caffeine and found no change even after 5 minutes. In addition, we stained the cell nuclei with a fluorescent dye, DAPI and found that cell nuclei remain intact over the same time span upon treatment with caffeine. Furthermore, we checked the membrane integrity of the cells by staining them with another fluorescent dye, merocyanine 540 and found that the cell membranes remain unperturbed upon treatment with caffeine. The plot of I_t/I_0 against time (Figure 6.7 (b)), gives the characteristic time constant for extraction of Et from these cells by caffeine as 8 seconds. However no

significant result has been observed in the removal of Et from A375, RAW and Vero by caffeine (Figure 6.8).

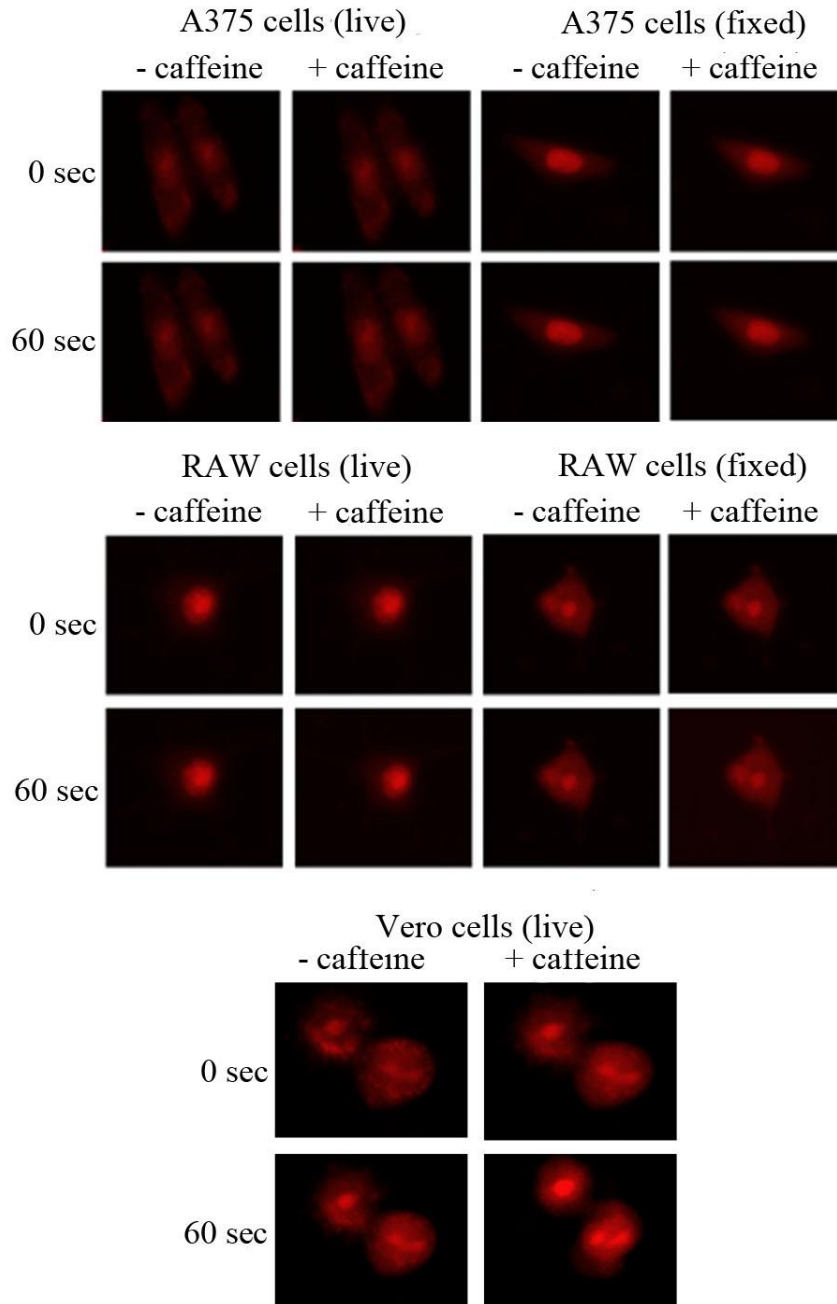


Figure 6.8. Fluorescence micrographs of Et stained A375 and RAW cells (both live and fixed) along with Vero (live) cells treated with caffeine (+ caffeine) and images taken at 0 second and 60 seconds interval. The control sets (- caffeine) treated with PBS without caffeine.

6.3. Conclusion:

Our steady state and time resolved fluorescence studies with synthetic DNA emphasize the interceptive role of well consumed caffeine molecules, forming heterocomplexes with Et. Temperature dependent picosecond resolved fluorescence experiments highlight the thermal stability of such complexes within and beyond the physiological temperature. Results from NMR and DLS studies were used to construct a model of caffeine-Et dimer representing the dominant structure of Et:caffeine complex in solution. Our cellular studies reveal the precise nature of the xanthine alkaloid in the exclusion of mutagenic Et from the cell nucleus. The specific molecular interaction of caffeine with Et molecule underlying the “interceptor” action of caffeine can be considered as one of the potential mechanism of Et release in our present study. For the physiological activity of the drugs in presence of caffeine another mechanism of action called “protector”, can also occur, in which there is a competition between caffeine and Et for the binding sites on DNA. It is likely that both mechanisms can act simultaneously and therefore must be taken into consideration when analysing a three-component equilibrium of the Et, caffeine and DNA. We believe that our studies may find relevance in the therapeutic use of caffeine as the non-invasive antimutagenic agent particularly for the prevention of oral cancers / squamous cell carcinomas which arises due to the activation of oncogenes as a result of DNA mutation.

References

- [1] C. P. Selby, A. Sancar, Molecular Mechanisms of DNA Repair Inhibition by Caffeine, *Proc. Natl. Acad. Sci.* 87 (1990) 3522.
- [2] F. Traganos, J. Kapuscinski, Z. Darzynkiewicz, Caffeine Modulates the Effects of DNA-Intercalating Drugs in vitro: A Flow Cytometric and Spectrophotometric Analysis of Caffeine Interaction with Novantrone, Doxorubicin, Ellipticine, and the Doxorubicin Analogue AD198, *Cancer Res.* 51 (1991) 3682.
- [3] R. W. Larsen, R. Jasuja, R. K. Hetzler, P. T. Muraoka, V. G. Andrada, D. M. Jameson, Spectroscopic and Molecular Modelling Studies of Caffeine Complexes with DNA Intercalators, *Biophys. J.* 70 (1996) 443.
- [4] R. Ganapathi, D. Grabowski, H. Schmidt, A. Yen, G. Iliakis, Modulation of Adriamycin and N-Trifluoroacetyladiamycin-14-valerate Induced Effects on Cell Cycle Traverse and Cytotoxicity in P388 Mouse Leukemia Cells by Caffeine and the Calmodulin Inhibitor Trifluoperazine, *Cancer Res.* 46 (1986) 5553.
- [5] H. Kimura, T. Aoyama, Decrease in Sensitivity to Ethidium Bromide by Caffeine, Dimethylsulfoxide or 3-Aminobenzamide Due to Reduced Permeability, *J. Pharmacobio-Dyn.* 12 (1989) 589.
- [6] F. Traganos, B. Kaminska-Eddy, Z. Darzynkiewicz, Caffeine Reverses the Cytotoxic and Cell Kinetic Effects of Novantrone (Mitoxantrone), *Cell Prolif.* 24 (1991) 305.
- [7] H. R. Mahler, P. S. Perlman, Effects of Mutagenic Treatment by Ethidium Bromide on Cellular and Mitochondrial Phenotype, *Arch. Biochem. Biophys.* 148 (1972) 115.
- [8] I. M. Johnson, S. G. B. Kumar, R. Malathi, De-intercalation of Ethidium Bromide and Acridine Orange by Xanthine Derivatives and their Modulatory Effect on Anticancer Agents: A Study of DNA-Directed Toxicity Enlightened by Time Correlated Single Photon Counting, *J. Biomol. Struct. Dyn.* 20 (2003) 677.
- [9] S. Banerjee, D. Bhowmik, P. K. Verma, R. K. Mitra, A. Sidhhanta, G. Basu, S. K. Pal, Ultrafast Spectroscopic Study on Caffeine Mediated Dissociation of Mutagenic Ethidium from Synthetic DNA and Various Cell Nuclei, *J. Phys. Chem. B* 115 (2011) 14776.
- [10] R. Sarkar, S. K. Pal, Ligand-DNA Interaction in a Nanocage of Reverse Micelle, *Biopolymers* 83 (2006) 675.

- [11] D. B. Davies, D. A. Veselkov, L. N. Djimant, A. N. Veselkov, Heteroassociation of Caffeine and Aromatic Drugs and their Competitive Binding with a DNA Oligomer, *Eur. Biophys. J.* 30 (2001) 354.
- [12] S. F. Baranovsky, P. A. Bolotin, M. P. Evstigneev, D. N. Chernyshev, Interaction of Ethidium Bromide and Caffeine with DNA in Aqueous Solution, *J. Appl. Spectrosc.* 76 (2009) 132.
- [13] K. Hirose, A Practical Guide for the Determination of Binding Constants, *J. Incl. Phenom. Macrocycl. Chem.* 39 (2001) 193.
- [14] M. Falk, W. Chew, J. A. Walter, W. Kwiatkowski, K. D. Barclay, G. A. Klassen, Molecular Modelling and NMR Studies of the Caffeine Dimer, *Can. J. Chem.* 76 (1998) 48.
- [15] A. Ortega, D. Amoros, J. García de la Torre, Prediction of Hydrodynamic and Other Solution Properties of Rigid Proteins from Atomic and Residue-Level Models, *Biophys. J.* 101 (2011) 892.
- [16] J. S. Lai, W. Herr, Ethidium Bromide Provides a Simple Tool for Identifying Genuine DNA-Independent Protein Associations, *Proc. Natl. Acad. Sci.* 89 (1992) 6958.

Chapter 7

Spectroscopic Studies on a Model Food Carcinogen in Various Restricted Environments: Exploration of the Molecular Basis for the Carcinogenic Activity:

7.1. Introduction:

Benzo[*a*]pyrene (BP), a polycyclic aromatic hydrocarbon (PAH), is one of the most potent carcinogens to which people are frequently exposed [1-3]. Its evolution during fuel and tobacco combustion and presence in grilled and smoked food products has made it the most studied carcinogen since its isolation [3-8]. The accepted hypothesis for carcinogens is that they are first converted to electrophilic metabolites which react covalently with the nucleophilic DNA. Such DNA adducts are the ultimate molecular lesion leading to the activation of oncogenes and ultimately giving rise to neoplasia [9]. Earlier studies [10] indicate the significance of one electron oxidation as a possible primary step in the chemical carcinogenesis of BP. ET reactions are well known for their importance in DNA damage [11] and recent findings suggest the role of ultrafast ET in inducing single strand and double strand breaks in DNA through reductive DNA damage [12]. Previous reports investigating BP-DNA complexes through fluorescence and triplet flash photolysis techniques have proposed that majority of the fluorescence in these complexes originates from BP bound to GC-GC intercalation sites [13]. Such conclusions are supported by the relative quenching efficiencies of BP by mononucleosides dissolved in aqueous ethanol mixtures suggesting 2'-deoxythymidine as an efficient quencher compared to cytidine, 2'-deoxyguanosine and -adenosine. Furthermore, it has also been reported [13] that the fluorescence of BP in aqueous BP-DNA complexes gets strongly quenched upon the addition of Ag⁺ ions which bind predominantly to guanosine in DNA, validating the fact that fluorescence of BP in BP-DNA complexes originates from GC sites. However, the study does not preclude the possibility of BP binding at AT rich sites. The same study reports shorter lifetime of BP in DNA complexes compared to that in degassed benzene

suggesting strong fluorescence quenching of BP upon complexation with DNA. BP fluorescence quenching by nucleoside solutions shows no association between the quencher and BP in the ground state, while a short lived charge transfer complex is formed when an excited state BP collides with a nucleoside [13]. In such charge transfer complexes, determination of the electron donor and acceptor is based on the relative ionization potentials and electron affinities of the two molecules forming the complex. The ionization potentials of the aromatic hydrocarbons are generally lower than the nitrogenous bases [13] and calculations indicate that pyrimidines are better electron acceptors than purines. However, strong experimental evidences highlighting the electron transfer (ET) reaction from BP to DNA are still lacking in the current literature.

Earlier studies [14] report that genotoxic carcinogens not only interact with DNAs but also with proteins. In this regard, serum proteins are particularly important because hepatocytes are not only the cells in which serum proteins are synthesized but also the cells in which most xenobiotic metabolism, including microsomal oxidations which activate carcinogens, takes place. Among serum proteins, serum albumin being abundant and because of its role as a carrier of fatty acids, endobiotics and xenobiotics, there is a high probability that it will bind and form covalent adducts with ultimate carcinogens. There have been extensive studies on the adduct formation of BP with serum albumin [15-16] yet there is no information regarding the ET reaction between the two in the present literature. Moreover, it is of great interest to investigate the effect of temperature on such ET reaction between BP and biological macromolecules like DNA and protein.

Apart from chemical carcinogens, ionizing radiations play a significant role in the induction of cancer [17-18]. Certain radiations like UVA are also known to cause DNA damage through ET in the presence of certain photosensitizers [19]. Earlier studies have shown how coexposure to BP and UVA induces double strand breaks (DSBs) in DNA, in both cell-free system (in vitro) and cultured Chinese hamster ovary (CHO-K1) cells [20-21], resulting in phototoxicity and photocarcinogenesis. A singlet oxygen scavenger sodium azide (NaN_3) effectively showed inhibition in the production of DSBs, suggesting singlet oxygen is the principal ROS generated by BP and UVA both in vitro and in vivo [21]. It has also been suggested that the mechanism of DNA damage by BP in presence of UVA differs in cell and cell-free systems. In spite of such extensive reports, the

exploration of photophysics lying behind the co-exposure of DNA to BP and UVA radiation is lacking in the literature to the best of our knowledge.

Recently, an ultrasensitive photoelectrochemical immunoassay comprising bifunctional gold nanoparticles modified with PAH antigen and horseradish peroxidase (HRP) on nanostructured TiO₂ electrode decorated with antibodies has been proposed as a means to quantify PAH, based on the changes in photocurrent with respect to the control (without PAH) [22]. However, studies emphasizing the application of nanostructure based photodevices in the detection of ET reaction, where flow of electrons can be directly monitored in the form of photocurrent, are sparse in the literature.

In our present study, we have used a well known electron acceptor [23], para-benzoquinone (BQ) as an organic molecule to emphasize the electron donating efficiency of BP upon excitation with UVA radiation, using a laser source of 375 nm. Both DNA and protein have been used as biological macromolecules to monitor the ET from BP in presence of UVA radiation. In addition, we have used zinc oxide (ZnO) nanorods (NRs)-based photodevice to directly monitor such photo-induced ET reaction from BP to the NRs. In order to study ET reaction from BP to organic molecules and macromolecules along with inorganic NRs, we have used both steady-state and picosecond-resolved fluorescence spectroscopy. Structural perturbation of DNA in the presence of BP has been investigated through temperature-dependent circular dichroism (CD) spectroscopy. Furthermore, to monitor the effect of temperature on ET from BP to biological macromolecules, we have performed temperature-dependent steady-state and time-resolved fluorescence spectroscopic studies.

7.2. Results and Discussion:

7.2.1. UVA Radiation Induced Ultrafast Electron Transfer from a Food Carcinogen Benzo[*a*]Pyrene to Organic Molecules, Biological Macromolecules and Inorganic Nano Structures [24]:

7.2.1.1. Electron transfer reaction from BP to BQ. Figure 7.1 (a) shows the steady-state fluorescence quenching of benzo[*a*]pyrene (BP) in DMSO with increasing concentration of para-benzoquinone (BQ), which is a well-known electron acceptor [23, 25]. The fluorescence spectrum of BP in absence of the quencher strongly corroborates with the spectral nature of BP emission reported earlier in different solvents [26]. While BP monomers produce three well characterized emission peaks around 410, 430 and 455 nm and a weak band near 485 nm due to different vibrational bands, BP aggregates are known to produce an emission feature that peaks around 490 nm [26]. Since a very low concentration of BP (1 μM) has been used in our sample, the contribution of aggregates does not appear to be significant. The observed decrease in fluorescence intensity of BP in the presence of BQ can arise either due to collisional/dynamic or static quenching or both or even through non-molecular mechanisms where fluorophore itself or other absorbing species attenuates the incident light [27]. For a better insight on the mechanism of the observed quenching, the relative change in fluorescence intensity of BP has been plotted as a function of the quencher (BQ) concentration at the different vibronic peaks of 410, 430 and 455 nm as shown in Figure 7.1 (b), (c) and (d), respectively. For collisional quenching the decrease in fluorescence intensity is described by the well-known Stern-Volmer (SV) equation [27],

$$\frac{F_0}{F} = 1 + k_q \tau_0 [Q] = 1 + K_{SV} [Q] \quad (7-1)$$

F_0 and F are the fluorescence intensities in the absence and presence of quencher, respectively; k_q is the bimolecular quenching constant; τ_0 is the lifetime of the fluorophore in the absence of quencher, and $[Q]$ is the concentration of quencher. The Stern-Volmer quenching constant is given by $K_{SV} = k_q \tau_0$. In case of dynamic quenching, the SV plot (F_0/F vs $[Q]$) becomes linear with an intercept of one on the y-axis and a slope equivalent to the dynamic quenching constant (K_D) [27]. However, as evident from Figures 7.1 (b), (c) and (d), the SV plots for the fluorescence quenching of BP by BQ (monitored at different wavelengths) appear as an upward curvature, concave towards the y-axis. Such curved SV plots are typical for fluorophores which are quenched simultaneously by collisions (dynamic quenching) and non-fluorescent ground state complex formation (static

quenching) with the same quencher [27]. When both static and dynamic quenching occur for the same fluorophore, the SV equation gets modified as [27],

$$\frac{F_0}{F} = (1 + K_D[Q])(1 + K_S[Q]) \quad (7-2)$$

where K_S represents the static quenching constant. The modified form of the SV equation being second order in $[Q]$, accounts for the upward curvature in our SV plots shown in Figures 7.1 (b), (c) and (d).

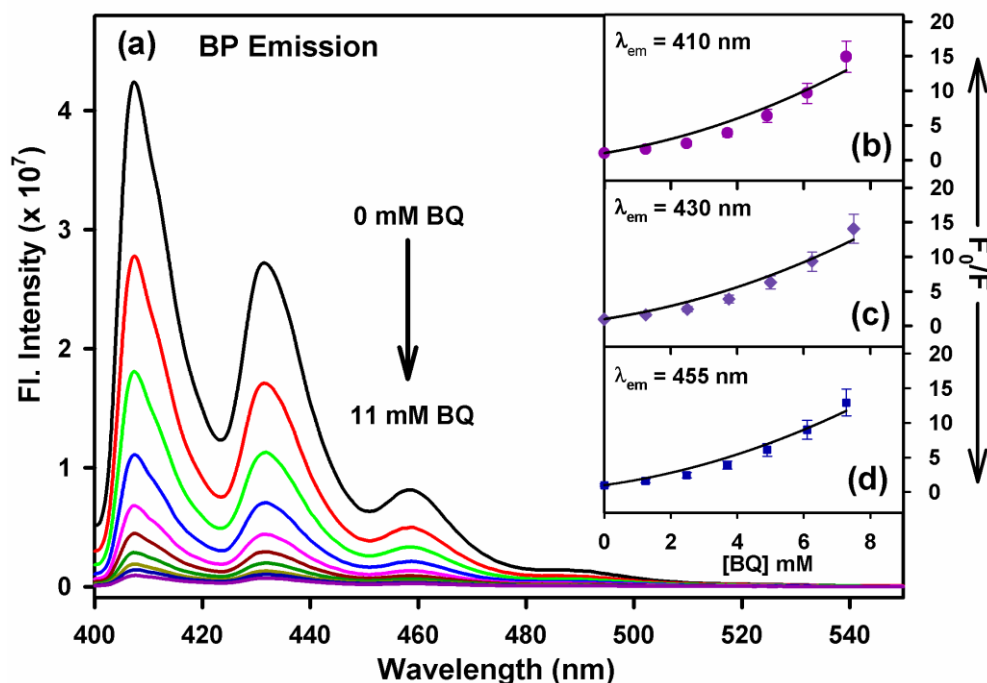


Figure 7.1. (a) Fluorescence quenching spectra of 1 μ M benzo[a]pyrene (BP) in DMSO with increasing concentrations of benzoquinone (BQ) (0, 1.25, 2.50, 3.75, 5.0, 6.25, 7.5, 8.75, 10 and 11 mM). Plots of F_0/F vs. BQ concentration at 410 nm (b), 430 nm (c) and 455 nm (d). F_0 and F represent fluorescence intensity of the fluorophore (BP) in absence and presence of the quencher (BQ), respectively. Excitation wavelength (λ_{ex} = 375 nm).

The dynamic portion of the observed quenching has been determined by lifetime measurements. Fluorescence transients of BP in the absence and presence of different concentrations of BQ monitored at 410, 430 and 455 nm are presented in Figure 7.2 (a), (b) and (c), respectively. The lifetime components of the transients are tabulated in Table 7.1. As evident from Table 7.1, a fast component of 2 ns appears in the fluorescence transients of BP at emission wavelengths of 430 and 455 nm both in the absence and presence of the

quencher, which accounts for the presence of some BP aggregates in the experimental solution, having higher contribution at 455 nm compared to that at 430 nm, while at 410 nm the fluorescence originates essentially from the BP monomers. Furthermore, it has also been observed that the contribution of the 2 ns component in the fluorescence transient of BP enhances with the increase in BP concentration due to the progressive formation of BP aggregates. As BP monomers are known to produce a weak band near 485 nm [26], at 490 nm both the emission from BP monomers and BP aggregates have significant contribution. However, as expected, the 2 ns component (due to BP aggregates) found to have higher contribution (27%) in the fluorescence transient of BP at 490nm compared to that at 430 (7%) or 455 nm (15%). The relative contribution of 2 ns component in the fluorescence transients of BP further increases at 520 (31%) and 560 nm (33%), due to the relatively higher contribution of BP aggregates (data not shown). For dynamic quenching, the average lifetimes in the absence (τ_0) and presence (τ) of quencher are given by [27],

$$\frac{\tau_0}{\tau} = 1 + k_q \tau_0 [Q] = 1 + K_D [Q] \quad (7-3)$$

The numerical values of τ_0 and τ at three different wavelengths are given in Table 7.1. τ_0 values are obtained as 19.32, 18.75 and 17.53 ns at 410, 430 and 455 nm, respectively. Plots of τ_0/τ vs quencher concentrations for the lifetime quenching of BP with increasing concentrations of BQ, yield a straight line with an intercept of one as shown in Figures 7.2 (d), (e) and (f) for emission wavelengths (λ_{em}) 410, 430 and 455 nm, respectively. The K_D values are obtained as 0.21 ± 0.01 , 0.21 ± 0.01 and $0.29 \pm 0.02 \text{ mM}^{-1}$ and the corresponding values of k_q are 10.87×10^9 , 11.20×10^9 and $16.54 \times 10^9 \text{ M}^{-1} \text{ s}^{-1}$ while monitoring lifetime quenching at 410, 430 and 455 nm, respectively. The k_q values obtained for BP are comparable to that of hypericin fluorescence quenching by the same quencher BQ, reported previously [28]. As shown in Figures 7.1 (b), (c) and (d), upon fitting the plots of F_0/F vs $[Q]$ with equation (7-2) considering the K_D values obtained from time-resolved studies, the values of K_S obtained at 410, 430 and 455 nm are 0.57 ± 0.08 , 0.51 ± 0.08 and $0.38 \pm 0.06 \text{ mM}^{-1}$, respectively. The quenching in lifetime being a measure of the rate process that depopulates the excited state can arise either due to energy transfer or electron transfer (ET) reactions. Since there is no overlap between the emission spectrum of BP and

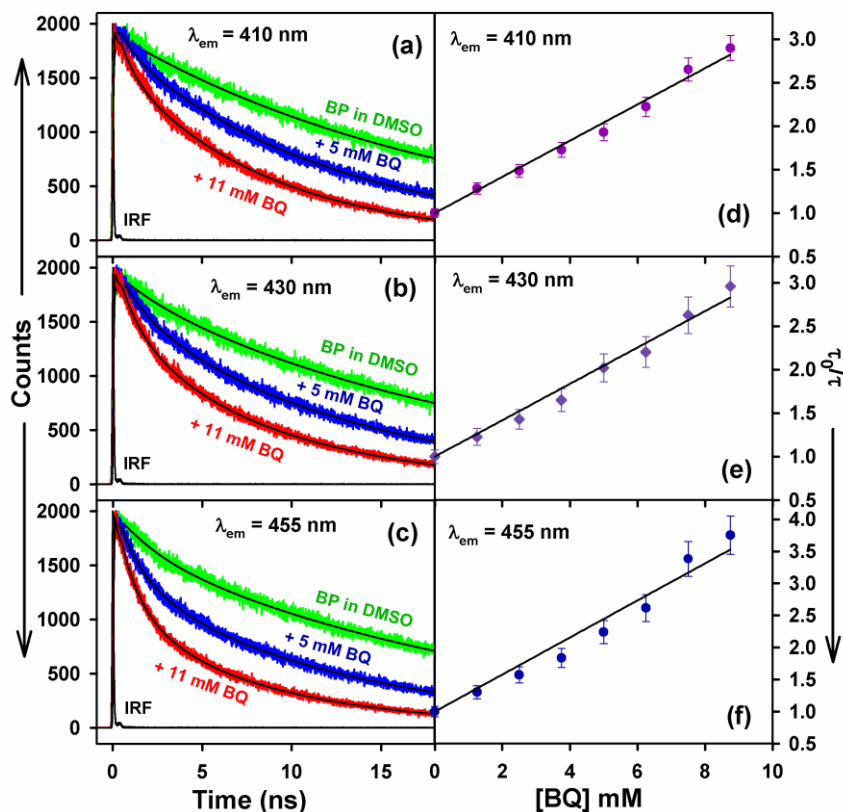


Figure 7.2. Picosecond-resolved fluorescence transients of BP in DMSO in absence and presence of different BQ concentrations and the corresponding plots of τ_0/τ vs. BQ concentration monitored at (λ_{em}) 410 nm (a and d), 430 nm (b and e) and 455 nm (c and f). τ_0 and τ represent lifetimes of the fluorophore (BP) in absence and presence of the quencher (BQ), respectively. Excitation wavelength (λ_{ex}) = 375 nm).

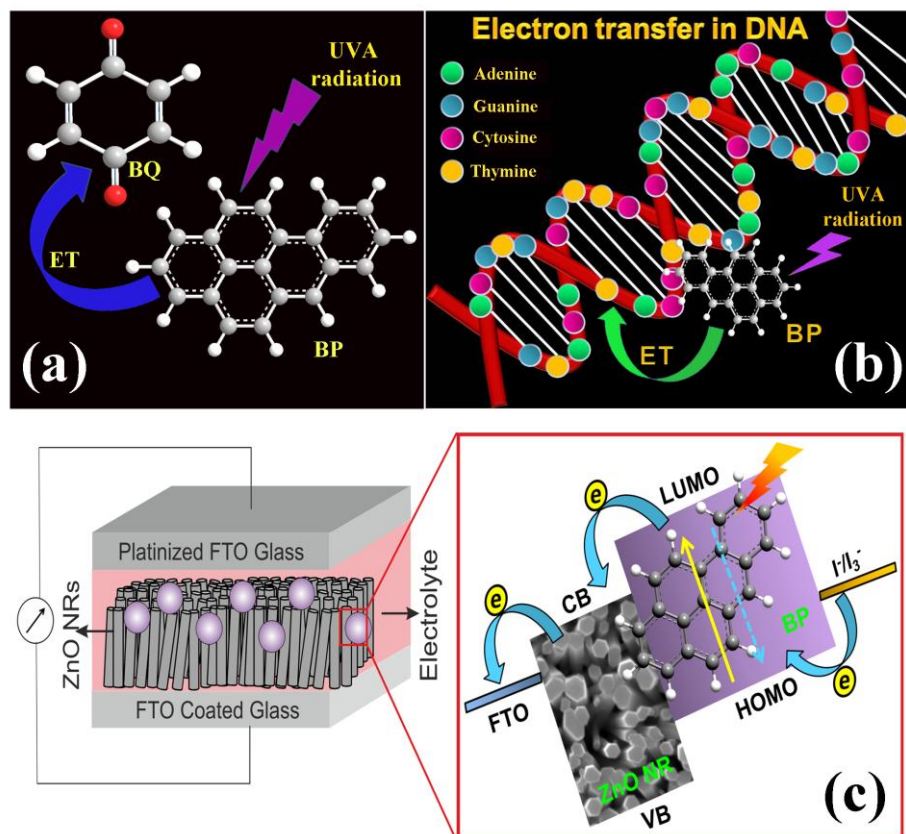
the absorption spectrum of BQ, the possibility of energy transfer from BP to BQ can be neglected, attributing the quenching to ET reactions. As evident from Table 7.1, at low quencher concentrations (1.25, 2.50 and 3.75 mM) the fluorescence transients of BP exhibit an ultrafast component around 500 ps while at higher BQ concentrations (5 to 11 mM) the fluorescence transients of the same exhibit two ultrafast components (~100 and ~800 ps) comparable to the ET components reported earlier in porphyrin-BQ models separated by different distances [29]. Such multiple ET components in the fluorescence transients of BP at different BQ concentrations strongly corroborate with the non-exponential nature of ET reactions and those components are attributed to the various modes of association (side to side or face to face) along with the different distances between BP and BQ in the solvent which control the ET rates [29]. As evident from earlier studies [25], BQ has a positive electron affinity of 1.89 eV and forms a stable negative ion

through charge transfer collisions. Furthermore, pyrene class of molecules are known to have a lower electron affinity (0.59 eV) [30] compared to BQ that further supports the ET from BP to BQ leading to the observed quenching in the fluorescence lifetime of BP with increasing BQ concentrations.

Table 7.1: The lifetime components of BP, at its characteristic emission peaks in presence of different quencher (BQ) concentrations ([Q]). λ_{em} represents the emission wavelength. τ represents the time constant in ns and the numbers in the parenthesis represent relative contribution of the component. τ_{av} represents the average lifetime in ns and is equivalent to τ_0 at [Q] = 0. $\tau_{av} = \tau$ at [Q] \neq 0. Error $\pm 5\%$

[Q] mM	λ_{em} (nm)	τ_1 (ns)	τ_2 (ns)	τ_3 (ns)	τ_4 (ns)	τ_{av} (ns)	τ_0/τ
0.00	410	19.32 (100%)				19.32	1.00
	430	2.00 (7%)	20.01 (93%)			18.75	1.00
	455	2.00 (15%)	20.27 (85%)			17.53	1.00
1.25	410	0.50 (10%)	16.67 (90%)			15.05	1.28
	430	0.50 (4%)	2.00 (9%)	17.32 (87%)		15.27	1.23
	455	0.50 (8%)	2.00 (16%)	17.24 (76%)		13.46	1.30
2.50	410	0.5 (12%)	14.72 (88%)			13.01	1.49
	430	0.50 (6%)	2.00 (10%)	15.34 (84%)		13.12	1.43
	455	0.50 (12%)	2.00 (18%)	15.33 (70%)		11.15	1.57
3.75	410	0.5 (16%)	13.22 (84%)			11.19	1.73
	430	0.50 (6%)	2.00 (14%)	13.83 (80%)		11.37	1.65
	455	0.50 (14%)	2.00 (20%)	13.76 (66%)		9.55	1.84
5.00	410	0.10 (4%)	0.80 (14%)	12.06 (82%)		10.01	1.93
	430	0.10 (8%)	0.80 (8%)	2.00 (12%)	12.46 (72%)	9.28	2.02
	455	0.10 (9%)	0.80 (13%)	2.00 (19%)	12.42 (59%)	7.82	2.24
6.25	410	0.10 (8%)	0.80 (15%)	11.13 (77%)		8.70	2.22
	430	0.10 (8%)	0.80 (8%)	2.00 (13%)	11.52 (71%)	8.51	2.20
	455	0.10 (11%)	0.80 (15%)	2.00 (20%)	11.42 (54%)	6.70	2.62
7.50	410	0.05 (14%)	0.80 (16%)	10.22 (70%)		7.29	2.65
	430	0.05 (14%)	0.80 (9%)	2.00 (13%)	10.62 (64%)	7.14	2.63
	455	0.05 (21%)	0.80 (18%)	2.00 (16%)	10.46 (45%)	5.18	3.38
8.75	410	0.05 (15%)	0.90 (17%)	9.57 (68%)		6.67	2.90
	430	0.05 (15%)	0.80 (12%)	2.00 (12%)	9.83 (61%)	6.34	2.96
	455	0.05 (21%)	0.80 (20%)	2.00 (16%)	9.72 (43%)	4.67	3.75
10.0	410	0.04 (20%)	0.80 (17%)	8.84 (63%)		5.71	3.38
	430	0.04 (21%)	0.80 (11%)	2.00 (13%)	9.23 (55%)	5.43	3.45
	455	0.04 (26%)	0.80 (20%)	2.00 (18%)	9.20 (36%)	3.84	4.57
11.0	410	0.04 (21%)	0.80 (18%)	8.34 (61%)		5.24	3.69
	430	0.04 (18%)	0.80 (15%)	2.00 (13%)	8.68 (54%)	5.07	3.70
	455	0.04 (28%)	0.80 (21%)	2.00 (18%)	8.61 (33%)	3.38	5.19

7.2.1.2. Ultrafast charge transfer reactions between BP and biological macromolecules. Upon monitoring the ET reaction from BP to BQ molecule as shown in Scheme 7.1 (a), another macromolecule, calf-thymus DNA (CT-DNA), has been considered to investigate the mode of interaction between BP and CT-DNA upon exciting the former with UVA radiation (Scheme 7.1 (b)). It has to be noted, as CT-DNA absorbs weakly above 300 nm [31], it will have negligible effect on the emission property of BP upon exciting the solution of BP-CT-DNA complex at 375 nm. Figure 7.3 (a) shows the temperature-dependent fluorescence spectra of BP-CT DNA complex. Emission spectra of BP in the presence of CT-DNA, show that the relative emission intensities of BP at the resolved peaks (410, 430 and 455 nm) are much higher compared to that of the aggregate peak around 490 nm. The relatively lower emission intensity of the aggregate peak compared to that of the monomer BP peaks in presence of CT-DNA is clear evidence of association between the two, particularly at low temperatures where the solubility of BP in aqueous medium is negligible being at around 10^{-8} M. As shown in the Figure 7.3 (a), the emission intensities of BP in CT-DNA enhance with the increase in temperature. Figure 7.3 (a) inset shows the emission intensities of the same, monitored at 410 nm as a function of temperature, where the enhancement in the emission intensity appears to initiate at about 25°C. To selectively monitor the interaction between BP monomers and the CT-DNA, fluorescence transients have been monitored at 410 nm where the contribution of BP aggregates is minimum or negligible. Figure 7.3 (b) shows the picosecond-resolved fluorescence transients of BP-CT-DNA complex at 20 and 87°C. The purpose of choosing high temperature around 87°C was to attain the melting temperature of genomic DNA, which has earlier been reported [32] to be 83°C. The corresponding lifetime components of the complex have been tabulated in Table 7.2. The ultrafast time components of 50 and 900 ps being comparable with the ET components observed in the fluorescence transient of BP undergoing ET reaction with BQ, are attributed to the UVA radiation induced ET between BP and DNA. Ionisation potential of aromatic hydrocarbons being lower than the nitrogenous bases in DNA [13] and pyrimidines being better electron acceptors than purines, it can be concluded that in the ET complex between BP and CT-DNA, electron flows from BP to DNA through the pyrimidine bases. As evident from Figure 7.3 (b) and



Scheme 7.1. UVA radiation induced electron transfer (ET) from benzo[a]pyrene (BP) to (a) organic molecule, benzoquinone (BQ) and (b) biological macromolecule, DNA. (c) Schematic representation of a model ZnO NR (gray)-based photodevice. BP (purple) molecules are anchored on ZnO NRs by surface adsorption. The charge separation and interparticle charge migration processes of the entire photodevice structure are shown.

Table 7.2, the relative contribution of the ET components of 50 and 900 ps decreases from 40 to 4% and from 33 to 11%, respectively, with the increase in temperature from 20 to 87°C. The time-resolved studies strongly corroborate with the temperature-dependent steady-state emission results of BP in CT-DNA as shown in Figure 7.3 (a), endorsing the fact that with the melting of DNA, the ET pathway from BP to DNA gets interrupted resulting in the enhancement of emission intensity of BP along with its excited state lifetime. The interruption in ET pathway from BP to DNA with the DNA melting can arise either due to the release of BP from DNA or due to the binding of BP to single stranded DNA in an orientation unfavourable for ET. As evident from Figure 7.3 (b) and Table 7.2, the fluorescence transient of BP in CT-DNA at 87°C can be fitted triexponentially with time components of 100 ps (4%), 800 ps (11%) and 22.04 ns (85%) while BP in buffer at

87°C produces a single lifetime component of 23 ns. Therefore, upon comparing the lifetime of BP in CT-DNA with that in buffer at 87°C, it can be concluded that at such high temperature, 85% of the DNA bound BP molecules get released to the surrounding buffer.

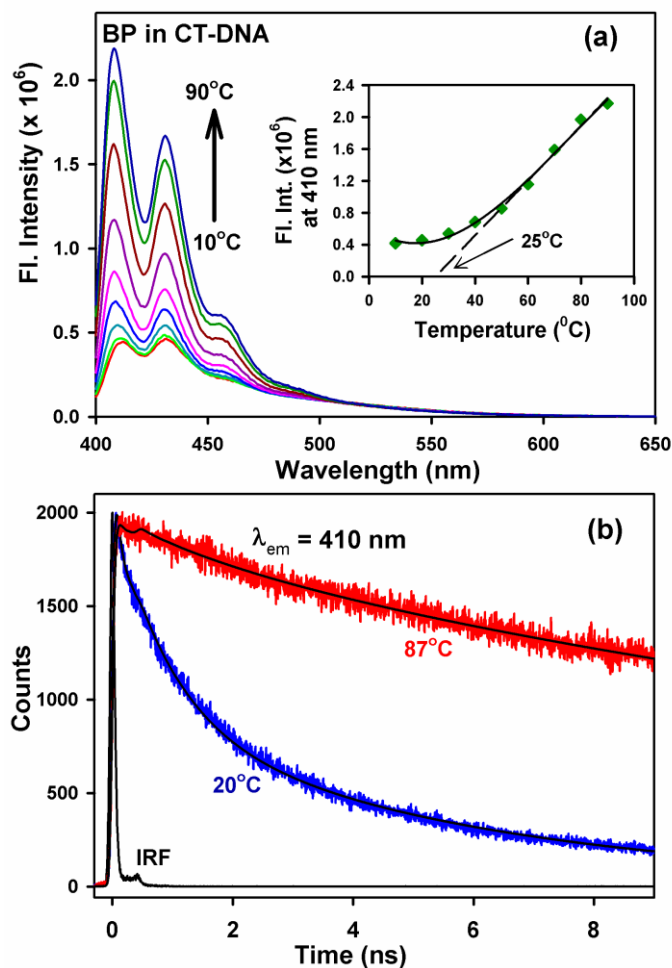


Figure 7.3. (a) Fluorescence spectra of BP in CT-DNA at different temperatures. Inset shows the fluorescence intensity of the same at 410 nm as a function of temperature and the bold line is the cubic polynomial fit. The broken line is the extrapolated linear fit of the exponentially rising part of the plot, where the intercept at x -axis represents the initiation temperature for such rise in the fluorescence intensity. (b) Picosecond-resolved fluorescence transients of the same at 20° and 87°C. Excitation wavelength (λ_{ex} = 375 nm).

The observed perturbation of ET from BP to CT-DNA, with the increase in temperature, motivated us to investigate the structural change of the latter associated with such thermal enhancement. Figures 7.4 (a) and (b) show the absorption spectra of CT-

DNA at different temperatures in absence and presence of BP, respectively. As evident from the Figures 7.4 (a) and (b), the absorption spectra of CT-DNA do not show any significant change while enhancing the temperature upto 70⁰C. The corresponding melting curves of CT-DNA, constructed from the absorbance at 260 nm [33] while increasing the

Table 7.2: Fluorescence lifetime components (τ) of BP in buffer and upon interaction with CT-DNA at different temperatures along with the rotational time constants (τ_r). Emission wavelength (λ_{em}) and excitation wavelength (λ_{ex}) are 410 and 375 nm respectively. The numbers in the parenthesis represent relative contribution of the component. τ_{av} represents the average lifetime in ns. Error $\pm 5\%$

Sample	Temperature ($^{\circ}$ C)	Fluorescence lifetime			Anisotropy		
		τ_1 (ns)	τ_2 (ns)	τ_3 (ns)	τ_{av} (ns)	τ_r (ns)	Offset (r_0)
BP in CT-DNA	20	0.05 (40%)	0.90 (33%)	5.61 (27%)	1.52	0.14	0.15
	87	0.10 (4%)	0.80 (11%)	22.04 (85%)	18.83	0.07	0.01
BP in buffer	87	23.08 (100%)			23.08	0.05	0.00

temperature upto 90⁰C are shown in the insets of Figures 7.4 (a) and (b) respectively. As evident from the insets of Figures 7.4 (a) and (b), both the curves look alike and do not reach the saturation at 90⁰C (upto which the temperature was enhanced) which suggest that BP induced structural changes in CT-DNA cannot be manifested through temperature dependent absorption spectroscopy. Hence we have used the temperature dependent CD spectroscopy to monitor the BP induced structural changes in the CT-DNA. Insets of Figures 7.5 (a) and (b) show the temperature-dependent optical rotation of CT-DNA in the absence and presence of BP, respectively. As evident from the insets of Figures 7.5 (a) and (b), at low temperatures, a positive peak around 270 nm and a negative peak around 245 nm in the far UV spectrum are in accordance with the average secondary structure of DNA [32] and the corresponding UV absorption spectra are dominated by the DNA absorption as shown in the Figures 7.4 (a) and (b). Therefore, it is difficult to infer the structural perturbation of CT-DNA in the presence of BP at low temperatures. It is clear from the insets of Figures 7.5 (a) and (b) that the peak at 270 nm is mostly affected by the temperature induced melting of the DNA. The change in the optical rotation associated with this peak has been monitored to construct the temperature-induced melting of the CT-

DNA in the absence and presence of BP, as shown in Figures 7.5 (a) and (b), respectively. As evident from the Figures, the corresponding DNA melting curves do not reach the saturation level at 90°C, up to which the temperature of the DNA has been raised. Thus, melting temperatures of CT-DNA in the absence and presence of BP cannot be calculated from the respective melting curves following the standard procedures. However, the

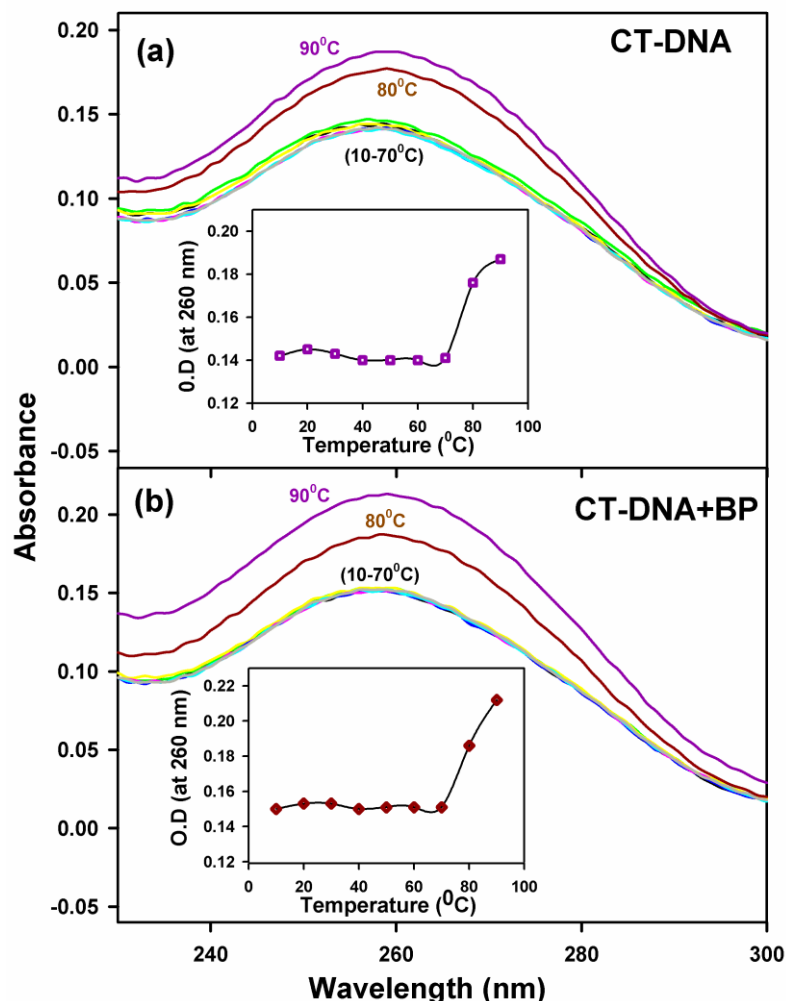


Figure 7.4. Temperature dependent absorption spectra of CT-DNA as a function of wavelength in absence (a) and presence (b) of BP. Insets show the respective optical density (O.D) at 260 nm with increase in temperature where solid lines are the guide to the eye.

temperature at which the melting initiates for either case can be approximated, by extrapolating the exponential part of the melting curves on x-axis. Though the temperatures are deduced from only three data points in each case, the overall nature of the temperature dependent change in the optical rotation of CT-DNA at 270 nm is completely

different in absence and presence of BP, as shown in Figures 7.5 (a) and (b). The uncertainties in the temperature, at which the DNA melting initiates, being same for both the cases (in absence and presence of BP), have not been considered. The corresponding temperatures, at which DNA melting initiates in the absence and presence of BP, have been found out to be 65 and 59°C respectively. The initiation of DNA melting at

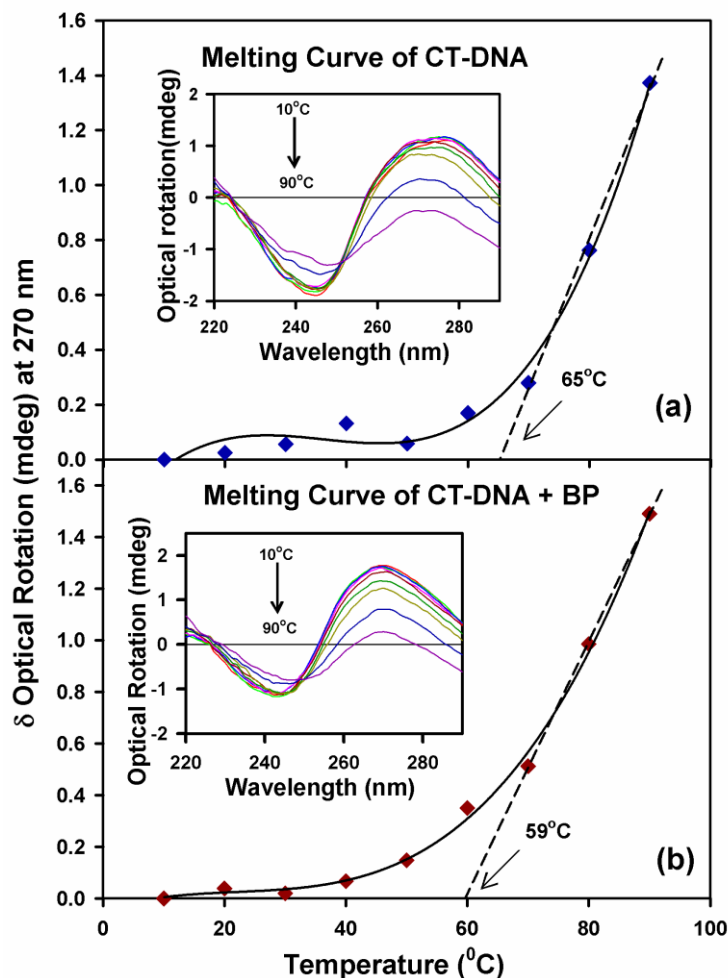


Figure 7.5. Difference in optical rotation (mdeg) of CT-DNA at 270 nm with increase in temperature in absence (a) and presence (b) of BP. Insets show the respective temperature-dependent optical rotation of the CT-DNA as a function of wavelength. Solid lines are the cubic polynomial fit. The broken lines are the extrapolated linear fits where the intercepts at x-axis represent the initiation temperature of the corresponding melting processes.

comparatively lower temperature in the presence of BP is a clear signature of the association of BP with DNA, leading to the weakening of hydrogen bonds between the two DNA strands. Thus, lower thermal energy is required to initiate DNA melting in the

presence of BP compared to that in its absence. Here, it has to be noted that the initiation temperature observed for the enhancement in emission intensity of BP in CT-DNA (Figure 7.3 (a) inset) is much lower compared to that of BP assisted DNA melting, which signifies that perturbation in ET from BP to CT-DNA initiates at some lower temperature prior to the DNA melting. Such perturbation in ET before the onset of DNA melting can arise due to some changes in the orientation of DNA bound BP molecules, interfering in the ET pathway.

For better understanding of the fate of BP with the melting of DNA, the fluorescence anisotropies of BP have been monitored in the presence of DNA at 20°C and at DNA melting temperature (~87°C), as shown in Figures 7.6 (a) and (b), respectively.

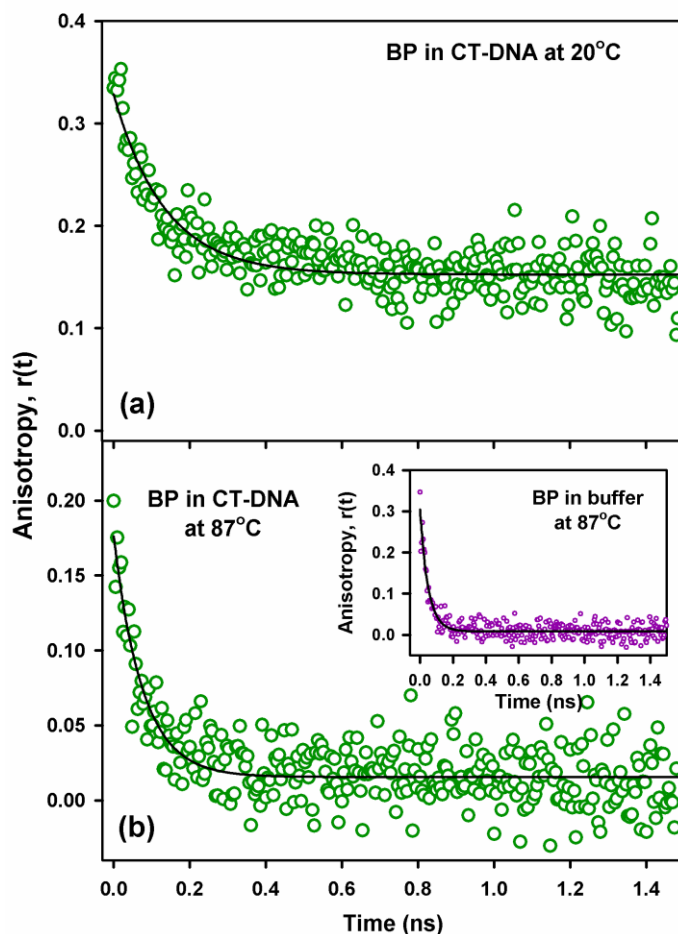


Figure 7.6. Fluorescence anisotropy of BP in CT-DNA at (a) 20°C and (b) 87°C and in 50 mM phosphate buffer at 87°C (inset of b). Solid lines indicate exponential fitting of the experimental data points.

The rotational time constants (τ_r) of BP in DNA have been calculated from the respective fluorescence anisotropies and have been compared with that of BP in phosphate buffer at 87°C (inset of Figure 7.6 (b)). The values of the respective τ_r have been tabulated in Table 7.2. The fluorescence anisotropy of BP in CT-DNA at 20°C produces a τ_r value of 140 ps which corresponds to the rotational motion of the probe BP in the DNA, along with a residual offset of 0.15. The origin of such offset is due to the overall motion of the DNA which does not decay within the experimental time window. Using the time-resolved fluorescence anisotropy study, Ghiggino and co-workers [34] have documented the dynamics of energy transfer in multiporphyrin functionalized dendrimers where they observed a fast decay (~80 ps) in the anisotropy profile with a residual offset similar to our observation. As shown in Figure 7.6 and Table 7.2, the rotational time constant of BP in CT-DNA decreases from 140 ps to 70 ps and the residual offset becomes negligible as the DNA reaches its melting temperature. The τ_r value calculated for BP in CT-DNA at 87°C is close to that calculated for BP in buffer at the same temperature, indicating the release of BP to buffer with the melting of DNA. Here it has to be noted that the solubility of BP in aqueous medium at low temperatures being extremely low, experiments could not be performed with the aqueous solution of BP at low temperatures. However, the solubility of the same in aqueous buffer medium increases from 10^{-8} M to 10^{-7} M, with enhancement in temperature from 20 to 87°C. Therefore, with the dilute aqueous solution of BP at 87°C in 0.05 M phosphate buffer, anisotropy experiments have been performed which gives the rotational time constant of 50 ps without any offset. The higher solubility of BP in buffer at elevated temperature further supports the release of BP from DNA at the DNA melting temperature around 87°C. Thus, unlike ethidium (Et), a well known DNA intercalator which significantly remains bound to single stranded (ss) DNA upon DNA melting producing a characteristic lifetime component [35] of about 18 ns and a DNA minor groove binder, Hoechst 33258 (H258) which also remains associated with DNA at high temperatures [32], BP almost completely dissociates from DNA at high temperature (beyond the melting temperature of DNA) with no signature of binding to ss DNA.

After investigating ET reaction from BP to CT-DNA in a temperature-dependent manner, we further investigated such interaction with another biological macromolecule, human serum albumin (HSA), as carcinogens are known to interact not only with DNAs

but also with proteins [14, 36]. Figure 7.7 (a) shows the emission spectra of BP in HSA at 20 and 87°C upon excitation with UVA radiation. The relatively lower emission intensity of BP at the aggregate peak around 490 nm compared to the monomer peaks at 410, 430 and 455 nm, similar to our observation for BP upon complexation with CT-DNA (Figure 7.3 (a)), is again a clear evidence of association between the carcinogen and HSA. As evident from the Figure 7.7 (a), the emission intensity of BP in the presence of HSA also enhances with the increase in temperature from 20 to 87°C similar to that observed for BP-CT-DNA complex. However, the extent of enhancement in the emission intensity of BP in the presence of HSA is much lower compared to that in the presence of CT-DNA. Therefore, with the increase in temperature the ET pathway of BP in the presence of HSA gets perturbed to some lower extent, compared to our previous observation in the presence of CT-DNA. Figure 7.7 (a) inset shows the time-resolved fluorescence transients of BP-HSA complex at 20 and 87°C while exciting with UVA radiation. The corresponding lifetime components have been tabulated in Table 7.3. The ultrafast time components of 70 and 870 ps in the lifetime of BP upon association with HSA strongly corroborate with the ET components observed in the fluorescence transients of BP while participating in ET reaction with BQ and DNA, mentioned above and thus have been attributed to the UVA radiation induced ET from BP to HSA. Amino acids in HSA possessing lower oxidation potential compared to BP can be involved in such ET reaction from BP to HSA. For example, the oxidation potential of tryptophan in HSA being lower (~ 1 V) [37] than that of BP (~ 1.18 V) [38], supports the flow of electrons from BP to HSA in the observed ET reaction between the two. In contrast to our previous observation in the presence of CT-DNA, the contribution of ET components of 70 and 870 ps in the fluorescence transient of BP in the presence of HSA found to get decreased from 39 to 37% and from 23 to 13%, respectively, with the similar increase in temperature from 20 to 87°C. The major contribution of the ET components in the fluorescence transient of BP in HSA even at 87°C, where the protein gets significantly unfolded [39], suggests that BP remains bound to unfolded HSA unlike CT-DNA at high temperature. For further confirmation regarding the association of BP with unfolded HSA, the fluorescence anisotropy of BP at 87°C has been compared with that at 20°C as shown in Figures 7.7 (b) and (c). At both the

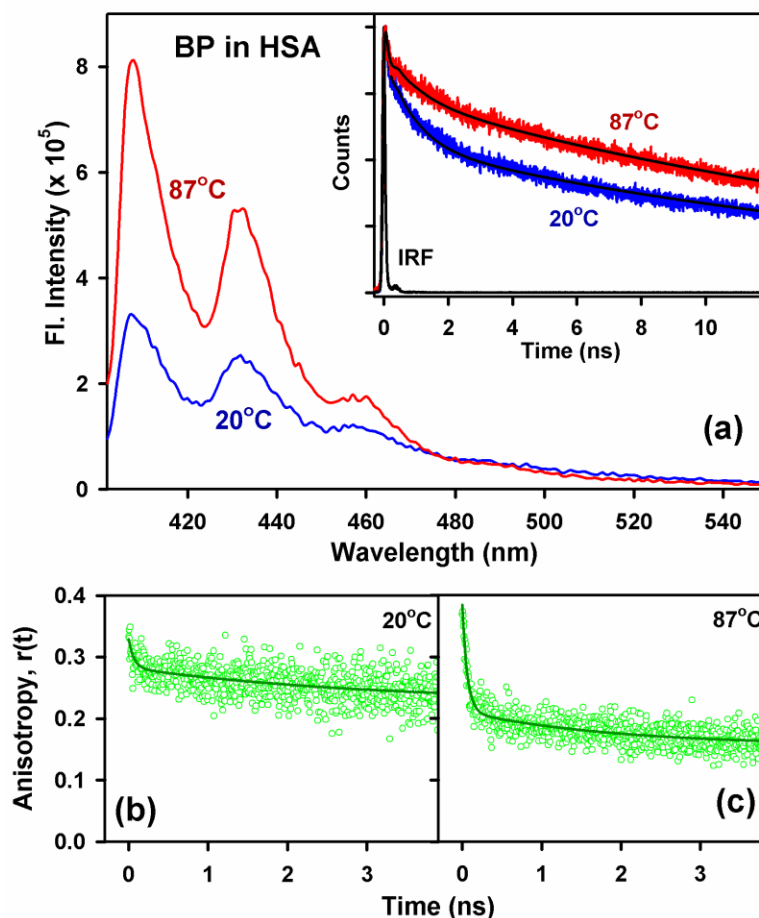


Figure 7.7. (a) Fluorescence spectra of BP in HSA at 20° and 87°C and inset shows the corresponding time-resolved fluorescence transients. Fluorescence anisotropy of the same at (b) 20°C and (c) 87°C. Solid lines indicate exponential fitting of the experimental data points.

temperatures 20 and 87°C, the anisotropy exhibits biexponential decay with a residual offset of 0.22 and 0.16, respectively. The corresponding τ_r values are tabulated in Table 7.3. The offset observed in BP-HSA complex at 20°C and 87°C is due to the overall motion of the protein HSA which does not decay within the experimental time window. The ultrafast time component ~ 70 ps with a huge offset, observed in the temporal decays of the rotational anisotropy of BP bound to HSA at 20 and 87°C, is comparable to the electronic energy transfer component in the anisotropy profile of multiporphyrin functionalized dendrimers [34] mentioned before. The presence of electronic energy transfer component along with a significant residual offset in the rotational anisotropy of BP in unfolded HSA at 87°C confirm the association of BP with unfolded HSA unlike

denatured CT-DNA. The association of BP with unfolded HSA strongly corroborates with one of our earlier studies [39], where it has been shown that an extremely hydrophobic probe can reside in the subdomain IIIA of the protein even at its thermally unfolded states.

Table 7.3: Fluorescence lifetime components (τ) of BP upon interaction with HSA at different temperatures along with the rotational time constants (τ_r). Emission wavelength (λ_{em}) and excitation wavelength (λ_{ex}) are 410 and 375 nm respectively. The numbers in the parenthesis represent relative contribution of the component. τ_{av} represents the average lifetime in ns. Error $\pm 5\%$

Sample	Temperature (°C)	Fluorescence lifetime				Anisotropy		Offset (r_0)
		τ_1 (ns)	τ_2 (ns)	τ_3 (ns)	τ_{av} (ns)	τ_r (ns)		
BP in HSA	20	0.07 (39%)	0.87 (23%)	19.09 (38%)	7.48	0.07 (46%)	2.99 (54%)	0.22
	87	0.07 (37%)	0.90 (13%)	20.12 (50%)	10.20	0.06 (76%)	1.89 (24%)	

7.2.1.3. Investigation on the ET reaction from BP to zinc oxide (ZnO) nanorods (NRs). Our investigation on the ET reaction from BP to organic molecules and biological macromolecules (shown in Scheme 7.1 (a) and (b)) has been further extended with inorganic zinc oxide (ZnO) nanorods (NRs). The purpose of this study is to probe whether ET from BP to ZnO NRs is achieved in terms of photocurrent. By making the use of basic working principle of a dye-sensitized solar cell, we have designed a photodevice, as schematically shown in Scheme 7.1 (c). Figure 7.8 (a) left inset shows the scanning electron micrographs (SEM images) of ZnO NRs. Morphological characterization by SEM (Figure 7.8 (a) left inset) indicates the formation of arrays of ZnO NRs with a preferential growth along the polar facets [002 direction] of the hexagonal wurtzite crystal. The NRs

Table 7.4: The lifetime components of BP monitored at 410 nm (λ_{em}) on thin film in presence ZnO NRs. τ represents the time constant in ns and the numbers in the parenthesis represent relative contribution of the components. Error $\pm 5\%$.

Sample	τ_1 (ns)	τ_2 (ns)	τ_3 (ns)
ZnO NR anchored BP	0.05 (89%)	0.88 (6%)	39.64 (5%)

growing perpendicular to the substrate are nearly uniform in length ($\sim 3 \mu\text{m}$) and possess a characteristic hexagonal cross-section with diameter in the range of 180 nm. For the investigation of UVA radiation induced ET reaction between BP monomers and ZnO NRs, picosecond-resolved fluorescence transient of BP has been monitored at 410 nm on thin film in the presence of ZnO NRs as shown in Figure 7.8 (a) and it is fitted with the values given in Table 7.4. As evident from Figure 7.8 (a) and Table 7.4, ultrafast components of 50 and 880 ps appear in the fluorescence transient of BP in presence of ZnO NRs, along with a long component ($\sim 39 \text{ ns}$) comparable to the lifetime of BP in degassed benzene [13]. To differentiate the ultrafast component of 50 ps from IRF, the fluorescence transient of ZnO NR anchored BP is shown over a narrow time window of 0.7 ns in Figure 7.8 (a) right inset. The ultrafast components in the fluorescence transient of BP in the presence of ZnO NRs being comparable with the ET components observed in the fluorescence transients of the same while undergoing ET reaction with organic molecules and biological macromolecules (mentioned before) validate the ET from BP to ZnO NRs. Here it has to be noted that the observed ET components in the lifetime of BP in different systems are similar but they are exactly not the same and this difference can be attributed to the difference in redox properties of the systems. Moreover the picosecond resolved lifetime measurements were all done in time correlated single photon counting (TCSPC) setup having instrument response function (IRF) of 80 ps hence very fine variations (in femtosecond time scale) of the ET process are beyond the resolution of the used setup. The ET from BP to ZnO NRs has been further confirmed by monitoring the flow of electrons in terms of photocurrent. Figure 7.8 (b) shows the wavelength dependent variation in photocurrent, monitored in ZnO NR fabricated photodevice in the presence and absence of BP. As shown by the broken lines in the Figure 7.8 (b), the photocurrent vs. wavelength curve in the presence of BP can be deconvoluted into three characteristic peaks at 350, 382 and 400 nm similar to the absorption peaks of BP [40] while that in absence of BP produces a single peak corresponding to the absorption peak of ZnO at 382 nm. The enhanced photocurrent obtained in the presence of BP from ZnO NR fabricated photodevice confirms the role of BP as the photosensitizer. Inset of Figure 7.8 (b) indicates that in the wavelength range of 300 to 380 nm, power remains almost constant while there

is a constant enhancement in photocurrent, suggesting that the photocurrent measured is solely dependent on the flow of electrons irrespective of the power.

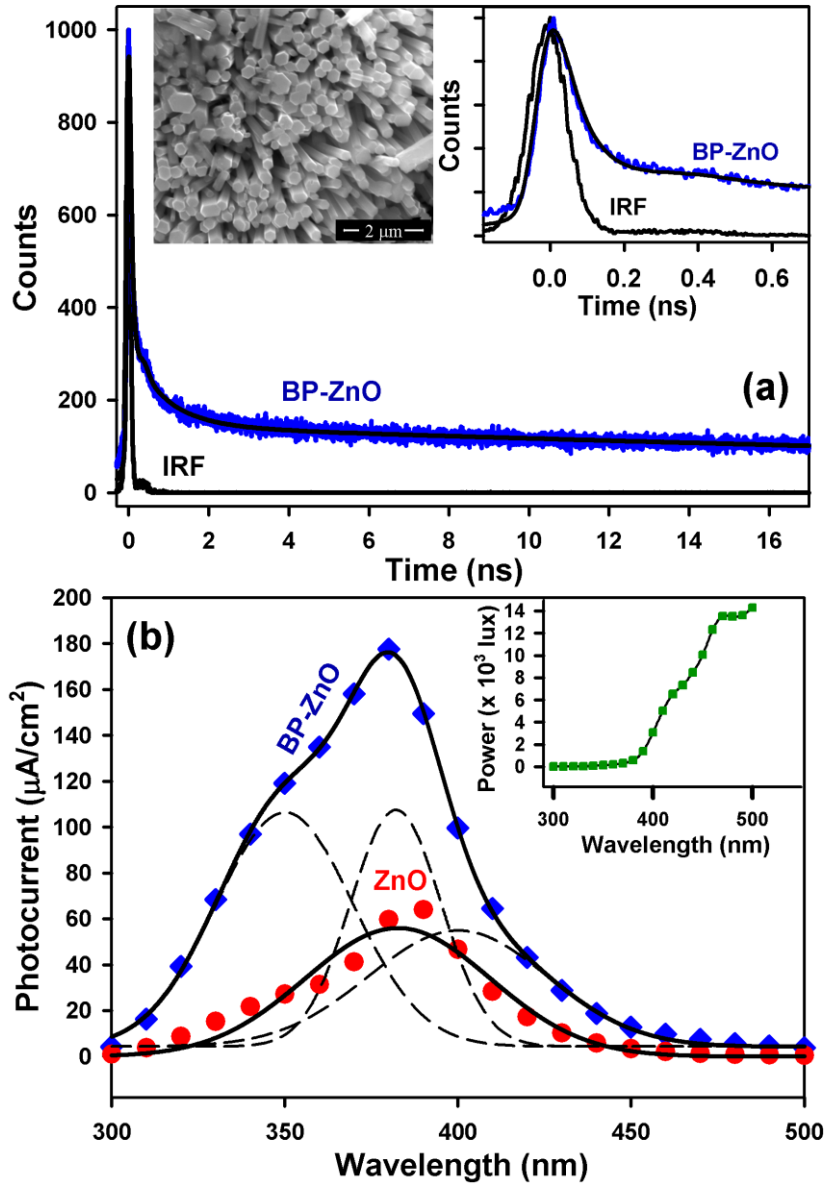


Figure 7.8. (a) The time-resolved fluorescence transient of BP-ZnO complex in thin film and the right inset shows the same in a narrow time window, the left inset shows the scanning electron micrographs (SEM images) of ZnO NRs, (b) the wavelength-dependent photocurrent obtained from ZnO NR fabricated photodevices in the presence and absence of BP. Bold lines represent the Gaussian fits of the respective plots and the broken lines represent the deconvoluted plots of BP-ZnO complex having peaks at 350, 382 and 400 nm. Inset shows the variation of power over the same wavelength range where the bold line is the guide to the eye.

7.3. Conclusion:

Electron transfer (ET) reactions are well known for their importance in DNA damage and cancer biochemistry. In the present study, we explored the strong affinity of the carcinogen benzo[*a*]pyrene (BP) to donate electrons to different class of molecules like para-benzoquinone (BQ), biological macromolecules like calf-thymus DNA and human serum albumin (HSA) and inorganic nano structures like zinc oxide (ZnO) nanorods (NRs). While steady state and time resolved fluorescence spectroscopy results reveal the quenching of the emission of BP in presence of organic molecules, biological macromolecules and nano structures, CD spectroscopy results monitor the BP induced structural changes in the CT-DNA and ZnO-NR based photodevice confirm the charge transfer reaction from BP by directly monitoring the flow of electrons in terms of photocurrent. Our ultrafast electron transfer studies from BP to four different types of molecules suggest BP as a strong electron donor which can be considered as one of its vital characteristics responsible for its carcinogenic activity. Therefore, our work hints that the ET pathway from BP can be targeted to prevent BP mediated carcinogenesis. It has to be noted that carcinogenesis of BP may involve other modes of interaction with biological macromolecules apart from ET which our objective does not include. We emphasize one of the key aspects of BP which can assist in further research on this carcinogen.

References

- [1] D. H. Phillips, Fifty Years of Benzo(a)pyrene, *Nature* 303 (1983) 468.
- [2] D. H. Phillips, Polycyclic Aromatic Hydrocarbons in the Diet, *Mutat. Res.* 443 (1999) 139.
- [3] H. Ling, J. M. Sayer, B. S. Plosky, H. Yagi, F. Boudsocq, R. Woodgate, D. M. Jerina, W. Yang, Crystal Structure of a Benzo[a]pyrene Diol Epoxide Adduct in a Ternary Complex with a DNA Polymerase, *Proc. Natl. Acad. Sci.* 101 (2004) 2265.
- [4] S. Alam, M. J. Conway, H. S. Chen, C. Meyers, The Cigarette Smoke Carcinogen Benzo[a]pyrene Enhances Human Papillomavirus Synthesis, *J. Virol.* 82 (2008) 1053.
- [5] K. Dutta, D. Ghosh, A. Nazmi, K. L. Kumawat, A. Basu, A Common Carcinogen Benzo[a]pyrene Causes Neuronal Death in Mouse via Microglial Activation, *Plos one* 5 (2010) 1.
- [6] Y. Shimizu, Y. Nakatsuru, M. Ichinose, Y. Takahashi, H. Kume, J. Mimura, Y. F. Kuriyama, T. Ishikawa, Benzo[a]pyrene Carcinogenicity is Lost in Mice Lacking the Aryl Hydrocarbon Receptor, *Proc. Natl. Acad. Sci.* 97 (2000) 779.
- [7] M. F. Denissenko, A. Pao, M. S. Tang, G. P. Pfeifer, Preferential Formation of Benzo[a]pyrene Adducts at Lung Cancer Mutational Hotspots in P53, *Science* 274 (1996) 430.
- [8] J. Kapitulnik, W. Levin, A. H. Conney, H. Yagi, D. M. Jerina, Benzo[a]pyrene 7,8-dihydrodiol is More Carcinogenic than Benzo[a]pyrene in New Born Mice, *Nature* 266 (1977) 378.
- [9] T. E. Eling, D. C. Thompson, G. L. Foureman, J. F. Curtis, M. F. Hughes, Prostaglandin H Synthase and Xenobiotic Oxidation, *Annu. Rev. Pharmacol. Toxicol.* 30 (1990) 1.
- [10] M. Wilk, W. Girke, Reactions Between Benzo[a]pyrene and Nucleo Bases by One-Electron Oxidation, *J. Natl. Cancer Inst.* 49 (1972) 1585.
- [11] C. Wan, T. Fiebig, S. O. Kelley, C. R. Treadway, J. K. Barton, A. H. Zewail, Femtosecond Dynamics of DNA-Mediated Electron Transfer, *Proc. Natl. Acad. Sci.* 96 (1999) 6014.

- [12] J. Nguyena, Y. Maa, T. Lua, R. G. Bristowb, D. A. Jaffrayc, Q. B. Lua, Direct Observation of Ultrafast-Electron-Transfer Reactions Unravels High Effectiveness of Reductive DNA Damage, *Proc. Natl. Acad. Sci.* 108 (2011) 11778.
- [13] N. E. Geacintov, T. Prusik, J. M. Khosrofian, Properties of Benzopyrene-DNA Complexes Investigated by Fluorescence and Triplet Flash Photolysis Techniques, *J. Am. Chem. Soc.* 98 (1976) 6444.
- [14] P. L. Skipper, S. R. Tannenbaum, Protein Adducts in the Molecular Dosimetry of Chemical Carcinogens, *Carcinogenesis* 11 (1990) 507.
- [15] E. H. Kure, A. Andreassen, S. Ovrebø, E. Grzybowska, Z. Fiala, M. Strozyk, M. Chorazy, A. Haugen, Benzo(a)pyrene-Albumin Adducts in Humans Exposed to Polycyclic Aromatic Hydrocarbons in an Industrial Area of Poland, *Occup. Environ. Med.* 54 (1997) 662.
- [16] B. N. Srinivasan, E. Fujimori, Benzo[a]pyrene-Serum: Albumin/Cysteine Interactions: Fluorescence and Electron Spin Resonance Studies, *Chem. Biol. Interact.* 28 (1979) 1.
- [17] D. J. Brenner, R. Doll, D. T. Goodhead, E. J. Hall, C. E. Land, J. B. Little, J. H. Lubin, D. L. Preston, R. J. Preston, J. S. Puskin, E. Ron, R. K. Sachs, J. M. Samet, R. B. Setlow, M. Zaider, Cancer Risks Attributable to Low doses of Ionizing radiation: Assessing What We Really Know, *Proc. Natl. Acad. Sci.* 100 (2003) 13761.
- [18] C. E. Land, J. D. Boice, R. E. Shore, J. E. Norman, M. Tokunaga, Breast Cancer Risk From Low-Dose Exposures to Ionizing Radiation: Results of Parallel Analysis of Three Exposed Populations of Women, *J. Natl. Cancer Inst.* 65 (1980) 353.
- [19] S. Kawanishi, Y. Hiraku, S. Oikawa, Mechanism of Guanine-Specific DNA Damage by Oxidative Stress and its Role in Carcinogenesis and Aging, *Mutat. Res. Rev. Mutat.* 488 (2001) 65.
- [20] T. Toyooka, Y. Ibuki, M. Koike, N. Ohashi, S. Takahashi, R. Goto, Coexposure to Benzo[a]pyrene Plus UVA Induced DNA Double Strand Breaks: Visualization of Ku Assembly in the Nucleus Having DNA Lesions, *Biochem. Biophys. Res. Commun.* 322 (2004) 631.
- [21] T. Toyooka, Y. Ibuki, F. Takabayashi, R. Goto, Coexposure to Benzo[a]pyrene and UVA Induces DNA Damage: First proof of Double-Strand Breaks in a Cell-Free System, *Environ. Mol. Mutagen.* 47 (2006) 38.

- [22] Q. Kang, Y. Chen, C. Li, Q. Cai, S. Yao, C. A. Grimes, P. Calabresi, A Photoelectrochemical Immunosensor for Benzo[a]pyrene Detection Amplified by Bifunctional Gold Nanoparticles, *Chem. Commun.* 47 (2011) 12509.
- [23] N. Atal, P. P. Saradhi, P. Mohanty, Inhibition of the Chloroplast Photochemical Reactions by Treatment of Wheat Seedlings with Low Concentrations of Cadmium: Analysis of Electron Transport Activities and Changes in Fluorescence Yield, *Plant Cell Physiol.* 32 (1991) 943.
- [24] S. Banerjee, S. Sarkar, K. Lakshman, J. Dutta, S. K. Pal, UVA Radiation Induced Ultrafast Electron Transfer from a Food Carcinogen Benzo[a]pyrene to Organic Molecules, Biological Macromolecules and Inorganic Nano Structures, *J. Phys. Chem. B* 117 (2013) 3726.
- [25] C. D. Cooper, W. T. Naff, R. N. Compton, Negative Ion Properties of p-Benzoquinone: Electron Affinity and Compound States, *J. Chem. Phys.* 63 (1975) 2752.
- [26] S. C. Beck, D. T. Cramb, Condensed Phase Dispersive Interactions of Benzo[a]pyrene with Various Solvents and with DNA: A Twist on Solvatochromism, *J. Phys. Chem. B* 104 (2000) 2767.
- [27] J. R. Lakowicz, *Principles of Fluorescence Spectroscopy*, Kluwer Academic/Plenum, New York, 1999.
- [28] T. A. Wells, A. Losi, R. Dai, P. Scott, S. M. Park, J. Golbeck, P. S. Song, Electron Transfer Quenching and Photoinduced EPR of Hypericin and the Ciliate Photoreceptor Stentorin, *J. Phys. Chem. A* 101 (1997) 366.
- [29] B. A. Leland, A. D. Joran, P. M. Felker, J. J. Hopfield, A. H. Zewail, P. B. Dervan, Picosecond Fluorescence Studies on Intramolecular Photochemical Electron Transfer in Porphyrins Linked to Quinones at Two Different Fixed Distances, *J. Phys. Chem.* 89 (1985) 5571.
- [30] G. Chen, R. G. Cooks, Electron Affinities of Polycyclic Aromatic Hydrocarbons Determined by the Kinetic Method, *J. Mass. Spectrom.* 30 (1995) 1167.
- [31] J. C. Sutherland, K. P. Griffin, Absorption Spectrum of DNA for Wavelengths Greater Than 300 nm, *Rad. Res.* 86 (1981) 399.
- [32] D. Banerjee, S. K. Pal, Direct Observation of Essential DNA Dynamics: Melting and Reformation of the DNA Minor Groove, *J. Phys. Chem. B* 111 (2007) 10833.

- [33] T. Douki, Effect of Denaturation on the Photochemistry of Pyrimidine Bases in Isolated DNA, *J. Photochem. Photobiol. B* 82 (2006) 45.
- [34] E. K. L. Yeow, K. P. Ghiggino, J. N. H. Reek, M. J. Crossley, A. W. Bosman, A. P. H. J. Schenning, E. W. Meijer, The Dynamics of Electronic Energy Transfer in Novel Multiporphyrin Functionalized Dendrimers: A Time-Resolved Fluorescence Anisotropy Study, *J. Phys. Chem. B* 104 (2000) 2596.
- [35] S. Banerjee, D. Bhowmik, P. K. Verma, R. K. Mitra, A. Sidhanta, G. Basu, S. K. Pal, Ultrafast Spectroscopic Study on Caffeine Mediated Dissociation of Mutagenic Ethidium from Synthetic DNA and Various Cell Nuclei, *J. Phys. Chem. B* 115 (2011) 14776.
- [36] B. Ketterer, Interactions Between Carcinogens and Proteins, *Br. Med. Bull.* 36 (1980) 71.
- [37] N. Marme, J. P. Knemeyer, M. Sauer, J. Wolfrum, Inter- and Intramolecular Fluorescence Quenching of Organic Dyes by Tryptophan, *Bioconjugate Chem.* 14 (2003) 1133.
- [38] E. Keskin, Y. Yardim, Z. Senturk, Voltammetry of Benzo[a]pyrene in Aqueous and Nonaqueous Media: Adsorptive Stripping Voltammetric Determination at Pencil Graphite Electrode, *Electroanalysis* 22 (2010) 1191.
- [39] S. S. Sinha, R. K. Mitra, S. K. Pal, Temperature-Dependent Simultaneous Ligand Binding in Human Serum Albumin, *J. Phys. Chem. B* 112 (2008) 4884.
- [40] J. S. Larsen, J. Waluk, S. Eriksson, E. W. Thulstrup, Electronic States of Benzo[a]pyrene. Linear and Magnetic Circular Dichroism, Polarized Fluorescence, and Quantum Chemical Calculations, *J. Am. Chem. Soc.* 114 (1992) 1942.

Chapter 8

Ultrafast Spectroscopic Studies on the Nonradiative Energy Transfer from Various Vibronic Bands of the Food Carcinogen Benzo[*a*]pyrene in Various Biologically Relevant Environments in Aqueous Medium:

8.1. Introduction:

Pyrene molecules belonging to a class of polycyclic aromatic hydrocarbons (PAHs) have several appealing photophysical properties which make them suitable for use as effective fluorescence probes [1-4]. One of those properties is the sensitivity of their spectral parameters, such as change in vibronic structure (especially intensity ratios of first and third vibronic bands) to the change of the environment [5]. The effects of temperature and solute-solvent interactions on the various vibronic fine structures in the emission spectra of pyrene class of molecules have been well explored [2, 6-7] and reveal the differential perturbation of the individual vibronic bands. Benzo[*a*]pyrene (BP), one of the well-known pyrene derivatives and a potential carcinogen to which humans are most frequently exposed [8], exhibits differential shifts of its individual vibronic structures as a function of the refractive index of the surrounding solvent [6]. BP is a by-product of grilled foods [9] and tobacco [10] and fuel combustion and has long been linked to various human cancers, particularly lung and skin. Though there have been extensive studies on the environmental effects on the steady-state fluorescence spectrum of pyrene [2], solvatochromism of BP manifested through their excitation and emission peak shifts in a wide variety of solvents [6], the effects of different solvents on the excited state lifetime at the different vibronic bands of such molecules, highlighting the consequence of solvent dipole/dielectric constant on the non-radiative rates are less attended.

Another important aspect is the dipolar interaction of the pyrene class of dyes with other molecules manifested in Förster resonance energy transfer (FRET). The differential

behavior of the individual vibronic bands, in the emission spectra of pyrene and its derivatives, in response to change in temperature [7], polarity² and refractive index [6] of the host solvent is well known while reports on such behavior of these bands while undergoing dipolar interactions with different molecules is still lacking in the literature. FRET, which is also known as “spectroscopic ruler” [11-13], is very often used to measure the distance between two sites on a macromolecule [14]. As pyrene and its derivatives are known to interact with biological macromolecules [6, 15], FRET can serve as an efficient tool for the investigation of the biomolecular recognition of these molecules. In one of the earlier studies [16], attempts to use FRET from pyrene class of molecules to perylene have been made for nucleic acid assays under homogeneous solution conditions using steady-state spectroscopy. In another recent study [17], FRET has been used as a tool for the detection of PAH’s antibody binding using a hydroxyl derivative of BP as a FRET donor and sulforhodamine B as the energy acceptor employing both steady-state and time resolved spectroscopy. However, investigation of the vibronic bands under dipolar coupling, was beyond the scope of the studies. It has also to be noted that estimation of D-A distance from steady-state FRET studies is found to be inconclusive [18].

Here, we have studied excited state fluorescence relaxation dynamics of BP in a number of solvents with various dipole moments/refractive index. We have compared the relaxation dynamics of the vibronic bands in the solvents in order to investigate the effect of solvent polarity, dipole moment on the excited state lifetime of BP at various emission wavelengths. Steady-state and time resolved experiments of BP in the anionic micellar solutions confirmed the location of the probe BP. In order to study the dipolar interaction of BP with another organic dye, we have monitored FRET from BP to a well-characterized acceptor (and potential mutagen [19]) ethidium (Et), which selectively binds to the surface of the micelle [20-21]. Steady-state and picosecond resolved studies on the FRET between BP and Et from various vibronic bands have been analyzed using conventional and differential methods. The differential method introduced in this study relies on the individual spectral overlap of the vibronic bands with the absorption spectrum of acceptor Et and found to be more realistic for the estimation of D-A distance. We have also studied FRET between BP and acridine orange (AO) in the micelle to establish generality of the technique for the estimation of D-A distance. Unambiguous confirmation of the introduced

technique is revealed from the FRET from BP to crystal violet [22] (CV) in the nano-environments. CV is observed to offer significant and negligibly small spectral overlap with the band 3 (emission peak at 455 nm) and band 1 (emission peak at 410 nm), respectively. The differential behaviour of the vibronic bands of BP undergoing dipolar interaction with energy acceptors in the micellar solution has been compared with that of different dyes in a model system of ‘dye-blend’ (mixture of dyes) representing different electronic systems undergoing FRET with CV in toluene. In this regard, three different quantum dots (QDs), QD480, QD570 and QD625 having emission maxima at 480, 570 and 625 nm, respectively have been considered as the components of the ‘dye-blend’. Theoretical framework employing well known ‘Infelta-Tachiya model’ [21] and D-A distance distribution analysis have also been considered in our study in order to further establish the validity of the introduced differential technique of FRET calculation.

8.2. Results and Discussion:

8.2.1. A Potential Carcinogenic Pyrene Derivative under FRET to Various Energy Acceptors in Nanoscopic Environments [23]:

8.2.1.1. Effect of different solvents on the excited state lifetime of BP. Normalized absorption and emission spectra of BP in various solvents are presented in Figure 8.1 (a). Solvent dependent shifting of both the absorption and the fluorescence spectra of BP is in close agreement with earlier studies [6] suggesting solvent sensitive changes in the ground as well as the excited state electronic properties of BP. The picosecond resolved fluorescence transients of BP in different solvents are shown in Figure 8.1 (b) and the multiexponential fitting parameters are tabulated in Table 8.1. Figure 8.1 (b) and Table 8.1 indicate that the lifetime of BP varies with solvents without much deviation at the different vibronic fine structures. As evident from Table 8.1, BP shows biexponential decays with time constants of 2-5 ns and 12-20 ns in all the solvents. It has to be noted that the absorption and emission spectra of BP in all the solvents are consistent with those of the monomeric form of BP [6]. No clear correlation of the excited state lifetime with the polarity/proticity of the solvents is evident from the Table 8.1. For example the lifetime

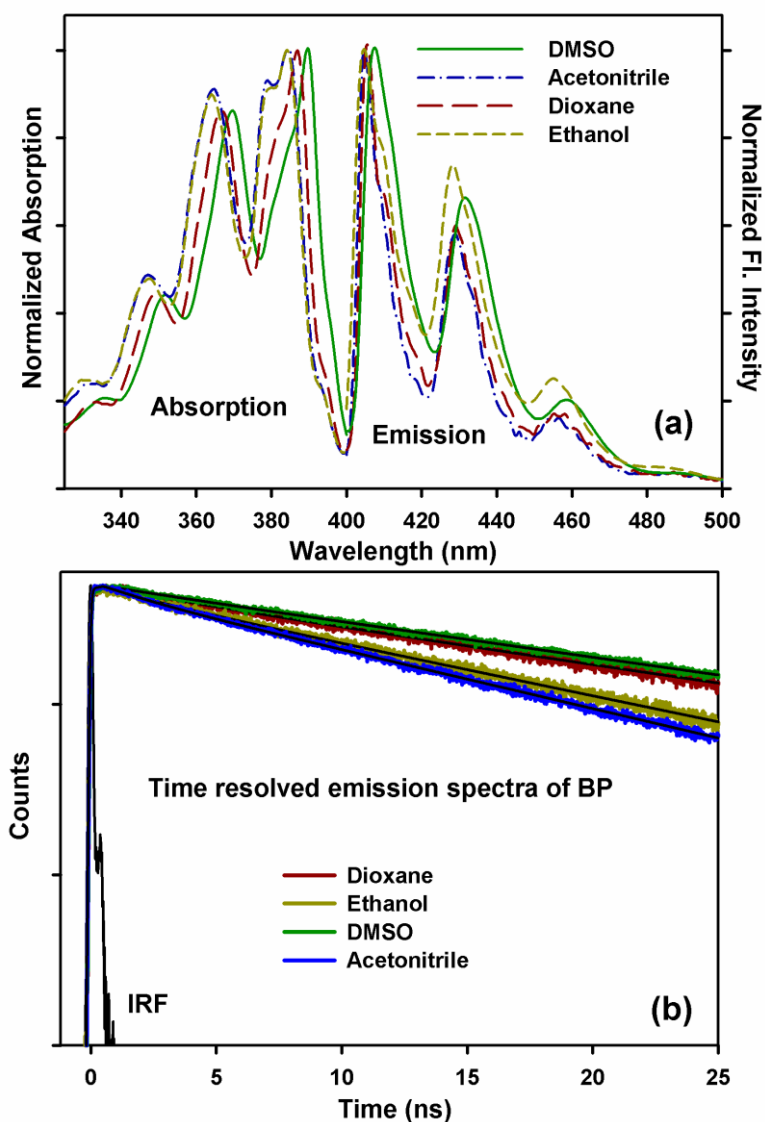


Figure 8.1. (a) Normalized absorption and emission spectra of BP in different solvents, DMSO, acetonitrile, dioxane and ethanol and (b) the time resolved fluorescence transients of the same at 410 nm (λ_{em}) upon exciting at 375 nm (λ_{ex}).

values of BP in DMSO (polar aprotic) and dioxane (non-polar aprotic) are similar. Similarity of lifetime values in ethanol (polar protic) and acetonitrile (polar aprotic) is also noticeable. In an earlier study using steady-state spectroscopy, it has been shown that spectral shifts of the vibronic bands of BP depend on the polarizability (rather dielectric constant) of the host solvents [6]. We have also investigated the polarizability dependence of radiative rate constants of BP in various solvents with different refractive indices. The excited state lifetime values of BP in various solvents are tabulated in Table 8.2. It is

evident from Figure 8.2 that the experimental values of radiative rate constants (k_r) (blue dots) of BP in different solvents are way off from the theoretical estimation (solid line) following different theoretical models [24]. Therefore, a distinct correlation of the spectral shift/lifetime of the vibronic fine structures with the dipole moment/dielectric constant/refractive index is not evident from our studies and invites more studies, which are motivations of our future works. However, the excited state photophysics including fluorescence lifetime of BP in various solvents are found to be useful to conclude the location of the probe BP in micro heterogeneous environment. The comparison of the emission spectra and excited state lifetime of BP in dioxane (non-polar and aprotic) with that in the sodium dodecyl sulphate (SDS) micelle (Figure 8.3) clearly reveals that probe BP prefers to stay in the hydrophobic core of the micelle which is in close agreement with the earlier studies [6].

Table 8.1: The lifetime components of BP at its characteristic emission peaks in various solvents. τ represents the time constant in ns and the numbers in the parenthesis represent relative contribution of the component. τ_{av} represents the average lifetime in ns. Error $\pm 5\%$

Sample	Wavelength (nm)	τ_1 (ns)	τ_2 (ns)	τ_3 (ns)	τ_{av} (ns)
BP in DMSO	410	2.00 (5%)	20.10 (95%)		19.20
	430	2.00 (10%)	20.10 (90%)		18.30
	455	2.00 (20%)	20.50 (80%)		16.80
BP in acetonitrile	410	2.10 (12%)	12.50 (88%)		11.30
	430	1.80 (14%)	12.60 (86%)		11.10
	455	1.60 (26%)	12.60 (74%)		9.70
BP in dioxane	410	5.00 (9%)	20.30 (91%)		18.90
	430	5.00 (11%)	20.40 (89%)		18.70
	455	5.00 (20%)	20.70 (80%)		17.60
BP in ethanol	410	3.60 (10%)	14.20 (90%)		13.20
	430	3.30 (11%)	14.20 (89%)		13.00
	455	3.30 (20%)	14.00 (80%)		11.90

8.2.1.2. Photophysical characterization of the excited BP molecules. Upon excitation with the laser source of 375 nm, the BP molecules are typically excited to S_1 , usually to an

excited vibrational level. The multiple peaks in the absorption spectrum of BP in SDS solution at 330, 349, 368 and 388 nm, as shown in Figure 8.3 are assigned to the individual

Table 8.2: The fluorescence lifetime components τ_1 and τ_2 represent fluorescence lifetimes of BP in different solvents. Figures in parentheses show relative contribution. Error $\pm 5\%$

Solvents	Refractive index (n)	Wavelength (nm)	τ_1 (ns)	τ_2 (ns)	τ_{av} (ns)	k_r (ns ⁻¹)
DMSO	1.479	410	2.00 (5%)	20.10 (95%)	19.20	0.05
		430	2.00 (10%)	20.10 (90%)	18.30	0.05
		455	2.00 (20%)	20.50 (80%)	16.80	0.06
Acetonitrile	1.346	410	2.10 (12%)	12.50 (88%)	11.30	0.09
		430	1.80 (14%)	12.60 (86%)	11.10	0.09
		455	1.60 (26%)	12.60 (74%)	9.70	0.10
Dioxane	1.4224	410	5.00 (9%)	20.30 (91%)	18.90	0.08
		430	5.00 (11%)	20.40 (89%)	18.70	0.09
		455	5.00 (20%)	20.70 (80%)	17.60	0.14
Ethanol	1.3624	410	3.60 (10%)	14.20 (90%)	13.20	0.09
		430	3.30 (11%)	14.20 (89%)	13.00	0.09
		455	3.30 (20%)	14.00 (80%)	11.90	0.12
Acetone	1.359	410	1.30 (7%)	26.00 (93%)	24.30	0.04
		430	1.00 (9%)	26.00 (91%)	23.70	0.04
		455	1.30 (14%)	24.80 (86%)	21.60	0.05
Benzene	1.5011	410	1.50 (9%)	11.70 (91%)	10.80	0.10
		430	1.40 (11%)	11.60 (89%)	10.50	0.10
		455	1.60 (20%)	11.40 (80%)	9.40	0.11
Cyclohexane	1.4262	410	1.10 (9%)	13.10 (91%)	12.00	0.08
		430	1.10 (11%)	13.20 (89%)	11.80	0.09
		455	1.30 (20%)	12.80 (80%)	10.50	0.10
Diethyl ether	1.3497	410	1.10 (9%)	13.10 (91%)	12.00	0.08
		430	1.20 (11%)	12.80 (89%)	11.50	0.09
		455	1.50 (20%)	12.60 (80%)	10.40	0.10
Dimethyl formamide (DMF)	1.4305	410	0.80 (7%)	16.50 (93%)	15.40	0.07
		430	1.00 (5%)	16.60 (95%)	15.90	0.06
		455	1.30 (9%)	16.30 (91%)	14.90	0.07
Ethylene glycol	1.4318	410	0.70 (9%)	27.00 (91%)	24.50	0.04
		430	0.70 (9%)	27.00 (91%)	24.50	0.04
		455	0.90 (11%)	26.30 (89%)	23.40	0.04
Methanol	1.3284	410	0.70 (11%)	11.60 (89%)	10.40	0.10
		430	0.60 (13%)	11.60 (87%)	10.20	0.10
		455	1.30 (16%)	11.50 (84%)	9.90	0.10
Heptane	1.387	410	1.30 (9%)	8.10 (91%)	7.50	0.13
		430	1.30 (11%)	8.10 (89%)	7.40	0.14
		455	1.20 (17%)	8.10 (83%)	6.90	0.15

electronic transitions of BP as reported earlier [25]. The molecular symmetry of BP [25] being C_s allows infinite possible moment directions for electric dipole allowed transitions: perpendicular to the molecular plane (e.g. $\sigma \rightarrow \pi^*$) or along any direction in it ($\pi \rightarrow \pi^*$). The angles Φ formed by the moments of observed transitions with a specific, well-defined molecular axis in the plane is reported [25] to be 30° for the electronic transition at 330, 349, 368 and 388 nm. The orientation factor K_i , the average cosine square of the angle between the moment of transition and the molecular orientation axis has also been reported with a value of 0.56 for the above electronic transitions [25].

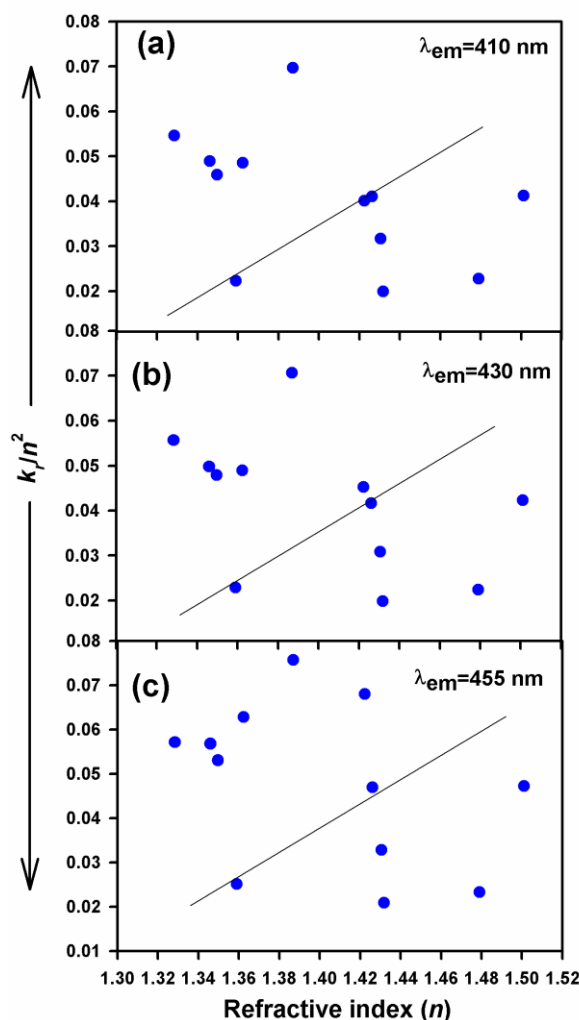


Figure 8.2. Plot of k_r/n^2 vs. refractive index (n) of the solvents at different vibronic bands of BP having emission maxima at (a) 410, (b) 430 and (c) 455 nm. k_r represents radiative rate constants of BP. Solid line represents estimation from theoretical models [24] while blue dots are the values obtained from experiments.

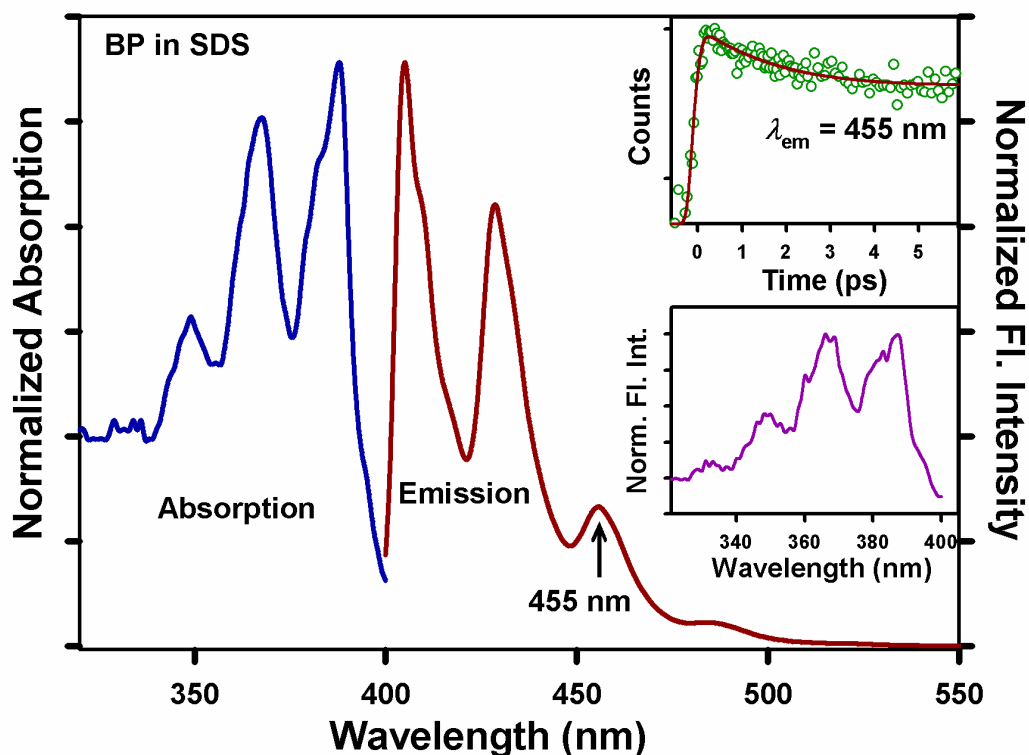


Figure 8.3. Normalized absorption and emission spectra of BP in SDS micelle. Lower inset shows the normalized excitation spectrum of the same. Upper inset shows femtosecond resolved fluorescence transient of BP at one of its emission peaks (455 nm) upon excitation at 375 nm.

An interesting consequence of emission to higher vibrational ground states is that the emission spectrum is typically a mirror image of the absorption spectrum of the $S_0 \rightarrow S_1$ transition (Figure 8.3). This similarity occurs because electronic excitation does not greatly alter the nuclear geometry [26]. Figure 8.3 upper inset shows the femtosecond resolved fluorescence transient of BP in SDS micelle at 455 nm, upon exciting the probe at 375 nm. The transient can be fitted biexponentially with the time constants of 1.33 ps (61%) and 30 ns (39 %). The slower component of 30 ns has been obtained from picosecond resolved experiments (see later) and has been fixed in the above fitting. The faster time constant (1.33 ps) is close to the time constant of ~ 2 ps which is assigned to the vibrational cooling of the S_1 local pyrene state, initially formed with excess vibrational energy [27]. Lower inset of Figure 8.3 shows the excitation spectra of BP in SDS micelle which is identical for each vibronic structure, thus, rules out the possibility of accumulation of different excited states.

8.2.1.3. Differential behaviour of the vibronic bands of BP under FRET. To monitor the characteristic behaviour of different vibronic bands of BP while undergoing dipolar interactions, we employed Förster resonance energy transfer (FRET) studies. For accomplishment of such studies, we have used a well-characterized FRET acceptor ethidium (Et) at the surface of the anionic micelle [20-21]. Figure 8.4 (a) shows spectral overlap between the emission spectrum of the BP (donor) and the absorption spectrum of

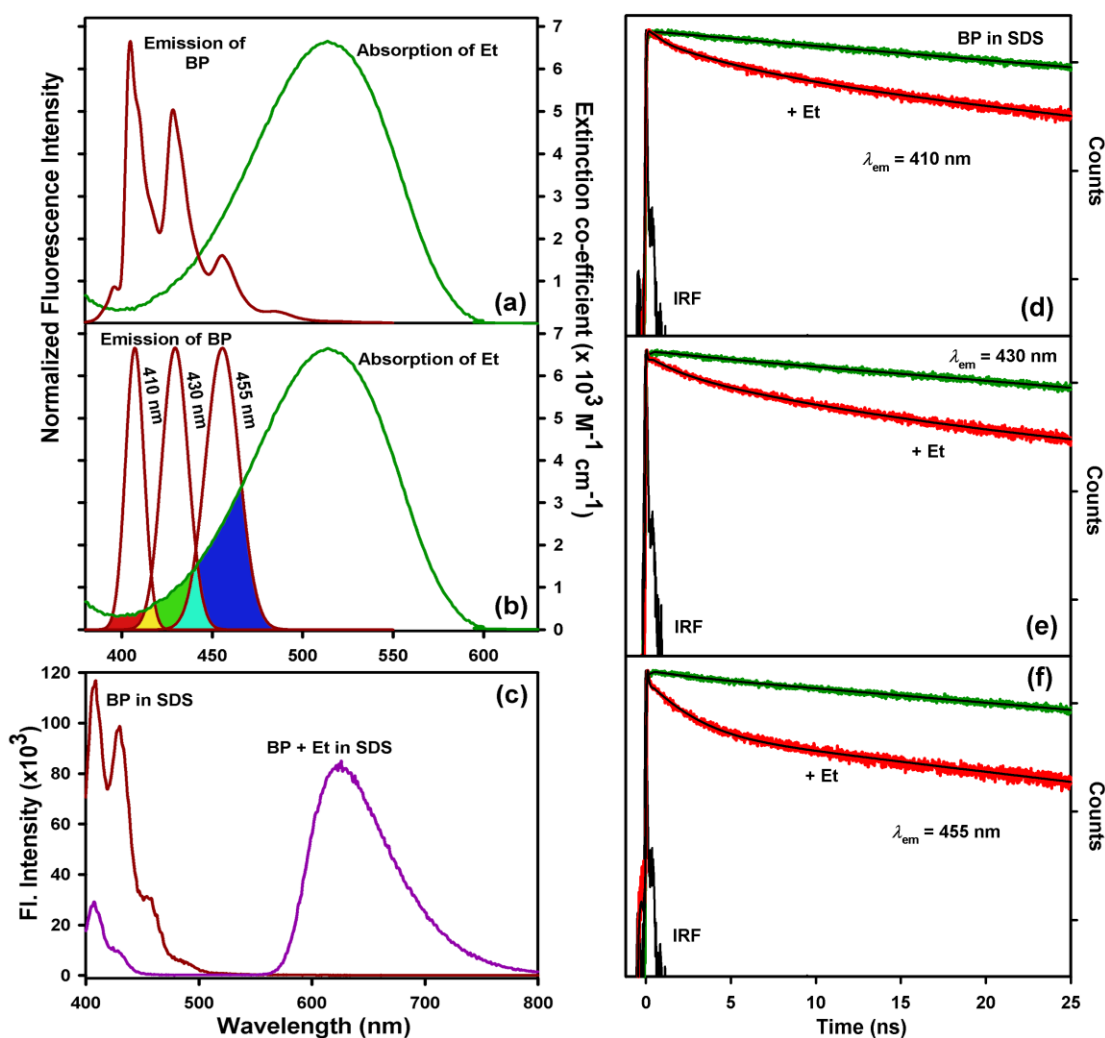


Figure 8.4. Spectral overlap of BP emission and Et absorption in 100 mM SDS ($\sim 1.48 \text{ mM}$ micellar concentration) without (a) and with (b) the deconvolution of the emission spectrum of BP at three specific wavelengths 410, 430 and 455 nm. (c) The emission spectrum of BP in SDS micelle before and after the addition of the acceptor Et. Picosecond resolved fluorescence transients of the donor BP molecules bound to SDS micelles with (red) and without (green) acceptor Et at (d) 410 nm, (e) 430 nm and (f) 455 nm. λ_{em} denotes emission wavelength. Excitation wavelength (λ_{ex}) is 350 nm for (a) and (b) and 375 nm for (c, d e and f).

the Et (acceptor) in SDS micelle. At this juncture it is worth mentioning that the FRET analysis considering overall overlap integral ($J(\lambda)$) of BP emission with Et absorption spectrum, unable to rationalize following two observations as evident from Figure 8.4. Firstly, different vibronic bands are undergoing different degrees of fluorescence

Table 8.3: Comparison of the Förster distance (R_0), overlap integral $J(\lambda)$ (between donor BP emission spectrum and acceptor Et absorption spectrum) obtained at the three deconvoluted emission peaks of the donor along with the energy transfer efficiency (E) and donor-acceptor distance (r) calculated from the time resolved experiments in presence of the acceptor Et.

Emission wavelength of donor BP (nm)	R_0 (nm)	$J(\lambda)$ ($M^{-1} cm^{-1} nm^4$)	E	r (nm)
410	2.16	1.09×10^{13}	64%	1.96
430	2.59	3.44×10^{13}	81%	2.03
455	2.47	1.12×10^{14}	84%	1.87

quenching (Figure 8.4 (c)). Secondly, the picosecond resolved non-radiative energy transfer rates from various vibronic bands are also found to be significantly different (Figure 8.4 (d), (e) and (f) and Table 8.4). The estimated D-A distance with this analysis process also reveals significant fluctuation in the values reported from different vibronic bands. The above anomaly can easily be taken care if the individual $J(\lambda)$ for each vibronic band with Et absorption spectrum is considered. The deconvoluted emission spectra of BP at its three well characterized emission peaks at 410, 430 and 455 nm are shown in Figure 8.4 (b). Here, it has to be noted that BP monomers also produce a weak emission band at around 480 nm [28] which has not been considered in the present study. The overlap integral, $J(\lambda)$, between the deconvoluted emission spectrum of the donor and the absorption spectrum of the acceptor, has been characterized for each vibronic band and the corresponding overlaps are shown in red, green and blue colors for emission maxima at 410, 430 and 455 nm respectively. The corresponding values of $J(\lambda)$ are tabulated in Table 8.3. The energy transfer takes place from the donor to the acceptor, as indicated by the quenching of fluorescence intensity (Figure 8.4 (c)) as well as the faster decay (Figure 8.4 (d), (e) and (f)) of the donor in the donor-acceptor complexes in micelles compared to that of only donor in the micelle. To compare the energy transfer efficiency of the donor from its various vibronic bands, the fluorescence transients of the donor at its different emission

peaks, 410, 430 and 455 nm have been monitored in absence and presence of the acceptor Et (Figure 8.4 (d), (e) and (f) and Table 8.4).

As evident from the Figure 8.4 (d), (e) and (f) and Table 8.4, the average lifetime of BP at 410, 430 and 455 nm is 29.92, 29.46 and 27.84 ns respectively. The slower component of 30 ns in the fluorescence transients of BP in SDS micelle, as given in Table 8.4 has been confirmed upon repeating the experiments with longer time window of 400 ns. Details of the FRET parameters from various vibronic bands are tabulated in Table 8.3. Here it has to be noted that the vibrational relaxation timescale as observed from our femtosecond resolved experiments is much faster than the energy transfer rates from the

Table 8.4: The lifetime components of the donor BP in SDS micelle in absence and presence of the acceptors Et, AO and CV. τ represents the time constant in ns and the numbers in the parenthesis represent relative contribution of the component. τ_{av} represents the average lifetime in ns. Error $\pm 5\%$

Sample	Wavelength (nm)	τ_1 (ns)	τ_2 (ns)	τ_3 (ns)	τ_{av} (ns)
BP in SDS micelle	410	4.80 (3%)	30.70 (97%)		29.90
	430	2.90 (5%)	30.90 (95%)		29.50
	455	2.50 (10%)	30.70 (90%)		27.80
BP in SDS micelle + acceptor (Et)	410	0.50 (28%)	4.50 (36%)	25.40 (36%)	10.90
	430	0.10 (59%)	4.20 (23%)	24.90 (18%)	5.50
	455	0.10 (56%)	2.30 (30%)	27.00 (14%)	4.50
BP in SDS micelle + acceptor (AO)	410	0.10 (21%)	2.10 (24%)	28.20 (55%)	16.00
	430	0.10 (63%)	2.50 (22%)	25.20 (15%)	4.40
	455	3.50 (96%)	15.50 (4%)		4.00
BP in SDS micelle + acceptor (CV)	410	4.90 (3%)	30.70 (97%)		29.90
	430	0.10 (81%)	1.90 (3%)	24.80 (16%)	4.10
	455	0.10 (89%)	2.20 (1%)	24.70 (10%)	2.60

vibronic bands. Thus, FRET is expected to occur after the thermalization process in the excited state. It is clear that the energy transfer efficiency (E) is higher at 455 nm compared to that at 410 nm and consistent with the overlap integral, $J(\lambda)$, between the deconvoluted donor emission at the corresponding wavelengths, with the absorption spectrum of the acceptor (Et), as shown in Figure 8.4 (b). From our time resolved studies the donor-acceptor distance (r) can be estimated to be 1.95 ± 0.08 nm and the fluctuation (0.8 \AA) is well within the experimental error limit.

Upon finding the different energy transfer efficiency of the individual vibronic bands of BP undergoing FRET with the acceptor Et molecules, another acceptor acridine orange (AO) has been chosen to find the consistency of such observation. AO, a cationic dye, is known to interact with SDS micelle through both hydrophobic and electrostatic

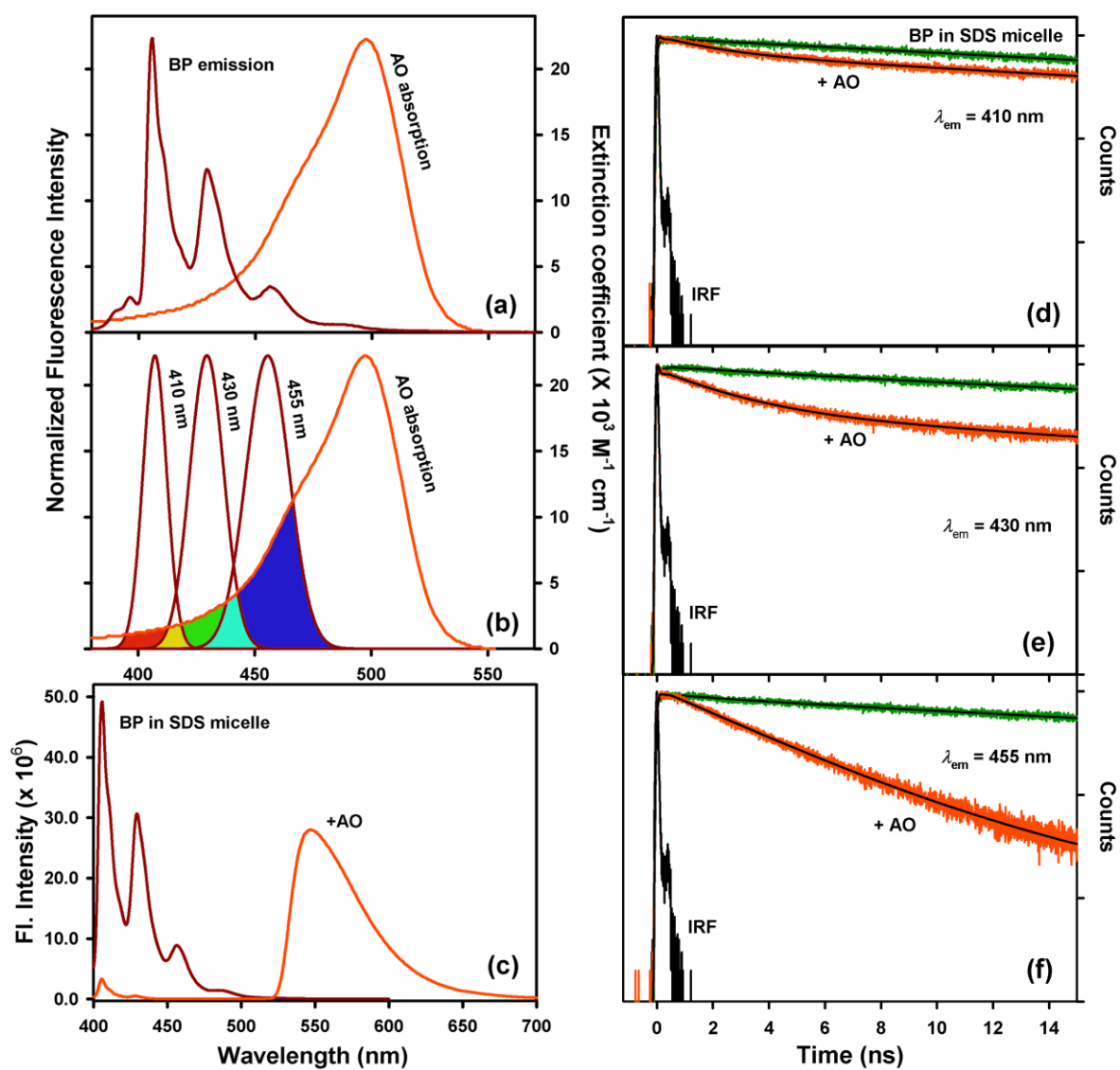


Figure 8.5. Spectral overlap of BP emission and AO absorption in 100 mM SDS ($\sim 1.48 \text{ mM}$ micellar concentration) without (a) and with (b) the deconvolution of the emission spectrum of BP at three specific wavelengths 410, 430 and 455 nm. (c) The emission spectrum of BP in SDS micelle before and after the addition of the acceptor AO. Picosecond resolved fluorescence transients of the donor BP molecules bound to SDS micelles with (orange) and without (green) acceptor AO at (d) 410 nm, (e) 430 nm and (f) 455 nm. λ_{em} denotes emission wavelength. Excitation wavelength (λ_{ex}) is 350 nm for (a) and (b) and 375 nm for (c, d e and f).

interactions as the hydrophobic aromatic rings of the AO molecule remain within the hydrophobic core of the SDS micelle, and the charged intracyclic imino group and the two terminal polar amino groups remain outward directed toward the stern layer [29-31]. Figure 8.5 (a) and (b) respectively show the overall and deconvoluted spectral overlap between the emission spectrum of the BP (donor) and the absorption spectrum of the AO (acceptor) in the micelle. The overlap integral, $J(\lambda)$, between the deconvoluted emission spectrum of the donor and the absorption spectrum of the acceptor AO, has been characterized for each emission peak and tabulated in Table 8.5. Quenching of the fluorescence intensity of the donor in presence of the acceptor AO is shown in Figure 8.5 (c). The picosecond resolved FRET is clearly evident from Figure 8.5 (d), (e) and (f) and Table 8.4. As evident from Figure 8.5, Table 8.4 and Table 8.5, the steady-state quenching and temporal behavior of the vibronic bands distinctly follows the individual overlap integral of the bands with the absorption of AO in the micelle. The estimated D-A distance 2.48 nm is also found to be comparable to that of BP-Et distance.

Table 8.5: Comparison of the Förster distance (R_0), overlap integral $J(\lambda)$ (between donor BP emission spectrum and acceptor AO absorption spectrum) obtained at the three deconvoluted emission peaks of the donor along with the energy transfer efficiency (E) and donor-acceptor distance (r) calculated from the time resolved experiments in presence of the acceptor AO.

Emission wavelength of donor BP (nm)	R_0 (nm)	$J(\lambda)$ ($M^{-1} cm^{-1} nm^4$)	E	r (nm)
410	2.68	3.99×10^{13}	46%	2.75
430	3.08	9.59×10^{13}	85%	2.31
455	2.99	3.46×10^{14}	86%	2.21

The energy acceptors Et and AO considered so far offer different degree of spectral overlap with all the vibronic bands of BP. The consequence of the differential $J(\lambda)$ with the vibronic bands are described in the earlier section. Unambiguous evidence of the effect of differential $J(\lambda)$ with the vibronic bands on the corresponding FRET efficiency from the bands can be achieved in a control experiment, where the acceptor offers essentially no overlap with some bands and partial with others. Use of crystal violet (CV) as potential acceptor offers essentially no overlap with band 1 (emission peak at 410 nm) and significant overlap with band 3 (emission peak at 455 nm). The interaction of CV probe molecules on SDS micelle has been investigated previously and concluded to reside at the

surface of the micelle [22]. The overall and deconvoluted $J(\lambda)$ s are shown in Figure 8.6 (a) and (b), respectively. The overlap integral, $J(\lambda)$, between the deconvoluted emission spectrum of the donor and the absorption spectrum of the acceptor CV, has been characterized for each emission peak and tabulated in Table 8.6. For the better view of the mentioned areas of overlap, between deconvoluted emission spectrum of the donor BP and absorption spectrum of acceptor CV, the overlapped region has been magnified and shown in Figure 8.6 (b) inset. The steady-state fluorescence quenching of the donor BP in presence of the acceptor CV is shown in Figure 8.6 (c). As evident from the Figure 8.6 (c), steady-state fluorescence quenching of BP occurs at all the vibronic bands of BP which can be due to formation of non-radiative donor-acceptor complexes in the ground state or due to energy transfer and hence steady-state fluorescence quenching is inconclusive as reported earlier [18, 26]. It has to be noted that band 3 is differentially quenched compared to others, as a consequence of larger $J(\lambda)$ with the acceptor CV. To compare the energy transfer efficiency of the donor from its various vibronic structures, the fluorescence transients of the donor at its different emission peaks, 410, 430 and 455 nm have been monitored in absence and presence of the acceptor CV (Figure 8.7 and Table 8.4). The corresponding FRET parameters are tabulated in Table 8.6. As evident from the Figure 8.6 (b) inset, there is negligible or almost no overlap between the emission spectrum of BP at 410 nm and the CV absorption spectrum, which consequently produces no fluorescence lifetime quenching of the donor BP at 410 nm in presence of the acceptor CV. However, there is significant lifetime quenching of the fluorophore at the other two vibronic bands (430 and 455 nm). The observation is consistent with our previous results considering other two acceptors showing overlap integral dependent fluorescence lifetime quenching of the individual vibronic bands. Furthermore, the present observation, where we find no quenching at vibronic band 1 due to negligible overlap with the absorption of the acceptor CV, highlights the conclusive evidence of differential FRET from the vibronic bands of the donor BP.

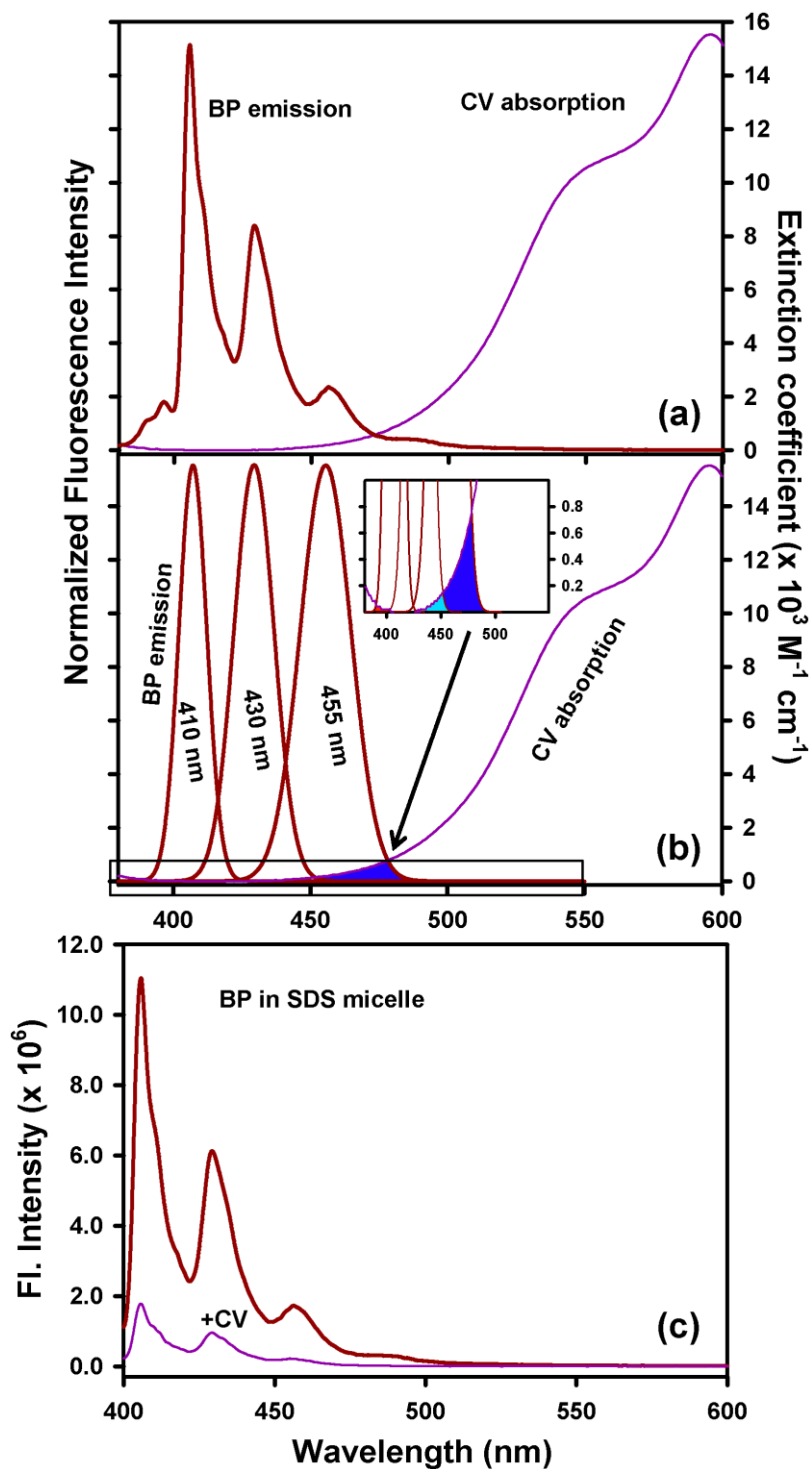


Figure 8.6. Spectral overlap of BP emission and CV absorption in 100 mM SDS (~ 1.48 mM micellar concentration) without (a) and with (b) the deconvolution of the emission spectrum of BP at three specific wavelengths 410, 430 and 455 nm. Figure 8.6 (b) inset is magnified view of the overlapped region marked by a rectangle on Figure 8.6 (b). (c) The emission spectrum of BP in SDS micelle before and after the addition of the acceptor CV [excitation wavelength (λ_{ex}) is 350 nm for (a) and (b) and 375 nm for (c)].

Table 8.6: Comparison of the Förster distance (R_0), overlap integral $J(\lambda)$ (between donor BP emission spectrum and acceptor CV absorption spectrum) obtained at the three deconvoluted emission peaks of the donor along with the energy transfer efficiency (E) and donor-acceptor distance (r) calculated from the time resolved experiments in presence of the acceptor CV.

Emission wavelength of donor BP (nm)	R_0 (nm)	$J(\lambda)$ ($M^{-1} cm^{-1} nm^4$)	E	r (nm)
410	1.03	1.26×10^{11}	0%	-
430	1.32	6.04×10^{11}	86%	0.75
455	1.66	1.02×10^{13}	91%	1.13

8.2.1.4. Comparison of the differential behaviour of the vibronic bands of BP under FRET with that of different dyes in a ‘dye blend’ representing different electronic states. From our studies, the differential FRET from various vibronic bands of BP can be compared with the case of ‘dye-blend’ (mixture of dyes) under FRET to an energy acceptor in solution. In this regard, we have investigated FRET of a mixture of three quantum dots (QDs) having different emission maxima, to an energy acceptor CV. Figures 8.8 (a) and (b) respectively show the overall and deconvoluted spectral overlap between the emission spectra of the QDs (donor) and the absorption spectrum of the CV (acceptor) in toluene. The overlap integral, $J(\lambda)$, between the deconvoluted emission spectrum of the donor QDs and the absorption spectrum of the acceptor CV, has been characterized and tabulated in Table 8.7. The picosecond resolved FRET is clearly evident from Figure 8.8 (c) and Table 8.8. As evident from Figure 8.8, Table 8.7 and 8.8, temporal behavior of the QDs in presence of the acceptor CV in toluene is comparable to the overlap integral dependent quenching behavior of the individual vibronic bands of BP with different acceptors in the micelle.

8.2.1.5. Verification of the introduced method of differential FRET calculation employing the standard theoretical framework and D-A distribution. The suitability of the differential over integral analysis procedure introduced in the present study in the standard theoretical frame work for the FRET to estimate average number of quenchers/quenching constants developed by Infelta and Tachiya [21] has also been investigated. We have determined the values of the parameters m , k_q , and k_0 as described

Table 8.7: Comparison of the Förster distance (R_0), overlap integral $J(\lambda)$ (between donor QDs emission spectra and acceptor CV absorption spectrum) obtained at the three deconvoluted emission peaks of the donor QDs along with the energy transfer efficiency (E) and donor-acceptor distance (r) calculated from the time resolved experiments in presence of the acceptor CV.

Emission wavelength of donor QDs (nm)	R_0 (nm)	$J(\lambda)$ ($M^{-1} cm^{-1} nm^4$)	E	r (nm)
480	5.2	7×10^{15}	95%	3.2
570	6.0	16.7×10^{15}	97%	3.4
625	6.4	22.5×10^{15}	99%	2.9

Table 8.8: The lifetime components of various QDs at their characteristic emission peaks in absence and presence of acceptor CV. QDs mixture consists of three quantum dots QD480, QD570 and QD625 having emission maxima at 480, 570 and 625 nm, respectively. τ represents the time constant in ns and the numbers in the parenthesis represent relative contribution of the component. τ_{av} represents the average lifetime in ns. Error $\pm 5\%$

Sample	Emission Wavelength (nm)	τ_1 (ns)	τ_2 (ns)	τ_3 (ns)	τ_{av} (ns)
QDs mixture	480	0.80 (36%)	12.70 (64%)	-	8.40
	570	1.10 (25%)	11.40 (75%)	-	8.70
	625	1.10 (17%)	16.20 (83%)	-	13.60
QDs mixture +CV	480	0.10 (72%)	0.90 (24%)	4.40 (4%)	0.40
	570	0.10 (85%)	0.70 (13%)	4.80 (2%)	0.30
	625	0.10 (93%)	0.50 (6%)	3.00 (1%)	0.10

under materials and methods section by fitting the equation (2-54) to the decay curves of the donor BP molecules in the absence and presence the acceptors Et, AO and CV (Figure 8.9 left panel and Table 8.9).

Figure 8.9 left panel shows the time resolved fluorescence transients of BP monitored at its different emission peaks, 410, 430 and 455 nm in absence and presence of Et, AO and CV fitted with equation (2-54). Since our time resolved studies (Figure 8.7 (a) and Table 8.4) show that CV does not quench the fluorescence lifetime of the donor BP at 410 nm, the corresponding fluorescence transient has not been fitted with the equation of

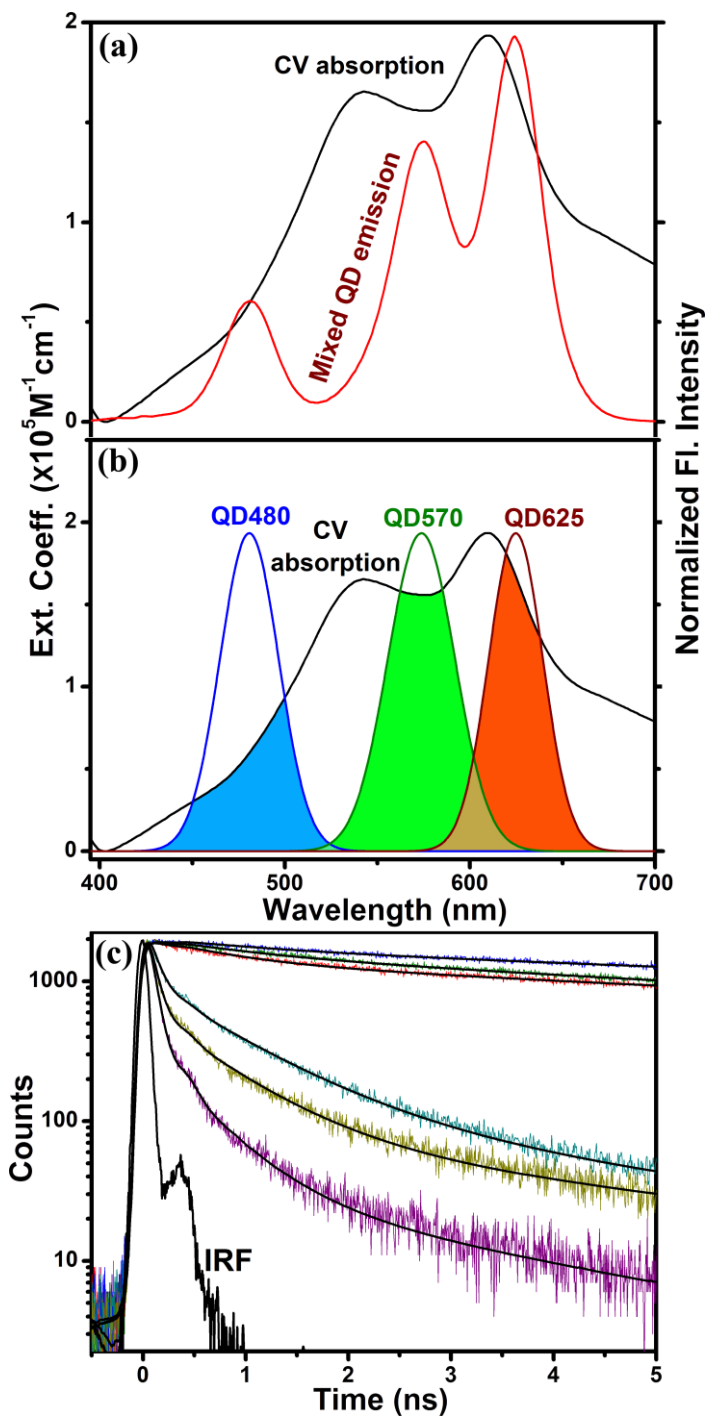


Figure 8.8. Spectral overlap between the emission of mixed QDs (donor) and the extinction of CV (acceptor) without (a) and with (b) the deconvolution of the emission spectrum of mixed QDs at three specific wavelengths 480, 570 and 625 nm. (c) Picosecond resolved fluorescence transients of the donor (mixed QDs) monitored at 625 nm (blue), 570 nm (green) and 480 nm (red). The quenching of the fluorescence transients in presence of acceptor CV has been shown where cyan represents the decay transient of donor in presence of CV when monitored at 480 nm, yellow represents the decay transient of donor in presence of CV when monitored at 570 nm and magenta represents the decay transient of donor in presence of CV when monitored at 625 nm. Excitation wavelength (λ_{ex}) is 375 nm for all the cases.

the kinetic model (equation 2-54). As evident from the Figure 8.9 left panel, the model describes the decay curves reasonably well. The quenching parameters are summarized in Table 8.9. Upon fitting the decay curves of BP with the kinetic model mentioned before, it is apparent that the distribution of acceptor molecules on the micellar surface does not change with the wavelength at which the donor emission is monitored.

As summarized in Table 8.9, the mean number of acceptor molecules associated with the micelle (m) remains same as 0.8, 1 and 0.7 respectively for Et, AO and CV at the three wavelengths corresponding to the three emission peaks of BP. The value of ' m ' being independent of the vibronic structure of the donor provides authenticity of the analysis procedure. However, the value of quenching rate constant (k_q) due to the acceptors depends on the wavelength at which the donor emission is monitored, being maximum at 455 nm and minimum at 410 nm with an intermediate value at 430 nm. The nature of change in k_q being similar to that of energy transfer efficiency mentioned before, holds well to the fact that k_q is also proportional to the overlap integral between the donor emission and acceptor absorption. Further studies are required for the better understanding of the observed variation of k_q with the emission wavelength of the donor BP molecules. The total decay constant (k_0) of the excited probe in absence of a quencher, remains same at all the three monitored wavelengths with a value of 0.032 ns^{-1} .

The above mentioned kinetic model has also been applied for the quenching of QDs by the acceptor CV in toluene. We have determined the values of the parameters m_t , k_{qt} , k_0 , m , and k_q by fitting equation (2-55) and (2-56) to the decay curves of QDs in the absence and presence of acceptor (as described in materials and methods section) and tabulated in Table 8.10. The corresponding fitting curves are shown in Figure 8.9 right panel.

In order to get idea of the probability distribution of donor-acceptor distance, we have analyzed the time resolved decay transients of donor BP in presence and absence of acceptor Et, as shown in Figure 8.10 (a) to construct the distance distribution function, $P(r)$ (see experimental section for details). As evident in Figure 8.10 (b), (c) and (d), the half width (hw) of the distance distribution is found to be 3.3 \AA for all the three vibronic bands under consideration. Similarly, for QDs the fluorescence transients of donor QD480,

QD570 and QD625 in toluene in absence and presence of the acceptor CV have been fitted upon considering the distance distribution between donor and acceptor in toluene as shown in Figure 8.11 (a) and the hw of the distance distribution has been found to be 3.3, 4.4 and 3.3 Å for QD480, QD570 and QD625, respectively as shown in Figure 8.11 (b), (c) and (d).

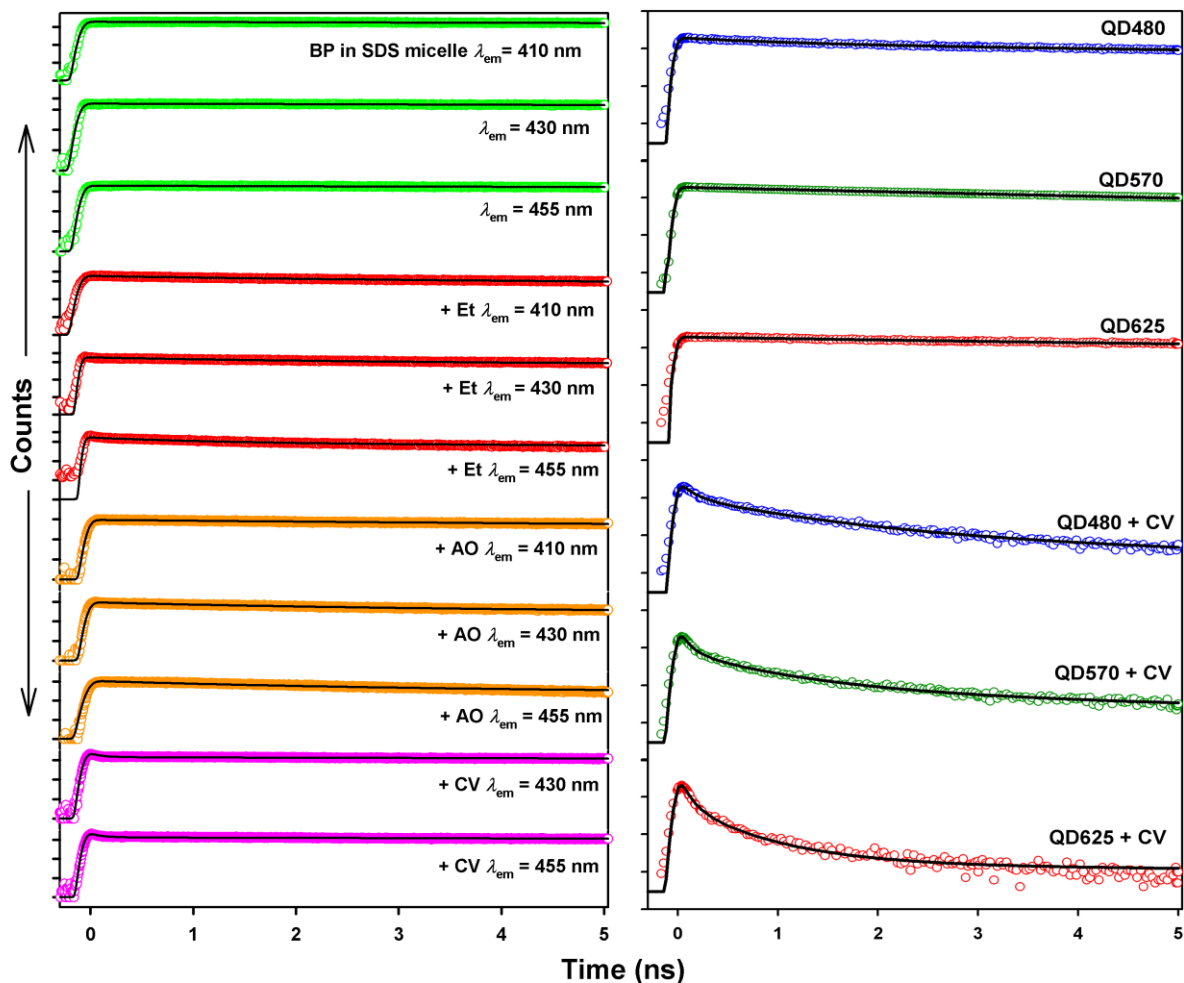


Figure 8.9. Left panel shows the fluorescence transients of the donor BP molecules bound to SDS micelle with (red, orange and pink circles) and without (green circles) acceptors Et, AO and CV molecules monitored at different wavelengths 410, 430 and 455 nm. Red, orange and pink colours in the fluorescence transients of BP represent the presence of Et, AO and CV acceptors in the micelle respectively. Right panel shows the fluorescence transients of the donor QDs (a) QD480 (blue) (b) QD570 (dark green) and (c) QD625 (dark red) in toluene in absence and presence of the acceptor CV. All the transients are fitted with the kinetic model developed by Infelta and Tachiya (see text). The Y-axis (Normalized Fl. Intensity) is presented in log scale and the baselines of the transients are vertically shifted for clarity.

Table 8.9: Values of the quenching parameters using the simplified version of the kinetic model developed by Infelta-Tachiya

Sample	λ_{em} (nm)	K_0 (ns ⁻¹)	K_q (ns ⁻¹)	m
BP in SDS micelle	410	0.032	-	-
	430	0.032	-	-
	455	0.032	-	-
BP + Et in SDS micelle	410	0.032	0.24	0.8
	430	0.032	0.35	0.8
	455	0.032	0.64	0.8
BP + AO in SDS micelle	410	0.032	0.07	1
	430	0.032	0.27	1
	455	0.032	0.30	1
BP + CV in SDS micelle	430	0.032	8.97	0.7
	455	0.032	9.23	0.7

Table 8.10: Overview of the value of quenching parameters for quantum dots in absence and presence of acceptor CV using kinetic model developed by Infelta-Tachiya. λ_{em} represents emission wavelength.

Sample	λ_{em} (nm)	k_o [ns ⁻¹]	m_t	k_{qt} [ns ⁻¹]	m	k_q [ns ⁻¹]
QDs mixture	480	0.07	0.41	0.67	-	-
	570	0.095	0.21	0.50	-	-
	625	0.03	1.12	0.06	-	-
QDs mixture + CV	480	0.07	3.31	0.38	0.93	6.40
	570	0.095	2.86	0.62	1.43	8.46
	625	0.03	4.03	0.99	1.56	8.20

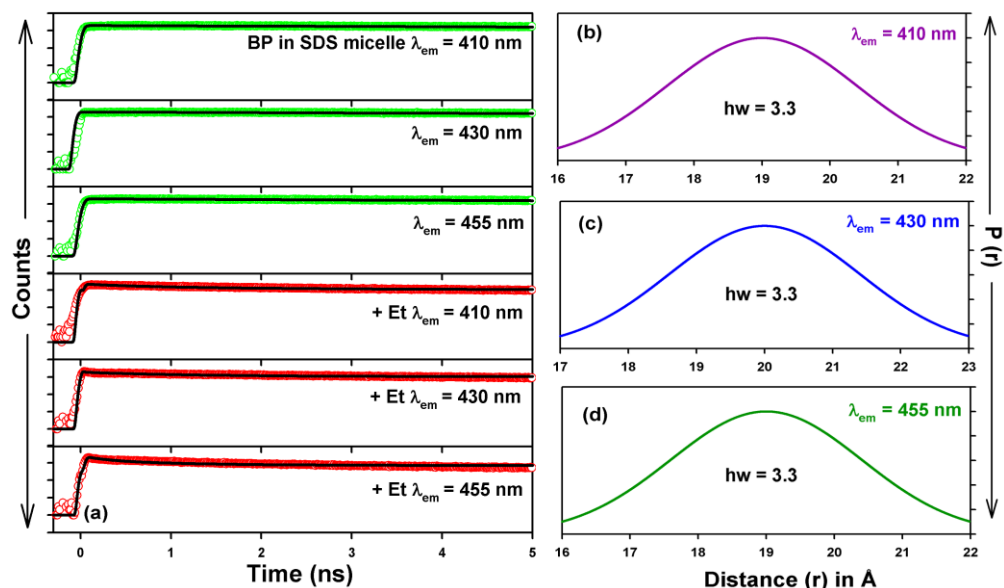


Figure 8.10. (a) Fluorescence transients of BP in SDS micelle in absence and presence of the acceptor Et, monitored at 410, 430 and 455 nm and fitted upon considering the distance distribution between donor and acceptor in SDS micelle. The probability of distance distribution ($P(r)$) with respect to mean distance between donor BP and acceptor Et for different vibronic bands under consideration having emission maxima at (b) 410, (c) 430 and (d) 455 nm.

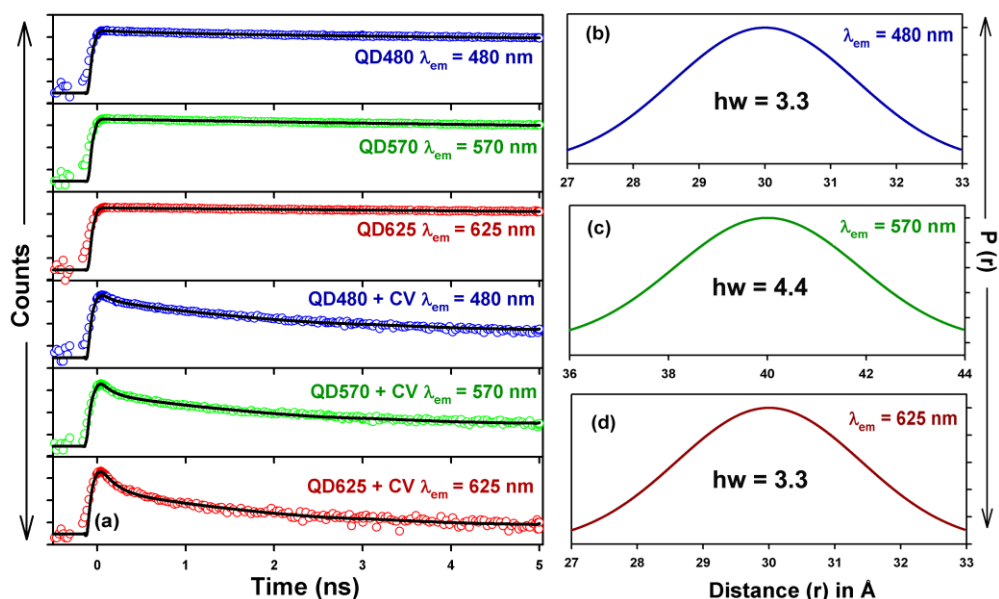


Figure 8.11. (a) Fluorescence transients of QD480, QD570 and QD625 in toluene in absence and presence of the acceptor CV and fitted upon considering the distance distribution between donor and acceptor in toluene. The probability of distance distribution ($P(r)$) with respect to mean distance between the donor QDs (b) QD480 (c) QD570 and (d) QD625 and acceptor CV in toluene.

8.3. Conclusion:

Here we have investigated the effect of excited state lifetime of a well known biological probe and food carcinogen benzo[*a*]pyrene (BP) in various solvents of different degrees polarity/proticity/dielectric constants and polarizabilities. Although the steady-state spectral shift is expected to follow the theoretical models, the time resolved studies on a number of solvents clearly invite better theoretical understanding of the photophysics of BP. Our present study also highlights the importance of the consideration of differential spectral overlap of the vibronic bands of BP undergoing FRET as a consequence of dipole-dipole interaction with an organic molecule in a confined environment. The differential behavior of the vibronic bands of BP under FRET has been compared with the behavior of a dye molecule in a dye-blend under FRET which shows reasonable similarity. Finally we have shown that the differential $J(\lambda)$ analysis is equally acceptable to the standard theoretical frame work for further interpretation of FRET data including the Infelta-Tachiya model and $P(r)$ analysis techniques. Our reported studies may find importance in the FRET analysis of biologically relevant pyrene class of molecules.

References

- [1] M. Gratzel, J. K. Thomas, On the Dynamics of Pyrene Fluorescence Quenching in Aqueous Ionic Micellar Systems. Factors Affecting the Permeability of Micelles, *J. Am. Chem. Soc.* 95 (1973) 6885.
- [2] K. Kalyanasundaram, J. K. Thomas, Environmental Effects on Vibronic Band Intensities in Pyrene Monomer Fluorescence and Their Application in Studies of Micellar Systems, *J. Am. Chem. Soc.* 99 (1977) 2039.
- [3] J. D. Morrisett, H. J. Pownall, R. T. Plumlee, L. C. Smith, Z. E. Zehner, Multiple Thermotropic Phase Transitions in Escherichia coli Membranes and Membrane Lipids. A comparison of Results Obtained by Nitroxyl Stearate Paramagnetic Resonance, Pyrene Excimer Fluorescence, and Enzyme Activity Measurements, *J. Biol. Chem.* 250 (1975) 6969.
- [4] J. A. Sigalat, J. S. SanMartin, C. E. A. Morales, E. Zaballos, R. E. Galian, J. P. Prieto, Further Insight into the Photostability of the Pyrene Fluorophore in Halogenated Solvents, *ChemPhysChem* 13 (2012) 835.
- [5] T. Shyamala, S. Sankararaman, A. K. Mishra, 1,3,6,8-Tetraethynylpyrene and 1,3,6,8-tetrakis (trimethylsilylethynyl) pyrene: Photophysical Properties in Homogeneous Media, *Chem. Phys.* 330 (2006) 469.
- [6] S. C. Beck, D. T. Cramb, Condensed Phase Dispersive Interactions of Benzo[a]pyrene with Various Solvents and with DNA: A Twist on Solvatochromism, *J. Phys. Chem. B* 104 (2000) 2767.
- [7] M. R. Vigil, J. Bravo, T. D. Z. Atvars, J. Baselga, Photochemical Sensing of Semicrystalline Morphology in Polymers: Pyrene in Polyethylene, *Macromolecules* 30 (1997) 4871.
- [8] G. W. Hsu, X. Huang, N. P. Luneva, N. E. Geacintov, L. S. Beese, Structure of a High Fidelity DNA Polymerase Bound to a Benzo[a]pyrene Adduct That Blocks Replication, *J. Biol. Chem.* 280 (2005) 3764.
- [9] K. Dutta, D. Ghosh, A. Nazmi, K. L. Kumawat, A. Basu, A Common Carcinogen Benzo[a]pyrene Causes Neuronal Death in Mouse via Microglial Activation, *Plos one* 5 (2010) 1.

- [10] T. Kometania, I. Yoshinob, N. Miuraa, H. Okazakia, T. Ohbaa, T. Takenakaa, F. Shojia, T. Yanoa, Y. Maeharaa, Benzo[a]pyrene Promotes Proliferation of Human Lung Cancer Cells by Accelerating the Epidermal Growth Factor Receptor Signaling Pathway, *Cancer Lett.* 278 (2009) 27.
- [11] B. Schuler, E. A. Lipman, P. J. Steinbach, M. Kumke, W. A. Eaton, Polyproline and the “Spectroscopic Ruler” Revisited with Single-Molecule Fluorescence, *Proc. Natl. Acad. Sci.* 102 (2005) 2754.
- [12] A. K. Shaw, R. Sarkar, S. K. Pal, Direct Observation of DNA Condensation in a Nano-Cage by Using a Molecular Ruler, *Chem. Phys. Lett.* 408 (2005) 366.
- [13] A. R. Clapp, I. L. Medintz, H. Mattoussi, Förster Resonance Energy Transfer Investigations Using Quantum-Dot Fluorophores, *ChemPhysChem* 7 (2006) 47.
- [14] D. Banerjee, S. K. Pal, Simultaneous Binding of Minor Groove Binder and Intercalator to Dodecamer DNA: Importance of Relative Orientation of Donor and Acceptor in FRET, *J. Phys. Chem. B* 111 (2007) 5047.
- [15] F. M. Chen, Binding of Pyrene to DNA, Base Sequence Specificity and its Implication, *Nucleic Acids Res.* 11 (1983) 7231.
- [16] M. Masuko, S. Ohuchi, K. Sode, H. Ohtani, A. Shimadzu, Fluorescence Resonance Energy Transfer from Pyrene to Perylene Labels for Nucleic Acid Hybridization Assays under Homogeneous Solution Conditions, *Nucleic Acids Res.* 28 (2000) e34i.
- [17] A. Kupstat, D. Knopp, R. Niessner, M. U. Kumke, Novel Intramolecular Energy Transfer Probe for the Detection of Benzo[a]pyrene Metabolites in a Homogeneous Competitive Fluorescence Immunoassay, *J. Phys. Chem. B* 114 (2010) 1666.
- [18] P. Majumder, R. Sarkar, A. K. Shaw, A. Chakraborty, S. K. Pal, Ultrafast Dynamics in a Nanocage of Enzymes: Solvation and Fluorescence Resonance Energy Transfer in Reverse Micelles, *J. Colloid Interface Sci.* 290 (2005) 462.
- [19] H. R. Mahler, P. S. Perlman, Effects of Mutagenic Treatment by Ethidium Bromide on Cellular and Mitochondrial Phenotype, *Arch. Biochem. Biophys.* 148 (1972) 115.
- [20] S. K. Pal, D. Mandal, K. Bhattacharyya, Photophysical Processes of Ethidium Bromide in Micelles and Reverse Micelles, *J. Phys. Chem. B* 102 (1998) 11017.

- [21] S. Banerjee, M. Tachiya, S. K. Pal, Caffeine-Mediated Detachment of Mutagenic Ethidium from Various Nanoscopic Micelles: An Ultrafast Förster Resonance Energy Transfer Study, *J. Phys. Chem. B* 116 (2012) 7841.
- [22] G. Revillod, I. R. Antoine, E. Benichou, C. Jonin, P. F. Brevet, Investigating the Interaction of Crystal Violet Probe Molecules on Sodium Dodecyl Sulfate Micelles with Hyper-Rayleigh Scattering, *J. Phys. Chem. B* 109 (2005) 5383.
- [23] S. Banerjee, N. Goswami, S. K. Pal, A Potential Carcinogenic Pyrene Derivative under Forster Resonance Energy Transfer to Various Energy Acceptors in Nanoscopic Environments, *ChemPhysChem* 14 (2013) 3581.
- [24] P. R. Ogilby, Solvent Effects on the Radiative Transitions of Singlet Oxygen, *Acc. Chem. Res.* 32 (1999) 512.
- [25] J. S. Larsen, J. Waluk, S. Eriksson, E. W. Thulstrup, Electronic States of Benzo[a]pyrene. Linear and Magnetic Circular Dichroism, Polarized Fluorescence, and Quantum Chemical Calculations, *J. Am. Chem. Soc.* 114 (1992) 1942.
- [26] J. R. Lakowicz, *Principles of Fluorescence Spectroscopy*, Kluwer Academic/Plenum, New York, 1999.
- [27] N. P. Gritsan, E. A. Pritchina, I. I. Barabanov, G. T. Burdzinski, M. S. Platz, Excited-State Dynamics in the Covalently Linked Systems: Pyrene-(CH₂)_n-Aryl Azide, *J. Phys. Chem. C* 113 (2009) 11579.
- [28] S. Banerjee, S. Sarkar, K. Lakshman, J. Dutta, S. K. Pal, UVA Radiation Induced Ultrafast Electron Transfer from a Food Carcinogen Benzo[a]pyrene to Organic Molecules, Biological Macromolecules and Inorganic Nano Structures, *J. Phys. Chem. B* 117 (2013) 3726.
- [29] A. K. Shaw, S. K. Pal, Fluorescence Relaxation Dynamics of Acridine Orange in Nanosized Micellar Systems and DNA, *J. Phys. Chem. B* 111 (2007) 4189.
- [30] J. W. Park, H. Chung, Aggregation and Dissolution of Cationic Dyes with an Anionic Surfactant, *Bull. Korean. Chem. Soc.* 7 (1986) 113.
- [31] A. M. Wiośetek-Reske, S. Wysocki, Spectral Studies of N-nonyl Acridine Orange in Anionic, Cationic and Neutral Surfactants, *Spectrochim. Acta A* 64 (2006) 1118.

List of Publications

(Peer-Reviewed Journals)

1. **S. Banerjee**, P. K. Verma, R. K. Mitra, G. Basu and S. K. Pal
“Probing the Interior of Self-Assembled Caffeine Dimer at Various Temperatures”, *J. Fluorescence*, 22 (2012) 753.
2. **S. Banerjee**, M. Tachiya and S. K. Pal
“Caffeine Mediated Detachment of Mutagenic Ethidium from Various Nanoscopic Micelle: An Ultrafast FRET Study”, *J. Phys. Chem. B*, 116 (2012) 7841.
3. **S. Banerjee**, D. Bhowmik, P. K. Verma, R. K. Mitra, A. Siddhanto, G. Basu and S. K. Pal
“Ultrafast Spectroscopic Study on Caffeine Mediated Dissociation of Mutagenic Ethidium from Synthetic DNA and Various Cell Nuclei”, *J. Phys. Chem. B*, 115 (2011) 14776.
4. **S. Banerjee** and S. K. Pal
“Caffeine Mediated Dissociation of a Potential Mutagen from DNA Mimetics, DNA and Cellular Nuclei: Ultrafast Spectroscopic Studies”, *Int. Review of Biophysical Chemistry*, 3 (2012) 173.
5. **S. Banerjee**, S. Sarkar, K. Lakshman, J. Dutta and S. K. Pal
“UVA Radiation Induced Ultrafast Electron Transfer from a Food Carcinogen Benzo[*a*]Pyrene to Organic Molecules, Biological Macromolecules and Inorganic Nano Structures”, *J. Phys. Chem. B*, 117 (2013) 3726.

6. **S. Banerjee**, N. Goswami and S. K. Pal
“A Potential Carcinogenic Pyrene Derivative under FRET to Various Energy Acceptors in Nanoscopic Environments”, *ChemPhysChem*, 14 (2013) 3581.
7. **S. Banerjee**, S. Chaudhuri and S. K. Pal
“Ultrafast Spectroscopic Studies on the Interaction of a Potential Food Carcinogen with Biologically Relevant Macromolecules”, *Int. Review of Biophysical Chemistry*, (2013).
- 8.* T. Mondol, **S. Banerjee**, S. Batabyal and S. K. Pal
“Study of Biomolecular Recognition Using Time-resolved Optical Spectroscopy”, *Int. Review of Biophysical Chemistry*, 2 (2011) 211.

(Patent Filed)

1. Mouthwash/Oral Care Formulation Involving Non-invasive Anti-Mutagenic Agent.
Indian Pat. Appl. (2011), 969/KOL/2011 dated 22nd July 2011.

* Not included in the thesis.